FINAL REPORT

Methods for the Efficient Estimation of the Reliability of Post-Elastic High-Rise Wind-Excited Structures Within a Performance-Based Design Setting

PREPARED BY:
Dr. Seymour MJ Spence
University of Michigan

SPONSOR:
Magnusson Klemencic Associates (MKA) Foundation

PROJECT PERIOD:
Jun. 01, 2017 - Dec. 31, 2018

Final Report:

Methods for the Efficient Estimation of the Reliability of Post-Elastic High-Rise Wind-Excited Structures Within a Performance-Based Design Setting

Prepared by: Dr. Seymour MJ Spence
University of Michigan

Sponsor: Magnusson Klemencic Associates (MKA) Foundation

Project Period: Jun. 01, 2017 - Dec. 31, 2018

Executive Summary

The aim of this project was the development of novel tools for the inelastic system-level reliability analysis of wind excited structural systems within the setting of state-of-the-art performance-based design. The underlying question was whether allowing controlled inelastic phenomena in the members of the main wind force-resisting system could increase the reliability of the system at ultimate load levels.

The main challenge in answering this question is the lack of theoretical and computational models for predicting the inelastic performance of wind excited structural systems. Indeed, while in seismic engineering there are an abundance of methodologies and numerical procedures for predicting inelastic behavior of structural systems, the same cannot be said for wind engineering. Certain fundamental features of wind excitation, which are not present in seismic excitation – for example the presence of a significant mean load component (leading to potential ratcheting failure), or long duration stationary cyclic loading (leading to potential low-cycle fatigue failure) – make the direct transfer of existing methods developed for seismic applications unfeasible.

This report outlines the development of a new generation of theoretical and computational models that respond to this challenge. The theoretical foundation on which these models are based is the theory of dynamic shakedown. Specifically, the state of dynamic shakedown is assumed as a safe system-level state for a wind excited structural system experiencing inelasticity. To enable this limit state to be assessed alongside any number of global and local limit states written in terms of inelastic responses such as residual drifts, peak interstory drifts, plastic deformations, a new class of path-following algorithms were developed. The computational efficiency of the algorithms in estimating the inelastic response of the system to a given wind load history, around two orders of magnitude faster than traditional step-by-step integration methods, allowed their integration with robust Monte Carlo simulation schemes, therefore enabling efficient reliability analyses of systems governed by inelastic system-level limit states.

To assess the feasibility and verify the models, a suite of example structures subject to stochastic wind loads were solved using both the proposed algorithms as well as computationally intensive step-by-step integration methods. Near perfect correspondence was seen in all cases, therefore providing confidence in the theoretical foundation of the approach. Finally, the proposed methods were applied to

the reliability analysis of a full scale 3D concrete core tower with outrigger system. The results demonstrated how a wind excited structural system designed to have controlled inelasticity can achieve system-level reliabilities that significantly exceed component-level reliabilities estimated through traditional design procedures.

Table of Contents

Acknowledgements ii
Table of Contents iv
List of Tables vii
List of Figures ix

1 A New Class of Shakedown Algorithms 1
1.1 Dynamic Shakedown 2
1.1.1 Classic solution 2
1.1.2 Underlying elastic solution 3
1.2 A Strain-Driven Concentrated Plasticity Model 4
1.2.1 Problem formulation 4
1.2.2 An iterative solution scheme 5
1.3 A Strain-Driven Distributed Plasticity Model 8
1.3.1 Mechanical model 8
1.3.2 Displacement-based element formulation 10
1.3.3 A fiber-based model 12
1.3.4 A section-based model 17
1.4 Concluding Remarks 20

Bibliography 21

2 A Probabilistic Dynamic Shakedown Framework 23
2.1 Problem Setting 24
2.2 The Proposed Framework 25
2.2.1 The artificial wind storm 25
2.2.2 The simulated load path 26
2.2.3 Remarks 26
2.3 Stochastic Wind Load Models 27
2.3.1 Wind tunnel driven model 27
2.3.2 Quasi-steady model 28
2.4 The Monte Carlo Simulation Strategy 30
2.5 Concluding Remarks 33

Bibliography 34

3 Verification and Examples **36**
3.1 Verification of the Simulated Load Path 37
3.1.1 Model description 37
3.1.2 Wind loads 39
3.1.3 Results 39
3.2 Statistical Validation of the Load Path 41
3.3 Verification of the Distributed Plasticity Model 48
3.3.1 Steel frame 48
3.3.2 Reinforced concrete frame 58
3.4 Example of the Monte Carlo Scheme 62
3.4.1 Description 62
3.4.2 Results 62
3.5 Concluding Remarks 66

Bibliography **67**

4 Case Study: Rainier Square Tower **69**
4.1 Numerical model of Rainier Square Tower 70
4.1.1 Finite element model 70
4.1.2 Verification of the FE model 74
4.2 Dynamic shakedown of Rainier Square Tower 75
4.2.1 Piecewise linearization of the yield surface 75
4.2.2 Stochastic wind loads 79
4.2.3 Shakedown analysis 81
4.3 System-level Susceptibility to Collapse 86
4.3.1 Uncertainties in the probabilistic framework 87
4.3.2 Calibration the probabilistic framework 89
4.3.3 Results 90
4.4 Concluding Remakes 94

Bibliography **95**

5 Reliability Analysis of Rainier Square Tower **96**
5.1 Code Development Consistent Uncertainties 97
5.1.1 Uncertainties in the structural system 97
5.1.2 Uncertainty propagation: steel beams 97
5.1.3 Uncertainty propagation: RC elements 98
5.1.4 Uncertainties in gravity and wind loads 101
5.2 Reliability of Rainier Square Tower 103
5.2.1 Design target for the structure 103
5.2.2 Reliability analysis 104
5.2.3 Results 105
5.3 Wind Record Selection Procedure 109

5.4 Concluding Remarks . . . 110

Bibliography **112**

6 Conclusions and Future Directions **115**

A Additional Information: Chapter 4 **117**
A.1 Model level elevations . . . 118
A.2 Elements assumed elastic in shakedown analysis . . . 120
A.3 Wind speed transformation scheme . . . 121
A.4 Inelastic elements for a representative sample . . . 122
A.4.1 Wind load of 300 MRI . . . 122
A.4.2 Wind load of 700 MRI . . . 129

B Inclusion of wind tunnel uncertainties **136**

C Element Layout: FEM Model of Rainier Square **138**

List of Tables

3.1 Section sizes of the steel frame. 38
3.2 Section sizes of the steel frame. 49
3.3 Comparison between the shakedown residual displacements obtained from proposed fiber-based strain-driven framework and direct integration of the steel frame under alongwind loads. 52
3.4 Comparison between the shakedown residual displacements obtained from proposed fiber-based strain-driven framework and direct integration of the steel frame under zero-mean loads. 56
3.5 The axial and bending strengths for all sections of the steel frame. 57
3.6 The shakedown residual displacements obtained from proposed section-based strain-driven framework of the steel frame under alongwind loads. 58
3.7 Bending strength for beam elements of the reinforced concrete frame. 60
3.8 The shakedown residual displacements obtained from the proposed section-based strain-driven framework of the reinforced concrete frame under alongwind loads. 60

4.1 Summary of material properties. 72
4.2 Summary of superimposed dead loading. 73
4.3 Natural periods of the FEM model fixed at level 01. 75
4.4 Mean and coefficient of variation (CV) of the elastic and plastic multipliers for all wind directions under wind loads of 300 MRI. . . 87
4.5 Mean and coefficient of variation (CV) of the elastic and plastic multipliers for all wind directions under wind loads of 700 MRI. . . 88
4.6 Probability of remaining elastic $P(E|\bar{v}_3)$ and of collapse susceptibility $P(C|\bar{v}_3)$ under 300 MRI wind loads. 90

5.1 Description of random variables in the structural system. 98
5.2 Bounds of sampling space. 99
5.3 Properties of the random variables used in modeling the gravity and wind loads. 103
5.4 List of redesigned coupling beams (Please see Appendix C for element locations). 104
5.5 Reliability indexes for the different limit states. 107

5.6 Elements with reliability indexes lower than the target reliability stipulated in ASCE 7-16 (Please see Appendix C for element locations). 107
5.7 Number of inelastic elements for the 3 samples of the Monte Carlo simulation for which Limit State 3 was not satisfied. 109
5.8 Ordered list of samples for which $s_e < 1$, i.e. for which inelasticity occurred in the system. Bold entries indicated samples for which the system did not satisfy Limit State 3 and was therefore susceptible to collapse. 110

A.1 Values of $\bar{v}_w$, K_R, and K_D for different wind directions. 121

List of Figures

1.1 Flowchart of the strain-based iterative dynamic shakedown algorithm. 7
1.2 Displacements, section forces and deformations for three-dimensional beam-column elements. 8
1.3 Discretization of fiber section. 9
1.4 Element nodal forces and displacements. 11

2.1 Illustration of a generic component of $\tilde{\mathbf{F}}$ for a wind storm of duration T. 27
2.2 Flowchart of the overall simulation strategy. 32

3.1 Schematic of the 37 story steel frame of the case study. 38
3.2 A realization of the top floor stochastic forcing function for (a) acrosswind direction, i.e. $\alpha = 0^o$; (b) alongwind direction, i.e. $\alpha = 90^o$. 40
3.3 Comparison between the residual displacements evaluated through the proposed framework and direct integration for the four randomly generated wind load histories. 42
3.4 Residual hinge rotation, θ_r, for (a) acrosswind and (b) alongwind responses of representative sample 1. 43
3.5 Residual hinge rotation, θ_r, for (a) acrosswind and (b) alongwind responses of representative sample 2. 43
3.6 Plastic hinge locations. 44
3.7 Deformed shape estimated from (a) strain-based dynamic shakedown and (b) direct integration for a representative acrosswind sample (deformed shape amplified by 250). 45
3.8 Deformed shape estimated from (a) strain-based dynamic shakedown and (b) direct integration for a representative alongwind sample (deformed shape amplified by 50). 46
3.9 Moment rotation history for a representative alongwind sample at (a) Hinge 1 (b) Hinge 223 and (c) Hinge 530. 47
3.10 Moment rotation history for a representative acrosswind sample at (a) Hinge 1 (b) Hinge 223 and (c) Hinge 530. 47
3.11 Comparison between residual displacements at the first floor for all 200 samples. 47
3.12 Comparison between plastic rotations at hinge 1 for all 200 samples. 48

3.13 Two-story two-bay frame. 49
3.14 Fiber discretization of (a) box section and (b) W-shape section. . . 50
3.15 The top floor stochastic wind loads for (a) alongwind excitation; (b) zero-mean loads. 51
3.16 Comparison between the fiber self-stresses obtained from fiber-based strain-driven method and direct integration of Element 1 of the steel frame subject to alongwind loads for: (a) Section 1; (b) Section 2; (c) Section 3; (d) Section 4 and (e) Section 5. 53
3.17 Element locations. 54
3.18 Plasticity distributed along Element 1 of the steel frame under alongwind loads obtained from the fiber-based framework. 54
3.19 Comparison between the fiber self-stresses obtained from the fiber-based strain-driven method and direct integration for Element 13 of the steel frame subject to zero-mean loads: (a) Section 1; (b) Section 2; (c) Section 3; (d) Section 4 and (e) Section 5. 55
3.20 Plasticity distributed along Element 13 of the steel frame under zero-mean loads obtained from the fiber-based framework. 56
3.21 Piecewise linear failure domain of steel box columns. 57
3.22 Plasticity distributed along Element 1 of the steel frame under alongwind loads obtained from the section-based framework. 58
3.23 Section sizes composing the reinforced concrete frame. 59
3.24 Fiber discretization of the rectangular elastic reinforced concrete section. 59
3.25 Piece-wise linear yield domains of: (a) Column C1; (b) Column C2. 61
3.26 Plasticity distributed along Element 13 of the reinforced concrete frame under alongwind loads obtained from the section-based framework. 61
3.27 Bounds on the probability of exceedance of the alongwind (MRI = 700 years) peak displacement responses at (a) Floor 1 (b) Floor 20 and (c) Floor 37. 63
3.28 Probability of exceedance of the residual displacements at Floor 1, 20 and 37 in the alongwind direction with MRI = 700 years. 63
3.29 Probability of exceedance of the residual hinge rotations for Hinge 1 and Hinge 223 in the alongwind direction with MRI = 700 years. 64
3.30 Probability of exceedance of the residual displacements at Floor 1, 20 and 37 in the acrosswind direction with MRI = 1700 years. . . . 64
3.31 Probability of exceedance of the residual displacements at Floor 1, 20 and 37 in the acrosswind direction with MRI = 1700 years. . . . 65
3.32 Probability of exceedance of the residual hinge rotations for Hinge 263 and Hinge 223 in the acrosswind direction with MRI = 1700 years. 65

4.1 Rainier Square Tower. (a) Architectural and structural system rendering of the building [**?**]; (b) OpenSees finite element model. . . . 71

4.2 Illustration of the deformed shape with rigid link elements. 72
4.3 Location of the five integration points along a typical DB element. 73
4.4 Deformed shapes of the FE model subject to unit loads at the top floor in (a) X-direction and (b) Y-direction. 74
4.5 The first five mode shapes of the FEM model. 75
4.6 Reference system for a typical rectangular section. 76
4.7 Linearized yield surface and the corresponding plastic resistance of a section. 77
4.8 Piecewise linear failure domain of reinforced concrete coupling beams. 78
4.9 Piecewise linear failure domain for steel beams. 79
4.10 Experimental loads and a realization of the Level 40 stochastic wind loads for: $F_{X,40}(t)$, $F_{Y,40}(t)$, and $M_{Z,40}(t)$ associated with $\bar{v}_3 = 103$ mph and $\alpha = 330°$. 82
4.11 Autocorrelation of experimental loads and simulated wind loads associated with $\bar{v}_3 = 103$ mph and $\alpha = 330°$ for: (a) $F_{X,40}(t)$, (b) $F_{Y,40}(t)$, (c) $M_{Z,40}(t)$. 83
4.12 Cross-correlation of experimental loads and simulated wind loads associated with $\bar{v}_3 = 103$ mph and $\alpha = 330°$ between: (a) $F_{X,38}(t)$ and $F_{X,40}(t)$, (b) $F_{Y,38}(t)$ and $F_{Y,40}(t)$, (b) $M_{Z,38}(t)$ and $M_{Z,40}(t)$. . 83
4.13 Mean values of the ratios s_p/s_e for all wind directions under (a) 300 MRI wind loads and (b) 700 MRI wind loads. 85
4.14 Number of inelastic elements for all wind directions of a representative simulation and for (a) 300 MRI wind loads and (b) 700 MRI wind loads. 86
4.15 Histogram of elastic, s_e, and plastic, s_p, multipliers over all simulations. 90
4.16 Exceedance probability of residual displacements at the master nodes in the global X-direction at (a) Level 20; (b) Level 40; (c) Core roof. 91
4.17 Exceedance probability of the residual displacements at the master nodes in the global Y-direction at (a) Level 20; (b) Level 40; (c) Core roof. 91
4.18 Exceedance probability of the residual rotations around the global Z-axis at the master nodes of (a) Level 20; (b) Level 40; (c) Core roof. 92
4.19 Exceedance probabilities of plastic curvatures at integration points 1 and 5 of element #182. 92
4.20 Exceedance probabilities of plastic curvatures at integration points 1 and 5 of element #1929. 93
4.21 Plasticity distributed along Element #182 of the structure for a representative sample. 93
4.22 Residual displacements in the (a) X-direction; (b) Y-direction and (c) residual rotation about the Z-axis for a representative sample. . 94

5.1 Illustration of the confidence interval of a Gaussian variable. 100
5.2 A 20-point sampling plan for Kriging model calibration. 100

5.3 Histogram of plastic reserve of the system, s_p/s_e, over all simulations. 106
5.4 Mean values of the ratios, s_p/s_e, over for all wind directions. 106
5.5 Target reliability stipulated in ASCE 7-16 [?]. 108

Chapter 1

A New Class of Shakedown Algorithms

The primary goals of the work outlined in this first chapter are:

1. Development of a dynamic shakedown framework within the setting of concentrated plasticity that enables the estimation of plastic strains and deformations together with the state of shakedown. Classic shakedown theory only allows for the determination of whether a structure shakes down to a safe state, but not of the strains and deformations involved in reaching this state.

2. Development of a dynamic shakedown framework that enables estimation of distributed plasticity along the element through application of fiber section model in dynamic shakedown analysis.

In reaching the first goal, the classic dynamic shakedown is reformulated in terms of a new solution algorithm that enables the estimation of the plastic strains and deformations occurring during shakedown. The algorithm is based on the approaches outlined in [1.2, 1.3], and therefore on a path-following iterative scheme, similar to the procedures used in limit analysis. The original method has been applied to various structures subjected to static loads and has been seen to be numerically efficient and well suited for finite element implementation [1.2, 1.8, 1.6]. By reformulating this iterative scheme to the dynamic shakedown setting, the foundations for the development of a framework is defined that will enable the rapid probabilistic assessment of the inelastic performance of wind-excited structures through the evaluation not only of the shakedown limit state, but also of the total plastic strains and deformations occurring in structures subject to general (e.g. alongwind, acrosswind, etc.) long duration dynamic wind load time histories.

In reaching the second goal, the dynamic shakedown framework of the first goal was reformulated in terms of fiber elements therfore enabling the estimation of distributed plasticity along the member length. The commonly used displacement-based (DB) finite element formulation is employed to model the distributed plasticity based on appropriate interpolation functions for the axial and transverse displacements of the member [1.7, 1.9]. By reformulating the iterative scheme in terms of section forces, including axial forces and moments, at each integration point of the element, the framework allows a rapid assessment of inelastic performance of wind-excited structures considering possibility of plasticity forming anywhere along the element. In particular, in the case of steel structures with material constitutive law assumed linear elastic-perfectly plastic, the iterative solution scheme is further formulated based on the fiber approach that discretizes the member section into several material fibers, in addition to discretization along the element length. This formulation enhances the framework for its ability to capture the distribution of plasticity within the section, from extreme fibers to those near the neutral axis.

1.1 Dynamic Shakedown

Dynamic shakedown defines a limit state in which plastic deformation is produced only during a first phase of finite duration, with the entire subsequent phase remaining purely elastic therefore implying finiteness of the overall plastic deformation. Of particular interest to this work is how the state of dynamic shakedown precludes, by definition, the possibility of failure due to: (1) low cycle fatigue (potential acrosswind failure); and (2) incremental plastic collapse or ratcheting (potential alongwind failure). This section firstly presents a short overview of classic dynamic shakedown theory followed by the description of the underlying elastic model used to estimate the dynamic responses.

1.1.1 Classic solution

The dynamic shakedown theory adopted in this project is based on Melan's well known static Shakedown Theorem and its extension to dynamic systems subject to known external load traces (restricted shakedown). This provides a lower bound on how much the external dynamic loads can be multiplied before shakedown will no longer occur. This multiplier defines what is commonly referred to as the shakedown safety factor s_p. A linear programming problem has been proposed to directly identify this limit state under the assumption that the external dynamic excitation is periodic and infinite [1.14, 1.4]:

$$
\begin{aligned}
& s_p = \max_{s,\boldsymbol{\rho}} s \\
& \text{subject to} \\
& \bar{\boldsymbol{Q}}^s = \max_{0 \le t \le T} \boldsymbol{N}^T \boldsymbol{Q}^s(t) \\
& \boldsymbol{f} = s\bar{\boldsymbol{Q}}^s + \boldsymbol{N}^T \boldsymbol{\rho} - \boldsymbol{R} \le 0 \\
& \boldsymbol{B}^T \boldsymbol{\rho} = \boldsymbol{0}
\end{aligned} \tag{1.1}
$$

where $\boldsymbol{f}$ is the piece-wise linearized yield vector; $\boldsymbol{N}$ is the block diagonal matrix of unit external normal to the yield surface; $\boldsymbol{R}$ is the plastic resistance vector; $\boldsymbol{\rho}$ is the time independent self-stress; $\bar{\boldsymbol{Q}}^s$ is vector of elastic envelope stress defined as the maximum of the plastic demand for each yielding mode in time; $\boldsymbol{Q}^s(t)$ is the purely elastic steady state response; while T represents the period of the forcing function. In particular, $\boldsymbol{Q}^s(t)$ are taken as generalized stresses, e.g. moments or axial forces of the sections, which can be efficiently estimated using the model outlined in Section 1.1.2. The last condition in Eqs. (1.1) represents the self-equilibrated stress state where $\boldsymbol{B}$ is the kinematic matrix depending on the undeformed geometry of the system, defined as:

$$\boldsymbol{\epsilon}(t) = \boldsymbol{B}\boldsymbol{u}(t) \tag{1.2}$$

with $\boldsymbol{\epsilon}(t)$ the vector collecting the time varying and elastic generalized strains. It should be observed that by setting $\boldsymbol{\rho} = \mathbf{0}$, the linear programming problem outlined above provides a means to estimate the elastic safety factor s_e, defining the limit state between an entirely elastic response and the onset of inelasticity.

1.1.2 Underlying elastic solution

The dynamic elastic response of the system is governed by the following equations of motion:

$$\boldsymbol{M}\ddot{\boldsymbol{u}}(t) + \boldsymbol{C}\dot{\boldsymbol{u}}(t) + \boldsymbol{K}\boldsymbol{u}(t) = \boldsymbol{F}(t; \bar{v}_y, \alpha) \tag{1.3}$$

where $\boldsymbol{M}$, $\boldsymbol{C}$ and $\boldsymbol{K}$ are respectively the mass, damping and stiffness matrices of the condensed system (considering horizontal displacements at each floor level as dynamically significant degrees of freedom), $\boldsymbol{F}(t; \bar{v}_y, \alpha)$ are the time-varying dynamic wind loads calibrated to a mean wind speed $\bar{v}_y$ at the building top with a mean recurrence interval (MRI) of y years, while α is the direction of wind with respect to the building.

The dynamic displacements $\boldsymbol{u}$, velocities $\dot{\boldsymbol{u}}$ and accelerations $\ddot{\boldsymbol{u}}$ can then be efficiently estimated through a modal analysis as:

$$\begin{cases} \boldsymbol{u}(t) = \boldsymbol{\Phi}_m \boldsymbol{q}_m(t) \\ \dot{\boldsymbol{u}}(t) = \boldsymbol{\Phi}_m \dot{\boldsymbol{q}}_m(t) \\ \ddot{\boldsymbol{u}}(t) = \boldsymbol{\Phi}_m \ddot{\boldsymbol{q}}_m(t) \end{cases} \tag{1.4}$$

where $\boldsymbol{\Phi}_m = [\boldsymbol{\phi}_1, \ldots, \boldsymbol{\phi}_m]$ is the mode shape matrix containing in the structure's first m modes while $\mathbf{q}_m(t) = \{q_1(t), \ldots, q_m(t)\}^T$, $\dot{\boldsymbol{q}}_m(t) = \{q_1(t), \ldots, q_m(t)\}^T$, and $\ddot{\boldsymbol{q}}_m(t) = \{q_1(t), \ldots, q_m(t)\}^T$ are vectors of the first m modal displacement, velocity and acceleration responses given by directly integrating the following modal equations:

$$\ddot{q}_i(t) + 2\xi_i\omega_i\dot{q}_i(t) + \omega_i^2 q_i(t) = \frac{\boldsymbol{\phi}_i^T \mathbf{F}(t; \bar{v}_y, \alpha)}{m_i} \tag{1.5}$$

where ω_i, m_i and ξ_i are the ith modal circular frequency, mass, and damping ratio respectively. The ith equation of the system of Eq. (1.5) can be efficiently solved through a piece-wise linear integrator based on the concept of digital filters [1.13, 1.12].

Once the responses in the condensed degrees of freedom $\boldsymbol{u}(t)$ are known, any generic response parameter of interest $Q(t)$, including rotational responses and vertical displacements, can be simply estimated through the expression:

$$Q(t) = \boldsymbol{\Gamma}_Q \boldsymbol{K} \boldsymbol{u}(t) \tag{1.6}$$

where $\boldsymbol{\Gamma}_Q$ is vector of influence function given by the response in Q due to a unit force applied one-by-one to the various degrees of freedom of the condensed system.

1.2 A Strain-Driven Concentrated Plasticity Model

Although the classic solution method, formulated as a linear programming problem, can be used to evaluate in an extremely efficient fashion the shakedown limit state of structures subject to dynamic loads, the plastic strains and deformations remain unknown. Therefore, if the inelastic deformations are required, an alternative approach to estimate shakedown has to be explored. To this end, the algorithms proposed in [1.2, 1.3] for estimating the shakedown multiplier under static loads are of interest. Indeed, these algorithms are based on using a path-following algorithm [1.11] which provides, as a byproduct, estimates of the plastic strains and deformations associated with reaching the state of shakedown. Unfortunately, these estimates are associated with a simulated load path and not the actual load path followed by the structure in reaching shakedown. However, by first extending these algorithms to dynamic shakedown problems, it can be observed that, under the conditions outlined in Sec. 2.2, accurate predictions of the plastic strains and deformations occurring during shakedown can be made. The first step towards this goal is the extension of the path-following algorithms outlined in [1.2, 1.3] to dynamic shakedown problems involving periodic and infinite duration dynamic loads.

1.2.1 Problem formulation

To formulate the dynamic shakedown problem for periodic and infinite duration dynamic loads in terms of strains and displacements, it is convenient to first consider a displacement increment $\boldsymbol{u}_r$ together with a load multiplier s satisfying $s_e \leq s \leq s_p$. From $\boldsymbol{u}_r$ the following strain increment can be defined [1.2]:

$$\boldsymbol{\epsilon}_r(\boldsymbol{u}_r) = \boldsymbol{B}\boldsymbol{u}_r \tag{1.7}$$

An admissible stress vector, $\boldsymbol{\rho}$, corresponding to $\boldsymbol{u}_r$ and s can be obtained through the following return mapping scheme:

$$\boldsymbol{\rho}(s, \boldsymbol{u}_r) = \boldsymbol{\rho}_E + \boldsymbol{\Delta\rho}, \quad \mathbf{f}(s, \boldsymbol{\rho}) \leq 0 \tag{1.8}$$

where $\boldsymbol{\rho}_E = \boldsymbol{\rho}_0 + \boldsymbol{E}\boldsymbol{B}\boldsymbol{u}_r$ is the elastic predictor of $\boldsymbol{\rho}$, while $\boldsymbol{\Delta\rho} = \boldsymbol{E}\boldsymbol{\epsilon}_p$ with $\boldsymbol{\epsilon}_p$ is the plastic component of the strain increment $\boldsymbol{\epsilon}_r$ defined by the Kuhn-Tucker condition:

$$\boldsymbol{\epsilon}_p = \mu\mathbf{n}, \quad \mathbf{n} \in \partial\mathbf{f}(s, \boldsymbol{u}_r), \quad \mu = \begin{cases} = 0 & \text{if } \mathbf{f}(s, \boldsymbol{\rho}_E) < 0 \\ \geq 0 & \text{if } \mathbf{f}(s, \boldsymbol{\rho}_E) \geq 0 \end{cases} \tag{1.9}$$

with μ the plastic multiplier. Instead of estimating $\boldsymbol{\rho}(s, \boldsymbol{u}_r)$ by directly solving the return mapping of Eqs. (1.8) and (1.9), $\boldsymbol{\rho}(s, \boldsymbol{u}_r)$ can be more conveniently estimated by minimizing the Haar-Kármán function subject to the dynamic shakedown feasibility conditions:

$$\begin{aligned} &\min_{\boldsymbol{\Delta\rho}} \frac{1}{2} \boldsymbol{\Delta\rho}^T \boldsymbol{E}^{-1} \boldsymbol{\Delta\rho} \\ &\text{subject to} \\ &\bar{\boldsymbol{Q}}^s = \max_{0 \leq t \leq T} \boldsymbol{N}^T \boldsymbol{Q}^s(t) \\ &\boldsymbol{f} = s\bar{\boldsymbol{Q}}^s + \boldsymbol{N}^T\boldsymbol{\rho} - \boldsymbol{R} \leq 0 \end{aligned} \tag{1.10}$$

Equation (1.10) represents a standard strictly convex quadratic programming problem that can be efficiently solved in high-dimensions through standard optimization algorithms.

By solving the return mapping scheme for a given s and $\mathbf{u}_r$, solutions in terms of $\boldsymbol{\rho}(s, \boldsymbol{u}_r)$ will be found that satisfy the shakedown feasibility condition $\mathbf{f}(s, \boldsymbol{\rho}) \leq 0$. However, for $\boldsymbol{\rho}(s, \boldsymbol{u}_r)$ to be a solution to the Shakedown Theorem, then it must also be self-equilibrated. This requirement can be imposed in terms of the internal force vector, $\boldsymbol{S}$, associated with the displacement field $\boldsymbol{u}_r$ and assigned multiplier s as:

$$\boldsymbol{S}(\boldsymbol{u}_r, s) = \boldsymbol{B}^T\boldsymbol{\rho} = 0 \tag{1.11}$$

By combining this condition with the strain-driven scheme for the identification of admissible values of $\boldsymbol{\rho}(s, \boldsymbol{u}_r)$, the following dynamic shakedown problem can be stated directly in terms of the displacement increments:

$$s_p = \max s : \exists \boldsymbol{u}_r : \boldsymbol{S}(\boldsymbol{u}_r, s) = \mathbf{0} \tag{1.12}$$

To solve Eq. (1.12), an incremental iterative scheme can be adopted based on producing a sequence of admissible safe states that are self-equilibrated.

1.2.2 An iterative solution scheme

Starting from the elastic limit state $(s_e, \mathbf{0}, \mathbf{0})$, the iterative solution method estimates the shakedown multiplier s_p and the corresponding admissible self-equilibrated stress state $\boldsymbol{\rho}$ with associated deformation vector $\boldsymbol{u}_r$ by producing a sequence of admissible safe states $(s^{(k)}, \boldsymbol{\rho}^{(k)}, \boldsymbol{u}_r^{(k)})$ with $s^{(k)}$ monotonously increasing at each step and convergent to s_p. The overall procedure is outlined in the flowchart of Fig. 1.1. In particular, at each step, the multiplier s and displacement field $\boldsymbol{u}_r$ are initialized through the following equations:

$$\begin{aligned} s_1 &= s^{(k-1)} + \beta(s^{(k-1)} - s^{(k-2)}) \\ \boldsymbol{u}_{r1} &= \boldsymbol{u}_r^{(k-1)} + \beta(\boldsymbol{u}_r^{(k-1)} - \boldsymbol{u}_r^{(k-2)}) \end{aligned} \tag{1.13}$$

where β is an appropriate scaling factor. The iterative process within each step produces a monotonically decreasing sequence, indexed with j, of nodal forces $\boldsymbol{S}(\boldsymbol{u}_r, s)$ until the self-equilibrated condition $\boldsymbol{S}(\boldsymbol{u}_{rj}, s_j) = \mathbf{0}$ is satisfied. To obtain this condition, corrections $\dot{\boldsymbol{u}}_{rj}$ and $\dot{s}$ for the jth iteration are defined as:

$$\begin{cases} \boldsymbol{S}(\boldsymbol{u}_{rj+1}, s_{j+1}) = \boldsymbol{S}(\boldsymbol{u}_{rj}, s_j) + \boldsymbol{K}_j \dot{\boldsymbol{u}}_{rj} + \boldsymbol{y}_j \dot{s}_j = \mathbf{0} \\ \boldsymbol{y}_j^T \dot{\boldsymbol{u}}_{rj} = \mathbf{0} \end{cases} \tag{1.14}$$

where $\boldsymbol{K}_j$ and $\boldsymbol{y}_j$ are the initial tangent in $(\boldsymbol{u}_{rj}, s_j)$ of the nodal force $\boldsymbol{S}(\boldsymbol{u}_{rj}, s_j)$, i.e.

$$\begin{cases} \boldsymbol{K}_j = \left.\frac{\partial \boldsymbol{S}(\boldsymbol{u}_r, s)}{\partial \boldsymbol{u}_r}\right|_{(\boldsymbol{u}_{rj}, s_j)} \\ \boldsymbol{y}_j = \left.\frac{\partial \boldsymbol{S}(\boldsymbol{u}_r, s)}{\partial s}\right|_{(\boldsymbol{u}_{rj}, s_j)} \end{cases} \tag{1.15}$$

To improve the efficiency of the solution process and to guarantee convergence of the iterative scheme, $\boldsymbol{K}_j$ is taken as the elastic stiffness matrix of the system $\boldsymbol{K_e}$, defined once and for all at the start of the process. This allows the new estimates to be calculated as:

$$\begin{cases} \boldsymbol{u}_{rj+1} = \boldsymbol{u}_{rj} + \dot{\boldsymbol{u}}_{rj} \\ s_{j+1} = s_j + \dot{s}_j \end{cases} \qquad \begin{cases} \dot{\boldsymbol{u}}_{rj} = -\boldsymbol{K_e}^{-1}(\boldsymbol{S}_j + \dot{s}_j \boldsymbol{y}_j) \\ \dot{s}_j = -\frac{\boldsymbol{y}_j^T \boldsymbol{K_e}^{-1} \boldsymbol{S}_j}{\boldsymbol{y}_j^T \boldsymbol{K_e}^{-1} \boldsymbol{y}_j} \end{cases} \tag{1.16}$$

The solution provided at each step k satisfies the plastic admissibility and self-equilibrium condition while the multiplier $s^{(k)}$ is less than or equal to s_p. As such, the solution process is terminated when $s^{(k)} = s^{(k-1)}$, providing the shakedown multiplier.

In addition to the self-stresses, $\boldsymbol{\rho}^{(k)}$ and displacements, $\boldsymbol{u}_r^{(k)}$, the solution process can also produce estimates of the total plastic strains to occur during the shakedown process, $\boldsymbol{\epsilon}_p$, through the following expression:

$$\boldsymbol{\epsilon}_p = \sum_{k=0}^{K} \boldsymbol{\epsilon}_p^{(k)} = \sum_{k=0}^{K} (\boldsymbol{B}\boldsymbol{u}_r^{(k)} - \boldsymbol{E}^{-1}\boldsymbol{\rho}^{(k)}) \tag{1.17}$$

with K the total number of steps required in obtaining s_p.

The plastic strains and deformations provided by this iterative scheme obviously follow the simulated load path. In general, this load path will differ from the actual load path followed during the adaptation process under the prescribed load history $\mathbf{F}(t; \bar{v}_y, \alpha)$. However, as will be outlined in the following, under certain conditions of particular practical interest, the simulated load path will provide a good approximation of the actual load path followed by the structure under $\mathbf{F}(t; \bar{v}_y, \alpha)$.

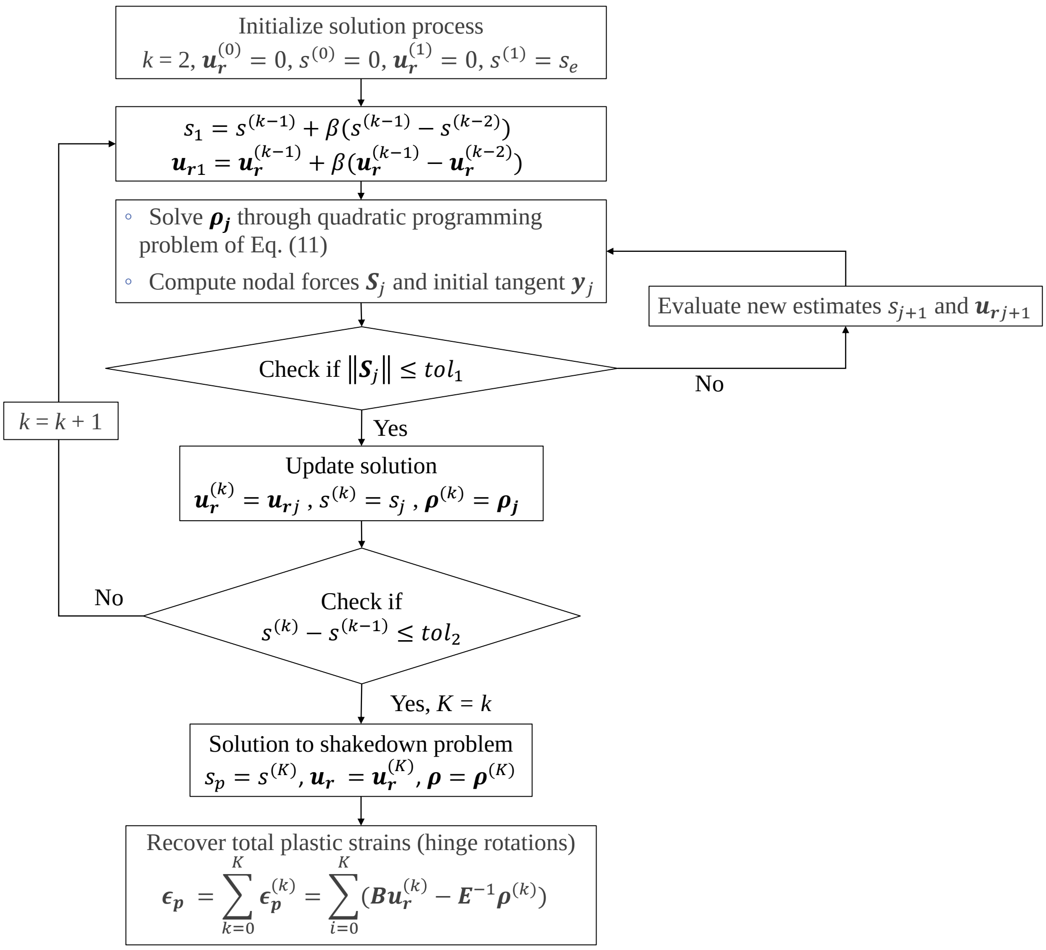

Figure 1.1: Flowchart of the strain-based iterative dynamic shakedown algorithm.

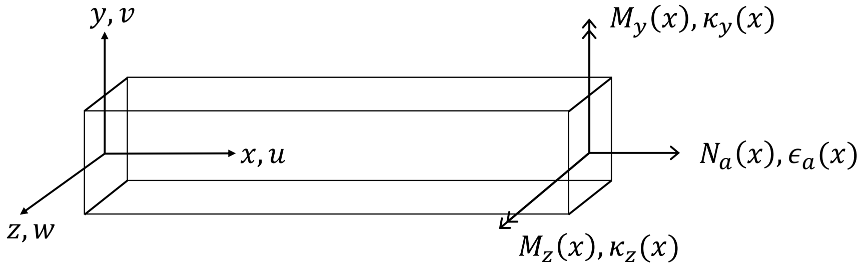

Figure 1.2: Displacements, section forces and deformations for three-dimensional beam-column elements.

1.3 A Strain-Driven Distributed Plasticity Model

To model the distribution of plasticity along structural elements as they experience inelasticity, a fiber-based finite element formulation is outlined in this section. To this end, state-of-art displacement-based (DB) finite elements are first introduced for modeling distributed plasticity. The dynamic shakedown framework is then formulated within this setting.

1.3.1 Mechanical model

The fiber-based formulation considered in this work is based on Euler-Bernoulli beam theory for which the displacement field of a three-dimensional (3D) element is given by:

$$\boldsymbol{u}(x) = \begin{bmatrix} u(x) & v(x) & w(x) \end{bmatrix}^T \tag{1.18}$$

where $u(x)$, $v(x)$ and $w(x)$ are displacements in x, y and z-direction respectively, as shown in Figure 1.2. The section deformation vector, which contains the axial strain $\epsilon_a(x)$ and curvatures $\kappa_z(x)$ and $\kappa_y(x)$, is given by

$$\begin{aligned} \boldsymbol{d}(x) &= \begin{bmatrix} \epsilon_a(x) & \kappa_z(x) & \kappa_y(x) \end{bmatrix}^T \\ &= \begin{bmatrix} \dfrac{\partial u(x)}{\partial x} & \dfrac{\partial^2 v(x)}{\partial x^2} & -\dfrac{\partial^2 w(x)}{\partial x^2} \end{bmatrix}^T \end{aligned} \tag{1.19}$$

The behavior at a section is described in terms of several longitudinal fibers in which the section has be subdivided. The geometric location of each fiber can be fully described by the location of the centroid of the fiber area A_f with respect to a local reference system (y, z) with origin coinciding with the neutral axis of the section, as illustrated in Figure 1.3 for a square section. From the assumption that plane sections remain plane during the element deformation history, the fiber strains and stresses act parallel to the neutral axis following a uniaxial relation. Hence, the vector collecting all fiber strains over the section, $\boldsymbol{\epsilon}(x)$, is related to section deformations as follows:

$$\boldsymbol{\epsilon}(x) = \boldsymbol{l}(x)\boldsymbol{d}(x) \tag{1.20}$$

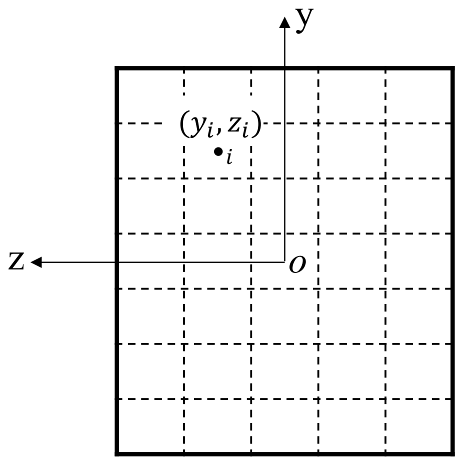

Figure 1.3: Discretization of fiber section.

where $\boldsymbol{l}(x)$ is the linear section compatibility matrix defined as:

$$\boldsymbol{l}(x) = \begin{bmatrix} 1 & -y_1 & z_1 \\ 1 & -y_2 & z_2 \\ \vdots & \vdots & \vdots \\ 1 & -y_{n_f} & z_{n_f} \end{bmatrix} \tag{1.21}$$

with (y_i, z_i) the location of the ith fiber of the section and n_f the total number of fibers of the section. The corresponding fiber stresses of the section are then obtained through the following constitutive relation:

$$\boldsymbol{\sigma}(x) = \boldsymbol{E}_f(x)\boldsymbol{\epsilon}(x) \tag{1.22}$$

where $\boldsymbol{E}_f(x)$ is a diagonal matrix containing the tangent moduli of all fibers, as follows:

$$\boldsymbol{E}_f(x) = \begin{bmatrix} E_{f_1} & 0 & \cdots & 0 \\ 0 & E_{f_2} & \cdots & 0 \\ \vdots & \vdots & \ddots & \vdots \\ 0 & 0 & \cdots & E_{f_{n_f}} \end{bmatrix} \tag{1.23}$$

Within this context, the constitutive relation of the section can be derived by integration of the fiber responses. Therefore, the section stiffness matrix $\boldsymbol{k}_s(x)$, assembled from the fiber stiffnesses, can be formulated as:

$$\boldsymbol{k}_s(x) = \boldsymbol{l}^T(x)\boldsymbol{E}_f(x)\boldsymbol{A}_f(x)\boldsymbol{l}(x) \tag{1.24}$$

where $\boldsymbol{A}_f(x)$ is a diagonal matrix collecting the areas of all fibers in the section:

$$\boldsymbol{A}_f(x) = \begin{bmatrix} A_{f_1} & 0 & \cdots & 0 \\ 0 & A_{f_2} & \cdots & 0 \\ \vdots & \vdots & \ddots & \vdots \\ 0 & 0 & \cdots & A_{f_{n_f}} \end{bmatrix} \tag{1.25}$$

The section forces, including axial force $N_a(x)$ and bending moments $M_z(x)$ and $M_y(x)$, corresponding to deformations $\boldsymbol{d}(x)$, are then defined through section constitutive relation, as follows:

$$\begin{aligned}\boldsymbol{D}(x) &= \begin{bmatrix} N_a(x) & M_z(x) & M_y(x) \end{bmatrix}^T \\ &= \boldsymbol{k}_s(x)\boldsymbol{d}(x)\end{aligned} \tag{1.26}$$

1.3.2 Displacement-based element formulation

The displacement-based (DB) stiffness method follows the standard finite element approach, in which the displacement field of the element is expressed by the end node displacements through appropriate interpolation functions [1.7, 1.5]. The most commonly used functions for beam-column elements are linear Lagrangian interpolation functions for the axial displacements and cubic Hermitian polynomials for the lateral translations and rotations. The degrees of freedom at each end node are three displacements and two rotations for a 3D beam-column element, as illustrated in Figure 1.4. The response in torsion is assumed linearly elastic and uncoupled from the axial and flexural response, therefore the associated displacements and forces are omitted in the following discussion. The displacement field along the element, $\boldsymbol{u}(x)$, can then be related to nodal displacements through the following expression:

$$\boldsymbol{u}(x) = \hat{\boldsymbol{N}}(x)\boldsymbol{q} \tag{1.27}$$

where $\boldsymbol{q} = [q_1, q_2, \cdots, q_{10}]^T$ is the nodal displacements at the element ends in local coordinate system while $\hat{\boldsymbol{N}}(x)$ is a matrix collecting the interpolation functions for all member end degrees of freedom, defined as:

$$\hat{\boldsymbol{N}}(x) = \begin{bmatrix} N_1(x) & 0 & 0 & 0 & 0 & N_2(x) & 0 & 0 & 0 & 0 \\ 0 & N_3(x) & 0 & 0 & N_4(x) & 0 & N_5(x) & 0 & 0 & N_6(x) \\ 0 & 0 & N_3(x) & -N_4(x) & 0 & 0 & 0 & N_5(x) & -N_6(x) & 0 \end{bmatrix} \tag{1.28}$$

where

$$\begin{aligned} N_1(x) &= \frac{L-x}{L} & N_2(x) &= \frac{x}{L} \\ N_3(x) &= 1 - \frac{3x^2}{L^2} + \frac{2x^3}{L^3} & N_4(x) &= x - \frac{2x^2}{L} + \frac{x^3}{L^2} \\ N_5(x) &= \frac{3x^2}{L^2} - \frac{2x^3}{L^3} & N_6(x) &= -\frac{x^2}{L} + \frac{x^3}{L^2} \end{aligned} \tag{1.29}$$

The section deformations $\boldsymbol{d}(x)$ are then related to the element end nodal displacements $\boldsymbol{q}$, as follows:

$$\boldsymbol{d}(x) = \hat{\boldsymbol{B}}(x)\boldsymbol{q} \tag{1.30}$$

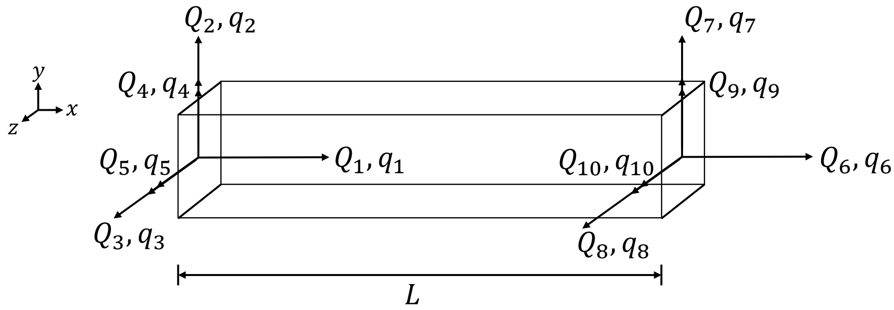

Figure 1.4: Element nodal forces and displacements.

where $\hat{\boldsymbol{B}}(x)$ is the strain-deformation matrix containing the first derivative of the axial displacement interpolation function and the second derivatives of the transverse displacement interpolation functions, that is

$$\hat{\boldsymbol{B}}(x) = \begin{bmatrix} N_1'(x) & 0 & 0 & 0 & 0 & N_2'(x) & 0 & 0 & 0 & 0 \\ 0 & N_3''(x) & 0 & 0 & N_4''(x) & 0 & N_5''(x) & 0 & 0 & N_6''(x) \\ 0 & 0 & N_3''(x) & -N_4''(x) & 0 & 0 & 0 & N_5''(x) & -N_6''(x) & 0 \end{bmatrix} \tag{1.31}$$

Since the displacement field is approximate, several displacement-based elements are required along the length of a member to represent the deformations. From the principle of virtual displacements, the element force vector $\boldsymbol{Q} = [Q_1, Q_2, \cdots, Q_{10}]^T$, i.e. nodal forces at element ends, can be expressed through equilibrium in the following form:

$$\boldsymbol{Q} = \int_0^L \hat{\boldsymbol{B}}^T(x)\boldsymbol{D}(x)dx \tag{1.32}$$

with L being the length of the element. The corresponding element stiffness matrix $\boldsymbol{k}_e$, defined as derivative of the element forces with respect to the element displacements, can then be formulated in terms of section stiffness by substituting the section force vector $\boldsymbol{D}(x)$ in Eq. (1.32) with Eq. (1.26) and (1.30), as follows:

$$\boldsymbol{k}_e = \frac{\partial \boldsymbol{Q}}{\partial \boldsymbol{q}} = \int_0^L \hat{\boldsymbol{B}}^T(x)\boldsymbol{k}_s(x)\hat{\boldsymbol{B}}(x)dx \tag{1.33}$$

To define a complete element stiffness matrix, the torsional stiffnesses, which are assumed uncoupled from axial and flexural stiffnesses and therefore omitted in the expression above, at the two element end nodes have to be added to the formulation of Eq. (1.33). The elastic stiffness matrix $\boldsymbol{K}$ for the overall system are then obtained by standard assemble over all n_b elements:

$$\boldsymbol{K} = \sum_{n_b} \mathcal{A}(\boldsymbol{k}_e) \tag{1.34}$$

The integrals involved in the element formulation, i.e. Eqs. (1.32) and (1.33), are evaluated numerically through a Gauss-Legendre integration scheme along the element, which can be expressed as:

$$I = \int_a^b f(x)dx = \sum_{n=1}^{NIP} w_n f(x_n) \tag{1.35}$$

where NIP is the number of integration points along the element while w_n is the weight for each integration point. Since Gauss quadrature is defined in a domain of $[-1,\ 1]$, a transformation of the interval $a \leq x \leq b$ into $-1 \leq \xi \leq 1$ is required to evaluate the integral. The integral is then approximated by

$$\frac{b-a}{2}\sum_{n=1}^{NIP} w_n\, f(\frac{b+a}{2} + \frac{b-a}{2}\,\xi_n) \tag{1.36}$$

in which ξ_n are integration points on the abscissa. In particular in the case of Gauss-Legendre quadrature, the n-th Gauss node, ξ_n, is given by the n-th root of the NIP-th Legendre polynomials, $P_{NIP}(\xi)$, defined as:

$$P_{NIP}(\xi) = \frac{1}{2^{(NIP)}(NIP)!}\frac{d^{(NIP)}}{d\xi^{(NIP)}}\left(\xi^2 - 1\right)^{NIP} \tag{1.37}$$

The corresponding weight, w_n, is given by [1.1]

$$w_n = \frac{2}{(1-\xi_n^2)\,[P'_{NIP}(\xi)]^2} \tag{1.38}$$

Therefore, the DB element formulation involves both numerical integration error due to the approximate nature of the Gauss integration scheme and the discretization error due to the approximate nature of the displacement interpolation, which can be reduced by increasing the number of element sub-divisions [1.9].

1.3.3 A fiber-based model

A finite element formulation that solves the dynamic shakedown problem through a strain-driven iterative scheme was developed in Section 1.2 in terms of generalized stress and strain, i.e. moments and rotations of plastic hinges at the element ends. In this section, this iterative scheme is further extended to account for plasticity distributed along the element. Two frameworks based on fiber stress and section forces (axial forces and moments of a section along the element) are developed, as will be discussed in the following sections.

Problem formulation

The DB element with fiber model discussed in section 1.3.1 and 1.3.2 is adopted here for modeling distributed plasticity. Accordingly, the strain-driven dynamic shakedown framework has to be reformulated in terms of fiber stresses and strains instead of the generalized stresses and strains at the member ends of Section 1.2. Consider a structure, modeled by the fiber approach, subject to an external dynamic load of infinite duration and the corresponding fiber stress responses $\boldsymbol{\sigma}(t)$, the yield surfaces associated with the fibers can be expressed as:

$$\boldsymbol{\varphi}(t) = \boldsymbol{N}^T \boldsymbol{\sigma}(t) - \hat{\boldsymbol{\sigma}} \leq \mathbf{0} \tag{1.39}$$

where $\boldsymbol{\varphi}$ represents the yield function, $\boldsymbol{N}$ is the block diagonal matrix collecting the unit external normals to the yield surfaces, which, in the case of uniaxial fiber behavior, are positive and negative unit values for all fibers of the structure, leading to the following $N_f \times 2N_f$ matrix:

$$\boldsymbol{N} = \begin{bmatrix} 1 & -1 & & & & & \\ & & 1 & -1 & & & \\ & & & & \ddots & & \\ & & & & & 1 & -1 \end{bmatrix}_{N_f \times 2N_f} \tag{1.40}$$

where N_f is the total number of fibers used in the discretization of the structure. $\hat{\boldsymbol{\sigma}}$ is the vector collecting the yield stresses σ_y in both tension and compression (indicated with subscripts T and C) of each fiber, defined as follows:

$$\hat{\boldsymbol{\sigma}} = \begin{bmatrix} \sigma_{y_{1_T}} & \sigma_{y_{1_C}} & \sigma_{y_{2_T}} & \sigma_{y_{2_C}} & \cdots & \sigma_{y_{N_{f_T}}} & \sigma_{y_{N_{f_C}}} \end{bmatrix}^T_{1 \times 2N_f} \tag{1.41}$$

For a structure to reach the state of dynamic shakedown, i.e. the state in which a finite field of plastic strains has formed to enable the structure to respond purely elastically in the subsequent load history, a necessary and sufficient condition is that there exists a finite time $t^* \geq 0$ and some arbitrary initial conditions such that the sum of the elastic stress solution and a time-independent self-equilibrated stress state $\boldsymbol{\sigma}_s$ lie within the elastic domain [1.10], i.e. such that the following holds:

$$\boldsymbol{N}^T \left(\boldsymbol{\sigma}^E(t) + \boldsymbol{\sigma}_s \right) - \hat{\boldsymbol{\sigma}} \leq \mathbf{0}, \qquad \forall t \geq t^* \tag{1.42}$$

where $\boldsymbol{\sigma}^E(t)$ is the purely elastic stress response to a dynamic load history, while $\boldsymbol{\sigma}_s$ is a time independent self stress distribution (associated with the time independent plastic distortions enabling shakedown). In this work, the special case of a not only infinite but also periodic load $\boldsymbol{F}(t)$ is considered, which significantly simplifies the dynamic shakedown problem. This artificial load is obtained by assuming an external load of duration T infinitely repeated. Under these circumstances, shakedown will occur if a time independent stress distribution, $\boldsymbol{\sigma}_s$, can be found for which Eq. (1.42) is satisfied for the steady state elastic response in $[0, T]$.

To formulate the dynamic shakedown problem in terms of fiber stresses and strains, it is first convenient to consider a residual displacement increment of $\boldsymbol{u}_r$ and load multiplier s. The associated fiber strain increment $\boldsymbol{\epsilon}_r$, collected in a vector over the entire structure, is related through the fiber model as:

$$\boldsymbol{\epsilon}_r(\boldsymbol{u}_r) = \boldsymbol{L}\hat{\boldsymbol{B}}\boldsymbol{T}\boldsymbol{u}_r \tag{1.43}$$

where $\boldsymbol{L}$ and $\hat{\boldsymbol{B}}$ are respectively block-diagonal matrices collecting the section compatibility matrix $\boldsymbol{l}(x)$ and strain-deformation matrix $\hat{\boldsymbol{B}}(x)$ of all sections of the structure:

$$\boldsymbol{L} = \begin{bmatrix} l(x_1) & 0 & \cdots & 0 \\ 0 & l(x_2) & \cdots & 0 \\ \vdots & \vdots & \ddots & \vdots \\ 0 & 0 & \cdots & l(x_{NIP^*n_b}) \end{bmatrix}, \quad \hat{\boldsymbol{B}} = \begin{bmatrix} \hat{\boldsymbol{B}}_{s_1} & 0 & \cdots & 0 \\ 0 & \hat{\boldsymbol{B}}_{s_2} & \cdots & 0 \\ \vdots & \vdots & \ddots & \vdots \\ 0 & 0 & \cdots & \hat{\boldsymbol{B}}_{s_{n_b}} \end{bmatrix} \tag{1.44}$$

where n_b is the total number of elements of the discretized structure while $\hat{\boldsymbol{B}}_{s_i}$ is the strain-deformation matrix for the ith element defined as:

$$\hat{\boldsymbol{B}}_{s_i} = \begin{bmatrix} \hat{\boldsymbol{B}}(x_1) \\ \hat{\boldsymbol{B}}(x_2) \\ \vdots \\ \hat{\boldsymbol{B}}(x_{NIP}) \end{bmatrix} \tag{1.45}$$

In Eq. (1.43), $\boldsymbol{T} = \boldsymbol{T}_C\boldsymbol{T}_A$ is a matrix relating residual displacements in global coordinates to element end displacements in local coordinates, i.e. $\boldsymbol{q} = \boldsymbol{T}\boldsymbol{u}_r$, where $\boldsymbol{T}_A$ is the connectivity matrix while $\boldsymbol{T}_C$ is the following block diagonal matrix collecting coordinate transformation matrices for all elements:

$$\boldsymbol{T}_C = \begin{bmatrix} \boldsymbol{T}_{C_1} & 0 & \cdots & 0 \\ 0 & \boldsymbol{T}_{C_2} & \cdots & 0 \\ \vdots & \vdots & \ddots & \vdots \\ 0 & 0 & \cdots & \boldsymbol{T}_{C_{n_b}} \end{bmatrix} \tag{1.46}$$

where, for a 2D element in the x-y plane, $\boldsymbol{T}_{C_j}$ for $j = 1, ..., n_b$ reduces to the following transformation matrix:

$$\boldsymbol{T}_{C_j} = \begin{bmatrix} \boldsymbol{R}_T & \\ & \boldsymbol{R}_T \end{bmatrix}, \text{with } \boldsymbol{R}_T = \begin{bmatrix} \cos\theta & \sin\theta & 0 \\ -\sin\theta & \cos\theta & 0 \\ 0 & 0 & 1 \end{bmatrix} \tag{1.47}$$

with θ the rotation counter-clockwise about the z-axis. Similar transformation matrices can be defined for 3D structures considering rotations also about x and y-axes.

Under the assumption of elastic perfectly plastic (EPP) material behavior, an admissible self stress vector $\boldsymbol{\sigma}_s$, that collects the stresses in all fibers, due to a residual strain increment $\boldsymbol{\epsilon}_r - \boldsymbol{\epsilon}_0$ can be obtained through the following return mapping scheme:

$$\boldsymbol{\sigma}_s = \boldsymbol{\sigma}_E + \Delta\boldsymbol{\sigma} = \boldsymbol{\sigma}_E - \boldsymbol{E}\boldsymbol{\epsilon}_p \tag{1.48}$$

where $\boldsymbol{E}$ is the elastic matrix defined as the following block-diagonal matrix that contains $\boldsymbol{E}_f(x)$ of all sections:

$$\boldsymbol{E} = \begin{bmatrix} \boldsymbol{E}_f(x_1) & 0 & \cdots & 0 \\ 0 & \boldsymbol{E}_f(x_2) & \cdots & 0 \\ \vdots & \vdots & \ddots & \vdots \\ 0 & 0 & \cdots & \boldsymbol{E}_f(x_{NIP^* n_b}) \end{bmatrix} \tag{1.49}$$

$\boldsymbol{\sigma}_E = \boldsymbol{\sigma}_0 + \boldsymbol{E}\,(\boldsymbol{\epsilon}_r - \boldsymbol{\epsilon}_0)$ is the elastic predictor of $\boldsymbol{\sigma}_s$ with $\boldsymbol{\sigma}_0$ and $\boldsymbol{\epsilon}_0$ the initial stress and strain distribution while $\Delta\boldsymbol{\sigma} = -\boldsymbol{E}\boldsymbol{\epsilon}_p$ with $\boldsymbol{\epsilon}_p$ the plastic strain, i.e. plastic part of $\boldsymbol{\epsilon}_r$, governed by the associated flow rule:

$$\dot{\boldsymbol{\epsilon}}_p = \boldsymbol{N}\dot{\boldsymbol{\lambda}}, \qquad \dot{\boldsymbol{\lambda}} \geq \boldsymbol{0} \tag{1.50}$$

where $\dot{\boldsymbol{\lambda}}$ is the vector of plastic multipliers satisfying the following loading-unloading condition and consistency condition:

$$\boldsymbol{\varphi}^T\dot{\boldsymbol{\lambda}} = \dot{\boldsymbol{\varphi}}^T\dot{\boldsymbol{\lambda}} = 0 \tag{1.51}$$

Instead of solving $\boldsymbol{\sigma}_s$ directly through Eq. (1.48), an equivalent approach is to solve the following Haar-Kàrmàn condition that is based on solving the standard and strictly convex quadratic programming problem (QPP):

$$\begin{aligned} &\min_{\Delta\boldsymbol{\sigma}} \frac{1}{2}\Delta\boldsymbol{\sigma}^T\boldsymbol{E}^{-1}\Delta\boldsymbol{\sigma} \\ &\text{subject to} \\ &\bar{\boldsymbol{\sigma}}^s = \max_{0\leq t\leq T} \boldsymbol{N}^T\boldsymbol{\sigma}_s^E(t) \\ &\boldsymbol{\phi}_s = s\bar{\boldsymbol{\sigma}}^s + \boldsymbol{N}^T\boldsymbol{\sigma}_s - \hat{\boldsymbol{\sigma}} \leq \boldsymbol{0} \end{aligned} \tag{1.52}$$

where $\boldsymbol{\sigma}_s^E(t)$ consists in the purely elastic fiber stress responses in $[0, T]$, which can be efficiently estimated by solving the dynamic equation of motion of the system in a modal framework with the fiber discretization described in Section 1.3.1 and 1.3.2, while $\bar{\boldsymbol{\sigma}}^s$ is the maximum stress demand for each yield mode of each fiber of the system. The last condition of Eq. (1.52) ensures that the solutions in terms of $\boldsymbol{\sigma}_s(\boldsymbol{u}_r, s)$ satisfy the shakedown feasibility condition $\boldsymbol{\phi}_s \leq \boldsymbol{0}$. To further satisfy the dynamic shakedown criterion, $\boldsymbol{\sigma}_s(\boldsymbol{u}_r, s)$ must also be self-equilibrated, which can be imposed in terms of the internal force vector, $\boldsymbol{S}(\boldsymbol{u}_r, s)$, as follows:

$$\boldsymbol{S}(\boldsymbol{u}_r, s) = \boldsymbol{T}^T\boldsymbol{D}_{sQ}\boldsymbol{\sigma}_s(\boldsymbol{u}_r, s) = \boldsymbol{0} \tag{1.53}$$

where $\boldsymbol{D}_{sQ}$ is the following block diagonal matrix collecting the matrices $\boldsymbol{D}_{sQ_i}$ transforming fiber stresses $\boldsymbol{\sigma}_s(\boldsymbol{u}_r, s)$ to element end forces $\boldsymbol{Q}$ for all n_b elements:

$$\boldsymbol{D}_{sQ} = \begin{bmatrix} \boldsymbol{D}_{sQ_1} & 0 & \cdots & 0 \\ 0 & \boldsymbol{D}_{sQ_2} & \cdots & 0 \\ \vdots & \vdots & \ddots & \vdots \\ 0 & 0 & \cdots & \boldsymbol{D}_{sQ_{n_b}} \end{bmatrix} \tag{1.54}$$

For each element, indexed with i, the transformation matrix $\boldsymbol{D}_{sQ_i}$ is defined through numerical integration as:

$$\boldsymbol{D}_{sQ_i} = \sum_{n=1}^{NIP} \frac{L_i}{2} \hat{\boldsymbol{B}}^T(x_n) \boldsymbol{l}^T(x_n) \boldsymbol{A}_f(x_n) w_n \tag{1.55}$$

By combining the self-equilibrated condition with the shakedown admissible stress state $\boldsymbol{\sigma}_s(\boldsymbol{u}_r, s)$, the dynamic shakedown problem can be written in the following form:

$$s_p = \max s : \exists \mathbf{u}_r : \boldsymbol{S}(\boldsymbol{u}_r, s) = \mathbf{0} \tag{1.56}$$

Eq. (1.56) is solved by an incremental iterative scheme that produces a series of admissible safe states $(s^{(k)}, \boldsymbol{\sigma}_s^{(k)}, \boldsymbol{u}_r^{(k)})$ that are self-equilibrated with monotonically non-decreasing $s^{(k)}$, eventually converging to the shakedown multiplier s_p when $s^{(k)} = s^{(k-1)}$.

It is worth mentioning that, in this formulation, the elastic matrix $\boldsymbol{E}$ is a simple diagonal matrix, i.e. the entries outside the main diagonal are all zero. Therefore, Eq. (1.52) that minimizes the objective function $\frac{1}{2}\Delta\boldsymbol{\sigma}^T\boldsymbol{E}^{-1}\Delta\boldsymbol{\sigma}$ can be decoupled and solved individually for each fiber. This particular characteristic greatly improves the scalability of the framework and facilitates the solution process that can be easily and efficiently applied to high-dimensional finite-element discretizations.

An iterative solution scheme

The dynamic shakedown problem described above can be solved through an iterative scheme, as discussed in Section 1.2. It is reformulated here for the fiber-based framework.

The iterative process starts from the elastic limit state ($s^{(1)} = s_e, \boldsymbol{\sigma}_s^{(1)} = \mathbf{0}, \boldsymbol{u}_r^{(1)} = \mathbf{0}$), where s_e is the maximum amount the external loads can be amplified before inelasticity will occur. Within each step k of the iterative process, the multiplier s and residual displacement field $\boldsymbol{u}_r$ are initialized through the following equations:

$$\begin{aligned} s_1 &= s^{(k-1)} + \beta(s^{(k-1)} - s^{(k-2)}) \\ \boldsymbol{u}_{r1} &= \boldsymbol{u}_r^{(k-1)} + \beta(\boldsymbol{u}_r^{(k-1)} - \boldsymbol{u}_r^{(k-2)}) \end{aligned} \tag{1.57}$$

with β being an appropriate scaling factor. To reach the self-equilibrated condition, the multiplier s and residual displacement field $\boldsymbol{u}_r$ are recursively updated, indexed with j, through the following conditions:

$$\begin{cases} \mathbf{u}_{rj+1} = \mathbf{u}_{rj} + \dot{\mathbf{u}}_{rj} \\ s_{j+1} = s_j + \dot{s}_j \end{cases} \qquad \begin{cases} \boldsymbol{S}(\mathbf{u}_{rj+1}, s_{j+1}) = \boldsymbol{S}(\boldsymbol{u}_{rj}, s_j) + \boldsymbol{K}_j \dot{\boldsymbol{u}}_{rj} + \boldsymbol{y}_j \dot{s}_j = \mathbf{0} \\ \boldsymbol{y}_j^T \dot{\boldsymbol{u}}_{rj} = \mathbf{0} \end{cases} \tag{1.58}$$

where $\boldsymbol{S}(\boldsymbol{u}_{rj}, s_j)$ is estimated by Eq. (1.53) in which $\boldsymbol{\sigma}_s(\boldsymbol{u}_r, s)$ is solved through Eq. (1.52) while $\boldsymbol{K}_j$ and $\boldsymbol{y}_j$ are the initial tangent in $(\boldsymbol{u}_{rj}, s_j)$ of the nodal force $\boldsymbol{S}(\boldsymbol{u}_{rj}, s_j)$ given by

$$\begin{cases} \boldsymbol{K}_j = \left.\frac{\partial \boldsymbol{S}(\boldsymbol{u}_r, s)}{\partial \boldsymbol{u}_r}\right|_{(\boldsymbol{u}_{rj}, s_j)} \\ \boldsymbol{y}_j = \left.\frac{\partial \boldsymbol{S}(\boldsymbol{u}_r, s)}{\partial s}\right|_{(\boldsymbol{u}_{rj}, s_j)} \end{cases} \tag{1.59}$$

In particular, to improve the efficiency of the solution process, $\boldsymbol{K}_j$ can be taken as the elastic stiffness matrix of the system $\boldsymbol{K}$, defined at the start of the process through Eq. (1.34). In this way, the iterative process produces a sequence of monotonically decreasing $\boldsymbol{S}(\boldsymbol{u}_r, s)$ until the self-equilibrated condition is satisfied in each step k, therefore resulting in a series of self-equilibrated and admissible safe states $(s^{(k)}, \boldsymbol{\sigma}_s^{(k)}, \boldsymbol{u}_r^{(k)})$. The solution process is then terminated when reaching a multiplier of interest, e.g. $s = 1$, or through the convergence to the shakedown multiplier s_p.

1.3.4 A section-based model

The framework described in section 1.3.3 provides solutions to the dynamic shakedown problem considering distributed plasticity in terms of fiber stress and strain. A limitation of this approach is that it requires linear elastic-perfectly plastic (EPP) material behavior for each fiber of the discretization. Hence, the fiber-based framework cannot be immediately applied to reinforced concrete structures due to the fact that concrete materials always exhibit a nonlinear constitutive relationship between stress and strain due to the lack of tensile strength. In other words, at the level of the fibers, concrete materials never exhibit linear elastic behavior. To circumvent this issue, it is here proposed to reformulate the strain-driven solution process in terms of section forces, e.g. section axial forces and bending moments, along the element instead of fiber stresses. In this setting, the section forces are assumed to follow a linear EPP behavior, allowing the application of the strain-driven iterative scheme. Following this approach, only plasticity distributed along the element is taken into consideration while that within the section is assumed to instantaneously occur once an appropriate yield condition is satisfied. In this section, the necessary reformulations of the strain-driven dynamic shakedown framework for implementing the aforementioned the section-based approach are presented in detail.

Problem formulation: section-level formulation

Following the strain-driven framework, the solution process commences from the elastic limit state with an increment in residual displacement $\boldsymbol{u}_r$ and load multiplier s. Rather than relating $\boldsymbol{u}_r$ to the fiber strains as in section 1.3.3, it is referred to section residual deformations $\boldsymbol{d}_r$, i.e. axial strains and curvatures, of all sections of the element. The kinematic equation of Eq. (1.43) then becomes:

$$\boldsymbol{d}_r(\boldsymbol{u}_r) = \hat{\boldsymbol{B}}\boldsymbol{T}\boldsymbol{u}_r \tag{1.60}$$

Furthermore, the time-dependent self stress of Eq. (1.48) is expressed in terms of section forces $\boldsymbol{D}_s$, i.e. axial force and moments of all sections, as follows:

$$\begin{aligned} \boldsymbol{D}_s &= \boldsymbol{D}_E + \Delta\boldsymbol{D} = \boldsymbol{D}_E - \boldsymbol{k}_s\boldsymbol{d}_p \\ \boldsymbol{D}_E &= \boldsymbol{D}_0 + \boldsymbol{k}_s\left(\boldsymbol{d}_r - \boldsymbol{d}_0\right) \end{aligned} \tag{1.61}$$

where $\boldsymbol{k}_s$ is the following block-diagonal matrix that contains section stiffnesses, $\boldsymbol{k}_s(x)$, of all sections:

$$\boldsymbol{k}_s = \begin{bmatrix} \boldsymbol{k}_s(x_1) & 0 & \cdots & 0 \\ 0 & \boldsymbol{k}_s(x_2) & \cdots & 0 \\ \vdots & \vdots & \ddots & \vdots \\ 0 & 0 & \cdots & \boldsymbol{k}_s(x_{NIP^* n_b}) \end{bmatrix} \tag{1.62}$$

$\boldsymbol{D}_0$ and $\boldsymbol{d}_0$ are respectively vectors of the initial section forces and deformations while $\boldsymbol{d}_p$ is the plastic section deformation vector. The corresponding element end force vector $\boldsymbol{S}(\boldsymbol{u}_r, s)$ in global coordinates can be rewritten as:

$$\boldsymbol{S}(\boldsymbol{u}_r, s) = \boldsymbol{T}^T\boldsymbol{D}_{DQ}\boldsymbol{D}_s(\boldsymbol{u}_r, s) \tag{1.63}$$

where $\boldsymbol{D}_{DQ}$ is the following block diagonal matrix collecting the matrices $\boldsymbol{D}_{DQ_j}$ transforming the section forces $\boldsymbol{D}_s(\boldsymbol{u}_r, s)$ into element end forces $\boldsymbol{Q}$ for all elements:

$$\boldsymbol{D}_{DQ} = \begin{bmatrix} \boldsymbol{D}_{DQ_1} & 0 & \cdots & 0 \\ 0 & \boldsymbol{D}_{DQ_2} & \cdots & 0 \\ \vdots & \vdots & \ddots & \vdots \\ 0 & 0 & \cdots & \boldsymbol{D}_{DQ_{n_b}} \end{bmatrix} \tag{1.64}$$

For each element, the transformation matrix is once again defined through numerical integration as:

$$\boldsymbol{D}_{DQ_i} = \sum_{n=1}^{NIP} \frac{L_i}{2}\hat{\boldsymbol{B}}^T(x_n)w_n \tag{1.65}$$

In this context, the iterative process is carried out for estimating the inelastic deformation of the structural system. Within each step k of the process, the time-dependent generalized self stress, $\boldsymbol{D}_s$, is evaluated iteratively based on $\boldsymbol{u}_r$ and s

until the self-equilibrated condition, $\boldsymbol{S}(\boldsymbol{u}_r, s) = \boldsymbol{0}$, is reached. The corresponding QPP problem of Eq. (1.52) for solving $\boldsymbol{D}_s$ is reformulated in terms of section forces as follows:

$$
\begin{aligned}
&\min_{\Delta \boldsymbol{D}} \frac{1}{2} \Delta \boldsymbol{D}^T \boldsymbol{k}_s^{-1} \Delta \boldsymbol{D} \\
&\text{subject to} \\
&\bar{\boldsymbol{D}}^s = \max_{0 \le t \le T} \boldsymbol{N}^T \boldsymbol{D}_s^E(t) \\
&\boldsymbol{\phi}_s = s \bar{\boldsymbol{D}}^s + \boldsymbol{N}^T \boldsymbol{D}_s - \boldsymbol{R} \le 0
\end{aligned}
\tag{1.66}
$$

where $\boldsymbol{D}_s^E(t)$ is the purely elastic section forces in $[0, T]$ that can be efficiently solved by modal analysis and the DB formulation of Section 1.3.2. The block diagonal matrix $\boldsymbol{N}$ now collects the unit external normals to the piecewise linearized yield surfaces of each section, as follows:

$$
\boldsymbol{N} = \begin{bmatrix} \boldsymbol{N}_{s_1} & & & \\ & \boldsymbol{N}_{s_2} & & \\ & & \ddots & \\ & & & \boldsymbol{N}_{s_{n_s}} \end{bmatrix} \tag{1.67}
$$

where $\boldsymbol{N}_{s_i}, i = 1, \cdots, n_s$ is the matrix containing external normal vectors $\boldsymbol{n}_k$ of the m linearized yield surfaces of the ith section with n_s being the total number of sections of the structure:

$$
\boldsymbol{N}_{s_i} = \begin{bmatrix} \boldsymbol{n}_1 & \boldsymbol{n}_2 & \cdots & \boldsymbol{n}_m \end{bmatrix} \tag{1.68}
$$

In Eq. (1.66), $\boldsymbol{R}$ defines the corresponding plastic resistances, defined as the distances from the origin to each linearized yield surface, of all sections and is given by:

$$
\boldsymbol{R} = \begin{bmatrix} \boldsymbol{R}_{s_1} \\ \boldsymbol{R}_{s_2} \\ \vdots \\ \boldsymbol{R}_{s_{n_s}} \end{bmatrix} \tag{1.69}
$$

where $\boldsymbol{R}_{s_i}, i = 1, \cdots, n_s$ is a $m \times 1$ plastic resistance vector for the ith section whose vector size depends on the number of linearized yield surfaces m.

An iterative solution scheme: section-level formulation

Within this context, the iterative solution scheme of section 1.3.3 is once again adopted for solving the section-based dynamic shakedown problem. The internal force vector $\boldsymbol{S}(\boldsymbol{u}_{rj}, s_j)$ in Eq. (1.58) is now calculated by Eq. (1.63) with section force $\boldsymbol{D}_s(\boldsymbol{u}_r, s)$ solved through the QPP problem of Eq. (1.66). As such, the solution process produces a sequence of self-equilibrated and admissible safe states $(s^{(k)}, \boldsymbol{D}_s^{(k)}, \boldsymbol{u}_r^{(k)})$ until reaching a multiplier of interest, e.g. unamplified load with $s = 1$, or convergence to the shakedown multiplier s_p.

1.4 Concluding Remarks

The primary objective of the work carried outlined in this chapter was the development of an efficient framework for estimating the inelastic responses of multi-degree-of-freedom wind-excited building system. Both concentrated and distributed plasticity modeling environments were introduced. Considering the behaviors of different materials, and in particular the difficulty arising in treating concrete, two specific distributed models were developed based on fiber stresses and section forces, respectively. For the fiber-based framework, plasticity distributing over the section height is further taken into consideration.

Bibliography

[1.1] M. Abramowitz and I. A. Stegun. *Handbook of Mathematical Functions: with Formulas, Graphs, and Mathematical Tables*. Dover Publications, 1972.

[1.2] R. Casciaro and G. Garcea. An iterative method for shakedown analysis. *Computer Methods in Applied Mechanics and Engineering*, 191:5761–5792, December 2002.

[1.3] R. Casciaro and G. Garcea. Erratum to "An iterative method for shakedown analysis". *Computer Methods in Applied Mechanics and Engineering*, 196:714–715, December 2006.

[1.4] W.-C. Chuang and S. M. J. Spence. A performance-based design framework for the integrated collapse and non-collapse assessment of wind excited buildings. *Engineering Structures*, 150:746–758, November 2017.

[1.5] R. D. Cook et al. *Concepts and Applications of Finite Element Analysis*. Wiley, 2001.

[1.6] G. Garcea, G. Armentano, S. Petrolo, and R. Casciaro. Finite element shakedown analysis of two-dimensional structures. *International Journal for Numerical Methods in Engineering*, 63:1174–1202, March 2005.

[1.7] T. J. R. Hughes. *The Finite Element Method: Linear Static and Dynamic Finite Element Analysis*. Dover Publications, Mineola, New York, 2000.

[1.8] M. Malena and R. Casciaro. Finite element shakedown analysis of reinforced concrete 3D frames. *Computers and Structures*, 86:1176–1188, June 2008.

[1.9] A. Neuenhofer and F. C. Filippou. Evaluation of nonlinear frame finite-element models. *Journal of Structural Engineering*, 123(7):958–966, 1997.

[1.10] C. Polizzotto, G. Borino, S. Caddemi, and P. Fuschi. Theorems of restricted dynamic shakedown. *International Journal of Mechanical Sciences*, 35(9):787–801, 1993.

[1.11] E. Riks. An incremental approach to the solution of snapping and buckling problems. *International Journal of Solids and Structures*, 15:529–551, 1979.

[1.12] S. M. J. Spence, M. Gioffrè, and A. Kareem. An efficient framework for the reliability-based design optimization of large-scale uncertain and stochastic linear systems. *Probabilistic Engineering Mechanics*, 44:174–182, 2016.

[1.13] S. M. J. Spence and A. Kareem. Data-enabled design and optimization (DEDOpt): Tall steel buildings frameworks. *Computers and Structures*, 134(12):134–147, 2013.

[1.14] P. Tabbuso, S. M. J. Spence, L. Palizzolo, A. Pirrotta, and A. Kareem. An efficient framework for the elasto-plastic reliability assessment of uncertain wind excited systems. *Structural Safety*, 58:69–78, 2016.

Chapter 2

A Probabilistic Dynamic Shakedown Framework

The primary goals of the work outlined in this chapter was:

1. Development of a framework for the probabilistic generation of any number of wind load histories that captures not only the record-to-record variability in the dynamic wind loads, but also the physics behind any complex aerodynamic phenomenon, such as acrosswind wake-induced vortex shedding, captured in wind tunnel tests.

2. Development of a stochastic simulation framework for estimating the probability of susceptibility to collapse of wind-excited structures within the setting of state-of-the-art performance-based wind engineering frameworks [2.2] and the dynamic shakedown models outlined in Chapter 1.

In reaching the the first goal, a data-driven simulation model is developed based on spectral proper orthogonal decomposition (POD) [2.7, 2.8, 2.9, 2.1, 2.10]. In particular, by allowing the frequency dependent spectral eigenvalues Λ_j and eigenvectors $\boldsymbol{\Psi}_j$ of the external wind loads to be estimated directly from classic wind tunnel data, a framework is outlined that can simulate dynamic wind load traces that contain any building induced aerodynamics captured in wind tunnel tests. Once the eigenvalues Λ_j and eigenvectors $\boldsymbol{\Psi}_j$ of the external loads are known, any number of realizations of the external load histories can be obtained using a classic spectral representation algorithm based on the Fast Fourier Transform [2.3]. Because only the first few eigenvalues/eigenvectors are generally necessary for accurately representing wind loads, the model is computationally extremely efficient allowing for the generation of probabilistically consistent wind loads of long duration in a matter of seconds. An alternative quasi-steady model is also outlined that can be used in cases when wind tunnel data is unavailable.

In reaching the second goal, the dynamic shakedown models outlined in the Chapter 1 are integrated with the above outlined stochastic wind load models within a stochastic simulation framework based on a Monte Carlo scheme. The efficiency with which any given stochastic wind load history can be analyzed ensures the computational feasibility of the scheme, while the possibility of estimating not only the state of shakedown for any given load history but also the deformations at shakedown (thanks to the models introduced in Chapter 1) enables a general definition of system-level collapse susceptibility.

2.1 Problem Setting

The Pacific Earthquake Engineering Research (PEER) Center's framework for performance-based earthquake engineering [2.4, 2.5, 2.6] was recently extended to wind engineering [2.11, 2.2], where structural performance is measured in terms of the annual exceedance probability, P_f, of decision variable thresholds, dv, estimated through the resolution of the following probabilistic integral:

$$P_f(dv) = \iiiint G(dv|dm) \cdot |dG(dm|edp)| \cdot \\ |dG(edp|ip)| \cdot |dG(ip|im)| \cdot p(im) \cdot dim \tag{2.1}$$

where $G(a|b)$ is the complementary cumulative distribution function of a conditional on b; dm is the damage measure; edp is the engineering demand parameter, which for structurally induced damage is generally taken as the peak structural response over the duration of the wind event; ip represents a set of interaction parameters (i.e. the aerodynamic loads acting on the structure); while $p(im)$ is the probability density function of the intensity measure im which, in the case of wind hazards, is generally taken as the largest yearly wind speeds.

This framework applies only to buildings that are repairable, i.e. those that do not exceed limits indicating irreparability during the wind storm. To further consider both irreparable (sucetable to collapse) and repairable (safe against collapse) scenarios, which are mutually exclusive events, the following decomposition based on the total probability theorem can be used [2.2]:

$$P(DV > dv) = P(DV > dv|NC)P(NC) + P(DV > dv|C)P(C) \tag{2.2}$$

where $P(C)$ and $P(NC)$ are the probability of collapse susceptibility and non-collapse susceptibility, $P(DV > dv|NC)$ is the annual exceedance probability of dv given that the building is not susceptible to collapse, while $P(DV > dv|C)$ is the annual exceedance probability of dv given that the building is susceptible to collapses during the wind event. In general, a wind-excited structure can be identified as susceptible to collapse under two possible scenarios: (1) failure due to low cycle fatigue (acrosswind failure) or incremental plastic collapse (alongwind failure); and (2) failure due to excessive deformations, e.g. excessive residual displacements or hinge rotations. In order to estimate the probability associated with the first failure scenario, dynamic shakedown theory can be applied to define a limit state separating susceptibility to low cycle fatigue and/or incremental plastic collapse from a safe state. This method, however, does not provide any information on the plastic strains and deformations of the structure, which are essential for estimating $P(DV > dv|NC)$ for the second failure scenario.

To address this issue, a stochastic simulation scheme is outlined in this chapter based on the models detailed in Chapter 1. In particular, the method is based on simulating a non-linear load deformation path (through the path-following iterative schemes of Chapter 1) for each wind load history of interest. The efficiency with which solutions can be found for any given load history of long duration (hours) allows simulation methods to be directly used to estimate quantities such as $P(DV > dv|C)$ and/or probabilities associated with exceeding strain limits in any inelastic response of interest.

2.2 The Proposed Framework

Sections 1.2 and 1.3 presented the solution schemes for evaluating the dynamic shakedown limit state and the associated plastic deformations and strains of the structure under a prescribed periodic and infinite duration load history. This solution method cannot be directly applied to wind storms due to their finite length. Also, even for a periodic and infinite duration wind load, the simulated and actual load paths will in general differ therefore limiting the usefulness of the plastic deformations and strains obtained from the solution scheme. However, under the conditions stated below, these limitations can be circumvented.

2.2.1 The artificial wind storm

A solution to the finiteness of real wind storms that has been recently proposed in [2.12, 2.2]–and used to date in this project–is to consider the wind storm of duration T infinitely repeated, thereby creating a periodic and infinite excitation that meets the assumptions of dynamic shakedown theory considered in this work. This "artificial" wind storm is mathematically defined as:

$$\tilde{\mathbf{F}}(t + nT; \bar{v}_y, \alpha) = \mathbf{F}(t; \bar{v}_y, \alpha) \;\text{ for }\; \begin{cases} n = 0, 1, ..., +\infty \\ t \in [0, T] \end{cases} \tag{2.3}$$

and is illustrated in Fig. 2.1. In particular, it should be observed that no restrictions on the loads of the "actual" wind storm $\mathbf{F}(t; \bar{v}_y, \alpha)$ have been imposed in defining $\tilde{\mathbf{F}}(t + nT; \bar{v}_y, \alpha)$. Therefore, $\mathbf{F}(t; \bar{v}_y, \alpha)$ can be stationary or non-stationary which enables the consideration of both synoptic and non-synoptic wind events in the proposed framework. The basic idea in defining $\tilde{\mathbf{F}}$ is that now the shakedown models of Chapter 1 can be applied to estimate whether the state of shakedown occurs. If so, then the structure must necessarily be safe against incremental plastic collapse as well as low-cycle fatigue for the "actual" wind storm $\mathbf{F}(t; \bar{v}_y, \alpha)$. In other words, if the structure is safe for $\tilde{\mathbf{F}}$, it must be safe for $\mathbf{F}$.

2.2.2 The simulated load path

By using the iterative schemes of Chapter 1 , estimates of the plastic strains, $\boldsymbol{\epsilon}_p$, and deformations, $\mathbf{u}_r$, will also be available. As already mentioned, the general validity of these is unknown as the load path is simulated and will in general differ from the actual load path. However, under the following two conditions, the simulated load path will provide a good approximation of the actual load path:

1. The structure at $t = 0$ has no plastic deformations, i.e. $\boldsymbol{\epsilon}_p = 0$.
2. The loads $\mathbf{F}(t; \bar{v}_y, \alpha)$ start at zero and end at zero, i.e. the wind storm is simulated over its entirety.

Indeed, if there are no previous plastic deformations, then $\boldsymbol{\epsilon}_p$ must be entirely produced during $\tilde{\mathbf{F}}$. Therefore, the simulated and actual load paths start from the same initial conditions. Also, because $\mathbf{F}$ is simulated over the entirety (i.e. from zero loads to zero loads), the structure will be in a steady state response regime from $t = 0$. In other words, no initial transient phase exists that could produce plastic strains and deformations not considered in the simulated load path which is based on the assumption of a steady state response regime in T. Finally, it should be observed that, under these conditions, the actual load path must be essentially monotonic as any alternating plasticity occurring in any given period T would be repeated indefinitely, therefore eliminating the possibility of shakedown. This behavior is reproduced by the simulated load path, which is also monotonic.

2.2.3 Remarks

Before closing this section, it should be observed that the plastic strains and deformations estimated by the proposed framework are an upper bound on the actual plastic strains and deformations, as the real wind storm has a duration of T while the estimated plastic strains and deformations are for $\tilde{\mathbf{F}}$ that has an infinite duration. This provides a safety factor against any differences between the actual and simulated load paths. Also, it should be observed that the need to simulate the wind loads from zero to zero does not pose any particular difficulty. Indeed, this condition is to ensure the absence of fictitious transient responses that would create artificial plastic strains and deformations. Therefore, any reasonable ramp-up/down can be used, including linear.

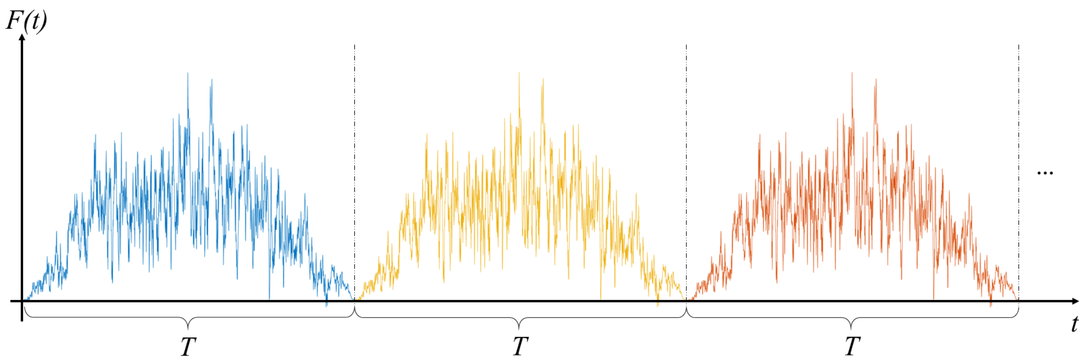

Figure 2.1: Illustration of a generic component of $\tilde{\mathbf{F}}$ for a wind storm of duration T.

2.3 Stochastic Wind Load Models

2.3.1 Wind tunnel driven model

In order to study the record-to-record variability in the inelastic response of the system as well as characterize these responses probabilistically in a fully performance-based design framework such as that outlined in Sec. 2.1, multiple wind load histories are required, i.e. multiple realizations of $\mathbf{F}(t;\bar{v}_y,\alpha)$ are necessary. While multiple wind tunnel tests could be carried out, one for each $\mathbf{F}(t;\bar{v}_y,\alpha)$, this fast becomes prohibitive from a time and cost perspective, especially for frameworks based in Monte Carlo simulation where thousands of wind records are necessary. To overcome this, simulation models can be used, which allows any number of realizations of $\mathbf{F}(t;\bar{v}_y,\alpha)$ to be rapidly generated.

In general, $\mathbf{F}(t;\bar{v}_y,\alpha)$ may be modeled as a vector-valued stochastic process [2.1]. Classic models for simulating $\mathbf{F}$ are based on a quasi-steady assumption which, in general, will not hold for high-rise structures where complex aerodynamic phenomena, such as acrosswind wake-induced vortex shedding, can occur. To overcome this, a data-driven spectral proper orthogonal decomposition (POD) model is here considered for $\mathbf{F}$. In this approach, $\mathbf{F}$ is decomposed into N, with N the total dimension of $\mathbf{F}$, independent vector valued subprocesses and therefore as [2.7, 2.8, 2.9, 2.1, 2.10]:

$$\mathbf{F}(t;\bar{v}_y,\alpha)=\sum_{j=1}^{N}\mathbf{F}_j(t;\bar{v}_y,\alpha) \tag{2.4}$$

with $\mathbf{F}_j(t)$ the jth subprocess of $\mathbf{F}(t)$ which can be given the following spectral representation:

$$\mathbf{F}_j(t;\bar{v}_y,\alpha)=\sum_{k=1}^{K}2|\boldsymbol{\Psi}_j(\omega_k;\alpha)|\sqrt{\Lambda_j(\omega_k;\bar{v}_y,\alpha)\Delta\omega}\times\cos(\omega_k t+\boldsymbol{\theta_j}(\omega_k)+\vartheta_{kj}) \tag{2.5}$$

where Λ_j is the jth frequency dependent eigenvalue of $\mathbf{F}$ with $\boldsymbol{\Psi}_j$ the corresponding frequency dependent eigenvector, $\Delta\omega$ is the frequency increment with a Nyquist (cutoff) frequency $K\Delta\omega/2$ with K the total number of discrete frequencies in the interval $[0, K\Delta\omega]$, $\omega_k = k\Delta\omega$, ϑ_{kj} are random variables with uniform distribution in $[0, 2\pi]$, while $\boldsymbol{\theta}_j$ is a vector of complex angles with ith component given by:

$$\theta_{ji}(\omega_k) = \tan^{-1}\left\{\frac{\mathrm{Im}[\Psi_{ji}(\omega_k)]}{\mathrm{Re}[\Psi_{ji}(\omega_k)]}\right\} \tag{2.6}$$

where $\mathrm{Im}[\Psi_{ij}(\omega_k)]$ and $\mathrm{Re}[\Psi_{ij}(\omega_k)]$ are the imaginary and real parts of the ith component of the jth frequency dependent eigenvector of $\mathbf{F}$.

Once the eigenvalues Λ_j and eigenvectors $\boldsymbol{\Psi}_j$ of $\mathbf{F}$ are known, Eq. (2.4) can be used to simulate realizations of the vector-valued stochastic process $\mathbf{F}$ by simulating independent realizations of the subprocesses using a classic spectral representation algorithm based on the Fast Fourier Transform [2.3]. Because the subprocesses can be generated independently, and only the first few eigenvalues/eigenvectors are generally necessary for accurately representing wind loads, Eq. (2.6) provides a computationally convenient representation of $\mathbf{F}$. In particular, in this work, Λ_j and $\boldsymbol{\Psi}_j$ are directly estimated from wind tunnel data therefore ensuring a full description of the complex aerodynamic response of the building under consideration.

2.3.2 Quasi-steady model

In alternative to the data-driven model of Sec. 2.3.1, $\mathbf{F}(t; \bar{v}_y, \alpha)$ can be modeled through a quasi-steady model. This will in general provide a good approximation of the alongwind loads but is unable to provide a general description of the acrosswind loads. Within this setting, the nth component of $\mathbf{F}(t; \bar{v}_y, \alpha)$ is described by the following relationship:

$$F_n(t; \bar{v}_y, \alpha) = \eta_n(\alpha)(\bar{v}_{z_n} + v_n(t))^2 \simeq \eta_n(\alpha)(\bar{v}_{z_n}^2 + 2\bar{v}_{z_n}v_n(t)), \quad n = 1, 2 \ldots, N \tag{2.7}$$

where N is the number of degrees of freedom of the system and $\bar{v}_{z_n}$ is the mean wind velocity at height z_n and related to $\bar{v}_y$ through the wind profile, $v_n(t)$ is the corresponding fluctuating component of the wind speed while η_n is a coefficient equal to $0.5\rho\bar{C}_n A_n$, in which ρ is the air density, $\bar{C}_n$ is a directional quasi-steady pressure coefficient and $A_n = h_n W$ is the influence area of the jth degree of freedom in the direction of the wind with W the influence width. To simulate the zero-mean fluctuating component over the height of the building, $v_n(t)$, a target power spectral density (PSD) function must be considered. For example:

$$S_n(\omega) = \frac{1}{2}\frac{200}{2\pi}v_*^2\frac{z_n}{\bar{v}_{z_n}}\frac{1}{[1 + 50\frac{\omega z_n}{2\pi\bar{v}_{z_n}}]^{5/3}}, \quad n = 1, 2, \ldots, N \tag{2.8}$$

where v_* is the shear velocity of the flow represented by:

$$v_* = v_{10}\beta\frac{k_a}{\ln(\frac{10}{z_0})} \tag{2.9}$$

where $k_a = 0.4$ is the Von Kármán's constant and the ground roughness height. The cross spectral density is given by:

$$S_{nk}(\omega) = \sqrt{S_n(\omega)S_k(\omega)}\gamma_{nk}(\omega), \quad n, k = 1, 2, \ldots, N, n \neq k \tag{2.10}$$

where γ_{nk} is the coherence function between $v_n(t)$ and $v_k(t)$ defined as

$$\gamma_{nk}(\Delta z, \omega) = \exp\left[-\frac{\omega}{2\pi}\frac{C_z \Delta z}{\frac{1}{2}(\bar{v}_1 + \bar{v}_2)}\right] \tag{2.11}$$

where $\bar{v}_1$ and $\bar{v}_2$ are the mean wind speeds at heights z_1 and z_2, respectively, $\Delta z = |z_1 - z_2|$ is the difference between two heights and C_z is a constant that can be set equal to 10 for design purposes.

The N-dimensional multivariate stochastic vector process $v(t)$ describing the fluctuating components of the wind is then simulated through the following series as $L \to \infty$:

$$v_n(t) = 2\sum_{m=1}^{N}\sum_{l=1}^{L}|H_{nm}(\omega_{ml})|\sqrt{\Delta\omega}cos[\,\omega_{ml}(t) - \theta_{nm}(\omega_{ml}) + \phi_{ml}], \qquad n = 1, 2, \ldots, N \tag{2.12}$$

where ϕ_{ml} for $m = 1, 2, \cdots, N$ and $l = 1, 2, \cdots, L$ are sequences of independent random phase angles uniformly distributed in $[0, 2\pi]$ while ω_{ml} is given by

$$\omega_{ml} = (l-1)\Delta\omega + \frac{m}{N}\Delta\omega, \quad l = 1, 2, \ldots, N \tag{2.13}$$

in which $\Delta\omega$ is the sampling frequency. $H_{nm}(\omega_{ml})$ is a typical element of the matrix $\mathbf{H}(\omega)$, defined through the following decomposition:

$$\mathbf{S}(\omega) = \mathbf{H}(\omega)\mathbf{H}^{T*}(\omega) \tag{2.14}$$

where $\mathbf{S}(\omega)$ is the cross spectral density matrix with diagonal components given by Eq. (2.8) and off-diagonal terms given by Eq. (2.10) and $(\cdot)^{T*}$ is the transpose of the complex conjugate.

In Eq. (2.12), $\theta_{nm}(\omega)$ is the complex angle that can be written in the following form if the offdiagonal elements $H_{nm}(\omega)$ of $\mathbf{H}(\omega)$ are written in the polar form:

$$\theta_{nm}(\omega) = \tan^{-1}\frac{\mathrm{Im}[H_{nm}(\omega)]}{\mathrm{Re}[H_{nm}(\omega)]} \tag{2.15}$$

where Im and Re are respectively the imaginary and real parts of the complex function. The period of the simulated forcing function is given by:

$$T = \frac{2\pi N}{\Delta\omega} = \frac{2\pi N L}{\omega_{up}} \tag{2.16}$$

where ω_{up} is the cut-off frequency.

2.4 The Monte Carlo Simulation Strategy

The stochastic wind load models outlined above allow the iterative solution schemes of Chapter 1 to be used to define a Monte Carlo simulation framework that can efficiently estimate the system-level probability that a wind-excited structural systems is susceptible to collapse whose inelasticity is idealized through the concentrated or distributed plasticity models of Chapter 1. The global safety of the structure, defined by the probabilities $P(C|\bar{v}_y)$ and $P(NC|\bar{v}_y) = 1 - P(C|\bar{v}_y)$, is determined by the dynamic shakedown multiplier, s_p, as well as any number of limit states placed on inelastic responses occurring at shakedown. With this in mind, the collapse probability of the structure can be estimated through the following expression:

$$P(C|\bar{v}_y, \alpha) = \frac{1}{N_s} \sum_{i=1}^{N_s} I_C^{(i)}(\bar{v}_y, \alpha) \tag{2.17}$$

where N_s is the total number of simulated wind events while $I_C^{(i)}$ is the following indicator function evaluated in $(\bar{v}_y, \alpha)$ as:

$$I_C^{(i)} = \begin{cases} 1 & \text{if} \quad (s_p^{(i)} < 1) \cup (\boldsymbol{u}_r^{(i)} \geq \tilde{\boldsymbol{u}}_r) \cup (\hat{\boldsymbol{u}}^{(i)} \geq \tilde{\hat{\boldsymbol{u}}}) \cup (\boldsymbol{\epsilon}_p^{(i)} \geq \tilde{\boldsymbol{\epsilon}}_p) \\ 0 & \text{if} \quad \text{otherwise} \end{cases} \tag{2.18}$$

where $s_p^{(i)}$, $\boldsymbol{u}_r^{(i)}$, $\hat{\boldsymbol{u}}^{(i)}$ and $\boldsymbol{\epsilon}_p^{(i)}$ are the ith sample of the shakedown multiplier, residual displacements, peak displacements, and plastic strains at shakedown, while $\tilde{\boldsymbol{u}}_r$, $\tilde{\hat{\boldsymbol{u}}}$ and $\tilde{\boldsymbol{\epsilon}}_p$ are user defined repairability limits set respectively on $\boldsymbol{u}_r$, $\hat{\boldsymbol{u}}$ and $\boldsymbol{\epsilon}_p$. In defining $I_C^{(i)}$ as above, susceptibility to collapse can be defined as:

1. the inability of the structure to reach the state of dynamic shakedown;

2. excessive residual $\boldsymbol{u}_r$ and/or peak $\hat{\boldsymbol{u}}$ displacements/drifts at shakedown;

3. excessive plastic deformations $\boldsymbol{\epsilon}_p$ at shakedown.

It is important to observe that any other limit state can be added to $I_C^{(i)}$ without computational consequences as the scheme is based on a Monte Carlo methods. Also, in evaluating $I_C^{(i)}$, the peak responses at shakedown $\hat{\mathbf{u}}$ are given by the sum of the peak elastic response $\hat{\mathbf{u}}_e$ and the residual response $\mathbf{u}_r$, i.e. as $\hat{\mathbf{u}} = \hat{\mathbf{u}}_e + \mathbf{u}_r$.

Similarly, the probability of the structure exiting an elastic regime can be simultaneously estimated as:

$$P(s_e < 1) = \frac{1}{N_s} \sum_{i=1}^{N_s} I(s_e^{(i)}) \tag{2.19}$$

where $I(s_e^{(i)})$ is the following indicator function:

$$I(s_e^{(i)}) = \begin{cases} 1 \text{ if } s_e^{(i)} < 1 \\ 0 \text{ if } s_p^{(i)} \geq 1 \end{cases} \tag{2.20}$$

In addition to the above probabilities, the proposed framework can also provide probability distributions on the plastic strains (e.g. plastic hinge rotations) and deformations (e.g. residual displacements). Indeed, a Monte Carlo scheme provides, as a by-product, unbiased sets of samples of all responses occurring throughout the system. These can the be used to directly estimate distribution functions.

A flowchart of the proposed Monte Carlo scheme is shown in Fig. 2.2. In particular, the step-by-step Monte Carlo algorithm is as follows:

1. Set the intensity of the wind storm of interest by selecting the mean wind speed $\bar{v}_y$ with a MRI of y years, the wind direction α, and total duration T.

2. Generate a realization of the wind loads $\boldsymbol{F}(t; \bar{v}_y, \alpha)$ through one of the stochastic wind load models of Sec. 2.3 after calibration to appropriate wind tunnel data.

3. Perform modal direct integration using the model outlined in Sec. 1.1.2.

4. Obtain a realization of $\boldsymbol{Q}^s(t)$ by extracting the elastic responses from Step 3.

5. Estimate realizations of the elastic and shakedown multipliers, s_e and s_p, by solving the linear programming problem of Eq. (1.1). Check if the structure has remained elastic, i.e. $s_e \geq 1$, or is susceptible to collapse during the wind event, i.e. if $s_p < 1$.

6. If the structure remains elastic, i.e. $s_e \geq 1$, the plastic deformation is set to be zero as the structure remains elastic.

7. If the system is susceptible to collapse, i.e. if $s_p < 1$, the structure is identified as irreparable and no plastic deformation estimation is needed.

8. If the structure is deemed repairable, i.e. is not susceptible to collapse, and the structure experiences plasticity, i.e. $s_e < 1$ and $s_p \geq 1$, estimate residual displacements, $\boldsymbol{u}_r$, peak responses $\hat{\mathbf{u}}$, and total strains, $\boldsymbol{\epsilon}_p$, for the unamplified wind storm, i.e. $s = 1$, using the iterative methods of Chapter 1 and evaluate Eq. (2.18).

By repeating steps 2 to 8 for N_s samples of the wind loads, the safety of the system can be estimated probabilistically using Eq. (2.17). For structures that exit the elastic regime, plastic deformations due to the unamplified wind storms, i.e. $s = 1$, will also be evaluated, thereby providing an insight into the inelastic behavior of the system.

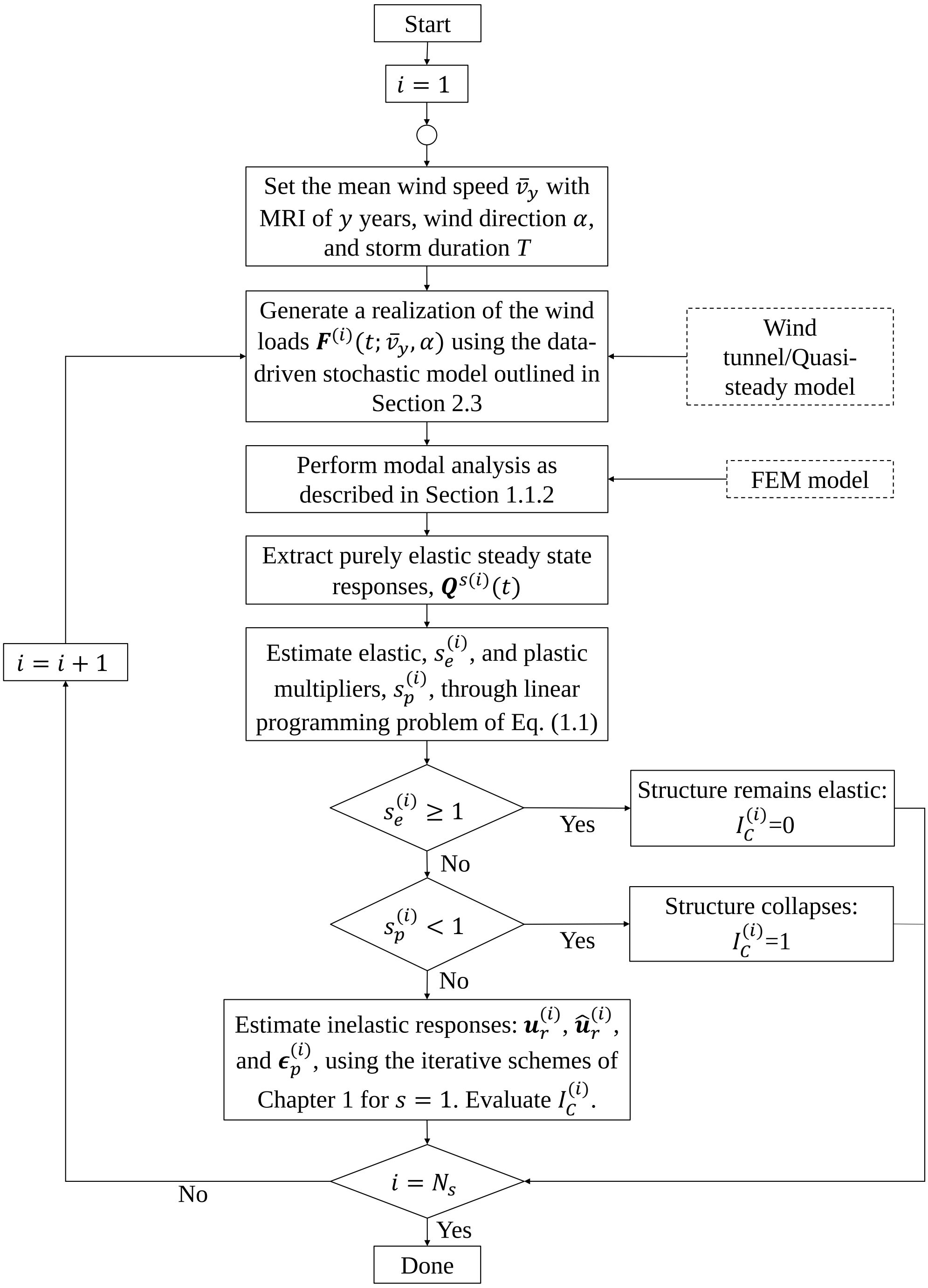

Figure 2.2: Flowchart of the overall simulation strategy.

2.5 Concluding Remarks

The primary objective of the work outlined in this chapter was the development of a general framework allowing the estimation of the probability associated with the susceptibility of the structure to system-level collapse based on the strain-based dynamic shakedown models presented in Chapter 1. Contrary to the computationally intensive direct integration method that requires hours to analyze a structure under a single wind storm, the proposed model–which combines the classic solution method for dynamic shakedown with the iterative strain-based schemes outlined in Chapter 1–can estimate the inelastic response for each wind storm in a matter of seconds therefore enabling the introduction of a stochastic simulation scheme based on robust Monte Carlo methods to be used to estimate the probabilities associated with exceeding inelastic system-level limit states modeling the susceptibility of the system to collapse.

Bibliography

[2.1] X. Chen and A. Kareem. Proper orthogonal decomposition-based modeling, analysis, and simulation of dynamic wind load effects on structures. *Journal of Engineering Mechanics*, 131(4):325–339, 2005.

[2.2] W.-C. Chuang and S. M. J. Spence. A performance-based design framework for the integrated collapse and non-collapse assessment of wind excited buildings. *Engineering Structures*, 150:746–758, November 2017.

[2.3] G. Deodatis. Simulation of ergodic multivariate stochastic processes. *Journal of Engineering Mechanics*, 122(8):778–787, 1996.

[2.4] Federal Emergency Management Agency (FEMA). *Seismic performance assessment of buildings, Volume 1 Methodology (FEMA Publication P-58-1)*. Washington, DC, 2012.

[2.5] Federal Emergency Management Agency (FEMA). *Seismic performance assessment of buildings, Volume 2 - Implementation (FEMA Publication P-58-2)*. Washington, DC, 2012.

[2.6] Federal Emergency Management Agency (FEMA). *Seismic performance assessment of buildings, Volume 3 - Supporting electronic materials and background documentation (FEMA Publication P-58-3)*. Washington, DC, 2012.

[2.7] Y. Li and A. Kareem. Simulation of multivariate nonstationary random processes by FFT. *Journal of Engineering Mechanics*, 117(5):1037–1058, 1991.

[2.8] Y. Li and A. Kareem. Simulation of multivariate random processes: Hybrid DFT and digital filtering approach. *Journal of Engineering Mechanics*, 119(5):1078–1098, 1993.

[2.9] Y. Li and A. Kareem. Simulation of multivariate nonstationary random processes: Hybrid DFT and digital filting approach. *Journal of Engineering Mechanics*, 123(12):13021310, 1997.

[2.10] L. Peng, G. Huang, X. Chen, and A. Kareem. Simulation of multivariate non-stationary random processes: Hybrid stochastic wave and proper orthogonal decomposition approach. *Journal of Engineering Mechanics*, 143(9), 2017.

[2.11] S. M. J. Spence and A. Kareem. Performance-based design and optimization of uncertain wind-excited dynamic building systems. *Engineering Structures*, 78:133–144, 2014.

[2.12] P. Tabbuso, S. M. J. Spence, L. Palizzolo, A. Pirrotta, and A. Kareem. An efficient framework for the elasto-plastic reliability assessment of uncertain wind excited systems. *Structural Safety*, 58:69–78, 2016.

Chapter 3

Verification and Examples

The primary goals of the work carried out in this chapter were:

1. Verification of the proposed concentrated plasticity dynamic shakedown framework for plastic strains and deformations through comparison with results obtained from direct integration.
2. Validation of the simulated load path through a comprehensive statistical study involving a full range of wind directions.
3. Application and verification of the proposed dynamic shakedown framework for fiber elements considering distributed plasticity through comparison with results obtained from direct integration.
4. Illustration of the Monte Carlo scheme developed in Chapter 2 on a 37 story 2D steel frame subject to both alongwind and acrosswind loads estimated through the data-driven wind load model of Chapter 2.

To achieve the first goal, alongwind and acrosswind loads histories were simulated for a 150 m steel framework using the model developed in Chapter 2. Wind tunnel data was used to calibrated the model. Direct integration of a fully non-linear OpenSees model was then carried out and compared to the plastic strains and deformations estimated from the dynamic shakedown framework developed in Chapters 1 and 2. Near perfect correspondence between the two approaches was seen therefore verifying the proposed dynamic shakedown framework.

In reaching the second goal, non-linear responses at shakedown obtained through direct integration were compared with those obtained from the proposed strain-based dynamic shakedown framework. In particular, randomly selected wind load histories over a full range of wind directions, including alongwind, acrosswind and intermediate wind directions, were considered.

To achieve the third goal, a two-story two-bay frame subject to both alongwind load and zero-mean wind load histories was used to illustrate the potential of the proposed framework. Direct integration of a fiber element OpenSees steel model was carried out and compared to the plastic deformation estimated from the fiber-element-based dynamic shakedown framework developed in Chapters 1 and 2. Near perfect correspondence between the two approaches was seen therefore verifying the proposed fiber-based dynamic shakedown framework. In addition, a framework based on section forces was also demonstrated on both steel and reinforced concrete frames subject to alongwind loads with predefined yield domains for each section. In this case, immediate comparison with direct integration is not available since there is no such element type available in OpenSees.

In reaching the forth goal, the 150 m steel framework developed for achieving the first goal of this chapter was analyzed while considering 5000 randomly generated alongwind and acrosswind wind storms within the Monte Carlo scheme of Chapter 2. To illustrate the versatility of the proposed framework, probability distributions for a few arbitrarily chosen inelastic responses where also estimated.

3.1 Verification of the Simulated Load Path

To illustrate the validity of the simulated load path of Sec. 2.2.2, this section focuses on the comparison of non-linear responses obtained for a 37 story wind-excited steel frame through direct integration to those obtained from the proposed incremental strain-based concentrated plasticity scheme. In particular, the finite element environment OpenSees (Open System for Earthquake Engineering Simulation) was used for carrying out the direct integration using the Newmark-Beta method.

3.1.1 Model description

The structure considered in this comparison is the 37-story six-span plane steel frame of Fig. 3.1. The geometry consists of beam span lengths of 5 m and inter-story heights of 6 m at ground level and 4 m for all other floors. The overall height of the structure is 150 m. The columns are box members, while the beams are wide flange standard W24 sections. A summary of the section sizes is reported in Table 1. The dimensions of the box columns are defined by their center line diameters D. The thickness of the section, t, is set to $D/20$. The steel composing the frame is assumed to be elastic-perfectly plastic, and is therefore completely described by the yield stress σ_y and Young's modulus E_s, which were respectively taken as 355 MPa and 200 GPa. The mass of the structure was lumped at each floor and calculated as as the sum of the element mass and carried mass derived from assuming a building density of 100 kg/m^3. The first two natural frequencies of the frame were respectively $f_1 = 0.1873$ Hz and $f_2 = 0.5340$ Hz. Rayleigh damping was considered, with damping ratios of the first two modes equal to 2.5%.

To evaluate the non-linear response of structure, rigid-perfectly plastic hinges were assumed at the extremes of all elements for a total of 962 possible hinges. In particular, in this case study, plastic hinges were purely moment based, neglecting

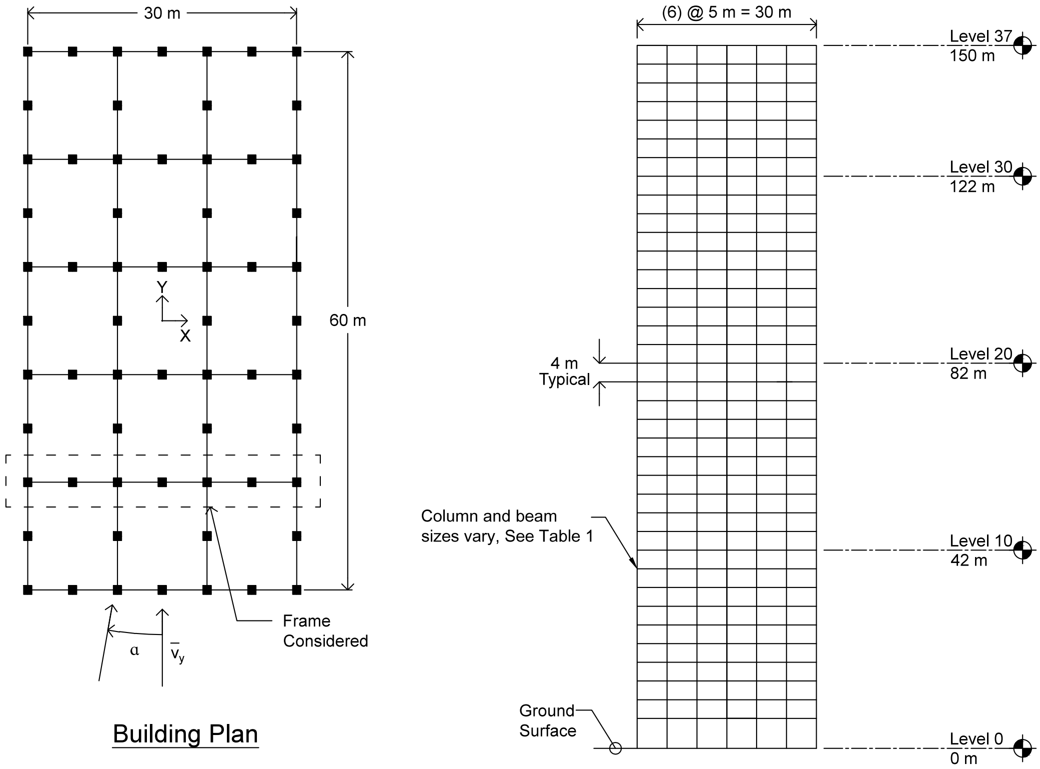

Figure 3.1: Schematic of the 37 story steel frame of the case study.

Table 3.1: Section sizes of the steel frame.

Level	Wide-flange Beams	Box Columns (cm)
1-10	W24 × 192	$D = 50$
11-20	W24 × 192	$D = 50$
21-30	W24 × 103	$D = 40$
31-37	W24 × 103	$D = 35$

axial load effects in both the beams and columns. The yield domains associated with plastic hinges were therefore defined by the ultimate moments of the sections, i.e. $M_u = \sigma_y Z$ with Z the plastic modulus of the cross section.

To model the rigid-perfectly plastic hinges in OpenSees, TwoNodeLink elements of 1 cm length were placed at the two ends of each beam and column. The moment capacity of the hinges were defined as the ultimate moment strengths of the section while the rotational stiffnesses were calculated based on the stiffness that would be provided by a 1 cm segment of the original elastic beam/column element. This ensures that the elastic response of the hinges is, for all intents and purposes, the same as the corresponding elastic beam-column element. Similarly, the shear and axial stiffnesses were taken so as to correspond to a 1 cm segment of elastic beam/column element.

3.1.2 Wind loads

The two wind directions $\alpha = 0^o$ and $\alpha = 90^o$, see Fig. 3.1, were considered in the comparison of this section. These directions corresponded to acrosswind and alongwind loads respectively. To simulate wind load histories for these two directions, the stochastic wind load model of Sec. 2.3 was calibrated to wind tunnel data collected on a 1/300 rigid model of the building geometry shown in Fig. 3.1. In particular, the data was part of the Tokyo Polytechnic University's (TPU) aerodynamic database [3.1] and was measured considering a sampling frequency of 1000 Hz and wind speed at the building top of 11 m/s. A total of 512 pressure taps were used for 32 s of recorded data. This data was integrated and scaled therefore defining X, Y and torsional loads at the center of mass of each floor. For the application here considered, 1/6 of the X direction loads were considered acting on the moment resisting frame. These loads were used to estimate the eigenvalues Λ_j and eigenvectors $\boldsymbol{\Psi}_j$ for the two wind directions of interest.

In calibrating Eq. (2.5), a sampling frequency of 2 Hz was considered for a cutoff frequency of 1 Hz. Five loading modes were considered for each wind direction. To ensure stability and accuracy when carrying out direct integration, the sampling frequency was increased through linear interpolation to 100 Hz. The mean wind speed at the building top was set to $\bar{v}_y = 52.5$ m/s, which corresponds to a MRI of $y = 700$ years for the Miami region of Florida. Due to the significant effort involved in performing direct integration, the total length of the wind storm was set to $T = 360$ s. The first and last minute of the loads were linearly ramped to ensure zero initial and final conditions. To fully capture the dynamic shakedown phenomena, the wind loads were repeated for 15 cycles before returning to zero for full cycle, as illustrated in Fig. 3.2. This final unloading cycle allowed for the dynamic responses to completely damp out therefore enabling the direct estimation of the residual displacements and plastic rotations in the hinges. These quantities were directly compared to those obtained from the strain-based dynamic shakedown framework developed in this work.

3.1.3 Results

The comparison was carried out for four randomly generated wind loads acting in the alongwind and acrosswind directions, i.e. $\alpha = 90^o$ and $\alpha = 0^o$. Figure 3.3 reports the residual displacements for the four acrosswind and alongwind wind loads. As can be seen, the residual displacements estimated through the proposed framework are almost identical to those obtained from direct integration in both the alongwind and acrosswind directions. Plastic strains, i.e. residual hinge rotations θ_r, for two samples are shown in Fig. 3.4 and 3.5 with hinge locations shown in Fig. 3.6. Once again, strong correspondence between the two approaches is seen. Figures 3.7 and 3.8 present the deformed shapes for a representative sample under acrosswind and alongwind loading where plastic hinge yielding occurred mostly in the first story

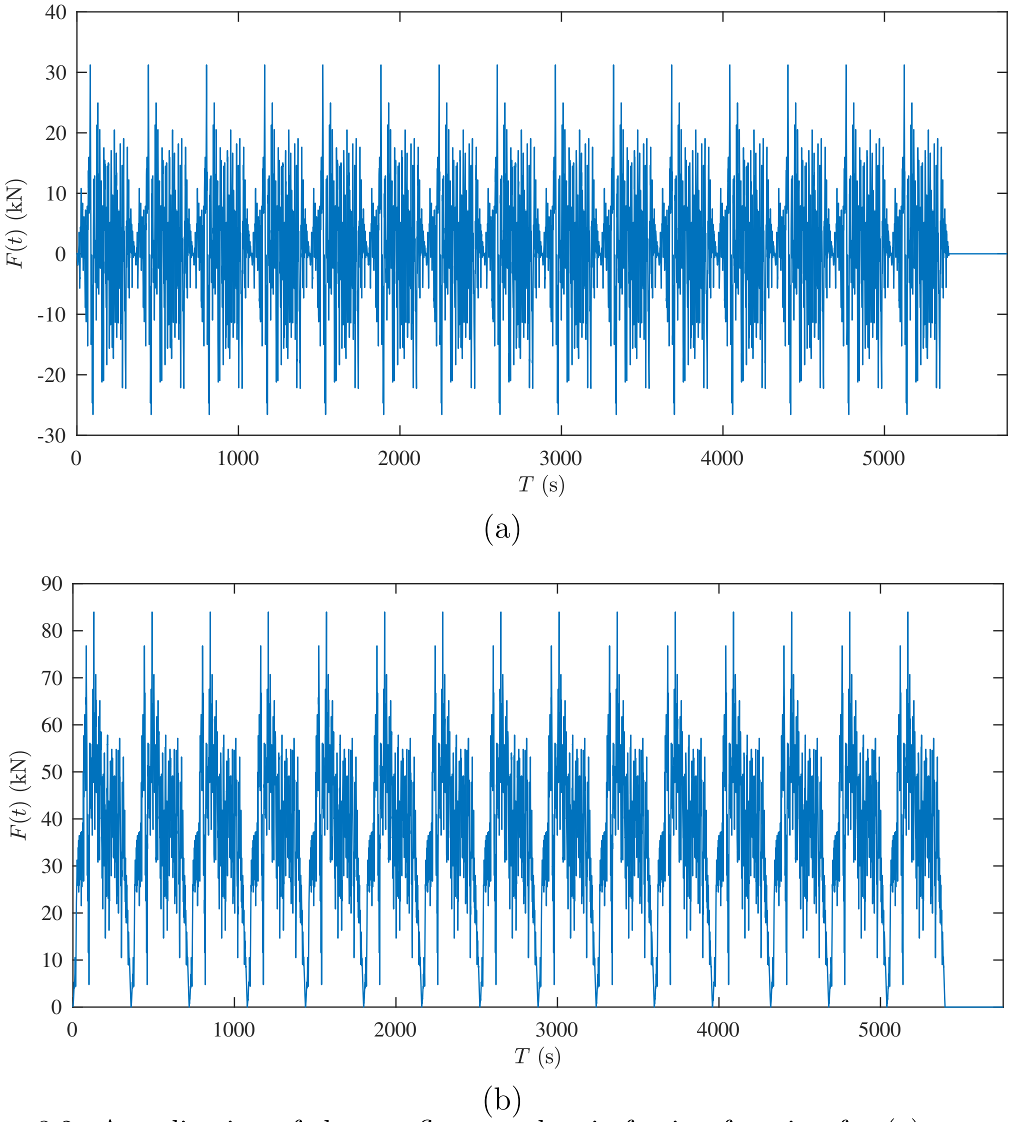

Figure 3.2: A realization of the top floor stochastic forcing function for (a) acrosswind direction, i.e. $\alpha = 0^o$; (b) alongwind direction, i.e. $\alpha = 90^o$.

and mid-height of the building. In particular, in these figures, plastic hinges were depicted by circles if only one hinge was present at the joint, while in the case of multiple hinges, e.g. hinges on more than one connecting beam or column, squares were used. It can be observed that under the assumptions outlined in Section 2.2, the proposed framework is capable of estimating the inelastic response in both the alongwind and acrosswind directions with high accuracy, proving that the simulated load path is quite comparable to the actual load path experienced by the structure.

To illustrate how the accumulation of plastic strain in the hinges is monotonically increasing, i.e. no alternating plasticity occurs during shakedown, the moment rotation histories of three representative plastic hinges are shown in Fig. 3.9 for an alongwind sample, while Fig. 3.10 shows the corresponding quantities for the acrosswind direction. In particular, the final residual moments and rotations are marked by squares. As can be seen, for shakedown to occur, plasticity increases monotonically for each cycle with, after several cycles of loading, an absence of further plastic accumulation as the structure begins respond in a purely elastic manner, i.e. the state of shakedown has been reached.

3.2 Statistical Validation of the Load Path

A comprehensive statistical study was carried out considering the 37-story frame described in Section 3.1, and shown in Figure 3.1. The wind tunnel data informed stochastic wind model described in Section 3.1.2 was adopted for generating the wind load histories. The mean wind speed at the building top was set to $\bar{v}_y =$ 52.5 m/s, which approximately corresponds to a MRI of $y = 700$ years for the Miami region of Florida. To make the comparison, 200 randomly selected wind load histories were considered. Wind directions were selected from the set $\alpha \in \{0^o, 10^o, 20^o, \ldots, 90^o\}$ following a uniform distribution. Therefore, both alongwind and acrosswind directions were considered as well as intermediate wind directions.

For all 200 samples, the estimation of plastic deformations by the strain-based dynamic shakedown scheme was confirmed by the direct integration. To illustrate this, Figure 3.11 shows the comparison between all 200 residual displacements estimated from the strain-based dynamic shakedown scheme and direct integration for the first floor, where most of the plasticity occurred in this case. In addition, comparison for the plastic rotations of a representative hinge with plasticity occurring for all 200 samples (i.e. Hinge 1 as shown in Figure 3.1) is shown in Figure 3.12. As can be seen from these figures, there is strong correspondence between the results of the two methods. Indeed, a correlation coefficient greater than 0.99 existed in both cases. Similar results were seen for all other responses.

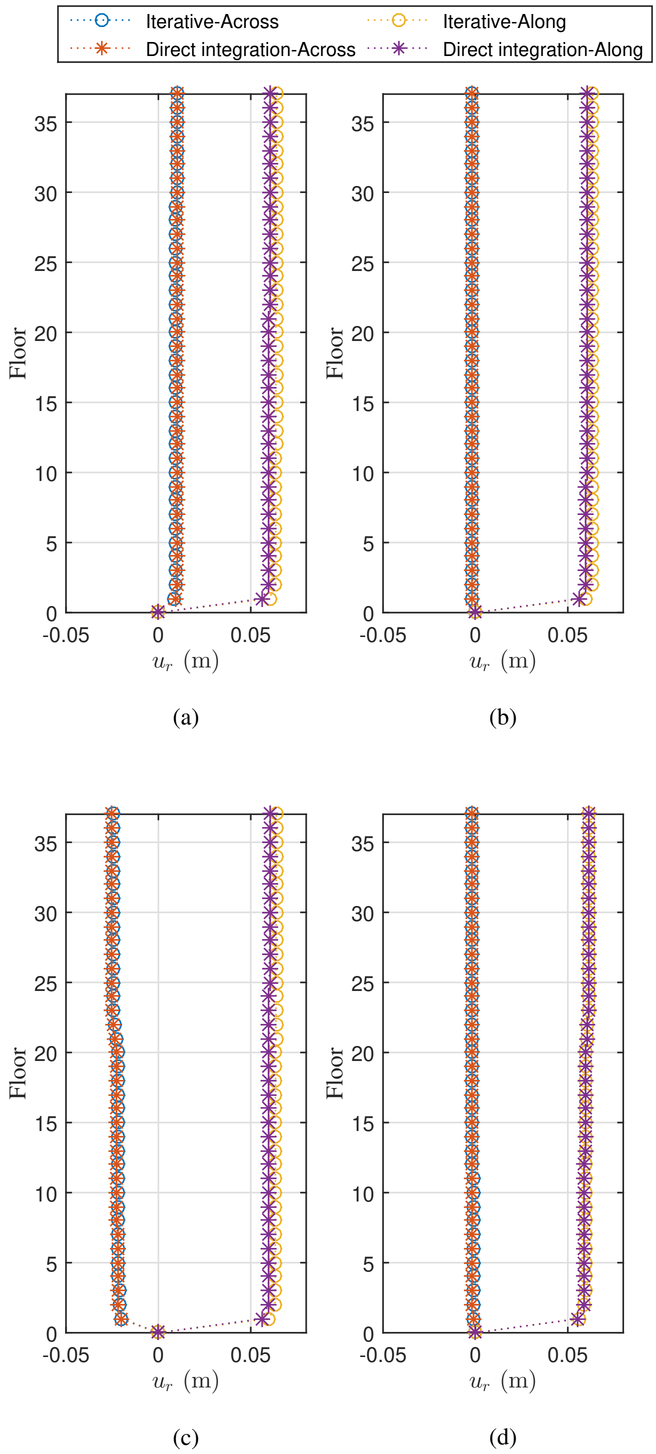

Figure 3.3: Comparison between the residual displacements evaluated through the proposed framework and direct integration for the four randomly generated wind load histories.

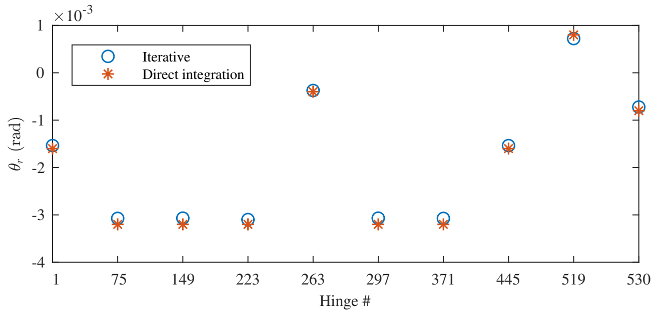

(a)

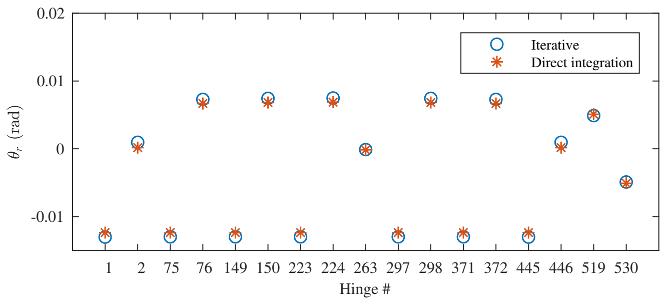

(b)

Figure 3.4: Residual hinge rotation, θ_r, for (a) acrosswind and (b) alongwind responses of representative sample 1.

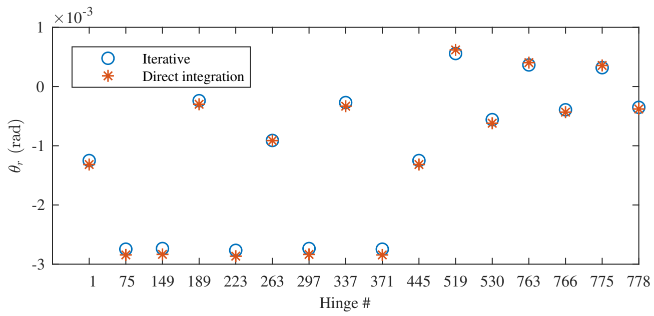

(a)

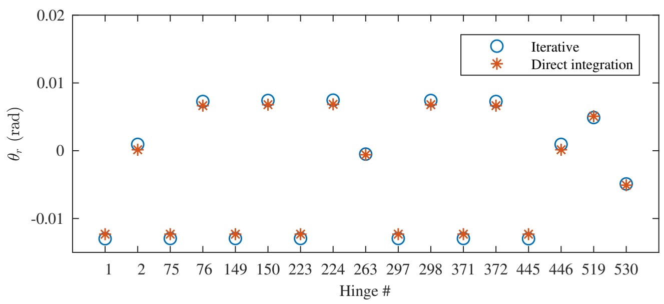

(b)

Figure 3.5: Residual hinge rotation, θ_r, for (a) acrosswind and (b) alongwind responses of representative sample 2.

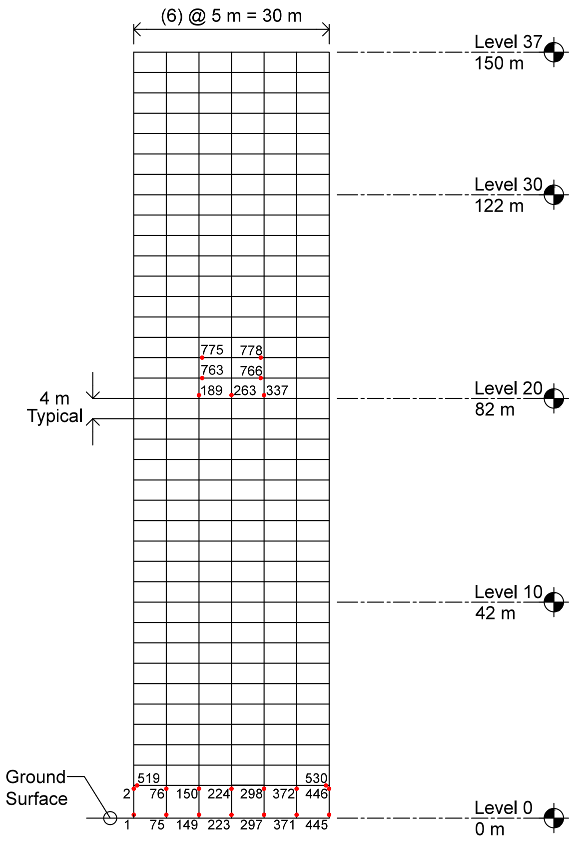

Figure 3.6: Plastic hinge locations.

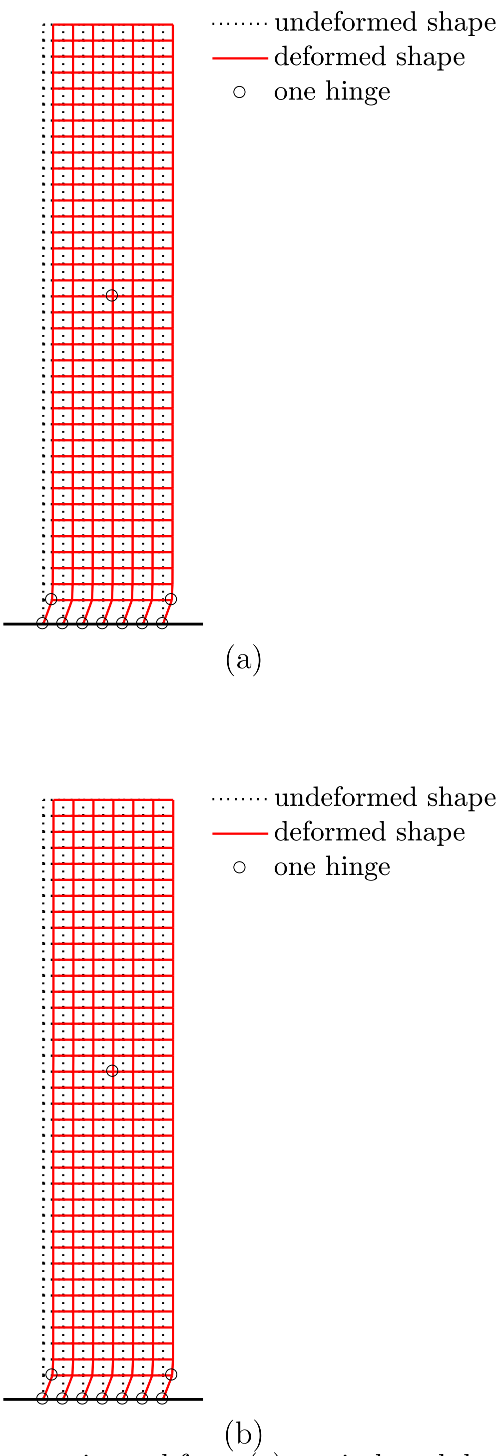

Figure 3.7: Deformed shape estimated from (a) strain-based dynamic shakedown and (b) direct integration for a representative acrosswind sample (deformed shape amplified by 250).

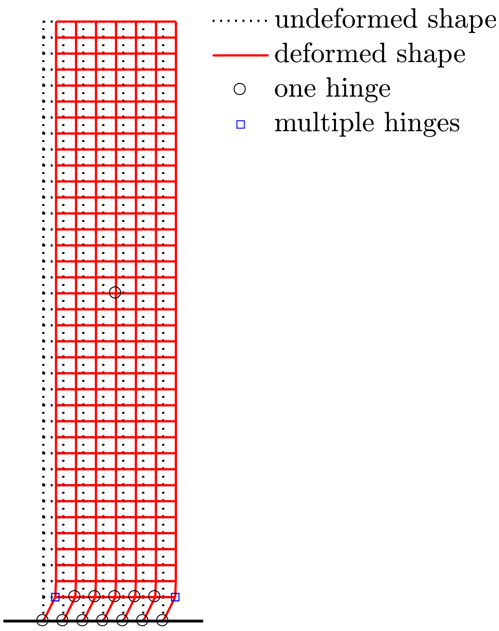

(a)

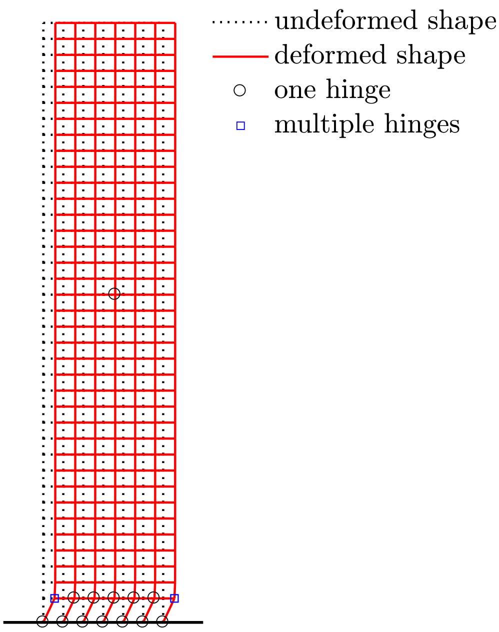

(b)

Figure 3.8: Deformed shape estimated from (a) strain-based dynamic shakedown and (b) direct integration for a representative alongwind sample (deformed shape amplified by 50).

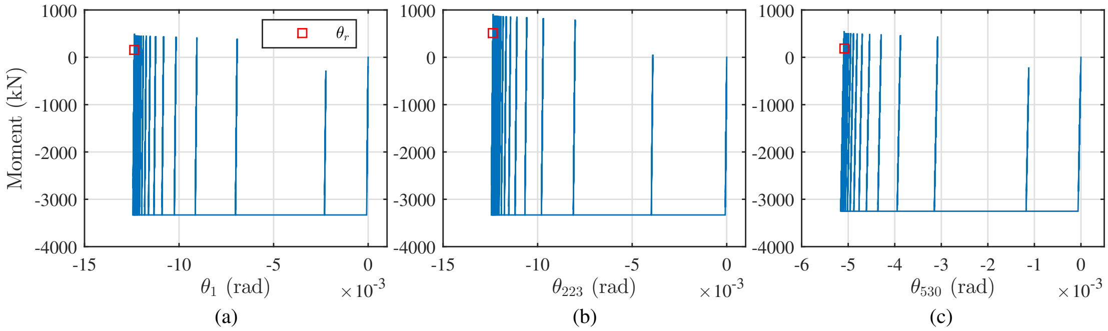

Figure 3.9: Moment rotation history for a representative alongwind sample at (a) Hinge 1 (b) Hinge 223 and (c) Hinge 530.

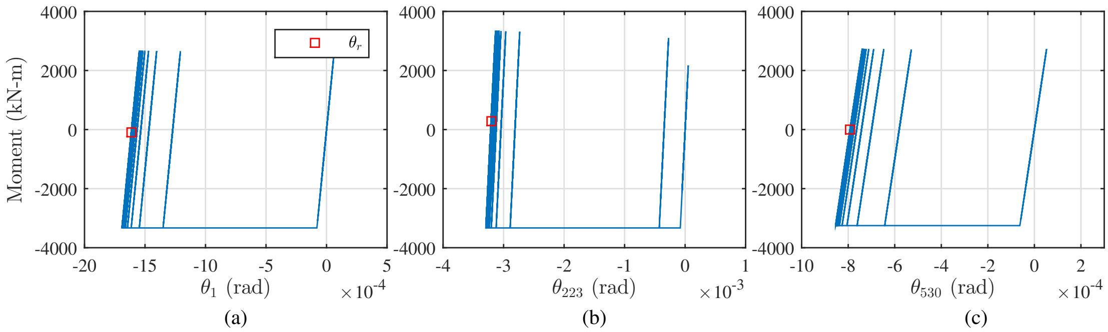

Figure 3.10: Moment rotation history for a representative acrosswind sample at (a) Hinge 1 (b) Hinge 223 and (c) Hinge 530.

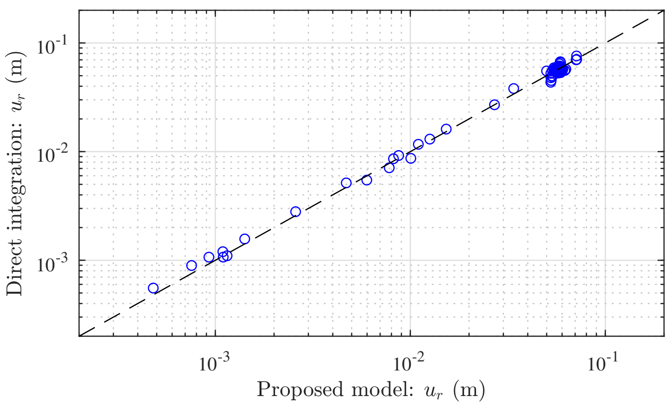

Figure 3.11: Comparison between residual displacements at the first floor for all 200 samples.

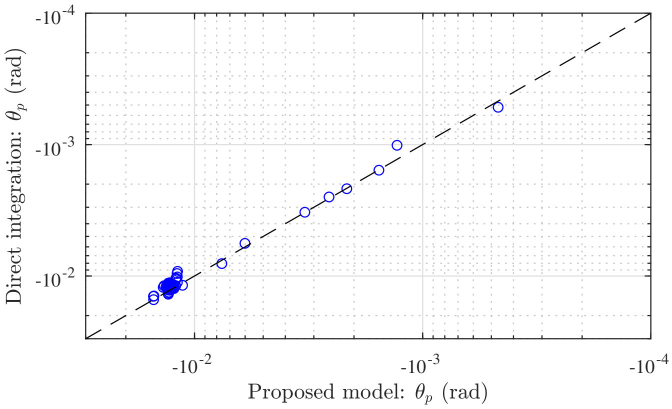

Figure 3.12: Comparison between plastic rotations at hinge 1 for all 200 samples.

3.3 Verification of the Distributed Plasticity Model

In this section, both the fiber-based and section-based framework of section 1.3.3 and 1.3.4 are illustrated on a 2D two-story two-bay frame. In particular, due to the requirement of linear EPP materials in the fiber-based framework, only steel frame was used for illustration of this model, while the section-based framework was demonstrated on both steel and reinforced concrete structures. Direct integration of an OpenSees steel fiber model was carried out and compared to the responses estimated from the fiber-based dynamic shakedown framework. For the section-based framework, unfortunately, this same comparison cannot be achieved since there is no such element that defines the interaction diagram at each section along the member length in OpenSees. The general validity of the section-based framework, however, can be inferred from the results of Sections 3.1 and 3.2, where concentrated plasticity was assumed at the element ends with moment plastic hinges.

3.3.1 Steel frame

The first case study refers to the two-story two-bay frame shown in Figure 3.13. Rigid floor diaphragms were assumed at each story of the frame. The columns are box members, while the beams are wide flange standard W24 sections. A summary of the section sizes is reported in Table 3.2. The dimensions of the box columns are defined by their center line diameters D while the thickness of the section's flanges is set to $D/20$. The steel composing the frame is assumed to be elastic-perfectly plastic, and is therefore completely described by the yield stress σ_y and Young's modulus E_s, which were respectively taken as 50 ksi and 29000 ksi. A lumped mass of 45 kips was considered at each floor in addition to the element mass (to ensure non negligible dynamic amplification, the element mass was artificially increased by a factor of 386). The first two natural frequencies of the frame were respectively $f_1 = 0.2013$ Hz and $f_2 = 0.6604$ Hz. Rayleigh damping was considered, with damping ratios of the first two modes equal to 1.5%.

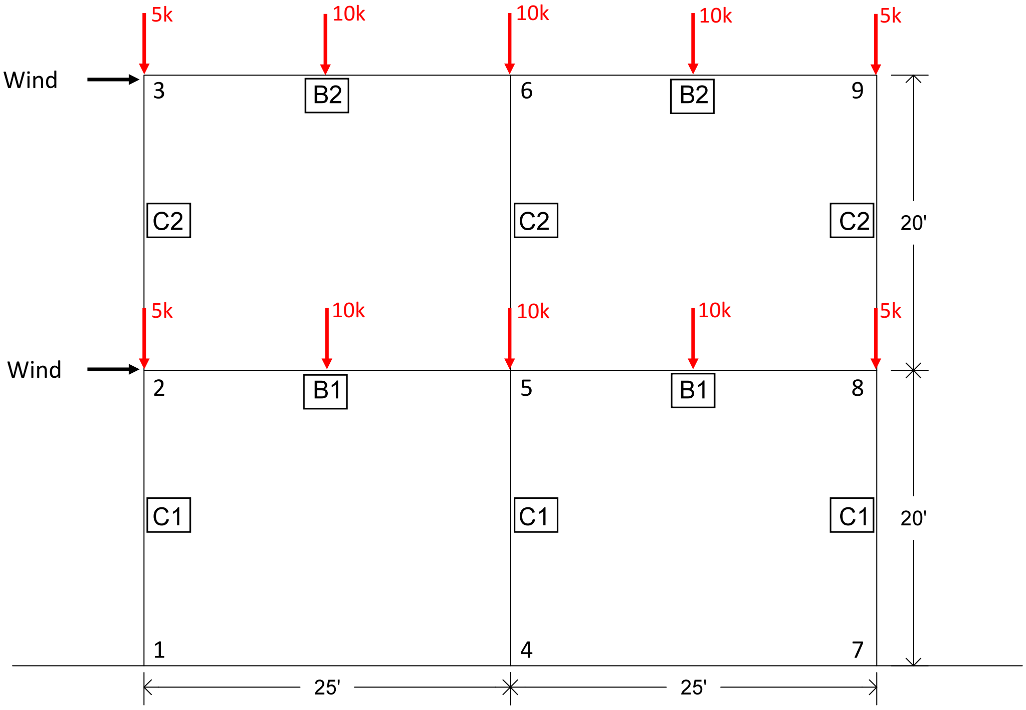

Figure 3.13: Two-story two-bay frame.

Table 3.2: Section sizes of the steel frame.

Section type	B1	B2	C1	C2
Section size	W24 $\times$ 146	W24 $\times$ 103	$D = 25$ (in.)	$D = 20$ (in.)

To model the distributed plasticity along the element, DB beam-column elements were considered with two elements for each member. Gauss-Legendre integration scheme was adopted with 5 integration points (control sections) along the element. External loads were defined by both static vertical point loads and the wind excitation, as shown in Figure 3.13. The quasi-steady model described in the Section 2.3.2 was used for generating stochastic wind loads considering a sampling frequency of 100 Hz and mean wind speed at the building top of 165 mi/h in alongwind direction. Due to the significant effort involved in performing direct integration, the total length of the wind storm was set to $T = 600$ s. The first and last two minutes of the loads were linearly ramped to ensure zero initial and final conditions and therefore, as outlined in Section 2.2.2, the validity of the simulated load path.

Fiber-based steel frame

To apply the fiber-based framework, each section of the steel frame is discretized into several fibers. Under uniaxial bending and plane section assumptions, fibers

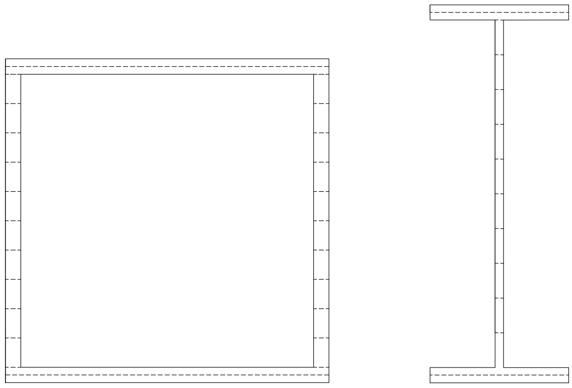

Figure 3.14: Fiber discretization of (a) box section and (b) W-shape section.

located at the same height of the section, i.e. same y coordinates, have the same stress-strain distribution. Therefore, each section considered in this case study was discretized vertically into 14 fibers (2 for both flanges and 10 for web), as shown in Figure 3.14, leading to a total of 1400 fibers for the frame.

In order to further compare the inelastic responses obtained from the proposed framework and those from direct integration, the steel frame was modeled in OpenSees using the DB element “dispBeamColumn” with 5-point Gauss-Legendre integration scheme. The nonlinear responses are integrated by the Newmark-Beta method with $\alpha = 0.5$ and $\beta = 0.25$ considering the limit load condition, i.e. external wind excitation multiplied by the shakedown multiplier s_p. To fully capture the dynamic shakedown phenomena, the wind loads were repeated for 15 cycles before returning to zero for a full cycle, as illustrated in Figure 3.15(a). This final unloading cycle allowed for the dynamic responses to completely damp out therefore enabling the direct estimation of the residual displacements and plasticity distributed along the element.

Given the set up described above, the fiber-based dynamic shakedown framework was applied yielding a shakedown multiplier of $s_p = 2.1817$. Table 3.3 reports the corresponding residual displacements at shakedown estimated by both the proposed framework and direct integration, including horizontal displacements at the first and second floor, i.e. u_1 and u_2, as well as the vertical displacements v_i and rotations ϕ_i at node i. The location of each node is shown in Figure 3.13. As can be seen from Table 3.3, responses obtained from both methods are almost identical. The time-independent self-stresses, i.e. fiber stresses $\boldsymbol{\sigma}(x)$, along the section height, y, obtained from the strain-driven framework are also compared with the direct integration results, as shown in Figure 3.16 for all sections belonging to Element 1. The location of the selected element on the frame is shown in Figure 3.17. Once again, the strain-driven framework has proved its ability to estimate inelastic responses with remarkable accuracy.

To illustrate the distributed plasticity, Figure 3.18 shows the fiber sections as-

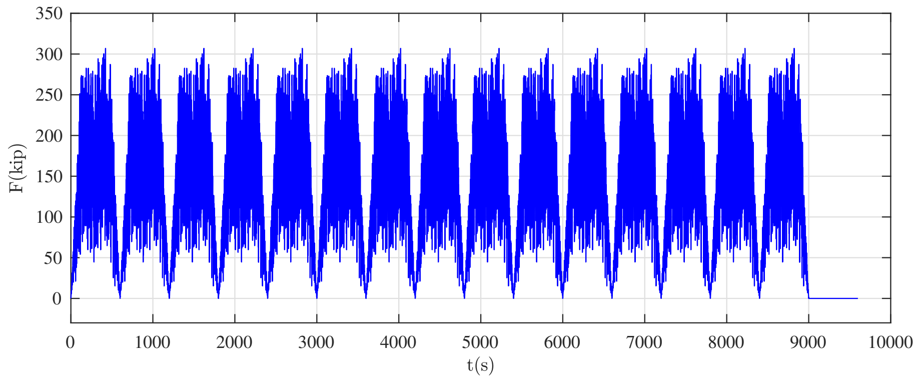

(a)

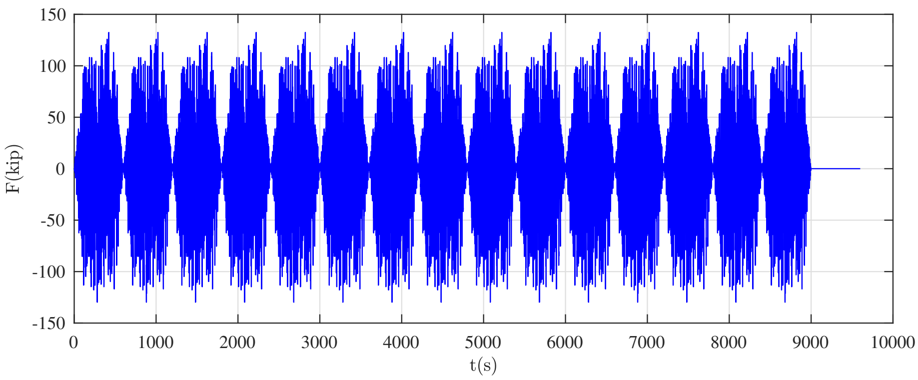

(b)

Figure 3.15: The top floor stochastic wind loads for (a) alongwind excitation; (b) zero-mean loads.

Table 3.3: Comparison between the shakedown residual displacements obtained from proposed fiber-based strain-driven framework and direct integration of the steel frame under alongwind loads.

DOF	u_1	u_2	v_2	ϕ_2	v_3	ϕ_3	v_5
Strain-driven framework	0.4721	1.4335	-0.0017	-0.0036	-0.0030	-0.0047	-0.0027
Direct integration	0.4770	1.4438	-0.0017	-0.0036	-0.0029	-0.0047	-0.0030
DOF	ϕ_5	v_6	ϕ_6	v_8	ϕ_8	v_9	ϕ_9
Strain-driven framework	-0.0035	-0.0049	-0.0029	-0.0008	-0.0035	-0.0016	-0.0045
Direct integration	-0.0035	-0.0054	-0.0029	-0.0012	-0.0035	-0.0020	-0.0046

sumed along the length of Element 1, i.e. 5 integration points, where fibers experiencing inelasticity are filled in with red. In addition, plasticity distributed along section height can also be obtained from the fiber-based framework. It can be observed that the plasticity distributes through the second section along the member with more fibers plastified in Section 1 than in Section 2 as the bottom of a column usually experiences a larger bending moment than the top. The last three sections of the selected member, as shown in the figure, remain elastic during the excitation, therefore no plastic deformations occur.

In addition, the fiber-based strain-driven framework was also applied to the same frame subject to zero-mean stochastic loads, as illustrated in Figure 3.15(b). In this case the dynamic shakedown framework yields a shakedown multiplier of $s_p = 2.1817$. The shakedown residual displacement comparison between the strain-driven framework and direct integration is reported in Table 3.4. As in the alongwind case, the two methods yield similar results, illustrating the immediate applicability of the proposed framework to zero-mean stochastic loads. This strong correspondence can also be observed in the residual fiber stresses distributed along the section, as shown in Figure 3.19 for all sections of the first floor beam (Element 13). The distributed plasticity, illustrated by fibers with plastic deformation, is shown in Figure 3.20 for the same Element. As can be seen, fibers in the flanges of Section 1 undergo inelastic deformations, illustrating that maximum moment in general occurs at the extremes of a section. Furthermore, the end sections of elements between two supports experience the largest forces and undergo the largest inelastic excursions. As a consequence, plasticities occur only in Section 1 (the left end of the beam element) of the selected element while fibers in all other sections remain elastic.

Section-based steel frame

In addition to the fiber-based strain-driven framework, the same steel frame of Figure 3.13 was used to illustrate the application of section-based framework. Prior to carrying out the analysis, the yield domain associated with each section was identified first. The yield domain of Figure 3.21 is considered for a steel box section

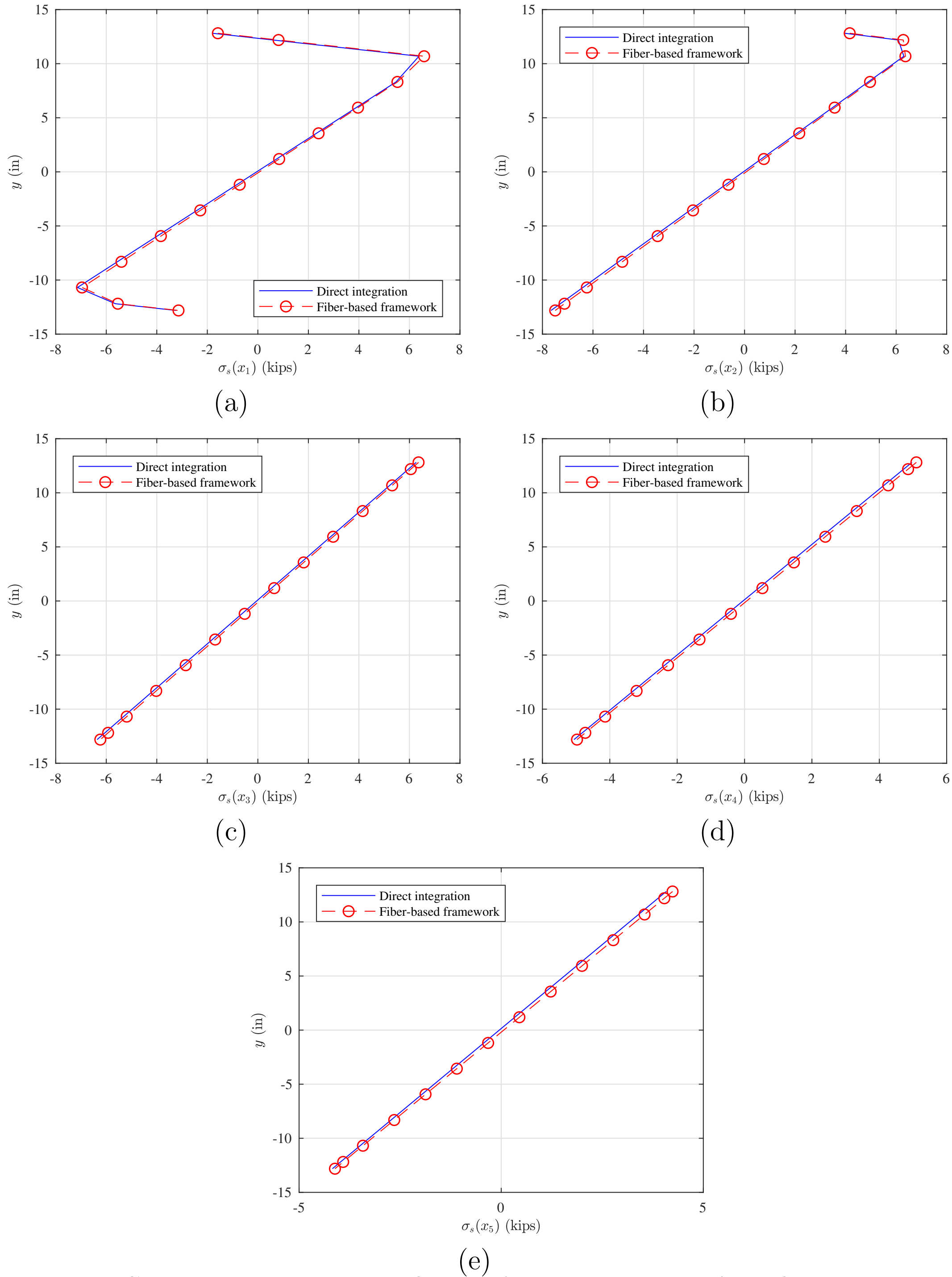

Figure 3.16: Comparison between the fiber self-stresses obtained from fiber-based strain-driven method and direct integration of Element 1 of the steel frame subject to alongwind loads for: (a) Section 1; (b) Section 2; (c) Section 3; (d) Section 4 and (e) Section 5.

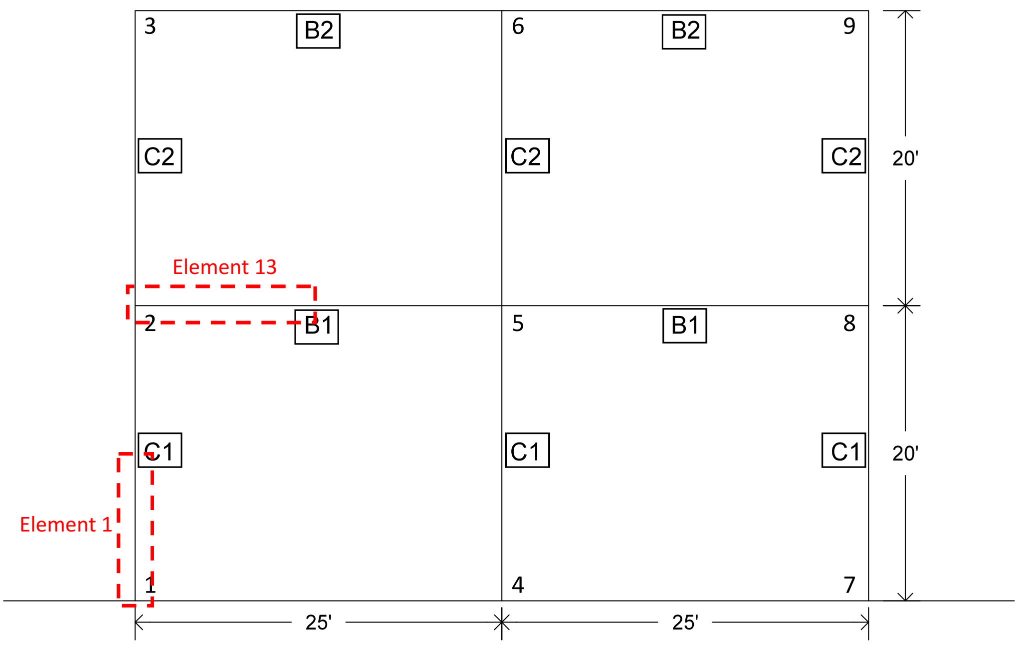

Figure 3.17: Element locations.

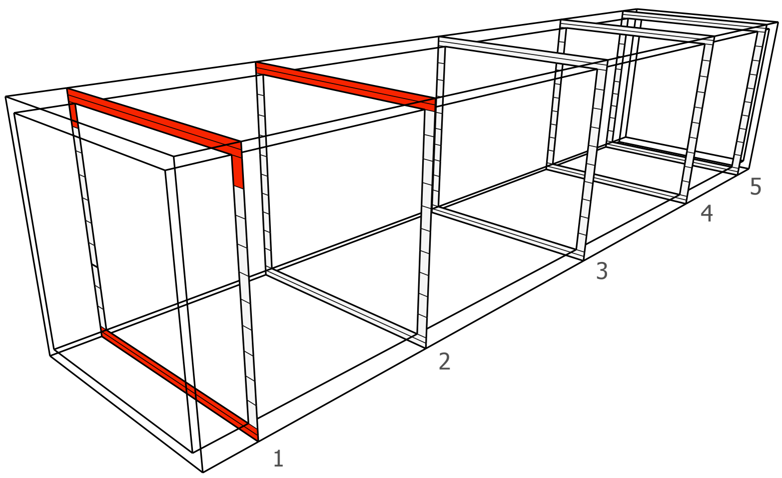

Figure 3.18: Plasticity distributed along Element 1 of the steel frame under alongwind loads obtained from the fiber-based framework.

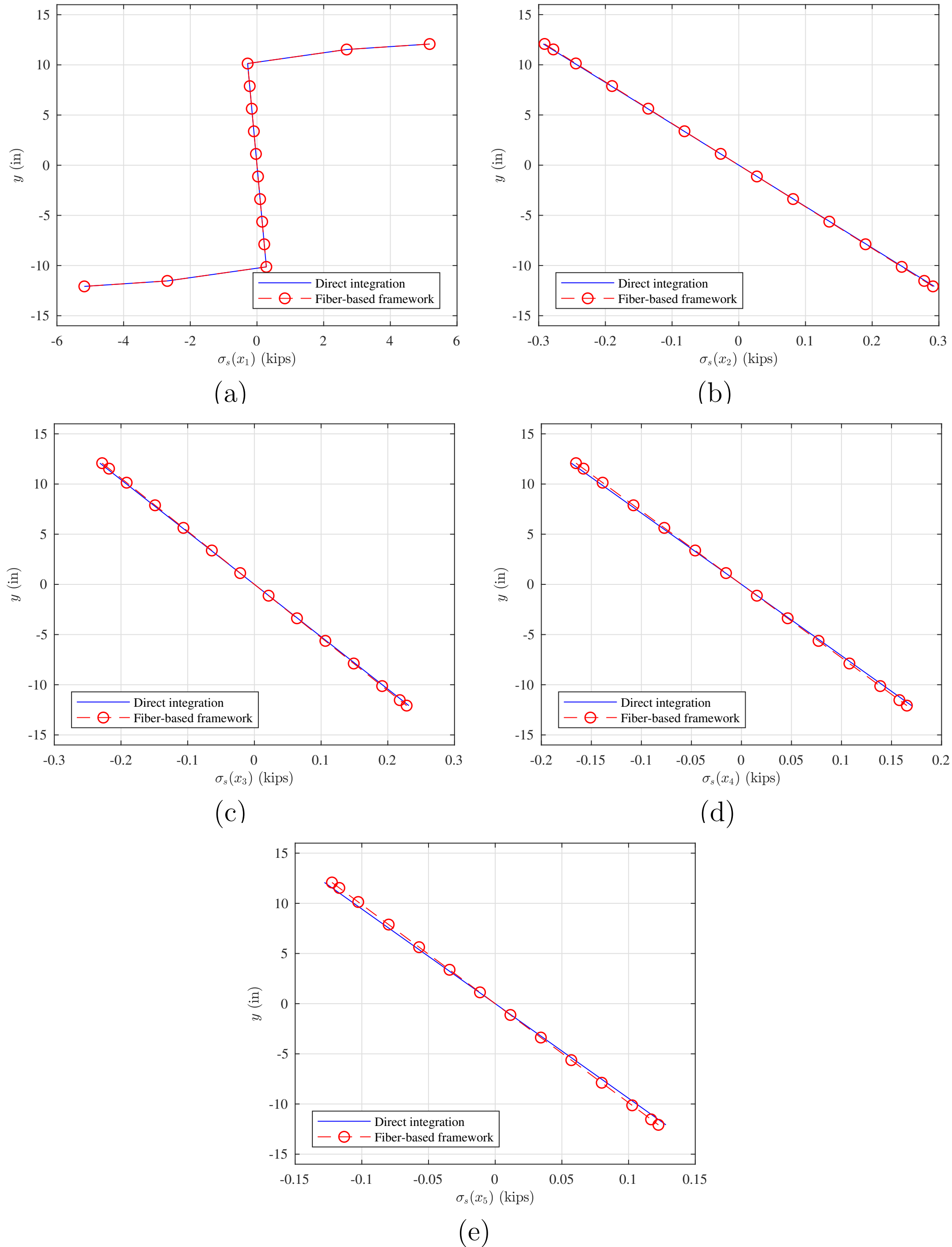

Figure 3.19: Comparison between the fiber self-stresses obtained from the fiber-based strain-driven method and direct integration for Element 13 of the steel frame subject to zero-mean loads: (a) Section 1; (b) Section 2; (c) Section 3; (d) Section 4 and (e) Section 5.

Table 3.4: Comparison between the shakedown residual displacements obtained from proposed fiber-based strain-driven framework and direct integration of the steel frame under zero-mean loads.

DOF	u_1	u_2	v_2	ϕ_2	v_3	ϕ_3	v_5
Strain-driven framework	0.0104	0.0275	-0.0013	-0.0001	-0.0023	-0.0001	-0.0028
Direct integration	0.0106	0.0281	-0.0013	-0.0001	-0.0023	-0.0001	-0.0028
DOF	ϕ_5	v_6	ϕ_6	v_8	ϕ_8	v_9	ϕ_9
Strain-driven framework	-0.0001	-0.0050	0	-0.0012	-0.0001	-0.0022	0
Direct integration	-0.0001	-0.0050	0	-0.0012	-0.0001	-0.0022	0

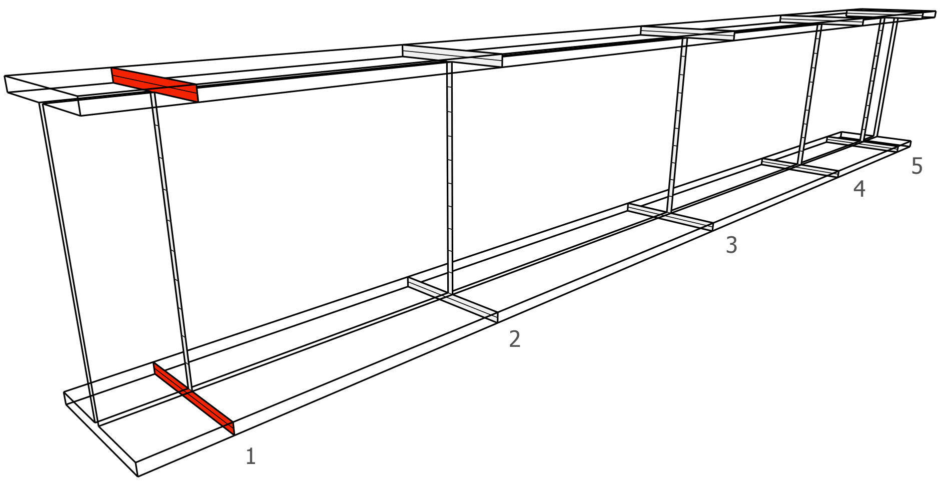

Figure 3.20: Plasticity distributed along Element 13 of the steel frame under zero-mean loads obtained from the fiber-based framework.

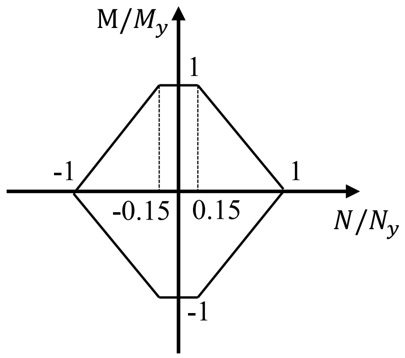

Figure 3.21: Piecewise linear failure domain of steel box columns.

Table 3.5: The axial and bending strengths for all sections of the steel frame.

Section Type	B1	B2	C1	C2
N_y (kip)	-	-	6250	4000
M_y (k-in.)	2.09×10^4	1.40×10^4	5.86×10^4	3.00×10^4

with $M_y = \sigma_y Z$ and $N_y = \sigma_y A$ being the moment and axial strength respectively, where A and Z are the area and the plastic section modulus of the relevant cross section [3.2]. For a beam section, the yield domain is defined by bending strength $M_y = \sigma_y Z$ alone. A summary of the strength of all sections is given in Table 3.5.

Given the set up described above, the section-based framework of Section 1.3.4 was applied yielding a shakedown multiplier of $s_p = 2.4295$, which is larger than the one estimated through the fiber-based framework. The reason behind this is due to the difference between the definition of the yield surface for the two methods. The yield surface for a section is defined as the ultimate strength that the entire cross section can reached in yielding, while that for a fiber-based framework is taken as yielding of any fiber of a section, which in general occurs at the extreme fibers and spreads over the height of the section. The shakedown residual displacements are reported in Table 3.6, which are also greater than the fiber-based results given the larger multiplier.

Figure 3.22 shows the plasticity distributed along Element 1 with 5 integration points along member length marked in dashed line. In this case, plasticity is identified by sections experiencing plastic deformations. The whole section is considered yielding at the same time since there is no information about the fiber strains and plasticity distributed along section height. Based on the assumption of linear curvature and constant axial strain along the element from the interpolation function of Eq. (1.31), plastic deformations between integration points can also be evaluated. For Element 1, plasticity occurs from the bottom of the column to about two-thirds the distance between sections 2 and 3, which coincides with the fiber-based results.

Table 3.6: The shakedown residual displacements obtained from proposed section-based strain-driven framework of the steel frame under alongwind loads.

DOF	u_1	u_2	v_2	ϕ_2	v_3	ϕ_3	v_5
Strain-driven framework	0.9994	2.8374	-0.0037	-0.0067	-0.0053	-0.0090	-0.0027
DOF	ϕ_5	v_6	ϕ_6	v_8	ϕ_8	v_9	ϕ_9
Strain-driven framework	-0.0066	-0.0049	-0.0057	-0.0012	-0.0067	0.0007	-0.0088

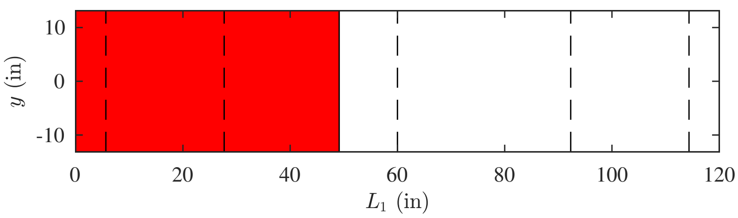

Figure 3.22: Plasticity distributed along Element 1 of the steel frame under alongwind loads obtained from the section-based framework.

3.3.2 Reinforced concrete frame

The second case study refers to a reinforced concrete frame of the same geometry as Figure 3.13. All elements of the frame consist of rectangular reinforcement concrete sections. A summary of the section sizes is reported in Figure 3.23. The yield stress of the concrete, f_c', is taken as 4000 psi. Considering a concrete with a density of 145 lb/ft^3, the modulus of elasticity can be defined as:

$$E_c = 57,000\sqrt{f_c'} \quad psi \tag{3.1}$$

The reinforcing steel is considered to have a yield stress of 60 ksi and Youngs modulus, E_s, of 29000 ksi. A lumped mass of 15 kips was considered at each floor in addition to the element mass (as before, to ensure non negligible dynamic amplification, the element mass was artificially increased by a factor of 386). The first two natural frequencies of the frame were respectively $f_1 = 0.1562$ Hz and $f_2 = 0.4811$ Hz. Rayleigh damping was considered, with damping ratios of the first two modes equal to 3%. The wind loads were simulated from the quasi-steady model with mean wind speed at the building top of 165 mi/h in alongwind direction and sampling frequency of 100 Hz. The total duration of the external wind load was again limited to 10 minutes with the first and last two minutes linearly ramped.

In defining the finite element model, fiber sections with tangent modulus of E_c were used to model the elastic response of the frame. Each section of the frame was discretized into 20 fibers in the y-direction, as illustrated in Figure 3.24, leading to a total of 2000 fibers. The section stiffness matrix $\boldsymbol{k}_s$ was then assembled from this fiber discretization through Eq. (1.24). To account for the reduction in stiffness after concrete cracking, the moment of inertia of a cracked section I_{cr} is generally used to compute the structural responses. In calculating I_{cr}, the concrete that is

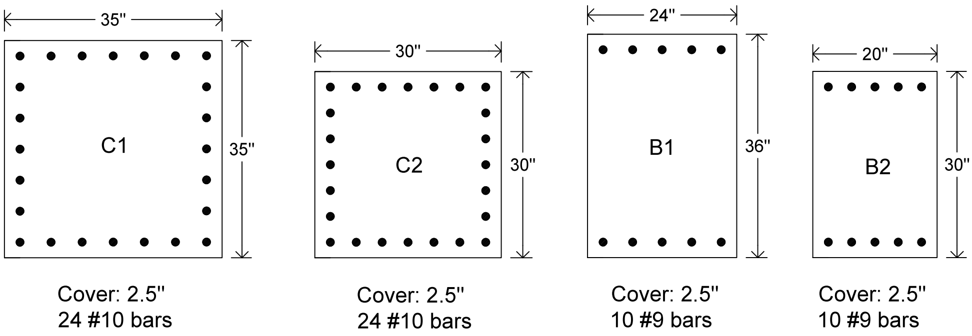

Figure 3.23: Section sizes composing the reinforced concrete frame.

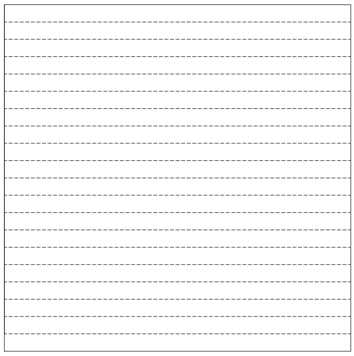

Figure 3.24: Fiber discretization of the rectangular elastic reinforced concrete section.

stressed in tension is assumed cracked, therefore effectively absent. The transformed section then consists of $n = E_s/E_c$ times the steel area in tension and $(n-1)$ times the steel area in compression. In the fiber element formulation, however, moment of inertia is not explicitly used in defining section stiffnesses $\boldsymbol{k}_s(x)$. Instead, a factor, I_r, relating the cracked and uncracked moment of inertia is applied to the bending related terms in section stiffness matrix, as follows;

$$I_r = \frac{I_{cr}}{I_g} \tag{3.2}$$

with I_g the moment of inertia of the gross concrete section.

To avoid the problem of concrete nonlinear behavior, section-based strain-driven framework was applied to model plasticity distributed along the DB beam-column elements with 5-point Gauss-Legendre integration scheme. Similar to the steel case, each member was broken into two elements for better accuracy.

In general, the yield domain of a reinforced concrete beam element is completely defined by the bending capacity of the section M_n while a P-M interaction diagram

Table 3.7: Bending strength for beam elements of the reinforced concrete frame.

RC Section type	B1	B2
M_n (k-in.)	9.553×10^3	7.707×10^3

Table 3.8: The shakedown residual displacements obtained from the proposed section-based strain-driven framework of the reinforced concrete frame under alongwind loads.

DOF	u_1	u_2	v_2	ϕ_2	v_3	ϕ_3	v_5
Strain-driven framework	0.2215	0.5123	-0.0015	-0.0018	-0.0019	-0.0007	-0.0022
DOF	ϕ_5	v_6	ϕ_6	v_8	ϕ_8	v_9	ϕ_9
Strain-driven framework	-0.0019	-0.0038	-0.0004	-0.0006	-0.0018	0.0016	-0.0006

has to be defined for the column considering the interaction between axial loads, P, and bending, M. The six characteristic points defining the interaction diagram are as follows [3.3]:

1. the case of centric axial compression with a strain of 0.003,
2. the case of incipient cracking, in which the compressive failure of concrete is reached on one face while the other has zero strain;
3. the balanced condition, in which the compression failure of concrete is reached simultaneously with tensile yielding of steel bars at the tensile face;
4. the limiting tension-controlled condition, in which the compression failure of concrete is reached simultaneously with tensile strain of -0.005 in the reinforcement layer nearest to the tensile face;
5. the case of pure bending, $P = 0$;
6. the case of centric axial tension, in which a uniform tensile strain of $-\epsilon_y = 0.002$ is reached in the steel with the concrete cracked.

The piece-wise linear yield domains associated with the two column sections are shown in Figure 3.25. The yield domains for the beam sections B1 and B2, on the other hand, are defined by their bending strength M_n, as given in Table 3.3.2.

In this case, the dynamic shakedown framework yields a shakedown multiplier of $s_p = 1.2879$ with the corresponding shakedown residual displacements, as given in Table 3.8. To illustrate plasticity distributed along the element, Figure 3.26 shows plasticity along the first floor beam (Element 13) based on section deformations at the integration points and the interpolation function. As can be seen, nearly half of the element undergoes inelastic deformation. Similar information can be obtained for all other elements.

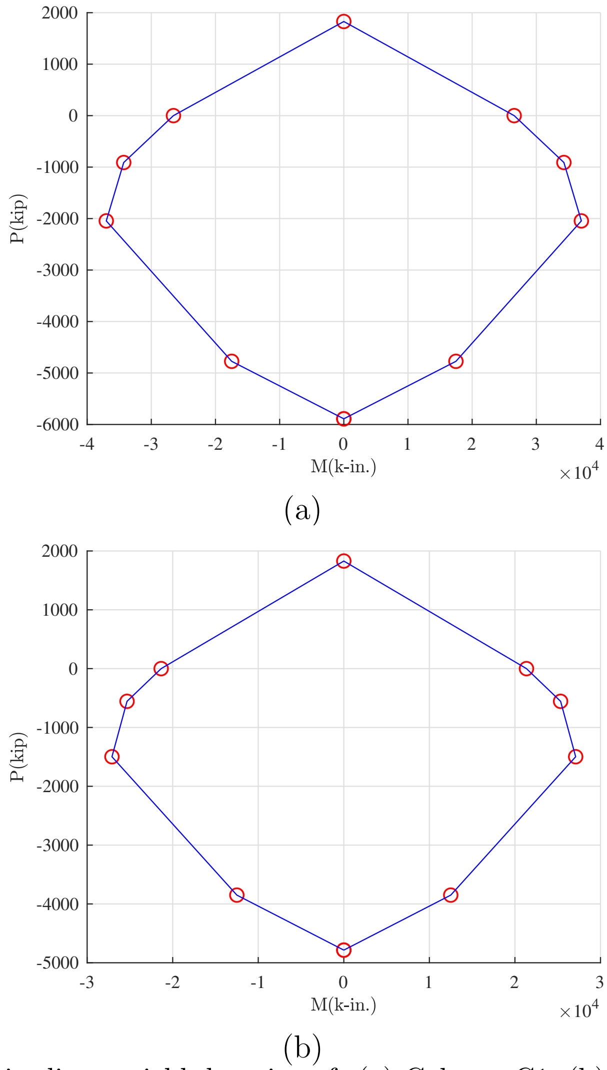

Figure 3.25: Piece-wise linear yield domains of: (a) Column C1; (b) Column C2.

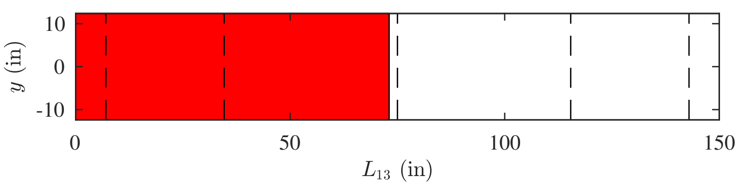

Figure 3.26: Plasticity distributed along Element 13 of the reinforced concrete frame under alongwind loads obtained from the section-based framework.

3.4 Example of the Monte Carlo Scheme

3.4.1 Description

In this section, the probabilistic framework of Sec. 2.2 is illustrated on the steel frame of Fig. 3.1. In addition to the horizontal loads, vertical dead loads due to the self weight of the elements as well as a super dead load of 23.5 kN/m were considered. Wind load histories of total length $T = 3600$ s were considered acting down the alongwind direction, $\alpha = 90°$, and acrosswind direction, $\alpha = 0°$, for mean wind speeds at the building top of $\bar{v}_y = 52.5$ m/s (approximately 700 year MRI for Miami) and $\bar{v}_y = 56.5$ m/s (approximately 1700 year MRI for Miami). To estimate the steady state elastic response of the system, $\boldsymbol{Q}^s(t)$, the first five modes were considered in the modal analysis with damping ratios of 2.5%.

As described in Section 2.4, the classic solution method is first employed to identify whether the structure remains elastic or is susceptible to collapse due to non-shakedown. To estimate the plastic deformations for the non-collapse scenarios, the iterative algorithm of Sec. 1.2.2 is continued until a load multiplier of $s = 1$ (i.e. estimates of the plastic deformations and strains under the unamplified loads are considered).

3.4.2 Results

The analyses were carried out for $N_s = 5000$ simulations in both the alongwind and acrosswind directions for the two intensity levels. Under the wind speed $\bar{v}_y = 52.5$ m/s of MRI 700 years, 98.6% of acrosswind responses remained elastic, i.e. $s_e \geq 1$, while 17.9% of alongwind responses remained elastic and 8.9% were susceptible to collapse, i.e. $s_p < 1$. For the non-collapse samples that went beyond the elastic limit, upper bounds on the peak responses were estimated as outlined in Sec.2.4, i.e. as $\hat{\mathbf{u}} = \hat{\mathbf{u}}_e + \mathbf{u}_r$. Figure 3.27 presents the probability of exceedance associated with the upper and lower bounds (purely elastic response) of the peak displacement responses at three different floor levels. As can be seen, the difference between the two curves were more significant at lower levels due to the fact that most plastic hinge rotations occurred in the first story while the other floors remained mainly elastic (see the typical deformed configurations of Figs. 3.7 and 3.8). For example, the peak response with 50% exceedance probability at the 1^{st} floor is bounded by 0.06 and 0.064 m while that of the 37^{th} floor is between 1.528 and 1.534 m.

Figure 3.28 shows the probability of exceedance associated with the residual displacements associated with non-collapse samples that experienced plastic deformation, i.e. non-collapse samples excluding those in which the structure remained elastic. Plastic deformations in the members, e.g. plastic hinge rotations, can also be estimated by the proposed framework, as shown in Fig. 3.29 for two representative hinges at the bottom of the exterior and middle columns of the first story. In particular, it can be seen that around 45% of Hinge 1 responses, θ_1, remained

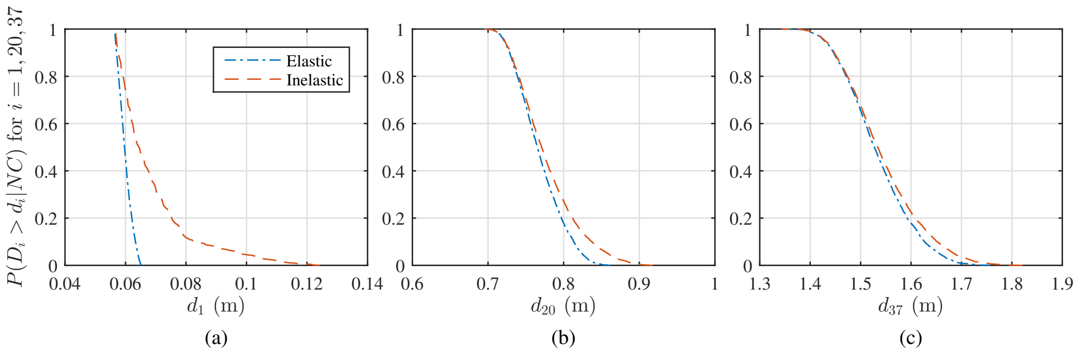

Figure 3.27: Bounds on the probability of exceedance of the alongwind (MRI = 700 years) peak displacement responses at (a) Floor 1 (b) Floor 20 and (c) Floor 37.

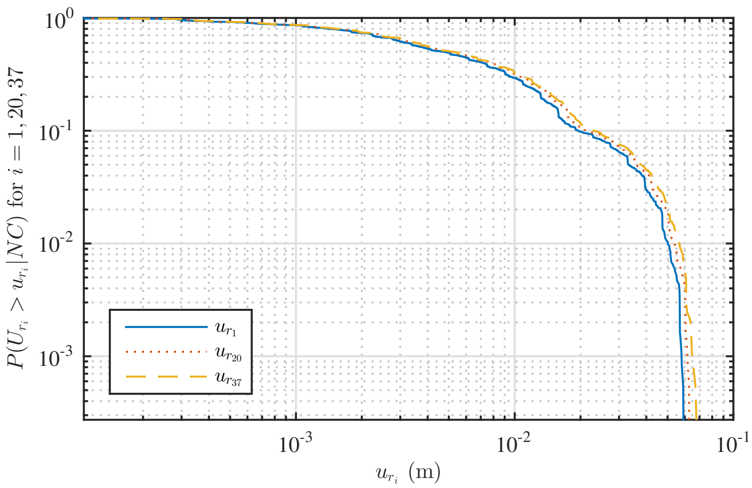

Figure 3.28: Probability of exceedance of the residual displacements at Floor 1, 20 and 37 in the alongwind direction with MRI = 700 years.

elastic, i.e. no plastic hinge rotations occurred, even though the structure exited the elastic limit, while plastic rotations occurred in Hinge 223 for all non-collapse inelastic samples.

For a larger wind storm with MRI of 1700 years, 98.7% samples were susceptible to collapse in the alongwind direction, i.e. $s_p < 1$, while 36.9% were susceptible to collapse in the acrosswind direction with 43.8% remaining purely elastic. Figure 3.30 reports the exceedance probability associated with the upper and lower bounds of the peak displacement responses at three different floor levels. Similarly to what was seen in the alongwind direction, larger differences between the bounds can be observed at the lower levels. Indeed, residual displacements at higher floors were negligible as compared to the elastic responses. Figure 3.31 reports the probability of exceedance associated with the residual displacements associated with non-collapse samples in which the structure sustained plasticity. As can be seen, around 52% of the residual displacements at the first floor were negligible. This was due to how, for

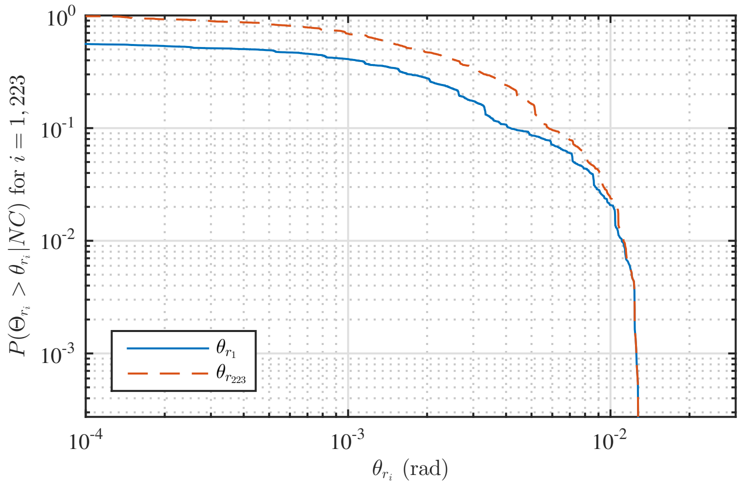

Figure 3.29: Probability of exceedance of the residual hinge rotations for Hinge 1 and Hinge 223 in the alongwind direction with MRI = 700 years.

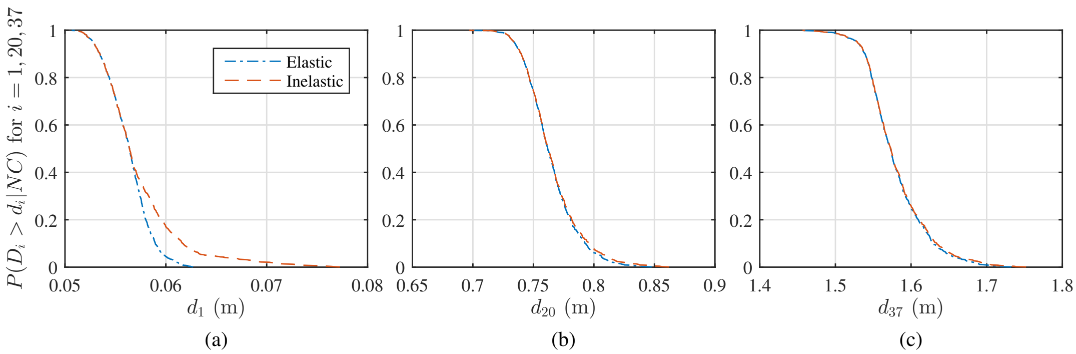

Figure 3.30: Probability of exceedance of the residual displacements at Floor 1, 20 and 37 in the acrosswind direction with MRI = 1700 years.

52% of the wind storms, the majority of the plastic hinges formed in stories other than the first. The probability of exceedance of plastic hinge rotations associated with hinges 263 and 223 for non-collapse samples with plasticity are presented in Fig. 3.32. It can be observed that 43% of Hinge 263 responses, located at the 21^{st} story, remained elastic while more than 60% of Hinge 223 responses were elastic, which illustrates how greater levels of plasticity occurred in higher stories under the acrosswind loads as compared to alongwind loads.

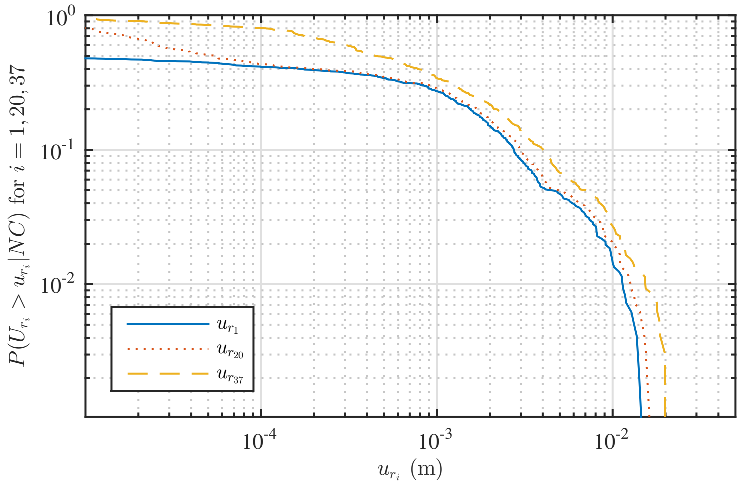

Figure 3.31: Probability of exceedance of the residual displacements at Floor 1, 20 and 37 in the acrosswind direction with MRI = 1700 years.

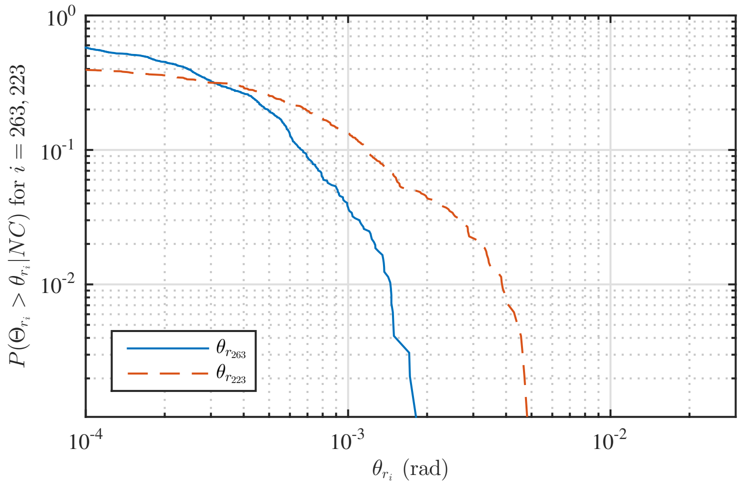

Figure 3.32: Probability of exceedance of the residual hinge rotations for Hinge 263 and Hinge 223 in the acrosswind direction with MRI = 1700 years.

3.5 Concluding Remarks

The primary objective of the work outlined in this chapter was the validation of the framework outlined in Chapter 2. To this end, a suite of concrete and steel structures were developed and solved through both the approach of Chapter 2 as well as through the implementation of direct integration methods. Near perfect correspondence between the proposed approach and direct integration provided an initial validation of the proposed concentrated and distributed shakedown models within the probabilistic setting of Chapter 2. An example was also presented of the Monte Carlo simulation strategy of section 2.4 while considering wind tunnel informed stochastic wind loads. This example clearly illustrated both the efficiency of the proposed approach as well as the wide variety of probabilistic output parameters provided by the scheme.

Bibliography

[3.1] Tokyo polytechnic university (TPU) wind pressure database, 2008.

[3.2] P. Tabbuso, S. M. J. Spence, L. Palizzolo, A. Pirrotta, and A. Kareem. An efficient framework for the elasto-plastic reliability assessment of uncertain wind excited systems. *Structural Safety*, 58:69–78, 2016.

[3.3] J. K. Wight. *Reinforced Concrete: Mechanics and Design (7th ed.)*. Pearson, 2015.

Chapter 4

Case Study: Rainier Square Tower

The primary goals of the work carried out in this chapter were:

1. Development and verification of a three-dimensional dynamic finite element model of the Rainier Square Tower.

2. Application of the section-based distributed plasticity dynamic shakedown framework to the 3D model of the Rainier Square Tower.

3. Inelastic performance assessment within the context of the system-level collapse susceptibility framework developed in Chapter 2.

In reaching the first goal, a three-dimensional finite element model of the Rainier Square Tower was developed in OpenSees. Displacement-based (DB) beam column elements were adopted with five integration points along each element. Walls were modeled by DB beam column elements. The width of the walls was modeled through rigid link elements connected to the axis of each wall element. Superimposed dead loads were considered in addition to the self-weight of the elements and the weight of the framing system. The deformed shape of the structure was verified with unit loads in both global X- and Y-directions at the building top. For further application to dynamic analysis, the mode shapes and natural frequencies of the 3D tower were evaluated through modal analysis.

In reaching the second goal, the section-based dynamic shakedown framework Chapter 1 was applied to the 3D tower. Prior to direct implementation, piecewise linear 3D yield surfaces were defined for all sections of the structure under consideration. In particular, in each reinforced concrete section, the yield domains were modeled through 26 flat surfaces that considered interaction between the axial force and biaxial bending, while, for steel sections, the yield surfaces suggested by the American Institute for Steel Construction (AISC) [4.1] were considered. Furthermore, the wind tunnel informed stochastic wind load model of Section 2.3.1, which is capable of capturing the record-to-record variability in the dynamic wind loads, was calibrated to building specific wind tunnel data for generating sets of synthetic wind records for the Rainier Square Tower. Dynamic shakedown analysis of the tower was then carried out considering wind loads of mean recurrence intervals (MRIs) of 300 and 700 years over a full range of wind directions, providing useful information on not only the safety but also the plastic reserves of the structure.

To achieve the third goal, stochastic wind loads were generated for wind directions selected from the set $\alpha \in \{10°, 20°, 30°, \cdots, 360°\}$ following a uniform distribution and a MRI of 300 years. The system-level collapse susceptibility framework developed in Chapter 2 for providing a general description of the susceptibility to collapse, considering both non-shakedown and failure due to excessive deformations, was then adopted along with the section-based strain-driven dynamic shakedown framework to estimate the system-level failure probability of the 3D tower. In addition, probability distributions of residual displacements over the height of the tower were generated together with plastic deformations for all elements of the structure.

4.1 Numerical model of Rainier Square Tower

A 3D finite element (FE) model was developed for dynamic analysis in OpenSees. In this section, this model will be described first. This will be followed by the verification of the model through static analyses considering unit loads at the building top, as well as dynamic analysis in the form of modal analysis.

4.1.1 Finite element model

The lateral load resisting system of the Rainier Square Tower consists of a concrete core and an outrigger truss connected at floors 38-40 that engages six outrigger columns. The concrete core walls are connected by coupling beams at the floor levels, while the outrigger columns extend from the foundation to the outrigger truss. The concrete core system is composed of three cells from the foundation to Level 18, two cells from Level 18 to 40, and one cell from Level 40 to the roof. In addition, the walls of the concrete core system reduce in thickness along the height of the building at designated levels. Complete views of the building and the lateral load resisting system are shown in Figure 4.1.

All the following analysis, i.e. shakedown analysis as well as dynamic response analysis, will consider the FEM model of the structure fixed at Level 1 (see Figure 4.4 for an illustration of the levels). Floor levels were taken to be at the coupling beam elevations as opposed to the indicated floor levels from the drawings (see Model Level Elevations in Appendix A.1). Each floor was considered to act as a rigid floor diaphragm for horizontal movements. Therefore, the floors could move freely in the X- and Y-directions and rotate about the Z-axis (indicated with u_X, u_Y and θ_Z respectively), giving the building a total of 177 degrees of freedom (The core roof acts as an additional floor level, giving the structure a total of 59 floors).

Materials with linear constitutive laws were assumed for both concrete and steel for elastic analysis. The material strengths considered are summarized in Table 4.1.

(a) (b)

Figure 4.1: Rainier Square Tower. (a) Architectural and structural system rendering of the building [4.4]; (b) OpenSees finite element model.

The Young's modulus of the concrete, E_c, was calculated as follows:

$$E_c = 57,000\sqrt{f'_c} = 5098\ ksi \tag{4.1}$$

The shear modulus of the concrete was calculated using basic mechanics of materials as follows, with the assumption that the Poisson's ratio, ν, for the concrete was 0.15:

$$G_c = \frac{E_c}{2(1+\nu)} = 2216\ ksi \tag{4.2}$$

For the steel, the Young's modulus, E_s, and the shear modulus, G_s, were taken to be 29,000 ksi and 10,900 ksi, respectively. The modulus of elasticity used for the rigid material assigned to all rigid link connections, modeled as "twoNodeLink" elements, was taken to be 2.32×10^{10} ksi to guarantee a rigid behavior. Figure 4.2 reports the deformed shape of the 3D tower, illustrating that the rigid link elements (the brown elements in the red dashed oval) connecting the center lines of the shear walls to the coupling beam element (black element in the figure) were stiff enough to model the shear wall behavior.

To implement the distributed dynamic shakedown framework, the concrete core system was modeled using displacement-based (DB) beam-column elements with their local x-axis oriented in the vertical direction of the building. All elements were

Table 4.1: Summary of material properties.

Material	Strength
Structural steel (wide flange)	$F_y = 50$ ksi
Concrete (shear walls and mega-columns)	$f'_c = 8$ ksi
Reinforcing steel	$f_y = 60$ ksi

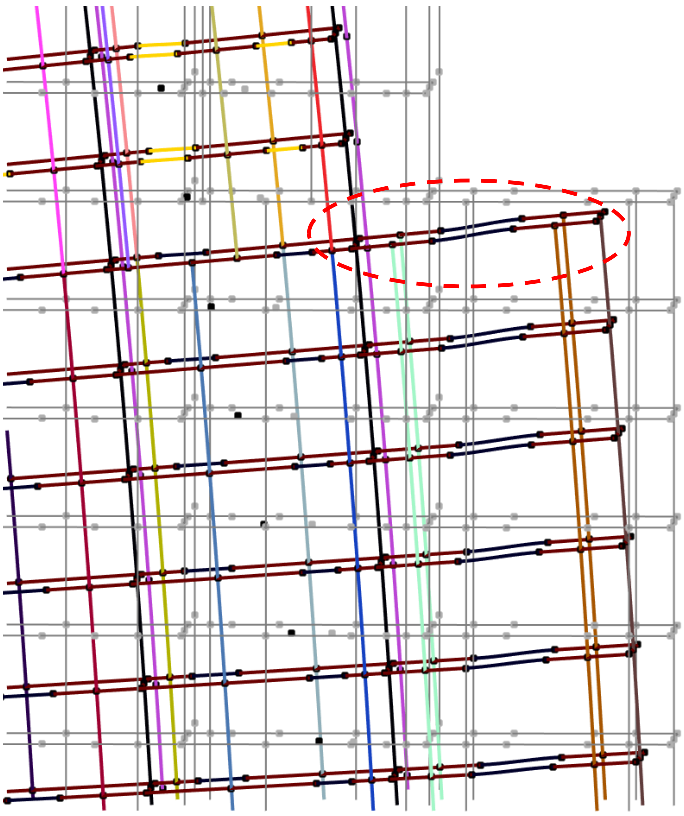

Figure 4.2: Illustration of the deformed shape with rigid link elements.

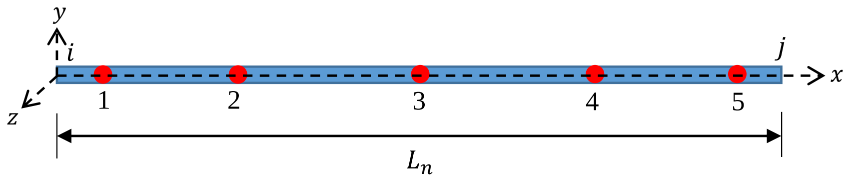

Figure 4.3: Location of the five integration points along a typical DB element.

Table 4.2: Summary of superimposed dead loading.

Use	Superimposed Dead Loading
Corridors and Stairs (within core)	15 psf
Level 2 to 38 and Level 59	10 psf
Level 39 to 58	30 psf
Level 60	25 psf

modeled with five integration points along their local x-axis and utilize a Gauss-Legendre integration scheme, as illustrated in Figure 4.3. To maintain continuity across all elements along the height of the building, adjacent wall elements were connected at each floor using two-node rigid link connections. The coupling beams, outrigger truss members, and outrigger columns were also modeled using DB beam-column elements with five integration points along their local x-axis, and utilizing Gauss-Legendre integration. All coupling beams were connected to adjacent wall elements using two node rigid link connections.

In addition to the mass of all elements and the framing system, which consists of 2-1/2 inches of normal-weight (145 pounds per cubic foot) concrete over 3-inch ribbed steel decking (490 pounds per cubic foot), additional lumped mass equal to the superimposed dead loads, summarized in Table 4.2, was applied at the mass node, taken to be located at the geometric center of each floor. Rigid floor diaphragms were then incorporated utilizing the Rigid Diaphragm multiple constraints function in OpenSees with the mass node assigned as the master node at each floor and all other nodes of the corresponding floor (outrigger column nodes included) assigned as slave nodes. The X- and Y-displacements of the slave nodes can then be defined in terms of the master node by the following kinematic relationship:

$$\begin{Bmatrix} u_{X1} \\ u_{Y1} \\ \vdots \\ u_{Xn_s} \\ u_{Yn_s} \end{Bmatrix} = \begin{bmatrix} 1 & 0 & -(Y_1 - Y_M) \\ 0 & 1 & (X_1 - X_M) \\ & \vdots & \\ 1 & 0 & -(Y_{n_s} - Y_M) \\ 0 & 1 & (X_{n_s} - X_M) \end{bmatrix} \begin{Bmatrix} u_{XM} \\ u_{XM} \\ \theta_{ZM} \end{Bmatrix} \tag{4.3}$$

where X_i, Y_i, X_M and Y_M are the X- and Y-coordinates of the slave nodes and master node while n_s is the number of slave nodes on the rigid diaphragm. This transformation was applied to the degrees of freedom of each floor.

4.1.2 Verification of the FE model

Static analysis

Before carrying out dynamic analysis, the 3D FE model was first verified with static loads at the building top. A unit load was applied to the master node of the top floor in both global X- and Y-directions. The structure deformed as expected under these loads, as shown in Figure 4.4 with amplification for illustration purpose.

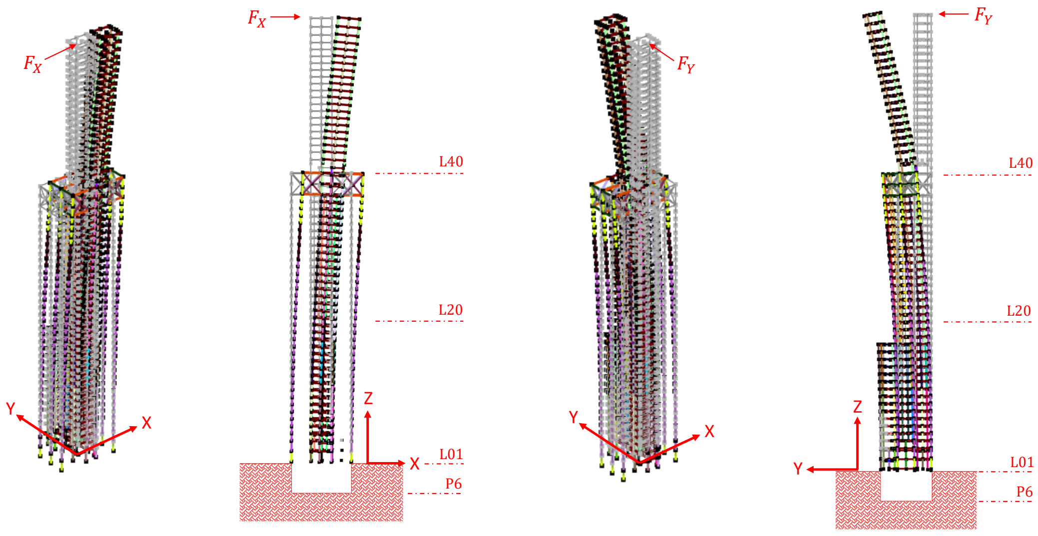

(a) (b)

Figure 4.4: Deformed shapes of the FE model subject to unit loads at the top floor in (a) X-direction and (b) Y-direction.

In applying the dynamic shakedown approach, the structure under gravity loading, including self-weight of the structure and the superimposed dead load, is considered as the initial safe state, where the strain-driven iterative approach starts from, before applying the wind loads. Therefore, the initial generalized stress state as well as the initial displacements due to gravity loading have to be estimated through static analysis prior to the implementation of the dynamic shakedown framework.

Modal analysis

Given the set-up described in Section 4.1.1, modal analysis was carried out yielding the first five natural periods as provided in Table 4.3. The first two modes were respectively in global X- and Y-direction while the rotational mode about global Z-axis was the fifth mode, which could be due to an underestimation of the rotational mass at each floor. The mode shapes are shown in Figure 4.5.

Table 4.3: Natural periods of the FEM model fixed at level 01.

Mode	1^{st}	2^{nd}	3^{rd}	4^{th}	5^{th}
Period (s)	6.05	5.71	1.80	1.64	1.28

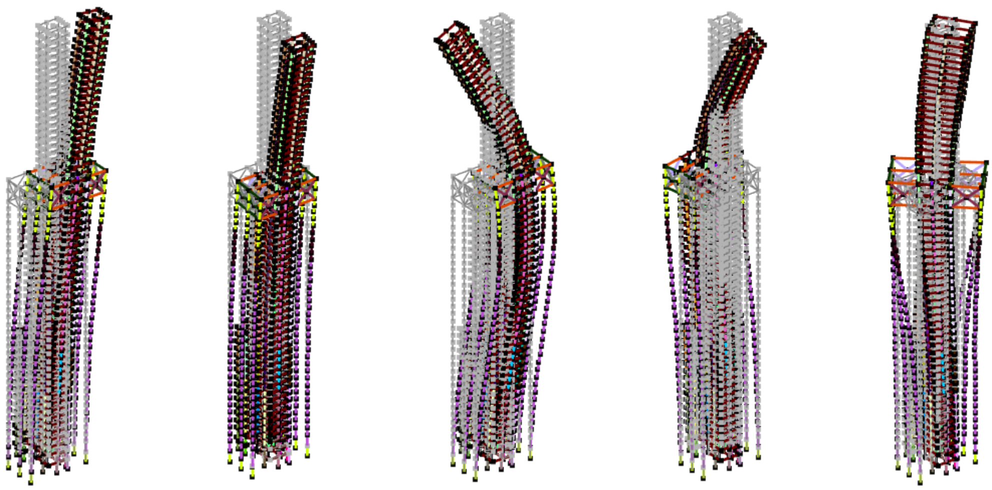

(a) 1^{st} (b) 2^{nd} (c) 3^{rd} (d) 4^{th} (e) 5^{th}

Figure 4.5: The first five mode shapes of the FEM model.

4.2 Dynamic shakedown of Rainier Square Tower

In this section, the section-based distributed plasticity dynamic shakedown framework is applied to the 3D tower of Section 4.1. The 3D piecewise linear yield surfaces for all sections of the structure under consideration will be defined first, followed by the wind load model for generating wind tunnel informed synthetic wind records to be applied to the 3D structure.

4.2.1 Piecewise linearization of the yield surface

The implementation of the dynamic shakedown analysis requires the yield surfaces to be defined for each section along the beam-column elements of the structure under consideration. Assuming local y and z axes in the principal directions of the section, as illustrated in Figure 4.6, the yield surface is defined as the interaction domain between the axial load P and the biaxial bending M_y, M_z based on the following assumptions [4.10]:

1. plane sections remain plane after deformation;

2. full strain compatibility exists between the steel reinforcements and the surrounding concrete;

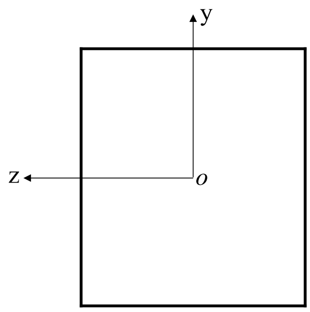

Figure 4.6: Reference system for a typical rectangular section.

3. elastic-perfectly plastic constitutive relation is assumed for both concrete (in compression) and reinforcing steel. Concrete is assumed to be a zero tension material;

4. shear and torsion failures are always prevented by the presence of appropriate transversal reinforcements.

In this section, piecewise linear three-dimensional yield surfaces will be defined for reinforced concrete wall and column sections, coupling beam sections, as well as steel beam sections.

Reinforced concrete wall and mega-column sections

Both mega-columns and walls elements are designed to resist lateral wind or earthquake loads in addition to the gravity loads. Therefore, they are subjected to combined axial and biaxial bending loads. A multisurface piecewise linearization of the yield surface, as proposed in [4.8], is adopted as an approximate representation of the elastic domain of the section. Each surface is associated with a possible collapse mechanism of the section, defined by the following plastic strain vector:

$$\boldsymbol{\epsilon}_p = \left\{\epsilon^p, \quad \chi_y^p, \quad \chi_z^p\right\}^T \tag{4.4}$$

where ϵ^p, χ_y^p and χ_z^p are respectively the plastic axial strain and curvatures about the local y- and z-axes of the section. The corresponding plastic resistance, R, can be determined through the following equation:

$$R = \max\{\boldsymbol{\epsilon}_p^T \mathbf{t} : \mathbf{t} \in \mathbb{E}\} \tag{4.5}$$

where $\mathbf{t} = \{P, M_y, M_z\}$ is the generalized stresses (i.e. section forces) of the section within the elastic domain $\mathbb{E}$. The failure stresses $\mathbf{t}_p$ associated with $\boldsymbol{\epsilon}_p$ can then be solved through the maximization of Eq. (4.5), as illustrated in Figure 4.7. In this work, since the full PMM yield surface was provided, the plastic resistance R, as well as the corresponding failure stresses $\mathbf{t}_p$ with respect to $\boldsymbol{\epsilon}_p$, can be conveniently

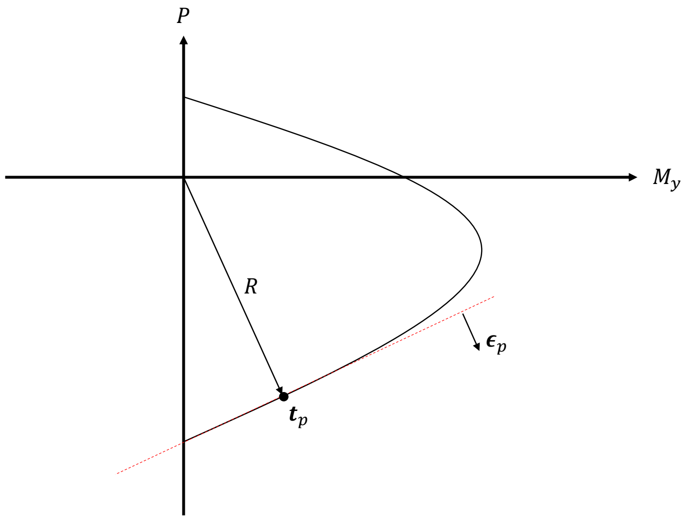

Figure 4.7: Linearized yield surface and the corresponding plastic resistance of a section.

estimated through the above equation by substituting $\mathbf{t}$ with all PMM points on the yield surface.

Considering both the precision and computational complexity, 26 flat surfaces are used for approximating the yield domain of the reinforced concrete column sections. The directions for all surfaces, collected in $\mathbf{N} = [\mathbf{n}_1, \mathbf{n}_2, \cdots, \mathbf{n}_{26}]$, are given as:

$$\mathbf{N} = \begin{bmatrix} 1 & -1 & 0 & 0 & 0 & 0 & 1 & 1 & -1 & -1 & 1 & -1 & 1 & -1 \\ 0 & 0 & 1 & -1 & 0 & 0 & c_z & -c_z & c_z & -c_z & 0 & 0 & 0 & 0 \\ 0 & 0 & 0 & 0 & 1 & -1 & 0 & 0 & 0 & 0 & c_x & c_x & -c_x & -c_x \end{bmatrix.$$
$$\begin{matrix} 0 & 0 & 0 & 0 & 1 & 1 & -1 & -1 & -1 & -1 & 1 & 1 \\ 1 & 1 & -1 & -1 & c_z & c_z & c_z & c_z & -c_z & -c_z & -c_z & -c_z \\ c_y & -c_y & c_y & -c_y & c & -c & c & -c & -c & c & c & -c \end{matrix}\Bigg] \tag{4.6}$$

where c_x, c_y and c_z are defined by limit stresses corresponding to principal directions through the following equations:

$$c_x = \frac{\|\mathbf{t}_{p_1} - \mathbf{t}_{p_2}\|}{\|\mathbf{t}_{p_5} - \mathbf{t}_{p_6}\|}, \qquad c_y = \frac{\|\mathbf{t}_{p_3} - \mathbf{t}_{p_4}\|}{\|\mathbf{t}_{p_5} - \mathbf{t}_{p_6}\|}, \qquad c_z = \frac{\|\mathbf{t}_{p_1} - \mathbf{t}_{p_2}\|}{\|\mathbf{t}_{p_3} - \mathbf{t}_{p_4}\|} \tag{4.7}$$

with $\mathbf{t}_{p_k}$ being the failure stresses corresponding to $\mathbf{n}_k$, while c is the average of c_x and c_z, i.e. $c = (c_x+c_z)/2$. Based on the normality condition, the direction of the k^{th} yield surface can be related to the plastic strain vector through $\mathbf{n}_k = \boldsymbol{\epsilon}_{p_k}$, therefore $\mathbf{t}_{p_k}$ can be easily solved through Eq. (4.5). In addition, it should be noted that this approximation provides an overestimate of the yield domain through external tangent linearization. The errors, however, are have been shown to be relatively small and therefore acceptable for applications to concrete sections [4.8].

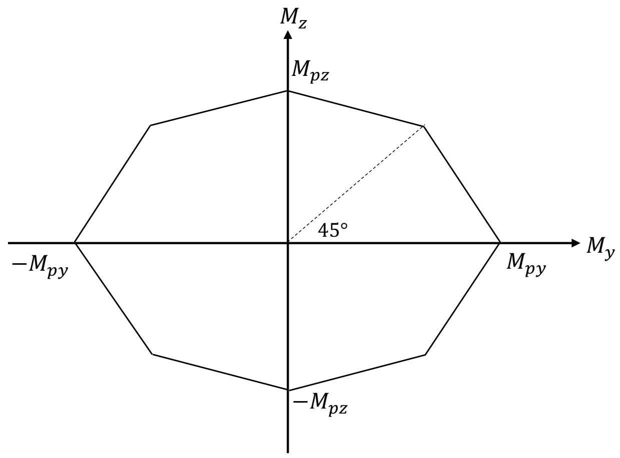

Figure 4.8: Piecewise linear failure domain of reinforced concrete coupling beams.

Reinforced concrete coupling beam sections

The axial loads P of the coupling beam elements are negligible due to the rigid diaphragm assumption, thereby allowing the definition of the yield surface to be completely governed by the interaction between the biaxial bending M_y and M_z. A yield domain of 8 flat surfaces, as shown in Figure 4.8, is therefore considered for a reinforced concrete beam with M_{py} and M_{pz} the moment strengths of the section with respect to bending around the y-axis and z-axis. In addition to these four points in the principal directions, the failure stresses at 45°, 135°, 225° and 315° of Figure 4.8 can also be determined by interpolating the full PMM yield surface data with $P = 0$.

Steel beam sections

Similar to the coupling beam elements, the yield surfaces of steel beam sections are also defined by the interaction between the biaxial bending as the axial load effects are negligible. The AISC yield surface [4.1], as shown in Figure 4.9, is used in this work. The equation governing the interaction between the biaxial bending when the axial force $P = 0$ is:

$$\frac{|M_y|}{M_{py}} + \frac{|M_z|}{M_{pz}} = 1 \tag{4.8}$$

where the moment strengths M_{py} and M_{pz} of a steel section can be determined through

$$M_{py} = F_y Z_y, \quad M_{pz} = F_y Z_z \tag{4.9}$$

with Z_y and Z_z the plastic section moduli with respect to the y- and z-axes of the relevant cross section.

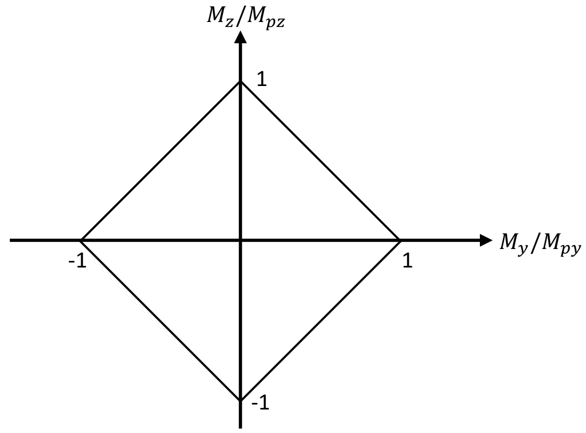

Figure 4.9: Piecewise linear failure domain for steel beams.

Elastic element assumption

To account for a few piers that are narrow and not pertinent to the global or local response of the structure, inelasticity is assumed not to occur in those elements, i.e. those elements are assumed elastic during the shakedown analysis. In addition, there are several small adjustment elements used during the modeling of the core walls that are used to connect the offset coupling beam to the actual floor level in the model (e.g. element #545 between Level 10 and 11 on Grid 3). These elements are also assumed elastic during shakedown analysis without compromising the accuracy of overall response of the structure. A list of DB elements that are considered elastic due to the aforementioned considerations is provided in A.2.

4.2.2 Stochastic wind loads

To enable Monte Carlo simulation for assessing failure probability, multiple realizations of the external aerodynamic loads $\mathbf{F}(t)$ are needed. For this application, the data-driven spectral proper orthogonal decomposition (POD) model of Sec. 2.3.1 is implemented. $\mathbf{F}(t)$ is therefore decomposed into N_l independent vector-valued subprocesses as follows [4.5, 4.6, 4.7, 4.3, 4.9]:

$$\mathbf{F}(t; \bar{v}_3, \alpha) = \sum_{j=1}^{N_l} \mathbf{F}_j(t; \bar{v}_b, \alpha) \tag{4.10}$$

where $\bar{v}_3$ is the 3-s gust basic wind speed at 33 ft [4.2]; $\bar{v}_b$ is the wind speed average over the total event duration (related to $\bar{v}_3$ through a deterministic transformation, as will be seen later); α is the wind angle measured from the true north, and $\mathbf{F}_j(t)$ is the jth vector-valued subprocess, which can be estimated through the following spectral representation:

$$\mathbf{F}_j(t;\bar{v}_3,\alpha)=\sum_{k=1}^{N_f}|\boldsymbol{\Psi}_j(\omega_k;\alpha)|\sqrt{2\Lambda_j(\omega_k;\bar{v}_3,\alpha)\Delta\omega_k}\times\cos(\omega_k t+\vartheta_{kj}+\boldsymbol{\theta_j}(\omega_k)) \tag{4.11}$$

where $\boldsymbol{\Psi}_j(\omega_k)$ and $\Lambda_j(\omega_k)$ are the jth frequency dependent eigenvector and eigenvalue of $\mathbf{F}(t)$, N_f is the total number of discrete frequencies considered in the interval $[0,N_f\Delta\omega_k]$ with $\Delta\omega_k$ representing the frequency increment that is related to the Nyquist (cutoff) frequency through $\omega_{\text{Nyquist}}=N_f\Delta\omega_k/2$, $\omega_k=k\Delta\omega_k$, ϑ_{kj} are independent and uniformly distributed random variables in $[0,2\pi]$, while $\boldsymbol{\theta}_j$ is a vector of complex angles with the ith component given by $\theta_{ji}(\omega_k)=\tan^{-1}(\text{Im}(\Psi_{ji}(\omega_k))/\text{Re}(\Psi_{ji}(\omega_k))$.

As discussed in Sec. 2.3.1 the eigenvalues and eigenvectors of $\mathbf{f}(t)$ used in Eq. (4.11) are to be estimated directly from the experimental loads obtained from the wind tunnel tests. In particular, $\Lambda_j(\omega_k)$ and $\boldsymbol{\Psi}_j(\omega_k)$ are related to the eigenvalues and eigenvectors of the scaled experimental wind tunnel load, $\mathbf{f}_w(\tilde{t})$, through the following relationships:

$$\Lambda_j(\omega_k;\bar{v}_3)=\left[\left(\frac{\bar{v}_{3600}}{\bar{v}_w}\right)^2\right]^2\left(\frac{\bar{v}_w}{\bar{v}_{3600}}\right)\Lambda_j^{(w)}(\tilde{\omega}_k) \tag{4.12}$$

$$\boldsymbol{\Psi}_j(\omega_k)=\boldsymbol{\Psi}_j^{(w)}(\tilde{\omega}_k) \tag{4.13}$$

where $\bar{v}_b=\bar{v}_{3600}$ is the mean hourly wind speed at a full-scale reference height that is related to the basic wind speed $\bar{v}_3$ of interest through a transformation of Appendix A.3, $\bar{v}_w$ is the mean hourly wind speed at the reference height to which the wind tunnel loads $\mathbf{f}_w(\tilde{t})$ were scaled, $\omega_k=\frac{\bar{v}_{3600}}{\bar{v}_w}\tilde{\omega}_k$ with $\tilde{\omega}_k$ the kth frequency step at the wind tunnel reference speed, while $\Lambda_j^{(w)}(\tilde{\omega})$ and $\boldsymbol{\Psi}_j^{(w)}(\tilde{\omega})$ are eigenvalues and eigenvectors of $\mathbf{f}_w(\tilde{t})$ and are obtained from solving the following eigenvalue problem:

$$[\mathbf{S}_{\mathbf{f}_w}(\tilde{\omega}_k;\bar{v}_w,\alpha)-\Lambda^{(w)}(\tilde{\omega}_k;\bar{v}_w,\alpha)\mathbf{I}]\boldsymbol{\Psi}^{(w)}(\tilde{\omega}_k;\alpha)=0 \tag{4.14}$$

where $\mathbf{S}_{\mathbf{f}_w}$ is the cross power spectral density of $\mathbf{f}_w(\tilde{t})$. It should be highlighted that, once $\Lambda_j^{(w)}(\tilde{\omega})$ and $\Psi_j^{(w)}(\tilde{\omega})$ are obtained through solving Eq. (4.14), they can be scaled to other wind speeds of interest simply through Eqs. (4.12)-(4.13). This scaling property, together with the POD scheme, which allows the subprocesses to be generated independently using only a few spectral modes, ensures the efficiency of the approach in generating the realizations of the stochastic wind loads process $\mathbf{F}(t)$. It should be observed that, the sampling frequency, $\tilde{\omega}$, associated with frequency points $\tilde{\omega}_k$, is related to the wind tunnel sampling frequency at model scale through $\tilde{\omega}=2\pi\frac{\bar{v}_w s_{ws}}{\bar{v}_{ws}s_L}$ where $\bar{v}_{ws}$ is the wind speed at which the wind tunnel tests were carried out, s_L is the length scale factor of the full-scaled building to the rigid model, while s_{ws} is the sampling frequency used in the wind tunnel tests.

Wind tunnel data for Rainier Square Tower

In generating wind load histories, the stochastic wind load model of Section 4.2.2 was calibrated to wind tunnel datasets provided by Rowan Williams Davies & Irwin (RWDI). These data consisted in measurements made through the high-frequency base balance (HFBB) collected on a 1:400 rigid model of the Rainier Square Tower. In particular, the data was measured considering a sampling frequency of $s_{ws} = 300$ Hz for a total recorded duration of 118 s. Datasets associated with 36 wind directions ($\alpha = \{10°, 20°, ..., 350°, 360°\}$) were obtained, while the mean wind speeds, $\bar{v}_{ws}$, at a 60-inch height in the wind tunnel corresponding to different angles can be found in Table A.1. These wind tunnel datasets were processed and scaled therefore defining horizontal force time series acting in the X and Y directions, $F_{X,j}(t)$ and $F_{Y,j}(t)$, and a torsional load time series, $M_{Z,j}(t)$, acting at the tower's reference center of coordinates (0 ft, -40 ft) at each floor. These full-scaled loading time histories were used in estimating the eigenvalues $\Lambda_j^{(w)}$ and eigenvectors $\mathbf{\Psi}_j^{(w)}$ of Eq. (4.14), which were related to Λ_j and $\mathbf{\Psi}_j$ of Eq. (4.11) through Eqs. (4.12)-(4.13). In calibrating Eq. (4.11), a sampling frequency of 2 Hz was considered for a cutoff frequency of 1 Hz. The first five POD spectral modes were considered in generating stochastic wind processes in this case study. The specific transformation scheme used in converting the basic wind speed $\bar{v}_3$ to the mean hourly wind speed $\bar{v}_{3600}$ is provided in Appendix A.3. An example of the scaled experimental dynamic wind loads and the corresponding simulated dynamic wind loads is presented in Figure 4.10. The effectiveness of the POD-based stochastic model in replicating correlation properties of experimental loads is illustrated through the autocorrelation and cross-correlation functions plotted in Figure 4.11 and Figure 4.12.

4.2.3 Shakedown analysis

Description

In this section, the section-based distributed plasticity dynamic shakedown framework is applied to the 3D tower with piecewise linear yield surfaces as defined in Section 4.2.1. The stochastic wind model of Section 4.2.2 was adopted for generating the wind loads at the reference point of each floor, which were then transferred to the master node of each level. Two intensity levels were considered with 3-s gust wind speeds $\bar{v}_3$ at 33 ft height of 91 and 96 mph, corresponding to MRI of 300 and 700 years respectively for Seattle. Wind load histories of total length of $T = 3600$ s were considered for all wind directions from 10° to 360° in 10° increments in order to provide a full description of the inelastic structural behavior of the system. In addition to the wind loads, gravity loads including the self-weight of the structure and the superimposed dead loads were considered in the analyses. To estimate the steady state elastic response of the system, the first five modes were considered in the modal analysis with damping ratios of 5%.

The linear programming (LP) solution method is first employed to identify

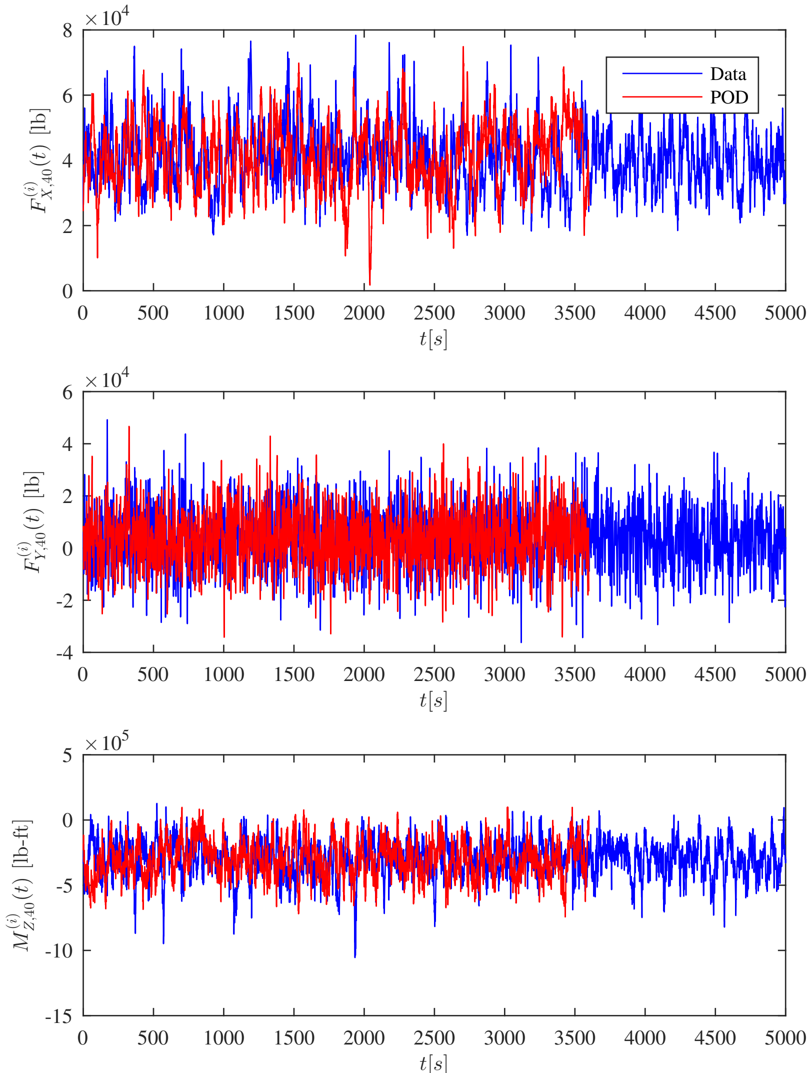

Figure 4.10: Experimental loads and a realization of the Level 40 stochastic wind loads for: $F_{X,40}(t)$, $F_{Y,40}(t)$, and $M_{Z,40}(t)$ associated with $\bar{v}_3 = 103$ mph and $\alpha = 330°$.

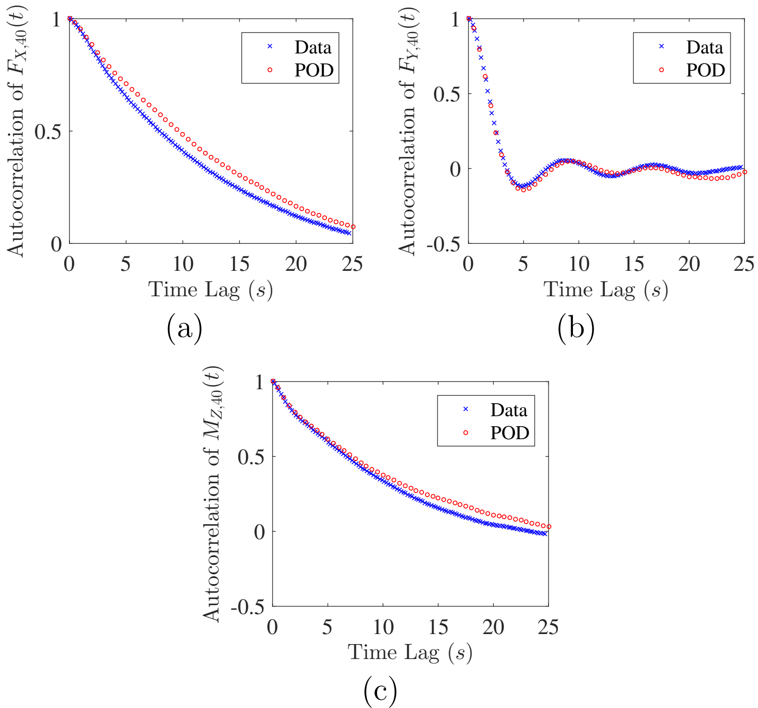

Figure 4.11: Autocorrelation of experimental loads and simulated wind loads associated with $\bar{v}_3 = 103$ mph and $\alpha = 330°$ for: (a) $F_{X,40}(t)$, (b) $F_{Y,40}(t)$, (c) $M_{Z,40}(t)$.

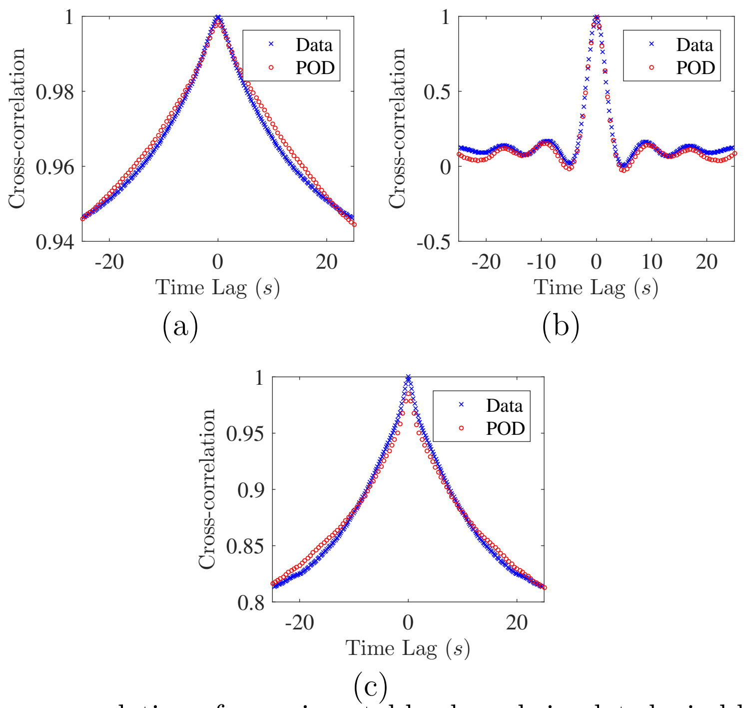

Figure 4.12: Cross-correlation of experimental loads and simulated wind loads associated with $\bar{v}_3 = 103$ mph and $\alpha = 330°$ between: (a) $F_{X,38}(t)$ and $F_{X,40}(t)$, (b) $F_{Y,38}(t)$ and $F_{Y,40}(t)$, (b) $M_{Z,38}(t)$ and $M_{Z,40}(t)$.

whether the structure remains elastic or is susceptible to collapses due to non-shakedown by estimating the elastic, s_e, and plastic multiplier, s_p. This method allows a preliminary evaluation of the structure in just a few seconds. In particular, if $s_e \geq 1$, the structure will remain elastic under the windstorm with no occurrence of inelasticity. If $s_p \geq 1$, the structure will eventually shakedown under the wind loads and is therefore safe against plastic fatigue failure and/or incremental plastic collapse during the windstorm. In addition, elements where inelasticity occurs at shakedown are also identified.

Results

The analyses were carried out for $N_s = 10$ simulations in all wind directions and the two intensity levels mentioned above (i.e. 300 MRI and 700 MRI wind loads). Table 4.4 and 4.5 report the mean and coefficient of variation (CV) of the elastic and plastic multipliers over all simulations for all directions respectively for the 300 and 700 MRI wind loads. It is worth noting how the multipliers vary from one direction to another, suggesting that the structure is more susceptible to wind excitation from certain wind directions. The structure is especially sensitive to wind loads coming from angles α between 190° and 280°. Indeed, for these directions, the elastic multipliers, s_e, are much smaller than those of other directions. It is of practical interest to observe that s_e can be interpreted as the fraction of external dynamic load that would be required to cause first yield somewhere in the structure. For example, for a wind direction of 250° and a 700 year MRI wind speed, Table 4.5 would suggest that on average 41% of the applied load would be enough to cause first yield somewhere in the system.

The plastic multipliers, s_p, on the other hand, are larger than 1 for all wind directions, i.e. the structure will shakedown and be safe against low cycle fatigue, ratcheting and incremental plastic collapse. Furthermore, the plastic reserve of the system, which allows the structure to have some inelasticity while still remaining safe with respect to shakedown, can also be estimated by calculating the ratio between the plastic and elastic multipliers, i.e. s_p/s_e. As can be seen from Figure 4.13, the plastic reserve of the system has a mean value larger than 1.5 for most wind directions for both intensity levels, suggesting that the structure will still shakedown even under wind loads that are multiplied by 1.5 in intensity. For those critical wind directions, the plastic reserves are even higher with a maximum ratio of 5.1.

In addition, elements where inelasticity occurs at shakedown, i.e. $s = s_p$, can also be identified through the LP solution method. An average of 44 elements (among the 1359 DB elements of the entire structure) experienced inelasticity over all wind directions and both intensity levels. Figure 4.14 shows the number of inelastic elements for one of the 10 simulations for each intensity level and all wind directions. In particular, most of the inelastic elements for wind loads associated with the critical wind directions are coupling beam elements, which also govern the elastic limit of the structure. A list of all inelastic elements with tags for a

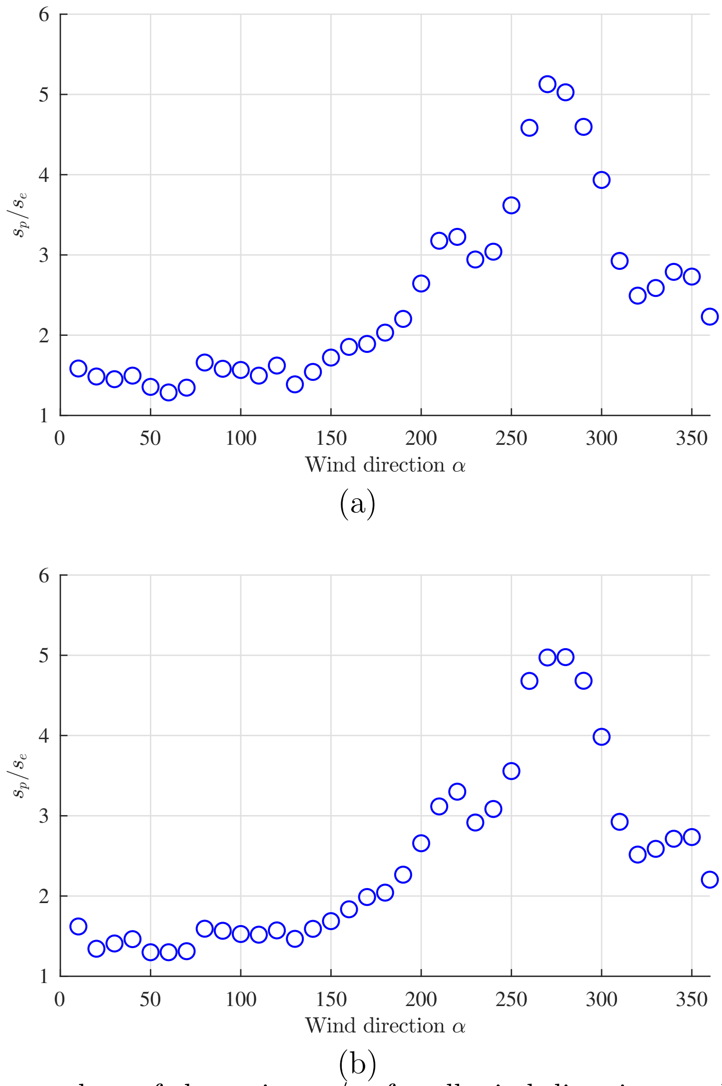

Figure 4.13: Mean values of the ratios s_p/s_e for all wind directions under (a) 300 MRI wind loads and (b) 700 MRI wind loads.

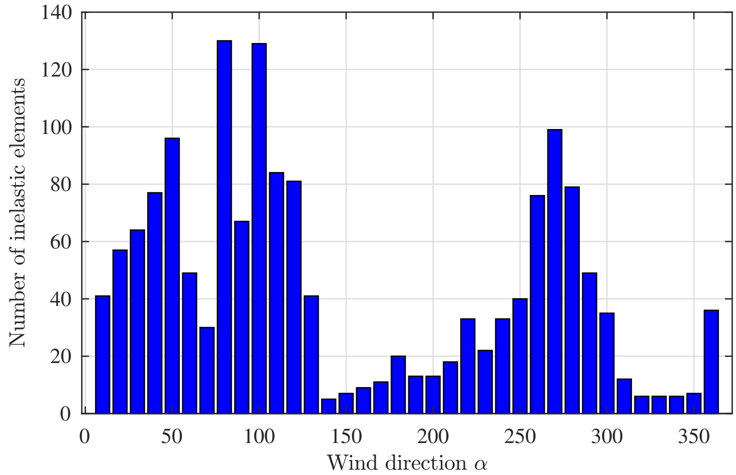

(a)

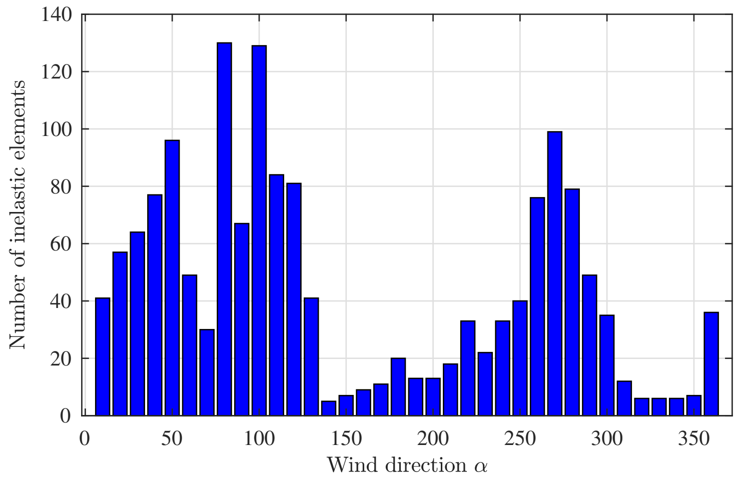

(b)

Figure 4.14: Number of inelastic elements for all wind directions of a representative simulation and for (a) 300 MRI wind loads and (b) 700 MRI wind loads.

representative case of both intensity levels is provided in Appendix A.4.

It should be observed that this preliminary analysis based on the LP shakedown approach can provide the information above in just a few seconds for each simulation, and is therefore suitable for a rapid preliminary evaluation of the safety and identification of the most critical elements of the structure.

4.3 System-level Susceptibility to Collapse

In this section, the probabilistic framework for assessing the susceptibility to system-level collapse was adopted for the probabilistic collapse susceptibility evaluation of the Rainier Square Tower. The uncertainties considered in this simulation-based

Table 4.4: Mean and coefficient of variation (CV) of the elastic and plastic multipliers for all wind directions under wind loads of 300 MRI.

Direction (°)		10	20	30	40	50	60	70	80
s_e	mean	2.2139	3.2968	3.2192	3.3957	2.7409	2.4369	2.3323	2.0777
	CV	0.0994	0.0367	0.0321	0.0424	0.0667	0.0576	0.0534	0.0558
s_p	mean	3.4889	4.8877	4.6715	5.0696	3.7115	3.1306	3.1324	3.4390
	CV	0.0514	0.0434	0.0504	0.0483	0.0739	0.0493	0.0585	0.0528
Direction (°)		90	100	110	120	130	140	150	160
s_e	mean	2.0316	2.2214	2.2333	2.0267	1.8113	1.2170	0.8018	0.7454
	CV	0.0287	0.0375	0.0451	0.0925	0.0669	0.1100	0.0650	0.0904
s_p	mean	3.2114	3.4794	3.3347	3.2622	2.5031	1.8682	1.3751	1.3776
	CV	0.0498	0.0512	0.0404	0.0707	0.0522	0.0765	0.0602	0.0638
Direction (°)		170	180	190	200	210	220	230	240
s_e	mean	0.8569	0.8982	0.8228	0.6091	0.5241	0.4835	0.5601	0.5351
	CV	0.0796	0.0794	0.0856	0.0815	0.0705	0.0488	0.0510	0.0643
s_p	mean	1.6174	1.8207	1.8098	1.6076	1.6633	1.5579	1.6481	1.6218
	CV	0.0703	0.0759	0.0787	0.0669	0.0647	0.0549	0.0684	0.0335
Direction (°)		250	260	270	280	290	300	310	320
s_e	mean	0.4544	0.4959	0.5762	0.6538	0.8855	1.1657	0.9573	0.7320
	CV	0.0557	0.0414	0.0202	0.0413	0.0426	0.0339	0.0676	0.1040
s_p	mean	1.6406	2.2735	2.9550	3.2868	4.0674	4.5843	2.8005	1.8180
	CV	0.0520	0.0672	0.0507	0.0581	0.0459	0.0389	0.0715	0.0823
Direction (°)		330	340	350	360				
s_e	mean	0.6480	0.7025	1.0093	1.3495				
	CV	0.0324	0.0703	0.0802	0.1071				
s_p	mean	1.6756	1.9584	2.7495	3.0003				
	CV	0.0421	0.0717	0.0570	0.0850				

framework will be first discussed.

4.3.1 Uncertainties in the probabilistic framework

To set up the Monte Carlo simulation, it is first convenient to define all uncertainties in both the structural system and the external loads. For the external wind loads, record-to-record variability, wind directions and intensities are generally taken as random variables. The wind model of Section 4.2.2 models the record-to-record variability in the dynamic wind loads, therefore the wind load histories will be different even with the same wind direction and intensity for each realization. To further take into account the wind directionality, a joint probability distribtuion of wind direction and intensity can be adopted. In this work, however, this site specific information is not available, therefore a non-directional wind speed is considered for all directions. To be consistent with ASCE 7-16 procedures [4.2], the

Table 4.5: Mean and coefficient of variation (CV) of the elastic and plastic multipliers for all wind directions under wind loads of 700 MRI.

Direction (°)		10	20	30	40	50	60	70	80
s_e	mean	1.8442	3.0273	2.8507	2.9492	2.4924	2.1077	2.0567	1.8871
	CV	0.1067	0.0340	0.0422	0.0496	0.0268	0.0779	0.0526	0.0373
s_p	mean	2.9642	4.0645	4.0139	4.3150	3.2384	2.6539	2.6967	3.0028
	CV	0.0725	0.0536	0.0591	0.0738	0.0521	0.0332	0.0848	0.0386
Direction (°)		90	100	110	120	130	140	150	160
s_e	mean	1.7912	1.9240	2.0153	1.7269	1.5965	0.9956	0.7053	0.6524
	CV	0.0479	0.0691	0.0427	0.0534	0.0924	0.1114	0.1064	0.1128
s_p	mean	2.8011	2.9285	3.0542	2.7088	2.3315	1.5762	1.1818	1.1915
	CV	0.0544	0.0624	0.0658	0.0737	0.0734	0.0700	0.0722	0.0780
Direction (°)		170	180	190	200	210	220	230	240
s_e	mean	0.7406	0.8172	0.6608	0.5191	0.4483	0.4176	0.4859	0.4813
	CV	0.0900	0.0730	0.0665	0.0497	0.0786	0.0722	0.0504	0.0463
s_p	mean	1.4708	1.6631	1.4940	1.3793	1.3917	1.3741	1.4150	1.4836
	CV	0.0881	0.0487	0.0441	0.0505	0.0326	0.0558	0.0442	0.0415
Direction (°)		250	260	270	280	290	300	310	320
s_e	mean	0.4146	0.4477	0.4920	0.5892	0.8078	1.0346	0.8453	0.6250
	CV	0.0439	0.0343	0.0493	0.0241	0.0384	0.0362	0.0698	0.0672
s_p	mean	1.4740	2.0933	2.4487	2.9327	3.7826	4.1193	2.4703	1.5741
	CV	0.0495	0.0337	0.0776	0.0458	0.0609	0.0398	0.0616	0.0893
Direction (°)		330	340	350	360				
s_e	mean	0.5468	0.6022	0.8695	1.2175				
	CV	0.1022	0.0406	0.0566	0.1057				
s_p	mean	1.3869	1.6339	2.3732	2.6646				
	CV	0.1017	0.0508	0.0332	0.0576				

same 3-s gust wind speed at 33 ft $\bar{v}_3$, i.e. the basic wind speed, is considered for all wind directions with directionality effects modeled as reported in Appendix A.3. Wind direction is then selected from the set $\alpha = \{10°, 20°, ..., 350°, 360°\}$ following a uniform distribution. The intensity of the wind is kept as constant in this work, therefore providing estimates of probabilities on the susceptibility to collapse that are conditional on a given intensity level (i.e. conditional on wind speeds of prescribed MRIs). The case in which $\bar{v}_3$ is taken as a random variable, therefore providing estimates of non-conditional failure probabilities, will be considered in Chapter 5 together with uncertainties in the structural system properties, e.g. stiffness and damping, and material strengths (e.g. f'_c, f_y). Indeed, the consideration of these additional uncertainties adds some complexity to the problem as a new set of yield domains for all sections must be generated for each new simulation which, if carried out in a directly, would increase simulation time. In addition, for concrete structures, the dependency between the material strength and the stiffness of the system (changes of E_c due to f'_c) should also be carefully examined before direct application. It should be observed that, consistently with previous studies, E_c and f'_c are considered constant throughout the structure, i.e. variability in E_c and f'_c from element to element is not considered.

4.3.2 Calibration the probabilistic framework

A general description of collapse susceptibility, considering both non-shakedown and failure due to excessive plastic deformations, was defined for estimating the conditional susceptibility to collapse probability $P(C|\bar{v}_3)$ as follows:

1. the inability of the structure to reach the state of dynamic shakedown;
2. peak interstory drift $\hat{\boldsymbol{u}} \geq h/100$;
3. permanent set $\boldsymbol{u}_r \geq h/500$;

where h is the interstory height of the structure, $\hat{\boldsymbol{u}}_r$ is the vector of residual interstory drifts, while $\hat{\boldsymbol{u}}$ are the peak interstory drifts at shakedown given by:

$$\hat{\boldsymbol{u}} = \max_{0 \leq t \leq T} [|\boldsymbol{u}(t) + \boldsymbol{u}_r|] \tag{4.15}$$

with $\boldsymbol{u}(t)$ the purely elastic interstory drift response at shakedown.

Wind loads of total length $T = 3600$ s with directions randomly selected from $\{10°, 20°, \cdots, 350°, 360°\}$ were simulated for a wind speed $\bar{v}_3$ of 91 mph (corresponding to a MRI of 300 years) using the wind load model of Section 4.2.2. The structure subjected to gravity loading was once again considered as the initial safe state. Similarly to Section 4.2.3, the first five modes with damping ratios of 5% were considered in the modal analysis for estimating steady state elastic responses. The LP solution method was adopted to quickly identify whether the structure remains elastic or is susceptible to collapse due to non-shakedown. Then, for the non-collapse susceptible scenarios, the strain-driven framework is applied to estimate the residual displacements and plastic deformations until a load multiplier of $s = 1$ is reached (i.e. estimates of the plastic deformations for unamplified loads is achieved). The system-level collapse susceptibility probability can then be estimated considering the above outlined collapse susceptibility criteria.

In addition, because the framework is based on Monte Carlo simulation, direct estimation of the probability distributions of the residual displacements, plastic deformations (in terms of axial strain and curvatures) at each integration point of each element, as well as peak responses of the inelastic system, is possible. For example, the probability of the residual displacements U_r exceeding a threshold u_r under wind loads of intensity $\bar{v}_3$ is simply estimated as:

$$P(U_r > u_r, \mathrm{SD}|\bar{v}_3) = P(U_r > u_r|\mathrm{SD}, \bar{v}_3)P(\mathrm{SD}|\bar{v}_3) \tag{4.16}$$

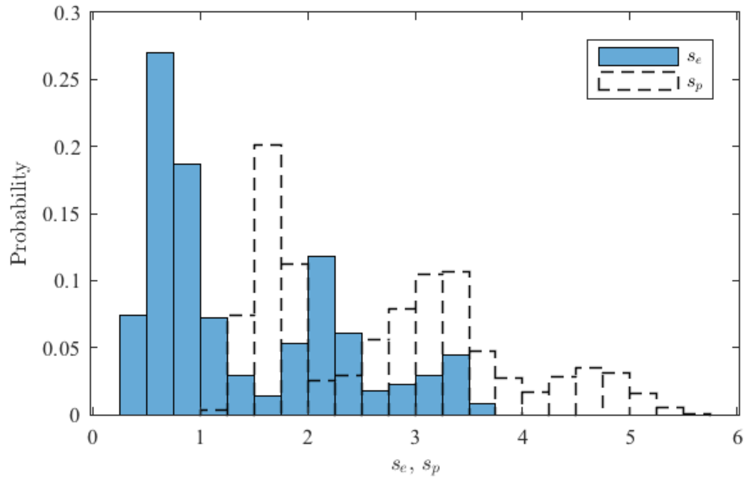

Figure 4.15: Histogram of elastic, s_e, and plastic, s_p, multipliers over all simulations.

Table 4.6: Probability of remaining elastic $P(E|\bar{v}_3)$ and of collapse susceptibility $P(C|\bar{v}_3)$ under 300 MRI wind loads.

	$P(E\|\bar{v}_3)$	$P(C\|\bar{v}_3)$
Probability	46.9%	0%

where $P(U_r > u_r|\text{SD}, \bar{v}_3)$ is the conditional exceedance probability given shakedown (SD) occurs under wind loads of intensity $\bar{v}_3$, while $P(\text{SD}|\bar{v}_3)$ is the probability that shakedown occurs under a wind load of intensity $\bar{v}_3$, i.e. $P(\text{SD}|\bar{v}_3) = P(s_p \geq 1|\bar{v}_3)$. Equivalent expressions hold for all other response parameters of interest, e.g. plastic deformations and peak responses at any degree of freedom (DOF) of the system.

4.3.3 Results

The analysis was carried out for $N_s = 5000$ simulations. Under 300 MRI wind loads, 46.9% of samples remained elastic while none of the 5000 samples showed susceptibility to collapse, as summarized in Table 4.6. The deformation limits on the peak interstory drift and permanent set were never exceeded. This can be explained by the fact that most of the inelastic elements were coupling beams, which cannot cause large residual deformations in the structure. Figure 4.15 reports the histograms of both the elastic, s_e, and plastic, s_p, multipliers over all simulations. The mean values for the elastic and plastic multipliers are respectively 1.38 and 2.73. It can be observed that less than 50% of the samples remained elastic (i.e. $s_e \geq 1$) under the 300 MRI wind loads. However, owing to the plastic reserve of the system, all of them could reach the state of dynamic shakedown (i.e. $s_p \geq 1$), and therefore achieve a safe state against plastic collapse.

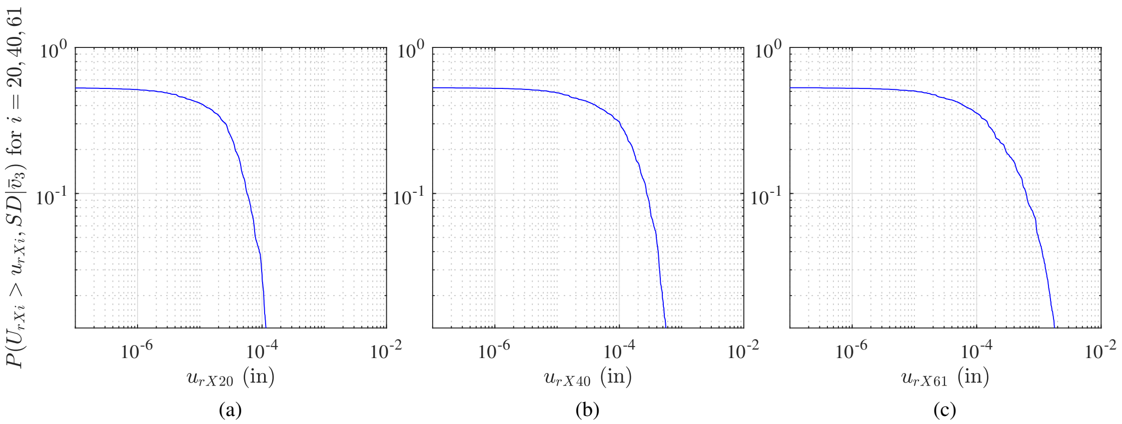

Figure 4.16: Exceedance probability of residual displacements at the master nodes in the global X-direction at (a) Level 20; (b) Level 40; (c) Core roof.

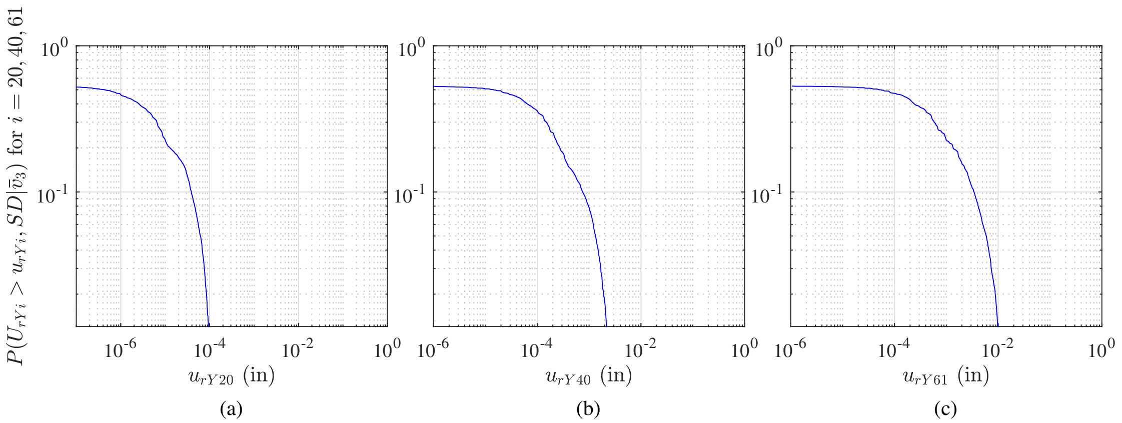

Figure 4.17: Exceedance probability of the residual displacements at the master nodes in the global Y-direction at (a) Level 20; (b) Level 40; (c) Core roof.

As mentioned in the previous section, this framework provides not only the system-level collapse susceptibility probability but also the probability distributions of plastic deformations and residual displacements, which are useful for estimating the non-collapse performance. Figures 4.16 to 4.18 respectively report the exceedance probability distributions associated with the residual displacements in the global X- and Y-directions and rotations about the Z-axis at shakedown for Level 20, Level 40 and Core roof (indicated with $i = 20, 40, 61$). The response at the master node of each floor was chosen for representation. It can be seen that residual displacements in the Y-direction are larger than those in the X-direction, even though both are within the deformation limits. To determine the responses at any other point of the rigid floor diaphragm, the transformation of Eq. (4.3) can be used.

Furthermore, exceedance probabilities can also be estimated for plastic deformations, in terms of plastic axial strain and curvatures about local y- and z-axes, at each section along the DB elements. To illustrate this, Figures 4.19 and 4.20 show

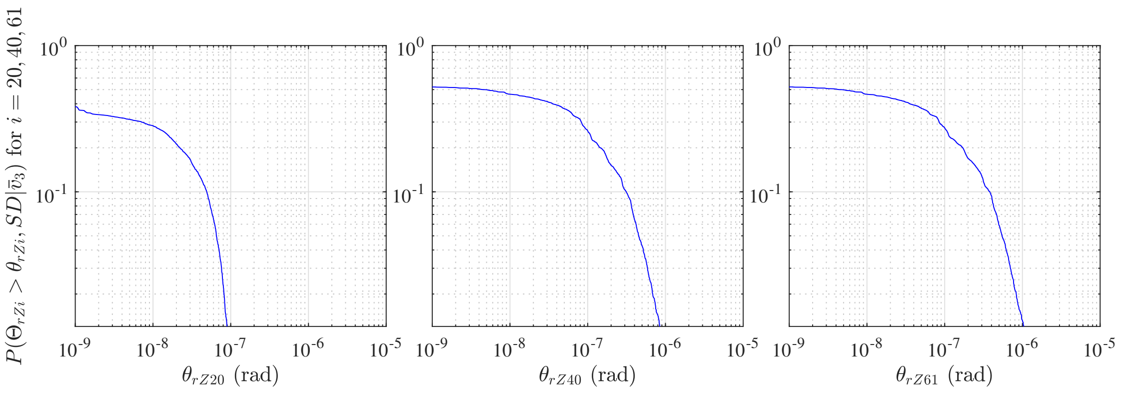

Figure 4.18: Exceedance probability of the residual rotations around the global Z-axis at the master nodes of (a) Level 20; (b) Level 40; (c) Core roof.

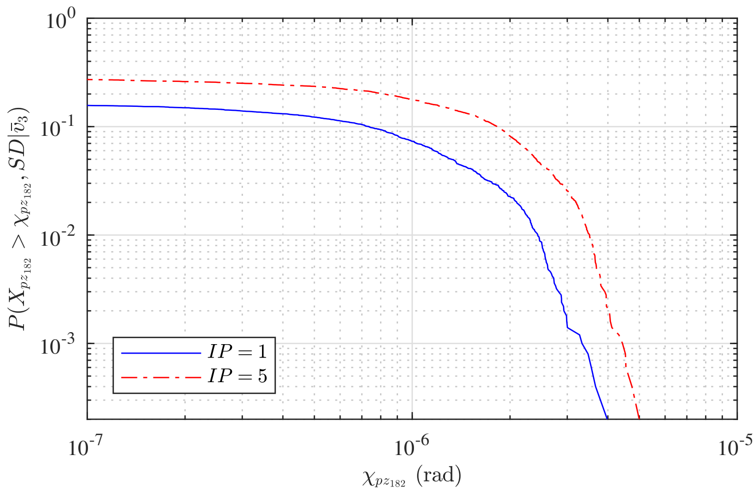

Figure 4.19: Exceedance probabilities of plastic curvatures at integration points 1 and 5 of element #182.

the exceedance probability distributions associated with the plastic curvatures about the strong axis of the section, χ_{pz}, for two representative coupling beam elements. Element #182 and #1929 (located on Grid D, Level 4 and 38) were chosen as they were the most critical elements over all simulations, i.e. the most likely elements to have inelasticity. In particular, for a beam element, the maximum moment response often occurs at the ends of the element, therefore integration points (IPs) 1 and 5, as illustrated in Figure 4.3, were selected for representation.

To illustrate the distributed plasticity, a sample with plastic multiplier s_p close to 1 was chosen. Figure 4.21 shows the plastic curvature χ_{pz} distributed along Element #182 together with the locations of the five integration points marked in dashed line. Based on the assumption of linear curvature and constant axial strain along the element from the interpolation function of a DB element, plastic deformations between integration points can also be evaluated. For the selected

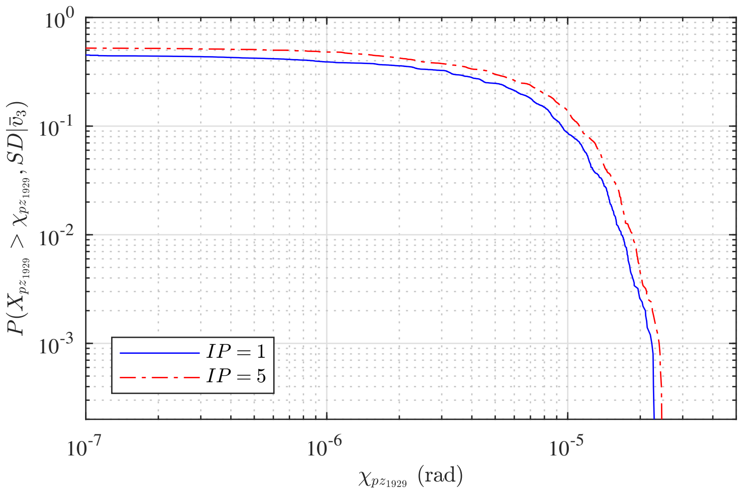

Figure 4.20: Exceedance probabilities of plastic curvatures at integration points 1 and 5 of element #1929.

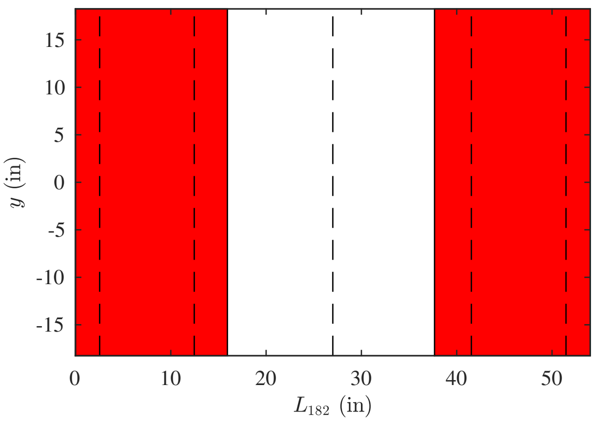

Figure 4.21: Plasticity distributed along Element #182 of the structure for a representative sample.

element, plasticity (colored in red) occurred from the two ends of the element to around half the distance to the midpoint of the element. The residual displacements at shakedown, in terms of u_{rX}, u_{rY} and θ_{rZ} at the mass node on each floor, of this selected sample are also presented in Figure 4.22.

Finally, it should be noted that the simulation-based approach provided the solutions discussed above in less than 72 hours while running the analysis on a typical dual processor desktop machine. If a similar analysis was carried out by direct integration for each of the $N_s = 5000$ windstorms of duration $T = 3600$ s considered in the simulation, the estimated run time would be in the order of months.

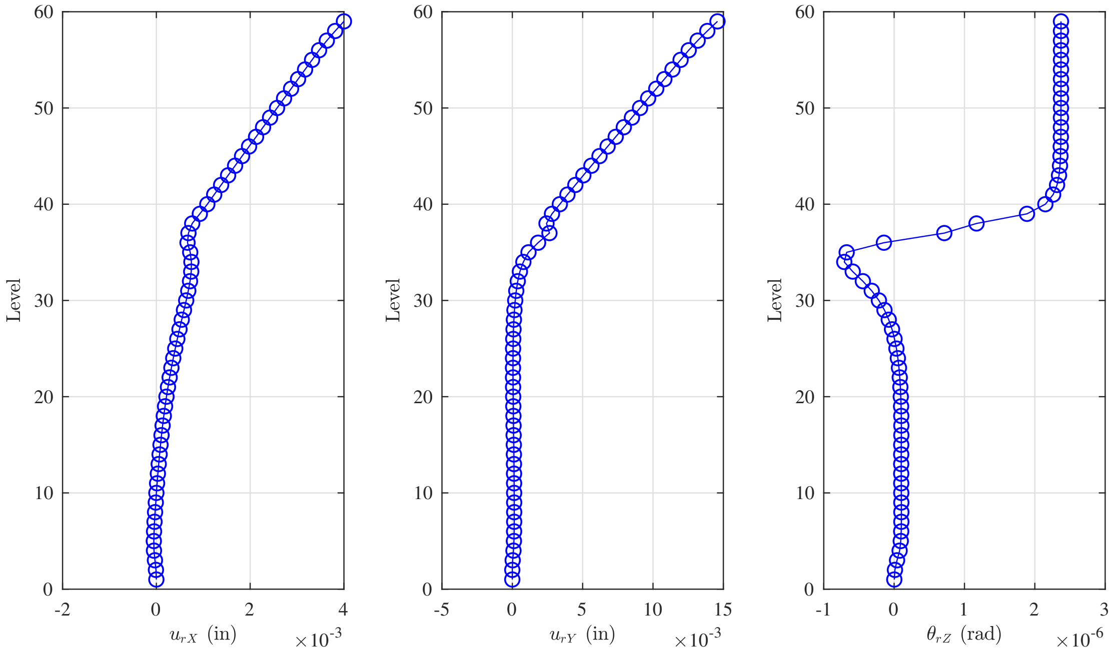

Figure 4.22: Residual displacements in the (a) X-direction; (b) Y-direction and (c) residual rotation about the Z-axis for a representative sample.

4.4 Concluding Remakes

The primary objective of the work was the application of the previously developed probabilistic system-level collapse susceptibility estimation framework based on the strain-driven dynamic shakedown algorithm to the Rainier Square Tower. In particular, considering the zero tension nature of concrete, the section-based distributed plasticity framework was adopted for the shakedown analysis. Contrary to methods based on direct integration (that would require days to analyze a structure of this scale under a single windstorm of one hour duration), it was seen that the dynamic shakedown approach was capable of estimating the inelastic responses at shakedown for each windstorm in a matter of minutes. By simulating over a suite of windstorms, the framework enabled the rapid identification of the critical wind directions as well as the elements experiencing inelasticity. With respect to the Rainier Square Tower as designed, collapse susceptibility was due exclusively to non-shakedown (i.e. deformation limits were not exceeded), as most of the critical elements experiencing inelasticity were coupling beams therefore leading to small residual deformations. Due to the significant difference between the elastic and plastic multipliers, on average the ratio between the elastic and plastic multipliers was over 1.5, the structure is safe against plastic collapse even though the probability of remaining elastic is less than 50 %, conditional on 300-year wind loads.

Bibliography

[4.1] AISC 360-16. *Specification for Structural Steel Buildings*. American Institute of Steel Construction (AISC), Chicago, IL, 2016.

[4.2] ASCE 7-10. *Minimum design loads for buildings and other structures*. American Society of Civil Engineers (ASCE), Reston, VA, 2010.

[4.3] X. Chen and A. Kareem. Proper orthogonal decomposition-based modeling, analysis, and simulation of dynamic wind load effects on structures. *Journal of Engineering Mechanics*, 131(4):325–339, 2005.

[4.4] J. Hilburg. Seattle's second tallest tower rises on steel plates, without rebar. *The Architect's Newspaper*, January 2018.

[4.5] Y. Li and A. Kareem. Simulation of multivariate nonstationary random processes by FFT. *Journal of Engineering Mechanics*, 117(5):1037–1058, 1991.

[4.6] Y. Li and A. Kareem. Simulation of multivariate random processes: Hybrid DFT and digital filtering approach. *Journal of Engineering Mechanics*, 119(5):1078–1098, 1993.

[4.7] Y. Li and A. Kareem. Simulation of multivariate nonstationary random processes: Hybrid DFT and digital filting approach. *Journal of Engineering Mechanics*, 123(12):13021310, 1997.

[4.8] M. Malena and R. Casciaro. Finite element shakedown analysis of reinforced concrete 3D frames. *Computers and Structures*, 86:1176–1188, June 2008.

[4.9] L. Peng, G. Huang, X. Chen, and A. Kareem. Simulation of multivariate nonstationary random processes: Hybrid stochastic wave and proper orthogonal decomposition approach. *Journal of Engineering Mechanics*, 143(9), 2017.

[4.10] J. K. Wight. *Reinforced Concrete: Mechanics and Design (7th ed.)*. Pearson, 2015.

Chapter 5

Reliability Analysis of Rainier Square Tower

The primary goals of the work outlined in this chapter were:

1. Identification and modeling of a range of uncertainties that are consistent with code development requirements.

2. Estimation of reliability indexes associated with inelastic system-level limit states and "classic" elastic component-level limit states for the Rainier Square Tower.

3. Outline a wind record selection procedure based on the results of a dynamic shakedown analysis.

In reaching the first goal, a full range of uncertainties affecting the structural system were defined in addition to those in the external loads described in Section 4.3.1. In particular, material properties, including yield strengths and elastic moduli of both the concrete and steel, were taken as random variables together with the damping capacity of the structure. As a result, the yield domain, i.e. the resistance, of each section of each member was considered uncertain. For the external loads, uncertainties in dead and live loads were considered in addition to the wind loads. In modeling uncertainties in the wind excitations, randomness in wind speeds, wind directions, and wind loading trace were considered.

To achieve the second goal, the collapse susceptibility framework, that is based on a system-level collapse susceptibility limit state defined in terms of both non-shakedown and failure due to excessive deformations, of Section 2.4 was adopted for estimating the system-level reliability of the tower while considering the uncertainties described above. In addition, reliability indexes associated with failure defined as the occurrence of inelasticity in any given component, i.e. classic component-based reliability, were estimated together with reliability indexes associated with system-level failure modeled as the elastic failure of any component in the system, i.e. system-level collapse susceptibility in terms of classic component limit states. These "classic" reliability indexes were compared to the reliability index obtained from considering the proposed system-level inelastic limit state, therefore providing insight into the differences in terms of reliability if damage is allowed at the ultimate limit state.

With respect to the third goal, it is outlined how the results of the reliability analysis can be directly used to identify limit sets of critical wind records to be used in subsequent validation studies and/or nonlinear time history analysis.

5.1 Code Development Consistent Uncertainties

As discussed in Section 4.1 of last report, uncertainties in both structural system and external loads have to be identified for estimating the reliability of a structure. In order to compare with the target reliability provided in ASCE 7-16 [5.1], all random variables considered in the analysis were carefully chosen so as to be compliant with those considered in the derivation of load factors stipulated in design codes. In particular, in this section, uncertainties in the structural system, gravity loads, and wind loads will be discussed.

5.1.1 Uncertainties in the structural system

Uncertainties in the structural system are considered in terms of both material and structural properties. In particular, the following parameters are taken as basic random variables:

1. Material properties: concrete compressive strength f_c'; reinforcing steel yield strength f_y; structural steel yield strength F_y; and Young's modulus of steel E_s.

2. Structural properties: modal damping ratios ξ.

The corresponding statistical information and nominal values are summarized in Table 5.1. As a consequence of the uncertainties outlined above, the Young's modulus of the concrete, defined as $E_c = 57,000\sqrt{f_c'}$ (psi), is also a random variable due to its dependence on the concrete compressive strength.

By taking material strengths as random, the yield domain, i.e. the resistance, of each section of any given member also becomes random. Within the setting stochastic simulation, this implies the need to generate yield domains for each realization of the material strengths.

5.1.2 Uncertainty propagation: steel beams

The linearized yield surfaces associated with sections of steel beams are completely governed by the moment strengths M_{py} and M_{pz} of the section. Therefore, the

Table 5.1: Description of random variables in the structural system.

	Nominal	$\frac{\text{Mean}}{\text{Nominal}}$	COV	Distribution	Reference
f'_c	8 (ksi)	1.1	0.11	Normal	[5.14]
f_y	60 (ksi)	1.13	0.03	Normal	[5.14]
F_y	50 (ksi)	1.1	0.06	Lognormal	[5.2, 5.17]
E_s	29000 (ksi)	1	0.04	Lognormal	[5.2, 5.17]
ξ	2.0%	1	0.4	Lognormal	[5.10, 5.11]

COV: coefficient of variation

propagation of uncertainty from the material properties to the yield domain can be directly evaluated through:

$$M_{py} = F_y Z_y, \quad M_{pz} = F_y Z_z \tag{5.1}$$

with Z_y and Z_z the plastic section moduli with respect to the $y-$ and $z-$axes of the cross section.

5.1.3 Uncertainty propagation: RC elements

In the case of reinforced concrete sections, however, the propagation of uncertainty from the material properties to the 3D yield domains is more complex due to a lack of explicit relationships between material properties and the 3D yield surface. To overcome this issue, surrogate models are used as proxies of yield surfaces that are treated as arbitrary black-box functions of the material properties. For example, consider the plastic resistances, R_s for $s = 1, ..., 26$, associated with the 26 planes of the general linearization scheme for 3D yield domains of concrete sections outlined in Section 4.2.1. In general, these are functions of both the strength of the concrete and reinforcing steel, i.e. $R_s = g_s(f'_c, f_y)$. Similarly, the components of the normal vectors defining the orientation of the 26 planes are also functions of f'_c and f_y, i.e. $n_{s,i} = g_n(f'_c, f_y)$ with $i = x, y, z$. Within this context, it is of interest to construct metamodels of how $g_s(f'_c, f_y)$ and $n_{s,i} = g_n(f'_c, f_y)$ vary over the space of f'_c and f_y. Among various available metamodeling approaches [5.9], ordinary Kriging [5.7] is adopted in this work due to its versatility in representing different typologies of functions.

Kriging metamodel

Given a set of n observed responses of g (i.e. plastic resistance or component of the normal vector of one of the planes defining the linearization) collected in the vector $\mathbf{y} = \{g(f_c'^{(1)}, f_y^{(1)}), \cdots, g(f_c'^{(n)}, f_y^{(n)})\}^T$, the Kriging prediction of g at $\{f'_c, f_y\}$ is expressed as:

$$\hat{g}(f'_c, f_y) = \hat{\mu} + \mathbf{\Psi}^T(f'_c, f_y)\mathbf{R}^{-1}(\mathbf{y} - \mathbf{1}\hat{\mu}) \tag{5.2}$$

Table 5.2: Bounds of sampling space.

Variable	Lower bound	Upper bound
f'_c	5.95 ksi	11.80 ksi
f_y	61.70 ksi	73.90 ksi

where $\hat{\mu}$ is the maximum likelihood estimator of the mean of the random field defined by considering $\mathbf{y}$ the realizations of a Guassian process, $\mathbf{\Psi}$ is a vector of basis functions with the ith term defined as

$$\Psi_i(f'_c, f_y) = \mathrm{Corr}[g(f'^{(i)}_c, f^{(i)}_y), g(f'_c, f_y)] \tag{5.3}$$

with Corr an appropriate correlation function, while $\mathbf{R}^{-1}(\mathbf{y} - \mathbf{1}\hat{\mu})$ are the weights assigned to each basis function with $\mathbf{R}$ the correlation matrix associated with the correlation function Corr. In particular, to define $\mathbf{\Psi}$ and $\mathbf{R}$, the following exponential correlation function was used:

$$\mathrm{Corr}[g(f'^{(i)}_c, f^{(i)}_y), g(f'^{(j)}_c, f^{(j)}_y)] = \exp\left(-\sum_{k=1}^{l} [\theta_k^{(f'_c)} |f'^{(i)}_{c_k} - f'^{(j)}_{c_k}|^{p_k{}^{(f'_c)}} + \theta_k^{(f_y)} |f^{(i)}_{y_k} - f^{(j)}_{y_k}|^{p_k{}^{(f_y)}}] \right) \tag{5.4}$$

where $\theta_k^{(f'_c)}$, $\theta_k^{(f_y)}$, $p_k{}^{(f'_c)}$ and $p_k{}^{(f_y)}$ are the parameters defining the Kriging model. In particular, here a square exponential model is considered, i.e. $p_k{}^{(f'_c)} = p_k{}^{(f_y)} = 2$. Based on this formulation, the maximum likelihood estimates of the mean value can then be derived as

$$\hat{\mu} = \frac{\mathbf{1}^T \mathbf{R}^{(-1)} \mathbf{y}}{\mathbf{1}^T \mathbf{R}^{(-1)} \mathbf{1}} \tag{5.5}$$

where $\mathbf{1}$ is a $n \times 1$ column vector of ones.

The first step towards calibrating the Kriging model g is the identification of the sampling space. For unbounded random variables, the upper and lower bounds of the sampling space can be defined in such a way that the confidence region spans a space sufficiently large to contain with high probability (e.g. 99-99.9%) all realizations of the random variable [5.13]. In the application that follows, a confidence interval of $C = 0.9973$ is selected for each random variable, which corresponds to $\mu + 3\sigma$ for a Gaussian variable, as illustrated in Figure 5.1. The upper and lower bounds for f'_c and f_y are summarized in Table 5.2 with mean and standard deviation defined in Table 5.1.

The second step is the choice of sampling points within the sampling space in which to calibrate the model, i.e. the choice of support points, within the identified space of f'_c and f_y, in which to evaluate the vector $\boldsymbol{y}$. To reduce the bias error of the metamodel, sampling plans that attempt to evenly fill the space are generally favored. In this work, a 20-point sampling plan was created based on optimal Latin

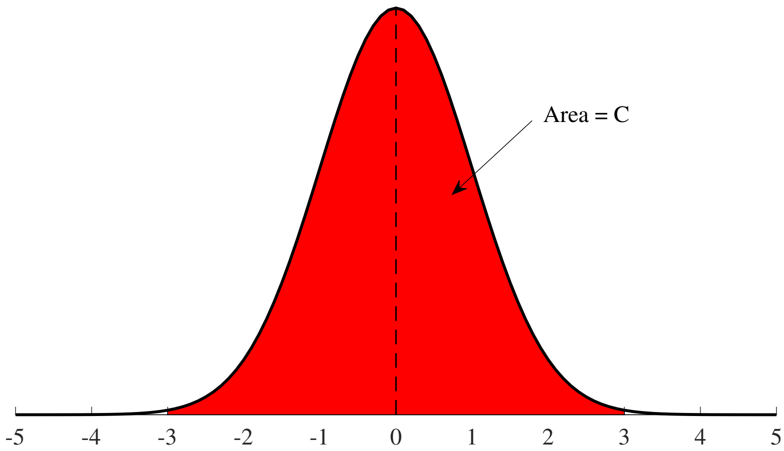

Figure 5.1: Illustration of the confidence interval of a Gaussian variable.

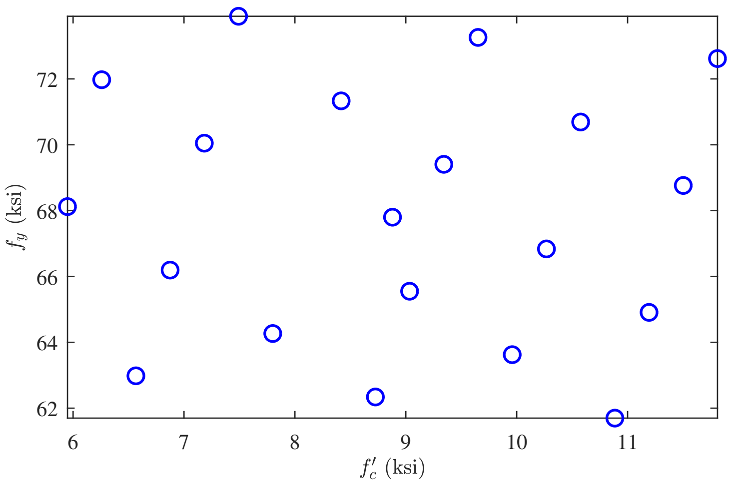

Figure 5.2: A 20-point sampling plan for Kriging model calibration.

hypercube sampling [5.6], ensuring the optimal space-filling properties of the sample points, as illustrated in Figure 5.2.

Based on the 3D yield domains evaluated at the sampling points (provided by MKA), i.e. the observed responses $\mathbf{y}$, Kriging models were created for the plastic resistances, R_s for $s = 1, ..., 26$, and components of the normal vectors of the planes defining the linearized yield surfaces of all reinforced concrete sections. The calibrated models were then used to rapidly update the 3D yield domains for each realization of f_c' and f_y considered in evaluating through stochastic simulation the reliability of the structure.

5.1.4 Uncertainties in gravity and wind loads

Gravity loads

To carry out the reliability analysis, uncertainties in the gravity loads, including live loads, should also be taken into account in addition to those in the wind loads. The dead loads and live loads are respectively taken as normal and gamma random variables with mean and coefficient of variation summarized in Table 5.3. In particular, "arbitrary point-in-time" live load, denoted as L_{apt}, are considered in reliability analysis.

Wind loads

In generating dynamic wind loads, the overall intensity is traditionally modeled through the site specific mean wind speed V_H. In general, V_H is a random variable which can be related to available meteorological data, v, collected at a meteorological height H_{met} at a nearby weather station characterized by a roughness length z_{01}. In this work, the following probabilistic model that explicitly accounts for the inevitable uncertainties in transforming limited data from the meteorological site to the building site is adopted [5.16]:

$$V_H(T, z_0) = e_3(\tau, T) \left(\frac{e_5 z_0}{e_6 z_{01}} \right)^{e_4 \cdot 0.0706} \cdot \frac{\ln \left[\frac{H}{e_5 z_0} \right]}{\ln \left[\frac{H_{met}}{e_6 z_{01}} \right]} e_1 e_2 v(\tau, H_{met}, z_{01}) \tag{5.6}$$

where V_H is the site-specific wind speed at a height of interest H (e.g. building height) averaged over a fixed interval T (e.g. an hour), v is the corresponding wind speed at the meteorological station averaged over a period τ, z_0 is the site specific roughness length, e_1 and e_2 are random variables characterizing the inevitable observational and sampling errors in v; $e_3(\tau, T)$ is a random variable accounting for the uncertainty involved in converting the time interval τ to T; e_4, e_5, and e_6 are random variables modeling the uncertainties with respect to the actual values of the empirical constant 0.0706 and of the roughness lengths z_0 and z_{01}, respectively.

A possible probabilistic description of the aforementioned variables is summarized in Table 5.3.

In applying Eq. (5.6) to the wind analysis of the Rainier Tower site, available wind data with a record length of 46 years, in terms of annual maximum 3-s gust wind speed at 33 ft height, i.e. $v = v_3$ with $\tau = 3$ s and $H_{met} = 33$ ft, collected at Seattle Tacoma International Airport was used. The roughness length z_{01} was taken as 0.1 ft (0.03 m), i.e. open terrain conditions were condiered at the meteorological station. Considering sampling errors generated by the limited amount of available climatological data, this wind speed, v_3, was assigned a Type I distribution with mean and standard deviation determined from the wind data (Table 5.3). The site of the building was characterized by a roughness length $z_0 = 9.8$ ft (3 m) while the averaging time of interest was one hour ($T = 3600$ s).

In addition to the site-specific wind speed, wind direction must also be considered. In this work, due to the lack of site specific information on the joint probability distribution of wind speed and direction, wind directionality was modeled by reducing the non-directional wind speed, V_H, in function of wind direction, α, through the following expression:

$$\tilde{V}_H(\alpha) = \mathrm{K}_R(\alpha)\mathrm{K}_D(\alpha)V_H \tag{5.7}$$

where K_R is a reduction factor while K_D is a directionality factor. In particular, appropriate values for K_R and K_D for Seattle were provided by Rowan Williams Davies & Irwin (RWDI). To use the model of Eq. (5.7) in a stochastic simulation, the wind direction α can be taken as a uniform distribution in $[0°, 360°]$. The values used for K_R and K_D are summarized in Appendix A.3.

Given a realization of wind speed $\tilde{V}_H$ and direction α, the wind tunnel driven wind load model of Section 3.2 of last report was adopted to simulate the stochastic wind loads, which takes into account the record-to-record variability. To further consider the uncertainties associated with the use of wind tunnels, three uncertain parameters were introduced, indicated respectively as w_1, w_2 and w_3 in Table 5.3. In particular, w_1 models the sampling errors due to the finite length of the wind tunnel record, w_2 accounts for the uncertainty due to the use of scale models, while w_3 accounts for the presence of observational errors. For a record length greater than 1 hour at full scale, w_1 was taken to have a coefficient of variation (COV) of 0.075. Through the mathematical derivation outlined in Appendix B, the aforementioned uncertain parameters can be directly applied to the simulated full scale wind loads as:

$$\mathbf{F}_w(t; \tilde{V}_H, \alpha) = w_1 w_2 w_3 \mathbf{F}(t; \tilde{V}_H, \alpha) \tag{5.8}$$

where $\mathbf{F}(t; \tilde{V}_H, \alpha)$ are the wind loads generated without considering wind tunnel uncertainties.

Table 5.3: Properties of the random variables used in modeling the gravity and wind loads.

	Mean	COV	Distribution	Reference
D	$1.05D_n$ [a]	0.1	Normal	[5.8, 5.17]
L_{apt}	$0.24L_n$ [a]	0.6	Gamma	[5.8, 5.17]
v_3	57.7 (mph)	0.14	Type I	—
e_1	1.0	0.10	Normal	—
e_2	1.0	0.025	Normal	[5.12]
e_3	[b]	0.05	Normal	[5.5]
e_4	1.0	0.10	Truncated Normal	[5.5]
e_5	1.0	0.30	Truncated Normal	[5.5]
e_6	1.0	0.30	Truncated Normal	[5.5]
w_1	1.0	[c]	Normal	[5.15]
w_2	1.0	0.05	Normal	[5.3]
w_3	1.0	0.05	Normal	[5.3]

[a] D_n, L_n: Nominal dead load and live load
[b] Depends on averaging times τ and T.
[c] Depends on the record length.

5.2 Reliability of Rainier Square Tower

In this section, the system-level collapse susceptibility framework proposed in Section 2.4 was adopted for the reliability evaluation of the Rainier Square Tower considering all uncertainties identified in completing Goal 1.

5.2.1 Design target for the structure

In order to achieve a target reliability stipulated in ASCE 7-16, several adjustments were made to the design of Rainier Square Tower supplied by MKA. In particular, target reliabilities for structural members and connections are provided in Table 1.3-1 of ASCE 7-16 [5.1] and were developed for common limit states, such as yielding in tension members, formation of plastic hinges, or column buckling and connection fracture for a nominal service period of 50 years. For a Risk Category III structure, the target component reliability is 3.25 for failure that is not sudden and does not lead to widespread progression of damage, a classification deemed appropriate for the members of the structural system of Rainier Square Tower. Here, this reliability target is taken as the system-level reliability target. The goal is to therefore re-size select members of the structure such that the system reliability $\beta_s^{(i)}$, estimated through the proposed dynamic shakedown framework (and therefore with respect to a system-level inelastic limit state), achieves a Risk Category III target reliability. To this end, the structure was preliminary redesigned to have an expected elastic response under dynamic wind loads calibrated to a 300 MRI wind speed.

Table 5.4: List of redesigned coupling beams (Please see Appendix C for element locations).

Element ID	90	182	212	1800	1929	1974	1994	1998	2012	2016	2058	2067
Substituted ID	1949	1974	1606	1647	559	86	508	2047	1364	1953	2078	2087

Wind direction was modeled as in Eq. 5.7 while all material properties were set to their nominal values. Based on this analyses, the most critical elements resulted to be the coupling beams. To achieve satisfactory performance, the most critical (i.e. most under-designed) coupling beam elements were redesigned by substituting the under-deigned element with one of greater capacity. For simplicity, the new elements were chosen from sections already used in the structure. The IDs of the redesigned coupling beams is reported in Table 5.4 together with the IDs identifying the coupling beams used in redesigning the member.

5.2.2 Reliability analysis

The reliability for the adjusted structure of Section 5.2.1 was determined through first-order reliability methods (FORM). In evaluating the reliability, the dead loads, D, and arbitrary-point-in-time live loads, L_{apt}, were combined with dynamic wind loads, W_{50}, calibrated to the largest wind speed to occur within a period of 50 years (the service lifetime of the structure). D, L_{apt} and W_{50} were considered uncertain due to the uncertainties outlined in the previous sections. In FORM, the reliability is measured by the "reliability index", β, which is related to the failure probability P_f through:

$$\beta = \Phi^{-1}(1 - P_f) \tag{5.9}$$

where $\Phi^{-1}()$ is the inverse of the standard normal probability distribution. To evaluate Eq. (5.9), and therefore the reliability index, P_f can be determined through Monte Carlo once the limit state of interest is defined.

In this work, given the random variables described in section 5.1, reliabilities are estimated for the following three limit states of interest:

1. LS1: component-level yield limit state (traditional limit state used in current design);
2. LS2: system-level yield limit state;
3. LS3: system-level inelastic limit state (defined as in the proposed dynamic shakedown framework).

The reliability associated with the first limit state, denoted as $\beta_c^{(LS1)}$, is defined by the most critical element, i.e. the element with lowest reliability index in the system. To estimate system reliabilities associated with the second and third limit states, denoted respectively as $\beta_s^{(LS2)}$ and $\beta_s^{(LS3)}$, the system-level collapse susceptibility framework proposed in Section 2.4 is applied. In particular, for the LS2, failure occurs if any of the components of the structure exits the elastic regime. This limit state can be rapidly identified by calculating the elastic multiplier s_e, i.e. the maximum amount the external loads can be multiplied by before any inelasticity would occur, through the linear programming problem outlined in [5.4]. The corresponding failure probability is therefore defined as $P_f = P(s_e < 1)$. This limit state probability is expected to be higher than or at least equal to the component limit state probability (LS1), therefore with a lower reliability, since it is defined as the probability of the union of all the failure events for all the elements of the structure.

The third limit state is as defined in Section 2.4. Safety is therefore defined at a system-level as the achievement of the state of dynamic shakedown. This limit state fundamentally differs from those considered in current design practice as it allows yielding to occur anywhere in the structure as long as shakedown is achieved. In general, and as outlined in Section 2.4, this limit state is augmented through the addition of any number of component level limit states on responses such as peak inelastic responses at shakedown and residual deformations. In the specific case of this example, this leads to the following definition of exceedance of LS3:

1. the inability of the structure to reach the state of dynamic shakedown;
2. peak interstory drift $\hat{\boldsymbol{u}} \geq h/100$;
3. permanent set $\boldsymbol{u}_r \geq h/500$;

where h is the interstory height of the structure, $\hat{\boldsymbol{u}}_r$ is the vector of residual interstory drifts, while $\hat{\boldsymbol{u}}$ are the peak interstory drifts at shakedown given by:

$$\hat{\boldsymbol{u}} = \max_{0 \leq t \leq T} [|\boldsymbol{u}(t) + \boldsymbol{u}_r|] \tag{5.10}$$

with $\boldsymbol{u}(t)$ the purely elastic interstory drift response at shakedown.

5.2.3 Results

To evaluate P_f, and therefore the reliability indexes with respect to LS1, LS2 and LS3 outlined above through Eq. (5.9), the Monte Carlo scheme of the outlined in Section 2.4 was implemented while considering $N_s = 12000$ (i.e. 12000 samples) and the uncertainties outlined in section 5.1. Figure 5.3 reports the histogram of the plastic reserves of the system in terms of s_p/s_e. As can be seen, the plastic reserve falls between 1.5 and 2 for most of the samples with a mean value of 1.81. In interpreting the ratio s_p/s_e, it should be kept in mind that larger ratios indicate greater potential for force redistribution and therefore safe inelastic behavior. To further illustrate the relation between wind directions and plastic reserves of the

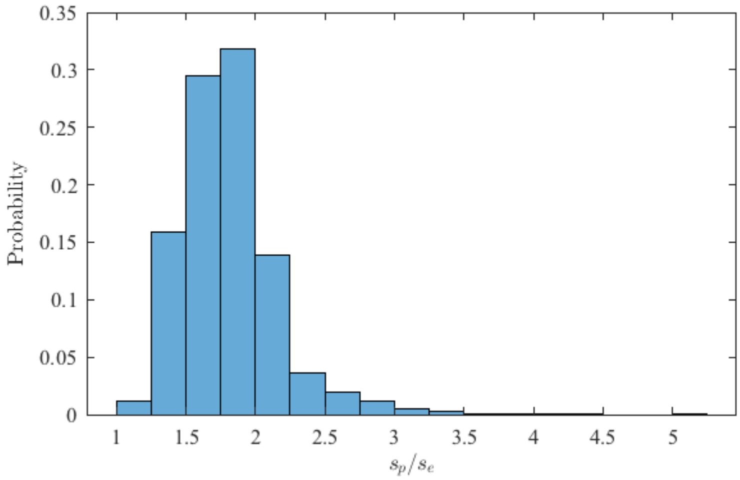

Figure 5.3: Histogram of plastic reserve of the system, s_p/s_e, over all simulations.

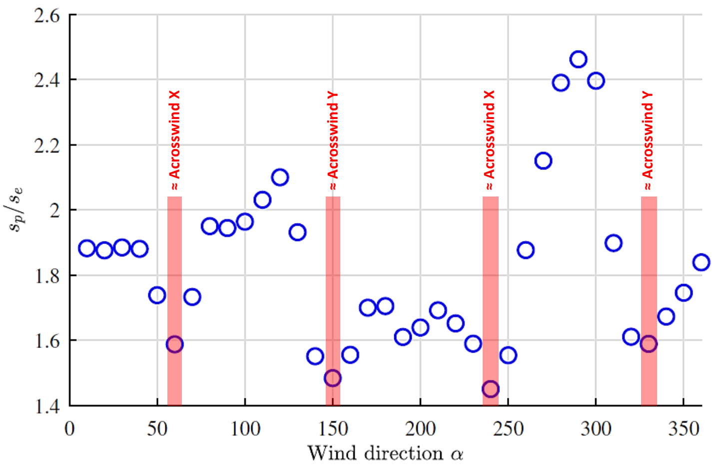

Figure 5.4: Mean values of the ratios, s_p/s_e, over for all wind directions.

system, Figure 5.4 shows the mean value of s_p/s_e for each direction. For wind loads coming from directions that would cause acrosswind response to the structure, i.e. close to $\alpha = \{60°, 150°, 240°, 330°\}$, the structure would have seem to have less capacity to shakedown, therefore resulting in a smaller ratio between the plastic and elastic multipliers.

For the 50-year design life considered in this work, 99.86% of samples remained elastic while 0.025% were susceptible to collapse due to non-shakedown. The reliability indexes for LS1, LS2 and LS3 defined in Section 5.2.2 are summarized in Table 5.5 for combined gravity and wind loads. Table 5.5 also reports the reliability indexes for two additional limit states, LS3a and LS3b. In particular, for LS3a failure is defined as the peak interstory drift exceeding $h/100$ anywhere over the height of the structure while for LS3b failure is defined as residual drift exceeding

Table 5.5: Reliability indexes for the different limit states.

Limit state	LS1	LS2	LS3	LS3a	LS3b
Description	First Component Yield	First System Yield	Non-shakedown or $\hat{\boldsymbol{u}} \geq h/100$ or $\boldsymbol{u}_r \geq h/500$	$\hat{\boldsymbol{u}} \geq h/100$	$\boldsymbol{u}_r \geq h/500$
Reliability index	3.14	2.99	3.48	4.92	7.51

Table 5.6: Elements with reliability indexes lower than the target reliability stipulated in ASCE 7-16 (Please see Appendix C for element locations).

Element ID	156	238	273	1998
Reliability index $\beta_c^{(LS1)}$	3.14	3.14	3.21	3.12

$h/500$ anywhere over the height of the structure. To estimate the reliability indexes associated with LS3a and LS3b, the following expression was used:

$$P_f^{(LS3a/LS3b)} = P(R > \tilde{r}, \mathrm{SD}) = P(R > \tilde{r}|\mathrm{SD})P(\mathrm{SD}) \tag{5.11}$$

where R is the response of interest (i.e. largest peak/residual drift occurring anywhere over the height of the structure), $\tilde{r}$ is the limit of interest (i.e. $h/100$ for peak drift and $h/500$ for residual drift), $P(R > \tilde{r}|\mathrm{SD})$ is the probability of R exceeding the limit $\tilde{r}$ conditional on shakedown, while $P(\mathrm{SD})$ is the probability of shakedown. In particular, $P(\mathrm{SD})$ can be directly estimated from the samples of the Monte Carlo simulation while $P(R > \tilde{r}|\mathrm{SD})$ can be estimated after fitting a lognormal to the samples of R. To estimate the reliability indexes, $P_f^{(LS3a/LS3b)}$ can then be substituted into Eq. (5.9)

The component reliability, $\beta_c^{(LS1)}$, associated with LS1 was 3.14 for the most critical element of the structure, which is lower than the target β of 3.25 for a Risk Category III building. Table 5.6 reports the most critical elements that have reliability indexes smaller than the target reliability. It can be observed that all elements correspond to coupling beams. The reliability index associated with the system-level first yield limit state, LS2, was estimated to be $\beta_s^{(LS2)} = 2.99$. As expected, the reliability index of LS2 was lower than the component-reliability index since the structure is considered failed if any one of the elements fail. Indeed, the limit case of $\beta_s^{(LS2)} = \beta_c^{(LS2)}$ occurs when the structure fails exclusively due to the failure of a single common element. For this case study, however, the component for which failure occurs depends, among other things, on the direction of the wind load and the particular distribution of resistances. Referring to Table 1.3-1 of ASCE 7-16, as shown in Figure 5.5, this system reliability index $\beta_s^{(LS2)}$ only exceeds the target reliability for a Risk Category I building. This is consistent with how, apart

Table 1.3-1 Target Reliability (Annual Probability of Failure, P_F) and Associated Reliability Indices (β)[1] for Load Conditions That Do Not Include Earthquake, Tsunami, or Extraordinary Events[2]

	Risk Category			
Basis	**I**	**II**	**III**	**IV**
Failure that is not sudden and does not lead to widespread progression of damage	$P_F = 1.25 \times 10^{-4}$/yr $\beta = 2.5$	$P_F = 3.0 \times 10^{-5}$/yr $\beta = 3.0$	$P_F = 1.25 \times 10^{-5}$/yr $\beta = 3.25$	$P_F = 5.0 \times 10^{-6}$/yr $\beta = 3.5$
Failure that is either sudden or leads to widespread progression of damage	$P_F = 3.0 \times 10^{-5}$/yr $\beta = 3.0$	$P_F = 5.0 \times 10^{-6}$/yr $\beta = 3.5$	$P_F = 2.0 \times 10^{-6}$/yr $\beta = 3.75$	$P_F = 7.0 \times 10^{-7}$/yr $\beta = 4.0$
Failure that is sudden and results in widespread progression of damage	$P_F = 5.0 \times 10^{-6}$/yr $\beta = 3.5$	$P_F = 7.0 \times 10^{-7}$/yr $\beta = 4.0$	$P_F = 2.5 \times 10^{-7}$/yr $\beta = 4.25$	$P_F = 1.0 \times 10^{-7}$/yr $\beta = 4.5$

[1]The target reliability indices are provided for a 50-year reference period, and the probabilities of failure have been annualized. The equations presented in Section 2.3.6 are based on reliability indices for 50 years because the load combination requirements in Section 2.3.2 are based on the maximum loads for the 50-year reference period.
[2]Commentary to Section 2.5 includes references to publications that describe the historic development of these target reliabilities.

Figure 5.5: Target reliability stipulated in ASCE 7-16 [5.1].

from the coupling elements of Table 5.4, all elements were initially designed (as supplied by MKA) for a 100-year windstorm. This behavior is also seen in Tables 4.4 and 4.5 through the mean values of s_e that, for certain wind directions, assume values significantly smaller than one. With respect to the system-level inelastic limit state, the reliability index was estimated to be $\beta_s^{(LS3)} = 3.48$. In particular, as observed from the analyses conducted in Chapter 4, failure occurs only due to non-shakedown (the deformation limits on peak interstory drift and permanent set are never exceeded). As compared with the system reliability considering first member yield, i.e. $\beta_s^{(LS2)}$, the reliability of the system increased from 2.99 to 3.48. From Table 5.5 it is interesting to observe that $\beta_s^{(LS3a)}$ and $\beta_s^{(LS3b)}$ well exceeded the reliability index associated with LS3, i.e. $\beta_s^{(LS3)} = 3.48$, indicating how the system was not susceptible to failure due to excessive peak or residual drifts.

The results of this section clearly illustrate the advantage of allowing controlled inelasticity in order to increase the reliability of the system. Indeed, by considering this limit state, the structure satisfied, for all intents and purposes, the target reliability for a Risk Category IV building. Of particular interest is the comparison of $\beta_s^{(LS3)}$ with $\beta_c^{(LS1)}$, i.e. classic component reliability, which shows how a system designed to satisfy a Risk Category II design using traditional approaches can achieve a Risk Category IV classification by adopting the inelastic system-level limit state proposed in this research and outlined in section 5.2.2.

In addition, Table 5.7 reports the elements experiencing inelasticity for the 3 samples of the Monte Carlo simulation for which LS3 was not satisfied, i.e. the structure was susceptible to collapse. It is interesting to observe how the number of elements experiencing damage reached as high as 147 and involved both coupling beams and wall elements.

Table 5.7: Number of inelastic elements for the 3 samples of the Monte Carlo simulation for which Limit State 3 was not satisfied.

Sample	1	2	3
Elastic multiplier s_e	0.6566	0.5419	0.6458
Plastic multiplier s_p	0.7502	0.8495	0.9030
# of Inelastic elements	147	126	65

5.3 Wind Record Selection Procedure

The algorithms developed in this work can also be used to identify the wind records (wind speed, direction and associated wind load history) causing inelasticity and susceptibility to collapse as defined through the limit states of Sec. 5.2.2. In particular, if the interest is exclusively the identification of the aforementioned wind records, then only the linear programming problem of Chapter 1 has to be solved therefore increasing computational efficiency. The overall wind record selection procedure entails the following steps:

1. Setup a shakedown model as outlined in this Chapter;
2. For each sample of the Monte Carlo simulation solve the linear programming problem of Chapter 1;
3. If for the i simulation point the following holds: $s_e^{(i)} < 1$, save the wind record and associated metadata, e.g. wind speed $\bar{v}_H^{(i)}$, wind direction $\alpha_H^{(i)}$, s_e, s_p, and number and location of elements experiencing inelasticity.

At the end of the simulation, the wind records can be ordered in terms of s_e, i.e. in terms of the fraction of the dynamic load necessary for first yield of the system. Because s_p is also available for each simulation, knowledge of whether the system can shakedown under the wind load history is also available. In particular, by also running the strain-driven shakedown models of Chapter 1, LS3 of Sec. 5.2.2 can be evaluated therefore enabling identification of the wind records associated with the β values of Table 5.5 and LS3.

To illustrate the procedure the samples for which $s_e < 1$ for the 12000 point Monte Carlo simulation of Sec. 5.2.3 are reported in Table 5.8 after ordering in ascending order of s_e. As can be seen, 17 records are identified as causing inelasticity with three (highlighted bold in Table 5.8) causing conditions that could lead to collapse, i.e. LS3 was not satisfied. In particular, these highlighted records are directly associated with the β values of LS3, while the remaining records are representative of the β values of LS1 and LS2 (i.e. first component/system yield). Finally, from the Monte Carlo seed number (i.e. MC sample #), the critical wind record of interest can be regenerated and used in a nonlinear response history analysis with the

Table 5.8: Ordered list of samples for which $s_e < 1$, i.e. for which inelasticity occurred in the system. Bold entries indicated samples for which the system did not satisfy Limit State 3 and was therefore susceptible to collapse.

MC sample	# of inelastic elements	s_e	s_p	$\bar{v}_H$	α
911	**126**	**0.5419**	**0.8495**	**51.9863**	**200**
11198	37	0.5552	1.0120	50.4816	220
2513	**65**	**0.6458**	**0.9030**	**53.0298**	**220**
9543	**147**	**0.6566**	**0.7502**	**57.0039**	**240**
1232	7	0.7292	1.3511	44.6625	160
1168	5	0.8390	1.4822	38.5584	250
4003	3	0.8558	1.7911	37.8207	220
8346	4	0.8571	1.1868	45.3168	250
1657	12	0.8987	1.2207	42.2747	320
4448	14	0.8992	1.0867	43.0450	220
7698	7	0.9071	1.4458	47.4065	210
5309	3	0.9556	1.1895	42.9522	250
2762	3	0.9593	1.3179	43.7758	220
2613	5	0.9632	1.2497	39.9690	250
5765	6	0.9684	1.2138	45.0684	250
534	3	0.9821	1.1230	40.1394	330
2630	3	0.9864	1.4728	49.3072	160

aim of validating the results of the shakedown model, or estimating the behavior of the system for load levels that are consistent with the β values of Table 5.5.

5.4 Concluding Remarks

The primary objective of the work carried out in this chapter was the estimation of the reliability of the Rainier Square Tower. In this respect, reliability indexes for three different limit states, including component yield, system-level first yield, and system-level inelastic failure due to non-shakedown and/or excessive plastic deformation, were evaluated. To carry out the reliability analysis, a carefully selected range of uncertainties consistent with modern code development was considered. To assess the reliability indexes, the Monte Carlo simulation framework developed in this project was implemented. In particular, it was seen that a building achieving a Risk Category II with respect to classic component-level limit states on strength could achieve a Risk Category IV classification at system-level by considering as a system-level limit state the achievement of dynamic shakedown without excessive residual/peak inelastic drifts. This is a particularly noteworthy result if it is kept in mind that, apart from the coupling elements of Table 5.4, all elements were initially designed (as supplied by MKA) for a 100-year windstorm. In other words, this

Chapter illustrated through an example how controlled inelastic behavior can provide a means to achieve equivalent Risk Category performances when starting with designs for reinforced concrete structures that use notably less rebar than required in traditional design approaches. This clearly illustrates the potential of designing wind-excited structures to have controlled inelasticity at ultimate load levels.

Bibliography

[5.1] ASCE 7-16. *Minimum design loads for buildings and other structures.* American Society of Civil Engineers (ASCE), Reston, VA, 2016.

[5.2] F. Bartlett, R. Dexter, M. Graeser, J. Jelinek, B. Schmidt, and T. Galambos. Updating standard shape material properties database for design and reliability. *Engineering Journal*, 40:2–14, 2003.

[5.3] R. Bashor, T. Kijewski-Correa, and A. Kareem. On the wind-induced response of tall buildings: the effect of uncertainties in dynamic properties and human comfort thresholds. In *10th Americas Conference on Wind Engineering*, 2005. CD-ROM.

[5.4] W.-C. Chuang and S. M. J. Spence. An efficient framework for the inelastic performance assessment of structural systems subject to stochastic wind loads. *Engineering Structures*, 179:92–105, January 2019.

[5.5] S. M. C. Diniz, F. Sadek, and E. Simiu. Wind speed estimation uncertainties: effects of climatological and micrometeorological parameters. *Prob. Engng Mech.*, 19:361–371, 2004.

[5.6] M. D.Morris and T. J. Mitchell. Exploratory designs for computational experiments. *Journal of Statistical Planning and Inference*, 43(3):381–402, February 1995.

[5.7] B. Echard, N. Gayton, and M. Lemaire. Ak-mcs: An active learning reliability method combining kriging and monte carlo simulation. *Structural Safety*, 33(2):145–154, 2011.

[5.8] B. Ellingwood, J. G. MacGregor, T. V. Galambos, and C. A. Cornell. Probability based load criteria: Load factors and load combinations. *Journal of the Structural Division*, 108:978–997, 1982.

[5.9] A. Forrester, A. Sobester, and A. Keane. *Engineering Design via Surrogate Modelling: A Practical Guide.* John Wiley & Sons, 2008.

[5.10] A. Kareem. Effect of parametric uncertainties on wind excited structural response. *Journal of Wind Engineering and Industrial Aerodynamics*, 30:233–241, 1998.

[5.11] D. K. Kwon, A. Kareem, R. Stansel, and B. Ellingwood. Wind load factors for dynamically sensitive structures with uncertainties. *Engineering Structures*, 103:53–62, 2015.

[5.12] F. Minciarelli, M. Gioffrè, M. Grigoriu, and E. Simiu. Estimates of extreme wind effects and wind load factors: Influence of knowledge uncertainties. *Prob. Engng Mech.*, 16:331–340, 2001.

[5.13] M. Moustapha, B. Sudret, J.-M. Bourinet, and B. Guillaume. Quantile-based optimization under uncertainties using adaptive kriging surrogate models. *Structural and Multidisciplinary Optimization*, 54(6):1403–1421, December 2016.

[5.14] A. S. Nowak and K. R. Collins. *Reliability of Structures*. CRC Press, 2013.

[5.15] F. Sadek, S. Diniz, M. Kasperski, M. Gioffrè, and E. Simiu. Sampling errors in the estimation of peak wind-induced internal forces in low-rise structures. *Journal of Engineering Mechanics*, 130(2):235–239, 2004.

[5.16] S. M. J. Spence and A. Kareem. Performance-based design and optimization of uncertain wind-excited dynamic building systems. *Engineering Structures*, 78:133–144, 2014.

[5.17] H. Zhang, B. R.Ellingwood, and K. J. Rasmussen. System reliabilities in steel structural frame design by inelastic analysis. *Engineering Structures*, 81:341–348, 2014.

Chapter 6

Conclusions and Future Directions

This project introduced a new generation of computational tools for the system-level inelastic performance assessment of wind excited structural systems. The tools were based on developing a class of path-following algorithms that enable the rapid estimation of the state of dynamic shakedown together with a full range of inelastic responses at shakedown. The models were developed within the setting of concentrated plasticity as well as distributed plasticity. In particular, with respect to distributed plasticity, models were introduced for estimating inelasticity at both the level of an individual fiber and the level of the member cross-section. To validate the models, a suite of example concrete and steel structures were considered. Dynamic and inelastic responses estimated from the proposed framework were compared with those estimated from direct integration. The near perfect correspondence between the results obtained through the two approaches provided an initial validation of the procedures.

The successful development of these models and procedures enables the introduction of a new system-level limit state, defined as the achievement of the state of dynamic shakedown together with the satisfaction of an arbitrary number of local limit states written in terms of inelastic responses at shakedown, against which to assess the adequate performance of a wind excited system experiencing inelasticity. Importantly, due to the nature of dynamic shakedown, this limit state inherently ensures safety against collapse mechanisms involving ratcheting in the alongwind direction, and low-cycle fatigue in the acrosswind direction. The computational efficiency with which the proposed algorithms can assess the limit state for any given wind load history enables the introduction of a Monte Carlo scheme for rapid probabilistic evaluation of the limit state while considering a full range of uncertainties, including record-to-record variability in the load histories. These developments allowed for the straightforward estimation of the reliability of the system against inelastic failure described through the aforementioned limit state, therefore opening the door to the design of wind excited systems with controlled inelasticity at ultimate load levels.

The potential of this fundamental shift in design philosophy was illustrated on a 3D concrete core system with outriggers, for which Risk Category IV ASCE 7-16 reliability targets were achieved for a design that achieved Risk Category II component reliability targets.

Future directions of this work would entail the development of additional theoretical models for describing a general class of nonlinear components, such as nonlinear hysteretic dissipation devices, or components specifically designed to experience continued inelasticity (i.e. buckling-restrained braces), that could be integrated with the path-following strain-driven dynamic shakedown algorithms of Chapter 1. This would enable a hybrid approach to inelastic performance where certain elements are designed to shakedown during the windstorm, while other elements are designed to dissipate energy through controlled but continuous inelasticity. Such developments would result in greater controlled excursion into the inelastic response regime, therefore further enhancing the already extremely promising results reported in Chapter 5. To guarantee the accuracy of predictions at such high levels of inelasticity, the framework would require the incorporation of procedures that model the effects of large displacements and therefore P-Delta effects. Finally, the development of a comprehensive user-friendly interface would enable the straightforward use of the models outlined in this report, as well as any future developments, by a wide range of design professionals of diverse backgrounds. This would unleash the full potential of allowing inelasticity at the ultimate load level in the design of wind excited structural systems.

Appendix A

Additional Information: Chapter 4

A.1 Model level elevations

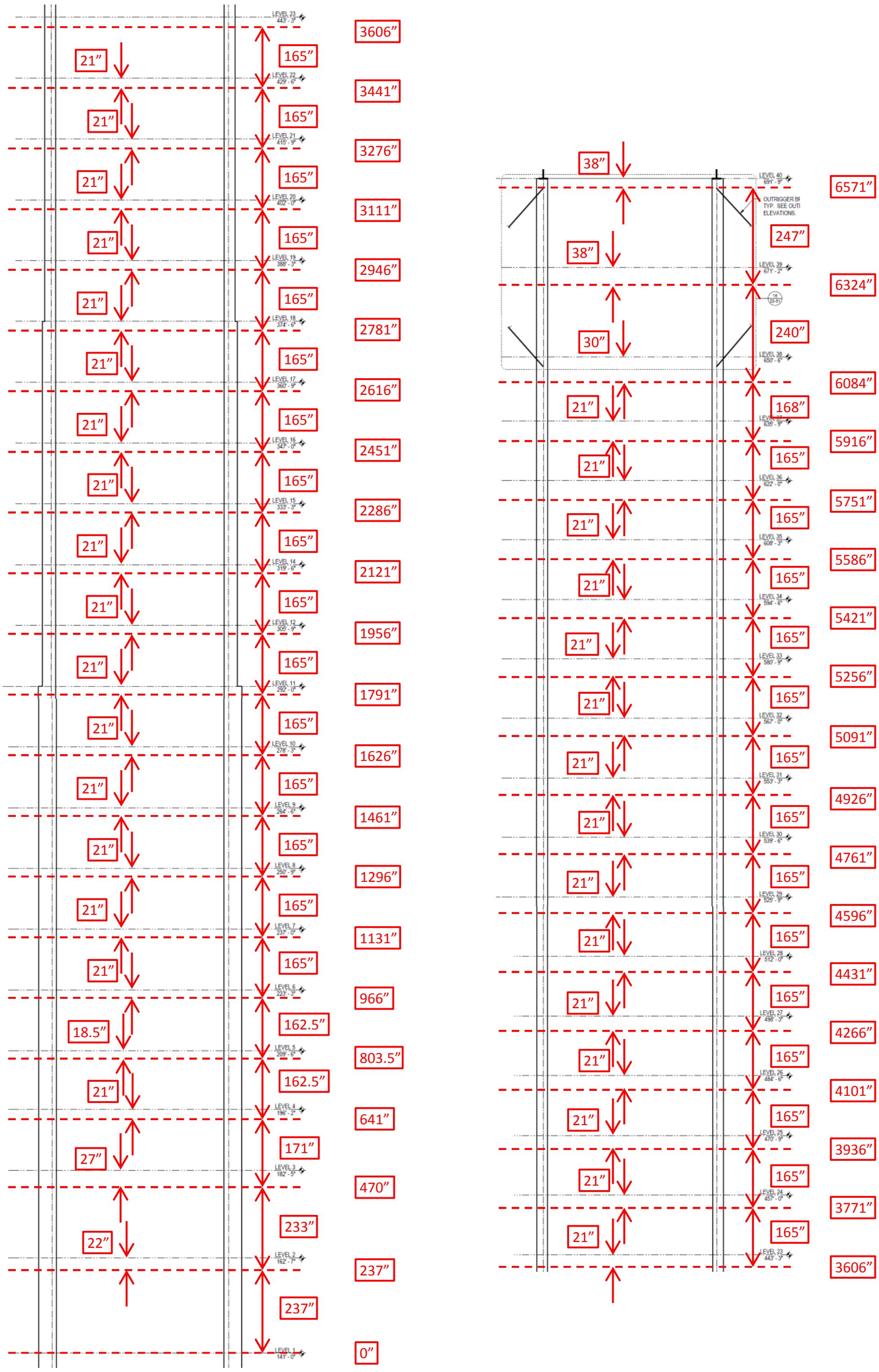

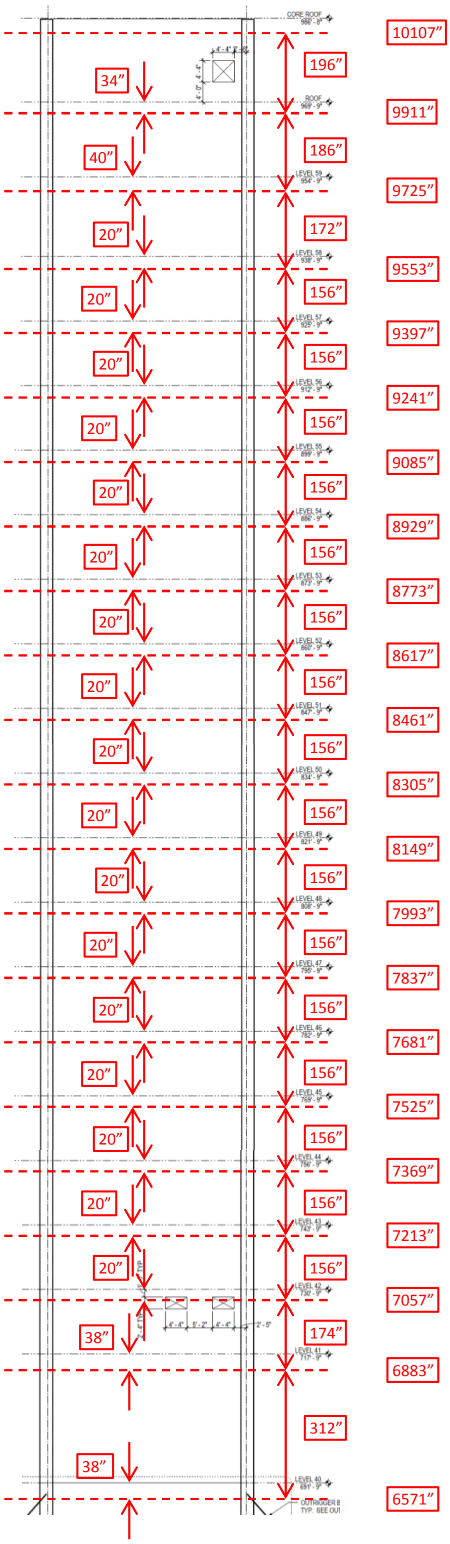
10107″
9911″
9725″
9553″
9397″
9241″
9085″
8929″
8773″
8617″
8461″
8305″
8149″
7993″
7837″
7681″
7525″
7369″
7213″
7057″
6883″
6571″
196″
186″
172″
156″
156″
156″
156″
156″
156″
156″
156″
156″
156″
156″
156″
156″
156″
156″
156″
174″
312″
34″
40″
20″
20″
20″
20″
20″
20″
20″
20″
20″
20″
20″
20″
20″
20″
20″
20″
20″
38″
38″

A.2 Elements assumed elastic in shakedown analysis

7	600	1123	1633
56	601	1124	1634
57	655	1173	1683
69	656	1174	1684
131	657	1175	1685
132	711	1224	1734
133	712	1225	1735
143	713	1226	1736
196	767	1275	1785
197	768	1276	1786
198	769	1277	1787
252	823	1326	1836
253	824	1327	1837
254	825	1328	1838
319	879	1377	1887
320	880	1378	1888
321	881	1379	1889
375	935	1428	1937
376	936	1429	1938
377	937	1430	1944
431	978	1479	1946
432	979	1480	1982
433	980	1481	1983
487	1021	1530	1989
488	1022	1531	1991
489	1023	1532	2027
543	1064	1581	
544	1065	1582	
545	1066	1583	
599	1122	1632	

A.3 Wind speed transformation scheme

In converting the 3-s gust basic wind speed $\bar{v}_3$ at 33-ft height to the mean hourly wind speed $\bar{v}_{3600}$ at 2000-ft reference height, this work adopts the following transformation scheme:

$$\bar{v}_{3600} = \left(\frac{600}{10}\right)^{0.14} \left(\frac{\bar{v}_3}{1.525}\right) \mathrm{K}_R \mathrm{K}_D \qquad \text{(A.1)}$$

where $\bar{v}_{3600}$ and $\bar{v}_3$ are in mph while the reduction factor K_R and the directionality factor K_D are provided in Table A.1.

Table A.1: Values of $\bar{v}_w$, K_R, and K_D for different wind directions.

$\alpha(°)$	$\bar{v}_{ws}$(ft/s)	$\mathrm{K_R}$	$\mathrm{K_D}$	$\alpha(°)$	$\bar{v}_{ws}$(ft/s)	$\mathrm{K_R}$	$\mathrm{K_D}$
10	20.2	0.976	0.78	190	20.5	0.992	1.00
20	20.3	0.986	0.69	200	20.4	1.015	1.00
30	20.3	0.986	0.69	210	20.0	0.986	0.99
40	20.2	0.984	0.65	220	20.0	0.986	0.97
50	20.2	0.995	0.70	230	20.0	0.986	0.97
60	20.2	0.995	0.76	240	19.9	0.986	0.97
70	20.3	0.985	0.80	250	19.9	0.989	0.97
80	20.5	0.985	0.81	260	20.4	0.989	0.94
90	20.6	0.999	0.82	270	20.3	0.989	0.87
100	21.0	0.999	0.82	280	20.3	0.989	0.80
110	20.9	0.985	0.82	290	20.3	0.989	0.72
120	20.7	0.995	0.82	300	20.0	0.955	0.69
130	20.4	0.995	0.82	310	19.8	1.006	0.74
140	20.3	1.001	0.88	320	19.8	1.006	0.77
150	20.2	0.988	0.96	330	20.1	1.006	0.78
160	20.2	0.988	1.00	340	20.2	1.006	0.78
170	20.2	0.981	1.00	350	20.0	0.976	0.78
180	20.4	0.992	1.00	360	20.1	0.970	0.78

A.4 Inelastic elements for a representative sample

A.4.1 Wind load of 300 MRI

MRI	300
$\bar{v}_3$ (mph)	91

Coupling beams

Direction										
10		20			30			40		
51	772	4	597	1929	10	883	1639	51	540	1077
52	939	51	604	2012	52	939	1690	52	541	1116
53	1014	52	660	2058	128	982	1741	53	548	1129
128	1019	53	716	2067	140	1014	1792	128	554	1133
129	1025	128	772	2071	193	1019	1800	129	604	1137
193	1057	129	820		194	1025	1929	193	610	1164
194	1062	193	876		201	1057	1994	194	660	1180
249	1072	194	933		250	1062	2012	201	666	1184
250	1244	249	939		262	1072	2058	212	716	1231
316	1295	250	976		317	1077	2067	249	721	1235
317	1346	262	982		324	1116	2218	250	722	1282
372	1397	316	1014		373	1129	2227	262	772	1333
373	1929	317	1019		380	1133		316	778	1384
428	2012	324	1025		429	1137		317	820	1435
429	2067	372	1057		436	1164		324	828	1486
484		373	1062		485	1180		372	876	1537
485		380	1072		492	1184		373	933	1588
492		428	1116		540	1231		380	939	1639
540		429	1120		541	1235		428	976	1800
541		436	1129		548	1282		429	982	1929
548		484	1171		604	1333		436	1014	1994
597		485	1180		660	1384		442	1019	2003
604		492	1231		716	1435		484	1025	2012
653		540	1282		722	1486		485	1057	2058
660		541	1333		772	1537		492	1062	2067
716		548	1800		828	1588		498	1072	

Direction														
50				60		70		80				
15	436	939	1397	15	541	128	1994	10	386	778	1077	1619
16	441	982	1435	16	548	373	2012	15	429	820	1116	1639
51	442	987	1448	51	554	380	2058	16	436	827	1129	1670
52	485	1014	1486	52	604	429	2067	52	441	828	1133	1690
73	492	1019	1499	74	609	436		64	442	833	1137	1741
74	497	1025	1537	75	610	485		73	485	844	1164	1792
75	498	1030	1550	90	660	492		75	492	865	1180	1800
128	540	1057	1588	128	666	548		90	497	870	1184	1843
147	541	1062	1601	147	716	604		128	498	876	1193	1929
193	548	1072	1759	194	722	660		140	548	883	1231	1994
194	553	1077	1800	206	778	716		147	553	900	1235	2003
206	554	1129	1929	212	923	772		194	554	923	1244	2012
207	604	1133	1958	250	1025	939		201	604	928	1282	2029
250	609	1137	1994	267	1077	982		206	609	933	1286	2053
262	610	1142	2003	268	1193	1014		207	610	939	1295	2058
267	660	1180	2012	317	1244	1019		212	641	944	1333	2067
268	665	1184	2058	329	1295	1025		250	660	971	1337	2073
317	666	1193	2067	330	1346	1057		262	665	982	1346	2093
324	716	1231		373	1397	1062		267	666	987	1384	2113
329	721	1235		385	1448	1072		268	715	1014	1388	2218
330	722	1244		386	1499	1077		324	716	1019	1435	2227
373	772	1282		429	1550	1129		329	721	1025	1486	2238
380	778	1295		442	2012	1180		330	722	1030	1517	2247
385	828	1333		485		1231		373	771	1057	1537	2318
386	865	1346		492		1800		380	772	1062	1568	2327
429	923	1384		498		1929		385	777	1072	1588	2347

Direction											
90			100					110			
16	828	1435	10	497	939	1346	1874	15	553	1129	1929
140	833	1486	15	498	944	1384	1885	16	554	1133	1958
201	865	1537	16	548	982	1388	1929	73	604	1142	1994
262	883	1588	73	553	987	1397	1958	74	609	1180	2003
268	923	1639	74	554	1014	1435	1974	75	610	1184	2058
324	939	1690	75	604	1025	1439	1994	90	660	1193	2067
330	982	1741	90	609	1030	1448	2003	147	665	1231	
380	987	1800	140	610	1057	1486	2012	206	666	1235	
386	1014	1929	147	641	1072	1499	2029	207	716	1244	
436	1025	1994	201	660	1077	1517	2053	212	721	1282	
442	1030	2003	206	665	1129	1537	2055	262	722	1286	
492	1057	2012	207	666	1133	1550	2058	267	772	1295	
498	1072	2058	212	716	1137	1568	2067	268	777	1333	
548	1077	2067	262	721	1142	1588	2075	324	778	1346	
554	1129	2218	267	722	1164	1601	2093	329	833	1384	
604	1133		268	771	1180	1619	2095	330	865	1397	
609	1137		324	772	1184	1639	2113	380	923	1435	
610	1164		329	777	1193	1652	2115	385	939	1448	
660	1180		330	778	1231	1670	2135	386	944	1486	
665	1184		380	809	1235	1690	2155	436	982	1499	
666	1231		385	828	1244	1721	2218	441	987	1517	
716	1235		386	833	1282	1741	2227	442	1014	1550	
721	1282		436	865	1286	1759	2238	492	1025	1568	
722	1286		441	883	1295	1783	2247	497	1030	1601	
772	1333		442	923	1333	1792	2318	498	1072	1652	
778	1384		492	928	1337	1800		548	1077	1800	

Direction												
120			130		140	150	160	170	180	190	200	210
15	660	1235	15	1129	182	90	90	90	90	90	90	90
16	665	1244	16	1133	212	182	182	182	182	182	182	182
73	666	1282	74	1193	1800	212	212	212	212	212	212	212
74	716	1286	90	1244	1929	1800	1800	273	273	273	1800	305
75	721	1295	147	1295	2012	1929	1929	722	610	722	1929	900
90	722	1333	206	1346		1994	1994	1800	666	778	1953	1677
147	772	1346	212	1397		2012	1998	1929	722	1800	1974	1728
206	777	1397	267	1448			2012	1994	778	1929	1994	1800
207	778	1448	268	1499			2016	1998	1193	1974	1998	1881
212	833	1499	330	1929				2012	1244	1994	2012	1929
267	865	1517	386	1994				2016	1295	1998	2016	1953
268	923	1550	442	2003					1346	2012	2058	1974
329	939	1568	498	2012					1397	2016	2067	1994
330	944	1601	548	2067					1448			1998
385	982	1619	554						1800			2012
386	987	1652	604						1929			2016
441	1025	1703	610						1994			2058
442	1030	1759	660						1998			2067
492	1072	1800	666						2012			
497	1077	1929	716						2016			
498	1129	1958	722									
548	1133	1994	778									
553	1142	2003	923									
554	1180	2012	939									
604	1184	2058	1025									
609	1193	2067	1072									
610	1231	2075	1077									

Direction										
220		230	240		250		260		
90	1974	90	90	1998	90	1800	1	1371	1994
156	1994	156	156	2003	156	1881	156	1397	1998
182	1998	182	182	2012	182	1929	182	1422	2003
212	2012	212	212	2016	212	1953	212	1448	2012
238	2016	273	273	2058	238	1958	238	1473	2016
305	2067	1320	1193	2067	273	1974	305	1499	2026
1142		1371	1244		305	1994	361	1517	2028
1193		1422	1295		844	1998	417	1524	2050
1244		1473	1320		870	2003	473	1550	2052
1295		1524	1346		900	2012	641	1568	2058
1320		1575	1371		928	2016	788	1575	2067
1346		1626	1397		1193	2058	814	1601	2070
1371		1677	1422		1244	2067	844	1619	2072
1397		1728	1448		1295		865	1626	2090
1422		1800	1473		1320		870	1652	2092
1448		1929	1499		1346		900	1670	2110
1473		1974	1524		1371		923	1677	2112
1499		1994	1550		1397		928	1703	2130
1524		1998	1575		1422		934	1728	2150
1550		2012	1626		1448		977	1754	2218
1575		2016	1677		1473		1014	1800	2227
1601		2067	1728		1499		1020	1881	2238
1626			1800		1524		1142	1929	
1677			1929		1575		1193	1953	
1728			1958		1626		1244	1958	
1800			1974		1677		1295	1971	
1929			1994		1728		1346	1974	

Direction											
270				280			290		300		310
1	870	1601	2050	1	934	1929	1	1652	182	1994	182
48	878	1619	2052	48	974	1953	182	1670	238	1998	373
49	900	1626	2058	49	977	1958	190	1703	305	2003	1244
51	923	1652	2067	51	1014	1974	238	1754	361	2016	1295
126	928	1670	2070	126	1020	1988	305	1800	865	2067	1346
156	931	1677	2072	182	1049	1994	361	1881	923	2070	1800
182	934	1703	2090	190	1090	1998	641	1929	928	2090	1929
190	971	1721	2092	238	1142	2003	844	1953	1142	2110	1974
212	974	1728	2110	246	1193	2012	865	1958	1193		1994
238	977	1754	2112	305	1244	2016	870	1974	1244		1998
246	1014	1800	2130	313	1295	2026	900	1994	1295		2012
305	1020	1881	2150	361	1346	2050	923	1998	1346		2016
313	1049	1929	2170	369	1397	2052	928	2003	1397		
361	1063	1953	2218	417	1448	2058	1090	2012	1448		
369	1090	1958	2227	425	1499	2067	1142	2016	1499		
417	1121	1971	2238	473	1517	2070	1193	2050	1517		
425	1142	1974	2247	641	1550	2090	1244	2058	1550		
473	1193	1977	2318	788	1568	2092	1295	2067	1568		
529	1244	1988		809	1601	2110	1346	2070	1601		
641	1295	1994		814	1619	2112	1397	2090	1619		
732	1346	1998		844	1652	2130	1448	2110	1652		
758	1397	2003		865	1670	2150	1499	2150	1703		
788	1448	2012		870	1703	2218	1517		1754		
809	1499	2016		900	1721	2227	1550		1800		
814	1517	2022		923	1754	2238	1568		1929		
844	1550	2026		928	1800		1601		1958		
865	1568	2028		931	1881		1619		1974		

Direction					
320	330	340	350	360	
182	182	182	182	51	1397
1800	1800	1800	1800	52	1448
1929	1929	1929	1929	53	1499
1974	1974	1974	1974	128	1550
1994	1994	1994	1994	129	1929
2016	2016	2016	2003	193	1974
			2016	194	1994
				249	2003
				250	2012
				316	
				317	
				372	
				373	
				428	
				429	
				484	
				485	
				540	
				541	
				597	
				653	
				1019	
				1062	
				1193	
				1244	
				1295	
				1346	

A.4.2 Wind load of 700 MRI

MRI	700
$\bar{v}_3$ (mph)	96

Coupling beams

Direction										
10			20		30			40		
4	604	1397	51	1929	10	660	1282	10	554	1077
51	653	1435	52	2012	52	666	1333	16	604	1116
52	660	1448	128	2058	64	716	1384	52	609	1129
53	716	1486	193	2067	128	721	1435	128	610	1133
128	772	1499	194		140	722	1486	140	660	1137
129	828	1537	250		193	772	1537	193	665	1164
193	933	1550	317		194	778	1588	194	666	1180
194	939	1588	373		201	828	1639	201	716	1184
249	976	1800	429		250	883	1690	250	721	1231
250	982	1929	485		262	900	1741	262	722	1235
262	1014	2012	492		317	939	1792	268	772	1282
316	1019	2058	540		324	982	1800	317	778	1286
317	1025	2067	541		373	1014	1929	324	820	1333
324	1057		548		380	1019	1994	330	828	1384
372	1062		604		429	1025	2003	373	865	1435
373	1072		660		436	1057	2012	380	876	1486
380	1116		716		442	1062	2058	386	923	1537
428	1129		772		484	1072	2067	429	939	1588
429	1180		939		485	1077	2218	436	982	1639
436	1193		982		492	1116	2227	442	987	1690
484	1231		1019		498	1129		484	1014	1800
485	1244		1025		540	1133		485	1019	1929
492	1282		1057		541	1137		492	1025	1994
540	1295		1062		548	1164		498	1030	2003
541	1333		1072		554	1180		540	1057	2012
548	1346		1129		604	1184		541	1062	2058
597	1384		1800		610	1231		548	1072	2067

Direction											
50		60		70				80			
15	722	52	1346	15	386	833	1295	10	484	900	1333
16	772	90	1397	16	429	865	1333	15	485	923	1384
128	778	128	1929	51	436	923	1346	16	492	933	1435
147	923	194	1994	52	441	939	1384	52	498	939	1486
206	939	212	2012	73	442	982	1397	64	540	976	1537
262	982	373		75	485	987	1435	128	541	982	1588
268	1014	429		90	492	1014	1486	129	548	987	1639
324	1025	442		128	497	1019	1517	140	554	1014	1690
330	1057	485		140	498	1025	1537	193	604	1019	1741
373	1072	492		147	540	1030	1568	194	609	1025	1792
380	1077	498		193	541	1057	1588	201	610	1057	1800
386	1129	548		194	548	1062	1639	206	641	1062	1929
429	1133	554		201	553	1072	1690	250	660	1072	1994
436	1180	604		206	554	1077	1800	262	665	1077	2003
442	1231	610		207	604	1116	1929	268	666	1116	2012
492	1282	660		212	609	1129	1994	316	716	1129	2053
498	1333	666		250	610	1133	2003	317	721	1133	2058
548	1384	716		262	660	1137	2012	324	722	1137	2067
554	1800	722		267	665	1164	2058	330	764	1164	2093
604	1929	778		268	666	1180	2067	372	771	1171	2218
609	1994	939		317	716	1184		373	772	1180	2227
610	2003	1019		324	721	1193		380	778	1184	
660	2012	1025		329	722	1231		386	820	1222	
665	2058	1072		330	772	1235		428	828	1231	
666	2067	1077		373	777	1244		429	865	1235	
716		1244		380	778	1282		436	876	1273	
721		1295		385	828	1286		442	883	1282	

Direction									
90				100					
15	553	1057	1568	10	497	900	1295	1800	2338
16	554	1072	1588	15	498	923	1333	1843	2347
73	604	1077	1619	16	548	928	1337	1874	2367
74	609	1129	1639	64	553	939	1346	1885	
75	610	1133	1670	73	554	944	1384	1929	
90	660	1137	1690	74	604	971	1388	1958	
140	665	1164	1800	75	609	982	1397	1974	
147	666	1180	1929	90	610	987	1435	1994	
201	716	1184	1958	140	641	1014	1439	2003	
206	721	1193	1994	147	660	1025	1448	2029	
207	722	1231	2003	201	665	1030	1486	2053	
262	772	1235	2012	206	666	1057	1490	2055	
267	777	1244	2058	207	715	1072	1499	2058	
268	778	1282	2067	212	716	1077	1517	2067	
324	828	1286	2075	262	721	1129	1537	2073	
329	833	1295		267	722	1133	1550	2075	
330	865	1333		268	771	1137	1568	2093	
380	883	1337		324	772	1142	1588	2095	
385	923	1346		329	777	1164	1601	2113	
386	939	1384		330	778	1180	1619	2115	
436	944	1397		380	809	1184	1639	2155	
441	982	1435		385	827	1193	1670	2218	
442	987	1448		386	828	1231	1690	2227	
492	1014	1486		436	833	1235	1741	2238	
497	1019	1499		441	865	1244	1759	2247	
498	1025	1517		442	870	1282	1783	2318	
548	1030	1537		492	883	1286	1792	2327	

Direction												
110					120				130	140	150	160
15	548	1057	1517	2075	15	660	1235	2095	90	182	182	90
16	553	1072	1537	2093	16	665	1244	2115	212	1800	212	182
73	554	1077	1550	2095	73	666	1286		442	1929	1800	212
74	604	1129	1568	2115	74	716	1295		498	1994	1929	1800
75	609	1133	1588	2135	75	721	1346		554	2012	1994	1929
90	610	1137	1601	2155	90	722	1397		610		2012	1994
140	660	1142	1619	2218	147	772	1448		666			1998
147	665	1164	1639	2227	206	777	1499		722			2012
201	666	1180	1652		207	778	1517		778			2016
206	716	1184	1670		212	833	1550		1077			
207	721	1193	1690		267	865	1568		1133			
212	722	1231	1703		268	923	1601		1929			
262	772	1235	1741		329	939	1619		1994			
267	777	1244	1754		330	944	1652		2012			
268	778	1282	1759		385	982	1703					
324	828	1286	1800		386	987	1759					
329	833	1295	1810		441	1025	1800					
330	865	1333	1874		442	1030	1874					
380	883	1337	1885		492	1072	1929					
385	923	1346	1929		497	1077	1958					
386	939	1384	1958		498	1129	1994					
436	944	1388	1974		548	1133	2003					
441	982	1397	1994		553	1142	2012					
442	987	1435	2003		554	1180	2055					
492	1014	1448	2055		604	1184	2058					
497	1025	1486	2058		609	1193	2067					
498	1030	1499	2067		610	1231	2075					

Direction												
170	180	190	200	210	220	230	240	250		260		
90	90	90	90	90	90	90	90	90	1974	90	1473	2052
156	156	182	182	182	182	156	156	156	1994	156	1499	2058
182	182	212	212	212	212	182	182	182	1998	182	1517	2067
212	212	1800	1800	238	238	212	212	212	2003	212	1524	2070
273	273	1929	1929	305	305	238	900	238	2012	238	1550	2090
610	442	1974	1974	1800	1728	273	1677	273	2016	305	1568	2092
666	498	1994	1994	1929	1800	305	1728	305	2058	361	1575	2110
722	554	1998	1998	1974	1929	900	1800	844	2067	417	1601	2130
778	610	2012	2012	1994	1974	1320	1929	870		641	1619	2150
1244	666	2016	2016	1998	1994	1371	1953	900		788	1626	2218
1295	722			2012	1998	1422	1974	928		814	1652	
1346	778			2016	2012	1473	1994	1193		844	1670	
1800	1142			2067	2016	1524	1998	1244		865	1677	
1929	1193				2067	1575	2003	1295		870	1703	
1994	1244					1626	2012	1346		900	1728	
1998	1295					1677	2016	1397		923	1754	
2012	1346					1728	2058	1448		928	1800	
2016	1397					1800		1499		1014	1881	
	1448					1881		1550		1142	1929	
	1499					1929		1575		1193	1953	
	1550					1953		1626		1244	1958	
	1601					1974		1677		1295	1974	
	1800					1994		1728		1320	1994	
	1929					1998		1800		1346	1998	
	1994					2012		1881		1371	2003	
	1998					2016		1929		1397	2012	
	2012					2058		1953		1422	2016	
	2016					2067		1958		1448	2050	

Direction												
270				280				290			300	
1	971	1874	2238	1	923	1703	2090	1	934	1929	51	1994
48	974	1881	2318	48	928	1721	2092	48	974	1953	182	1998
49	977	1929	2338	49	931	1728	2110	49	977	1958	238	2003
126	1014	1953		51	934	1754	2112	51	1014	1974	305	2012
182	1020	1958		126	971	1800	2130	126	1049	1994	865	2016
190	1049	1971		156	974	1805	2150	182	1090	1998	923	2050
212	1090	1974		182	977	1874	2170	190	1142	2003	928	2058
238	1142	1988		190	1014	1881	2218	191	1193	2012	1142	2067
246	1193	1994		212	1020	1929	2227	238	1244	2016	1193	2070
305	1244	1998		238	1049	1953	2238	246	1295	2022	1244	2090
313	1295	2003		246	1090	1958	2318	283	1346	2026	1295	2110
361	1346	2012		305	1121	1971	2338	305	1397	2050	1346	
369	1397	2016		313	1142	1974		313	1448	2052	1397	
417	1448	2026		361	1193	1988		361	1499	2058	1448	
473	1499	2050		369	1244	1994		369	1517	2067	1499	
529	1517	2052		417	1295	1998		417	1550	2070	1517	
641	1550	2058		425	1346	2003		425	1568	2090	1550	
788	1568	2067		473	1397	2012		641	1601	2092	1568	
809	1601	2070		529	1448	2016		788	1619	2110	1601	
814	1619	2090		641	1499	2022		809	1652	2112	1619	
844	1652	2092		758	1517	2026		814	1670	2130	1652	
865	1670	2110		788	1550	2028		844	1703	2150	1703	
870	1703	2112		809	1568	2050		865	1721	2170	1754	
900	1721	2130		814	1601	2052		870	1754	2218	1800	
923	1728	2150		844	1619	2058		900	1800	2227	1929	
928	1754	2170		865	1652	2067		923	1805	2238	1953	
931	1800	2218		870	1670	2070		928	1874		1958	
934	1805	2227		900	1677	2072		931	1881		1974	

Direction					
310	320	330	340	350	360
182	182	182	182	182	51
1800	1800	1800	1800	1193	52
1929	1929	1929	1929	1244	53
1974	1974	1974	1974	1295	128
1994	1994	1994	1994	1346	129
2016	2012	2016	2016	1397	193
	2016			1448	194
				1800	249
				1929	250
				1974	317
				1994	373
				2003	429
				2016	485
					492
					541
					548
					604
					660
					1019
					1057
					1244
					1295
					1346
					1929
					1974
					1994
					2012

Appendix B

Inclusion of wind tunnel uncertainties

As presented in Section 3.2 of last report, the stochastic wind loads $\mathbf{F}(t)$ corresponding to the intensity measure $\tilde{V}_H$ and the wind direction α is represented by the superposition of N_l independent vector-valued subprocesses as follows:

$$\mathbf{F}(t;\tilde{V}_H,\alpha)=\sum_{j=1}^{N_l}\mathbf{F}_j(t;\tilde{V}_H,\alpha) \tag{B.1}$$

where $\mathbf{F}_j(t)$ is the jth vector-valued subprocess given by:

$$\mathbf{F}_j(t;\tilde{V}_H,\alpha)=\sum_{k=1}^{N_f}|\mathbf{\Psi}_j(\omega_k;\alpha)|\sqrt{2\Lambda_j(\omega_k;\tilde{V}_H,\alpha)\Delta\omega_k}\times\cos(\omega_k t+\vartheta_{kj}+\boldsymbol{\theta_j}(\omega_k)) \tag{B.2}$$

where $\mathbf{\Psi}_j(\omega_k)$ and $\Lambda_j(\omega_k)$ are the jth frequency dependent eigenvector and eigenvalue of $\mathbf{F}(t)$, N_f is the total number of discrete frequencies considered in the interval $[0, N_f\Delta\omega_k]$ with $\Delta\omega_k$ representing the frequency increment, ϑ_{kj} are independent and uniformly distributed random variables in $[0,2\pi]$, while $\boldsymbol{\theta}_j$ is a vector of complex angles. In particular, $\Lambda_j(\omega_k)$ and $\mathbf{\Psi}_j(\omega_k)$ are related to eigenvalues and eigenvectors of scaled experimental loads, $\mathbf{f}_w(\tilde{t})$, through the following scheme:

$$\Lambda_j(\omega_k;\tilde{V}_H)=\left[\left(\frac{\tilde{V}_H}{\bar{v}_w}\right)^2\right]^2\left(\frac{\bar{v}_w}{\tilde{V}_H}\right)\Lambda_j^{(w)}(\tilde{\omega}_k) \tag{B.3}$$

$$\mathbf{\Psi}_j(\omega_k)=\mathbf{\Psi}_j^{(w)}(\tilde{\omega}_k) \tag{B.4}$$

where $\bar{v}_w$ is the mean hourly wind speed at the reference height to which the wind tunnel loads $\mathbf{f}_w(\tilde{t})$ were scaled, $\omega_k=\frac{\tilde{V}_H}{\bar{v}_w}\tilde{\omega}_k$ with $\tilde{\omega}_k$ the kth frequency step at the wind tunnel reference speed, while $\Lambda_j^{(w)}(\tilde{\omega}_k)$ and $\mathbf{\Psi}_j^{(w)}(\tilde{\omega}_k)$ are eigenvalues and eigenvectors of $\mathbf{f}_w(\tilde{t})$ determined from the following eigenvalue problem:

$$[\mathbf{S}_{\mathbf{f}_w}(\tilde{\omega}_k;\bar{v}_w,\alpha) - \Lambda^{(w)}(\tilde{\omega}_k;\bar{v}_w,\alpha)\mathbf{I}]\mathbf{\Psi}^{(w)}(\tilde{\omega}_k;\alpha) = 0 \tag{B.5}$$

where $\mathbf{S}_{\mathbf{f}_w}$ is the cross power spectral density of $\mathbf{f}_w(\tilde{t})$. To consider uncertainties associated with the use of wind tunnel data, the wind tunnel loads $\mathbf{f}_w(\tilde{t})$ should be multiplied by the uncertain parameters w_1, w_2 and w_3 of Table 5.3. This multiplication will obviously affect the simulated wind loads $\mathbf{F}(t)$. To model this effect, consider a corrected wind tunnel load, i.e. $\tilde{\mathbf{f}}_w(\tilde{t}) = w_1 w_2 w_3 \mathbf{f}_w(\tilde{t})$. The associated cross power spectral density is:

$$\tilde{\mathbf{S}}_{\mathbf{f}_w} = (w_1 w_2 w_3)^2 \mathbf{S}_{\mathbf{f}_w} \tag{B.6}$$

The corresponding eigenvalues become $\tilde{\Lambda}_j^{(w)}(\tilde{\omega}_k) = (w_1 w_2 w_3)^2 \Lambda_j^{(w)}(\tilde{\omega}_k)$, while the eigenvectors remain the same. The eigenvalues of the simulated wind loads $\mathbf{f}(t)$ can then be determined through the transformation of Eq. (B.3), which yields $\tilde{\Lambda}_j(\omega_k;\tilde{V}_H) = (w_1 w_2 w_3)^2 \Lambda_j(\omega_k;\tilde{V}_H)$. Hence, by substituting into Eq. (B.2) and summing over all N_l modes, the corrected stochastic wind loads can be expressed as:

$$\mathbf{F}_w(t;\tilde{V}_H,\alpha) = w_1 w_2 w_3 \mathbf{f}(t;\tilde{V}_H,\alpha) \tag{B.7}$$

Appendix C

Element Layout: FEM Model of Rainier Square

Rigid Link

Beam-Column element
(with tag)

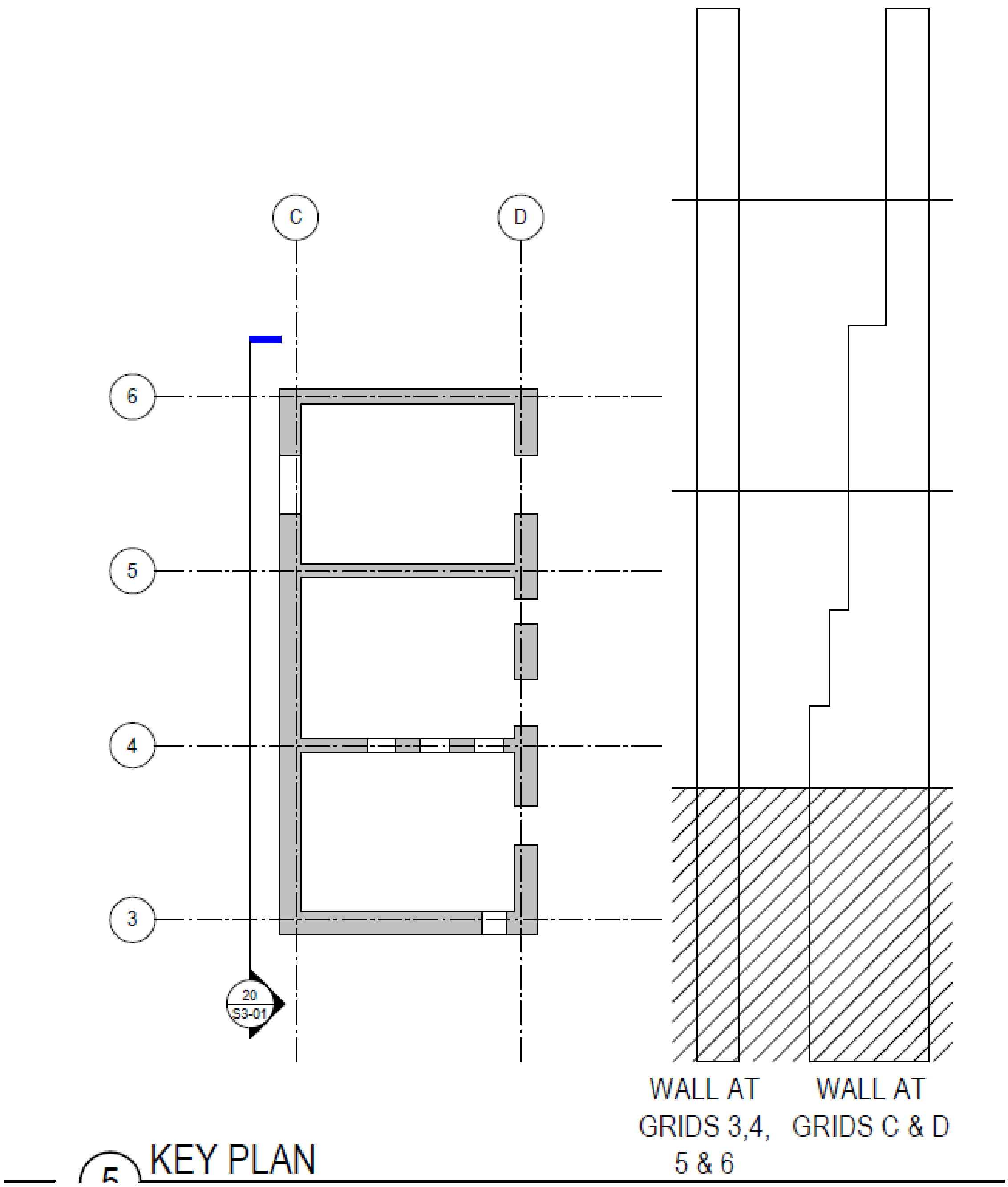

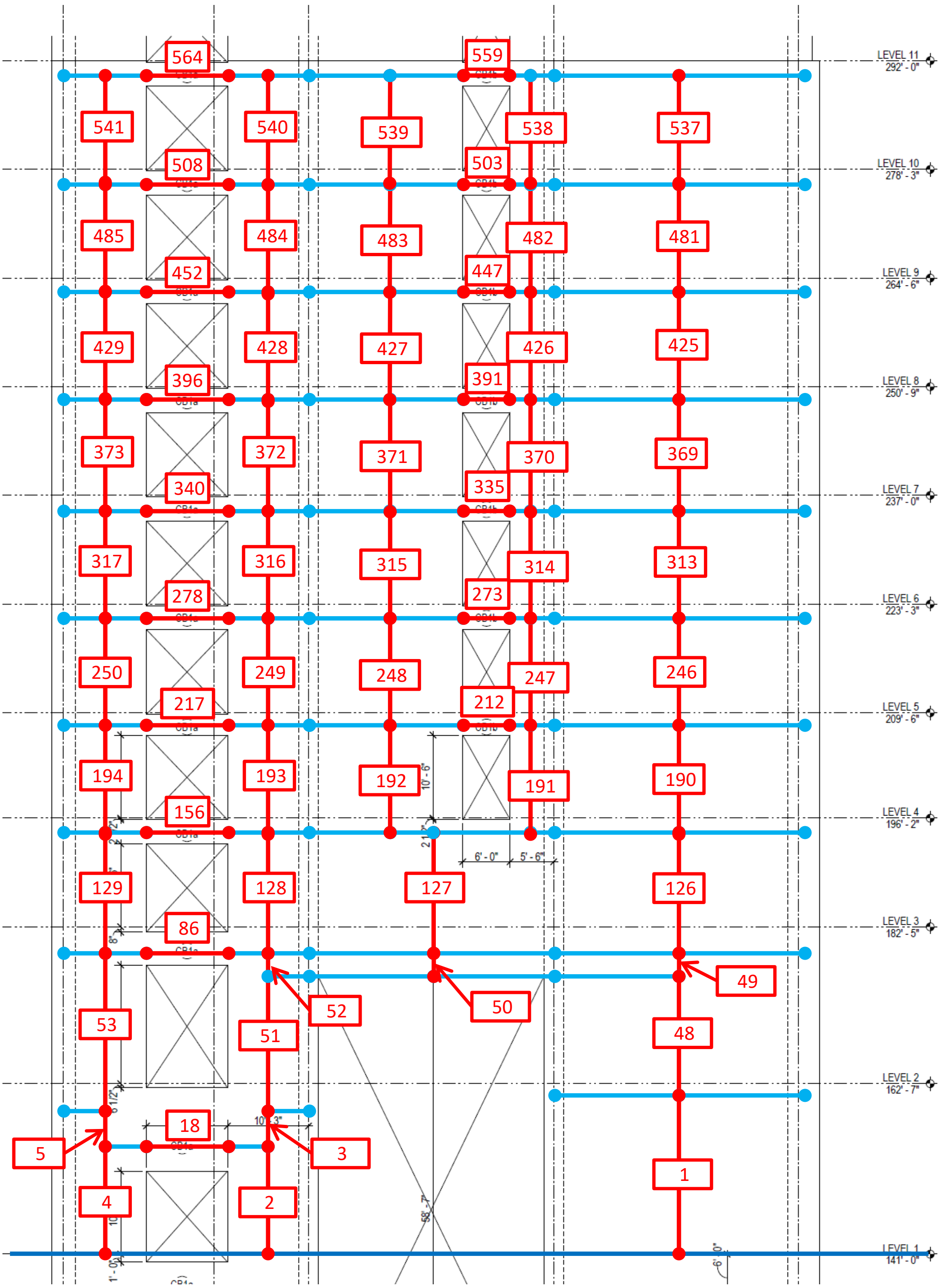

564
559
541
540
539
538
537
508
503
485
484
483
482
481
452
447
429
428
427
426
425
396
391
373
372
371
370
369
340
335
317
316
315
314
313
278
273
250
249
248
247
246
217
212
194
193
192
191
190
156
129
128
127
126
86
49
52
50
53
51
48
18
5
3
4
2
1
LEVEL 11
292' - 0"
LEVEL 10
278' - 3"
LEVEL 9
264' - 6"
LEVEL 8
250' - 9"
LEVEL 7
237' - 0"
LEVEL 6
223' - 3"
LEVEL 5
209' - 6"
LEVEL 4
196' - 2"
LEVEL 3
182' - 5"
LEVEL 2
162' - 7"
LEVEL 1
141' - 0"
6' - 0"
5' - 6"
10' - 6"

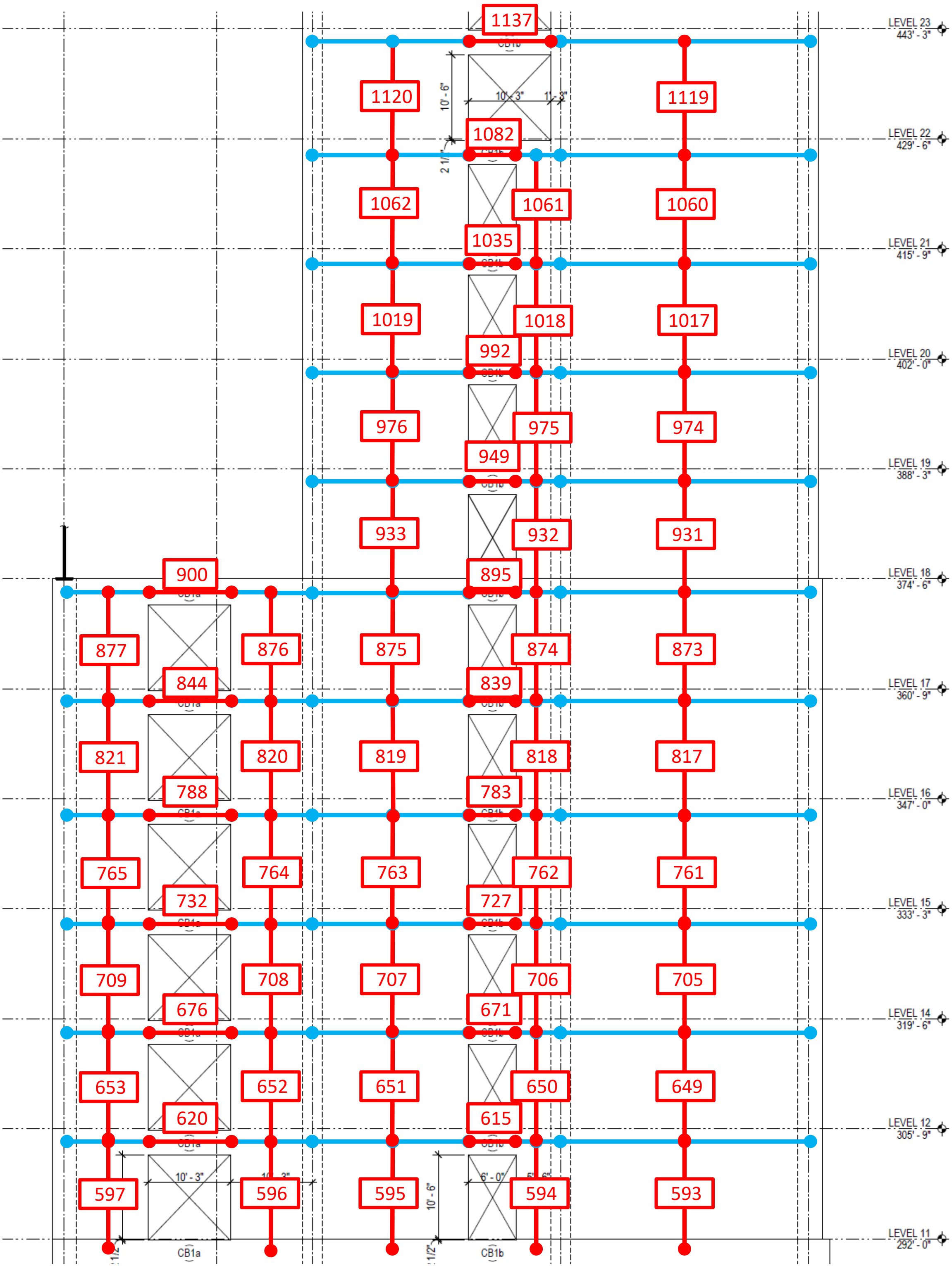
1137
1120
1119
1082
1062
1061
1060
1035
1019
1018
1017
992
976
975
974
949
933
932
931
900
895
877
876
875
874
873
844
839
821
820
819
818
817
788
783
765
764
763
762
761
732
727
709
708
707
706
705
676
671
653
652
651
650
649
620
615
597
596
595
594
593
LEVEL 23
443' - 3"
LEVEL 22
429' - 6"
LEVEL 21
415' - 9"
LEVEL 20
402' - 0"
LEVEL 19
388' - 3"
LEVEL 18
374' - 6"
LEVEL 17
360' - 9"
LEVEL 16
347' - 0"
LEVEL 15
333' - 3"
LEVEL 14
319' - 6"
LEVEL 12
305' - 9"
LEVEL 11
292' - 0"
CB1a
CB1b

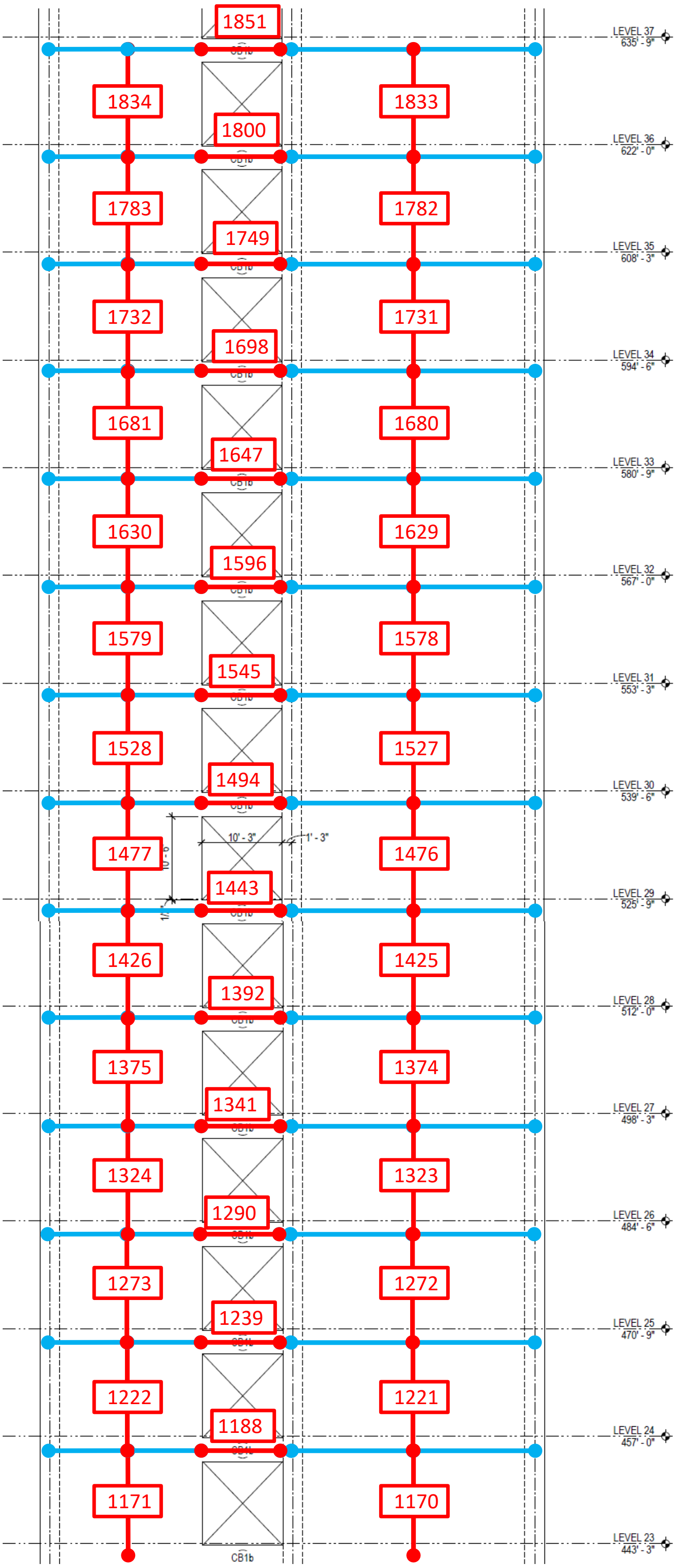
1851
LEVEL 37
635' - 9"
1834
1833
1800
LEVEL 36
622' - 0"
1783
1782
1749
LEVEL 35
608' - 3"
1732
1731
1698
LEVEL 34
594' - 6"
1681
1680
1647
LEVEL 33
580' - 9"
1630
1629
1596
LEVEL 32
567' - 0"
1579
1578
1545
LEVEL 31
553' - 3"
1528
1527
1494
LEVEL 30
539' - 6"
10' - 3"
1' - 3"
1477
1476
1443
LEVEL 29
525' - 9"
1426
1425
1392
LEVEL 28
512' - 0"
1375
1374
1341
LEVEL 27
498' - 3"
1324
1323
1290
LEVEL 26
484' - 6"
1273
1272
1239
LEVEL 25
470' - 9"
1222
1221
1188
LEVEL 24
457' - 0"
1171
1170
CB1b
LEVEL 23
443' - 3"

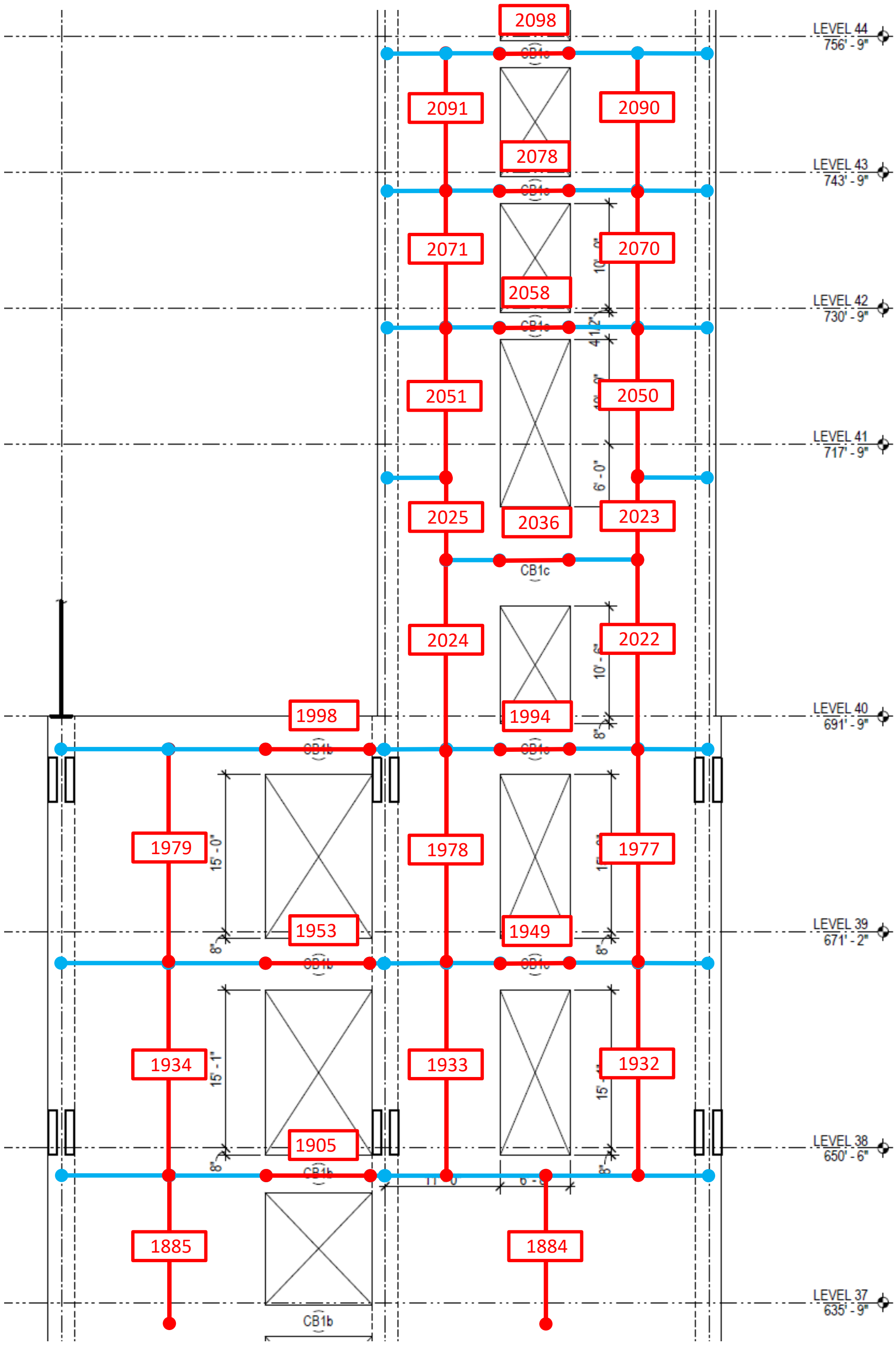
2098
2091
2090
2078
2071
2070
2058
2051
2050
2025
2036
2023
CB1c
2024
2022
1998
1994
1979
1978
1977
1953
1949
1934
1933
1932
1905
1885
1884
CB1b
LEVEL 44
756' - 9"
LEVEL 43
743' - 9"
LEVEL 42
730' - 9"
LEVEL 41
717' - 9"
LEVEL 40
691' - 9"
LEVEL 39
671' - 2"
LEVEL 38
650' - 6"
LEVEL 37
635' - 9"

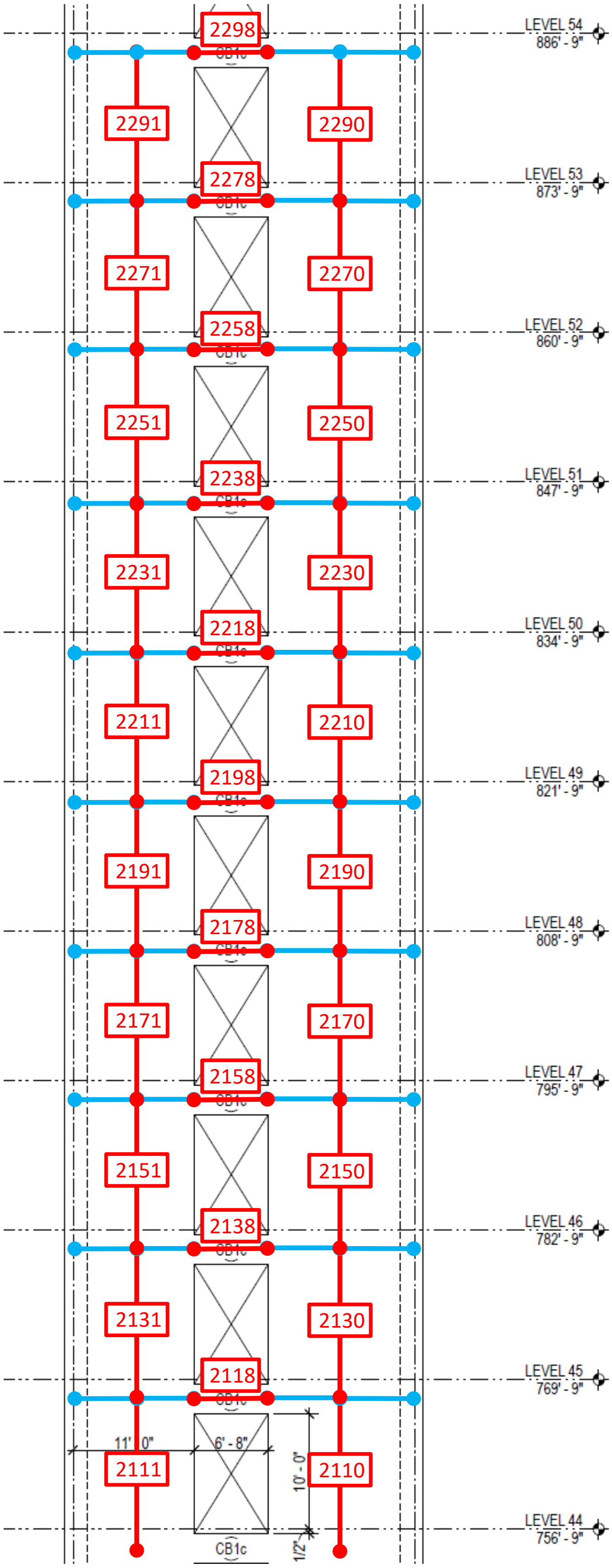

2298
2291
2290
2278
2271
2270
2258
2251
2250
2238
2231
2230
2218
2211
2210
2198
2191
2190
2178
2171
2170
2158
2151
2150
2138
2131
2130
2118
2111
2110
11' 0"
6' - 8"
10' - 0"
1/2"
CB1c
LEVEL 54 886' - 9"
LEVEL 53 873' - 9"
LEVEL 52 860' - 9"
LEVEL 51 847' - 9"
LEVEL 50 834' - 9"
LEVEL 49 821' - 9"
LEVEL 48 808' - 9"
LEVEL 47 795' - 9"
LEVEL 46 782' - 9"
LEVEL 45 769' - 9"
LEVEL 44 756' - 9"

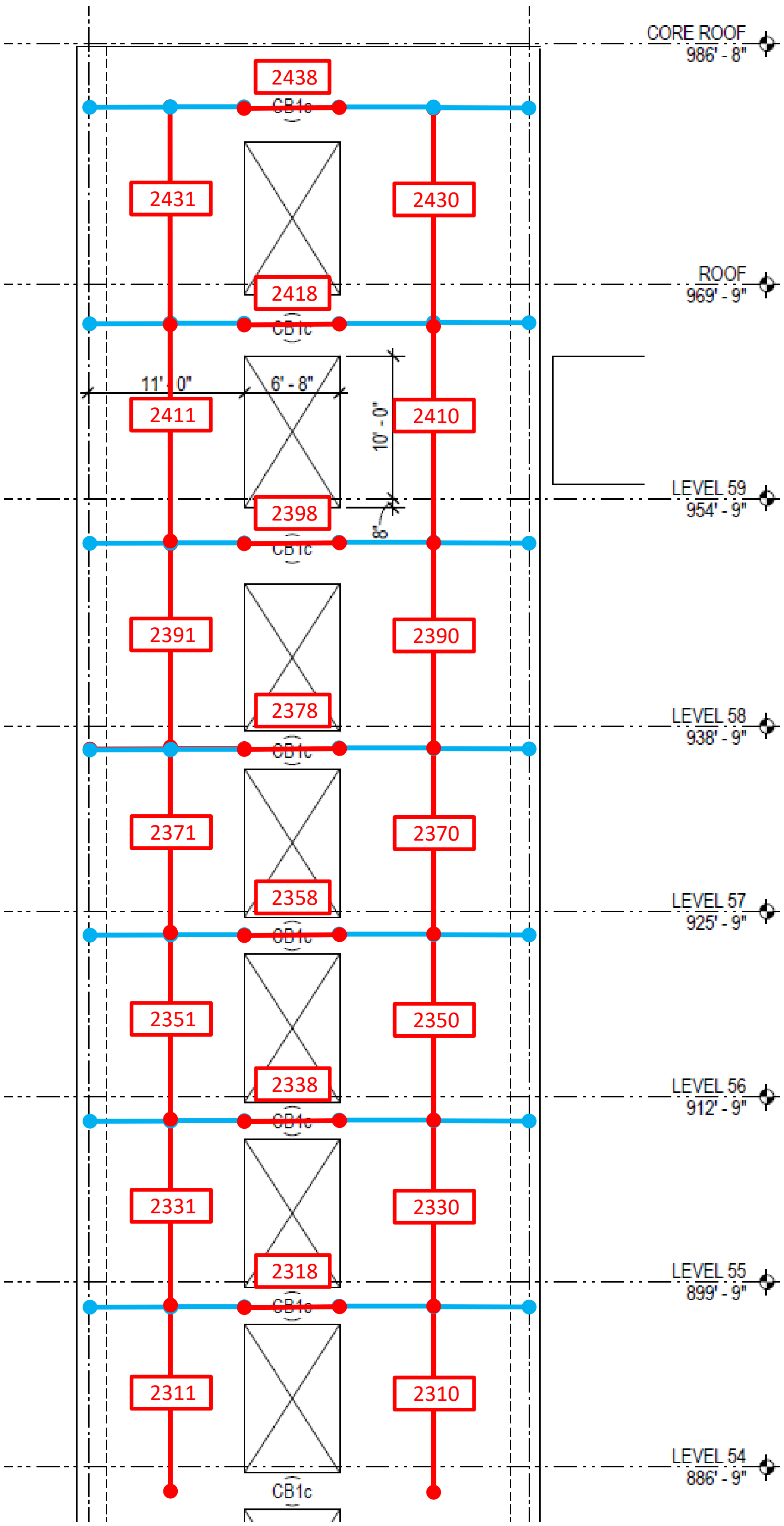
CORE ROOF
986' - 8"
ROOF
969' - 9"
LEVEL 59
954' - 9"
LEVEL 58
938' - 9"
LEVEL 57
925' - 9"
LEVEL 56
912' - 9"
LEVEL 55
899' - 9"
LEVEL 54
886' - 9"
2438
2431
2430
2418
11' - 0"
6' - 8"
10' - 0"
8"
2411
2410
2398
2391
2390
2378
2371
2370
2358
2351
2350
2338
2331
2330
2318
2311
2310
CB1c

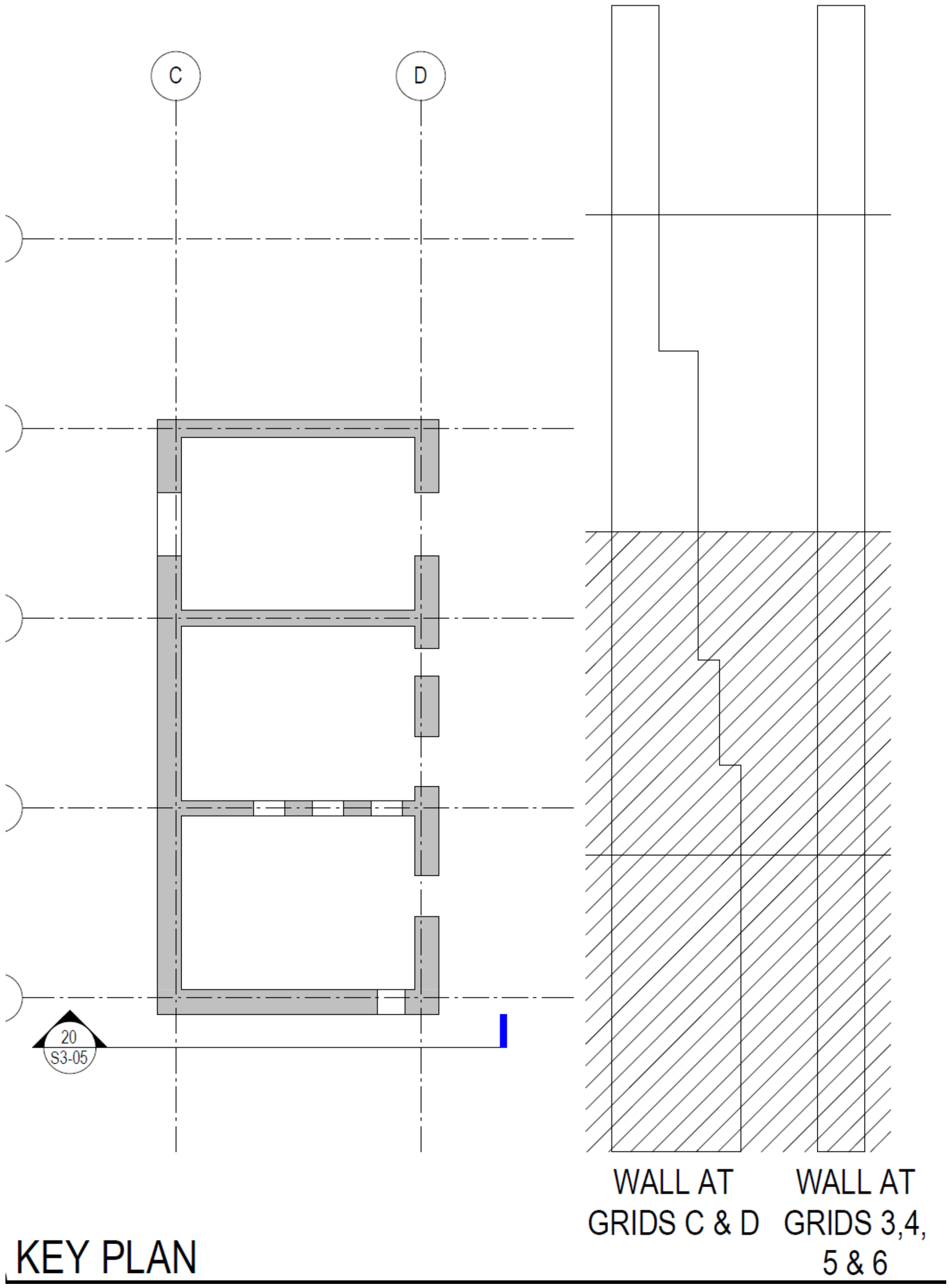
C
D
20
S3-05
WALL AT
GRIDS C & D
WALL AT
GRIDS 3,4,
5 & 6
KEY PLAN

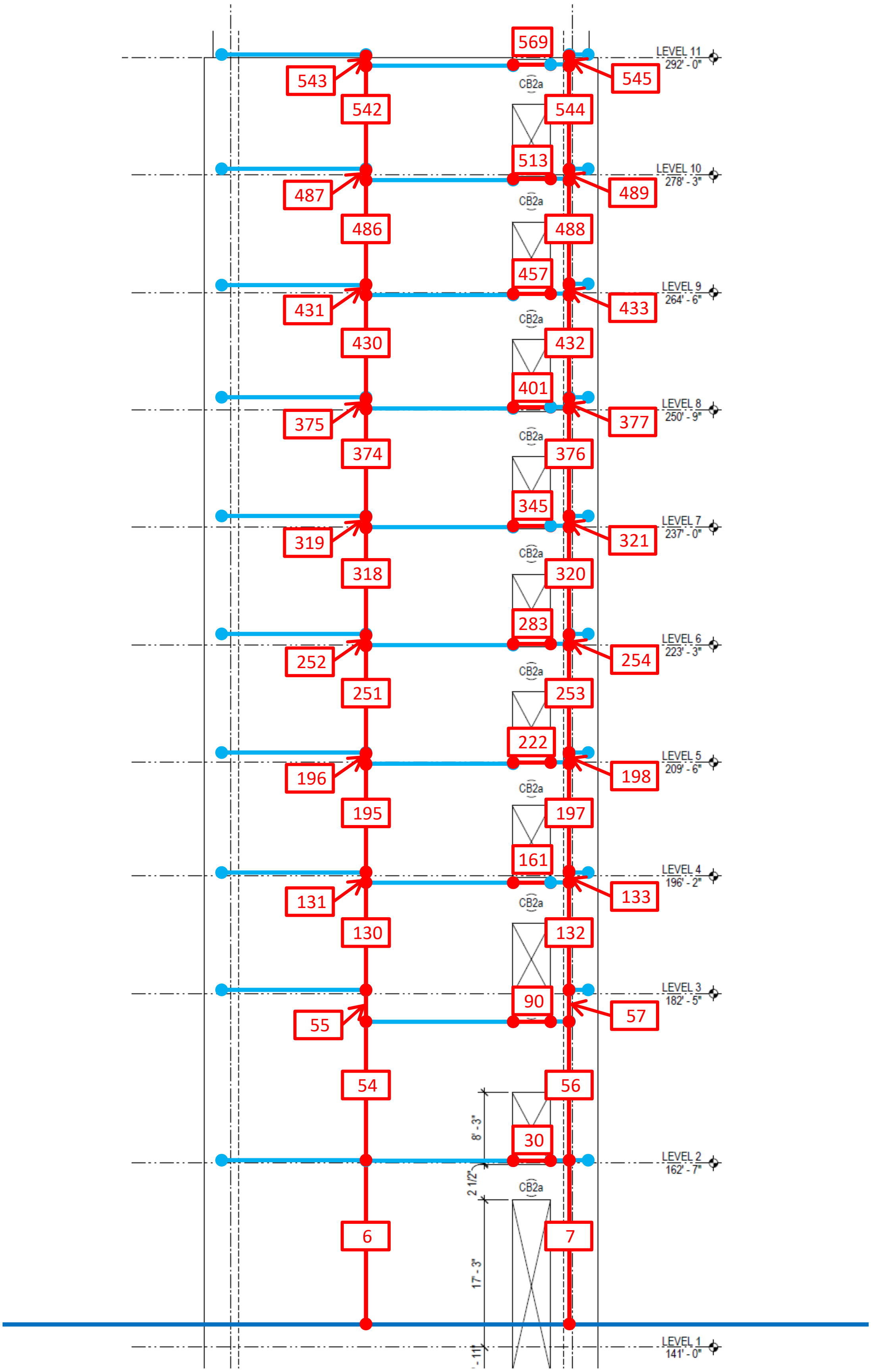
569
543
542
544
545
LEVEL 11
292' - 0"
CB2a
513
487
486
488
489
LEVEL 10
278' - 3"
457
431
430
432
433
LEVEL 9
264' - 6"
401
375
374
376
377
LEVEL 8
250' - 9"
345
319
318
320
321
LEVEL 7
237' - 0"
283
252
251
253
254
LEVEL 6
223' - 3"
222
196
195
197
198
LEVEL 5
209' - 6"
161
131
130
132
133
LEVEL 4
196' - 2"
90
55
57
LEVEL 3
182' - 5"
54
56
8' - 3"
30
LEVEL 2
162' - 7"
2 1/2"
6
7
17' - 3"
LEVEL 1
141' - 0"

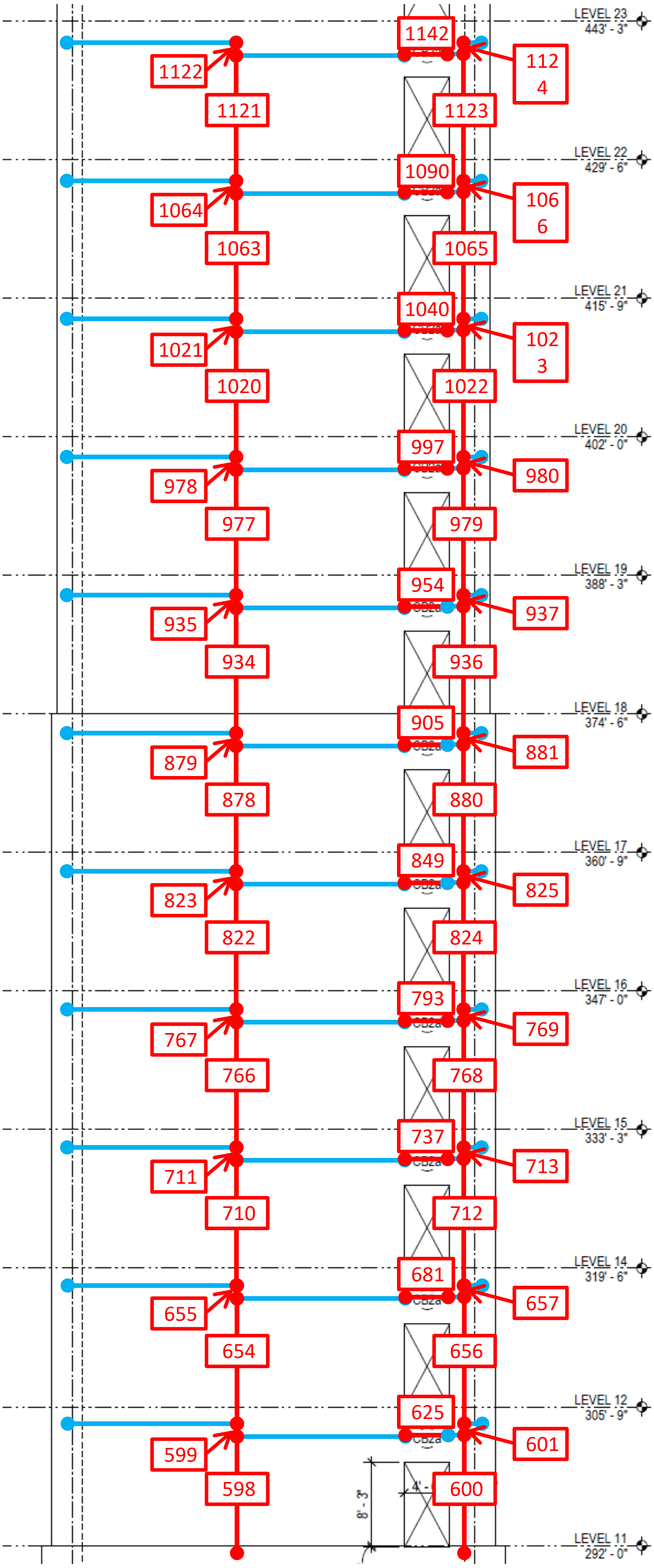
LEVEL 23
443' - 3"
1142
1122
112
4
1121
1123
LEVEL 22
429' - 6"
1090
1064
106
6
1063
1065
LEVEL 21
415' - 9"
1040
1021
102
3
1020
1022
LEVEL 20
402' - 0"
997
978
980
977
979
LEVEL 19
388' - 3"
954
935
937
934
936
LEVEL 18
374' - 6"
905
879
881
878
880
LEVEL 17
360' - 9"
849
823
825
822
824
LEVEL 16
347' - 0"
793
767
769
766
768
LEVEL 15
333' - 3"
737
711
713
710
712
LEVEL 14
319' - 6"
681
655
657
654
656
LEVEL 12
305' - 9"
625
599
601
598
600
8' - 3"
LEVEL 11
292' - 0"

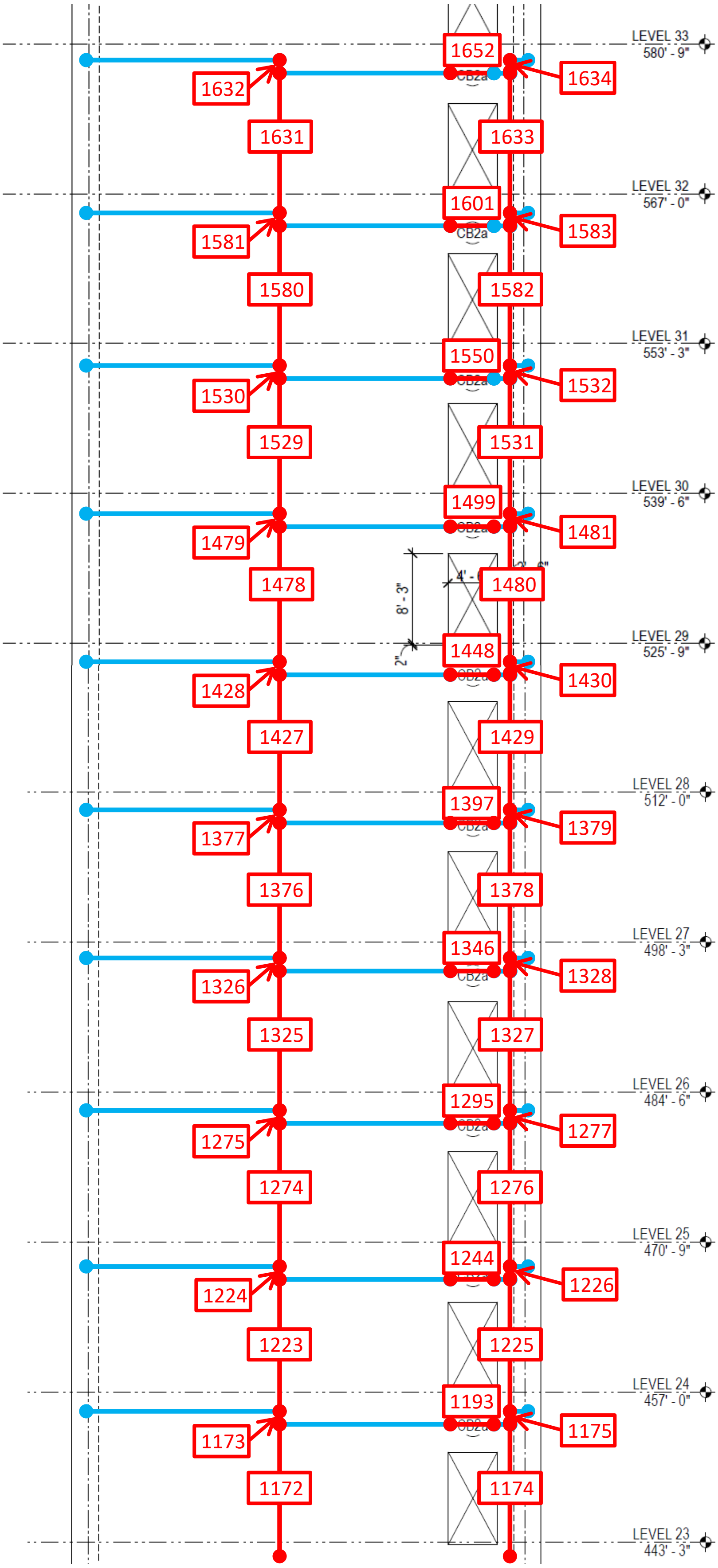

LEVEL 33
580' - 9"
1652
1632
1634
1631
1633
LEVEL 32
567' - 0"
1601
1581
1583
1580
1582
LEVEL 31
553' - 3"
1550
1530
1532
1529
1531
LEVEL 30
539' - 6"
1499
1479
1481
1478
1480
8' - 3"
LEVEL 29
525' - 9"
1448
1428
1430
1427
1429
LEVEL 28
512' - 0"
1397
1377
1379
1376
1378
LEVEL 27
498' - 3"
1346
1326
1328
1325
1327
LEVEL 26
484' - 6"
1295
1275
1277
1274
1276
LEVEL 25
470' - 9"
1244
1224
1226
1223
1225
LEVEL 24
457' - 0"
1193
1173
1175
1172
1174
LEVEL 23
443' - 3"

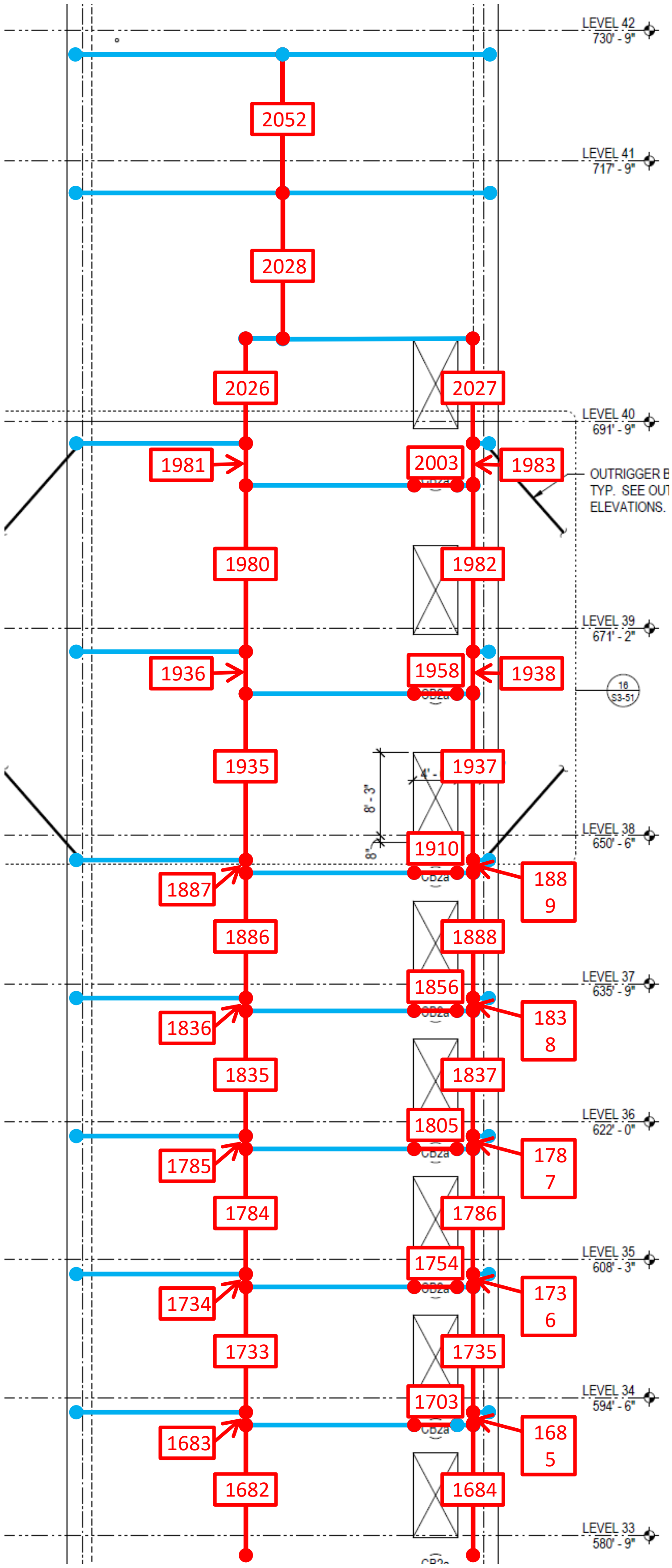
LEVEL 42
730' - 9"
2052
LEVEL 41
717' - 9"
2028
2026
2027
LEVEL 40
691' - 9"
1981
2003
1983
OUTRIGGER B
TYP. SEE OUT
ELEVATIONS.
1980
1982
LEVEL 39
671' - 2"
1936
1958
1938
1935
1937
8' - 3"
LEVEL 38
650' - 6"
1910
1887
188
9
1886
1888
LEVEL 37
635' - 9"
1856
1836
183
8
1835
1837
LEVEL 36
622' - 0"
1805
1785
178
7
1784
1786
LEVEL 35
608' - 3"
1754
1734
173
6
1733
1735
LEVEL 34
594' - 6"
1703
1683
168
5
1682
1684
LEVEL 33
580' - 9"

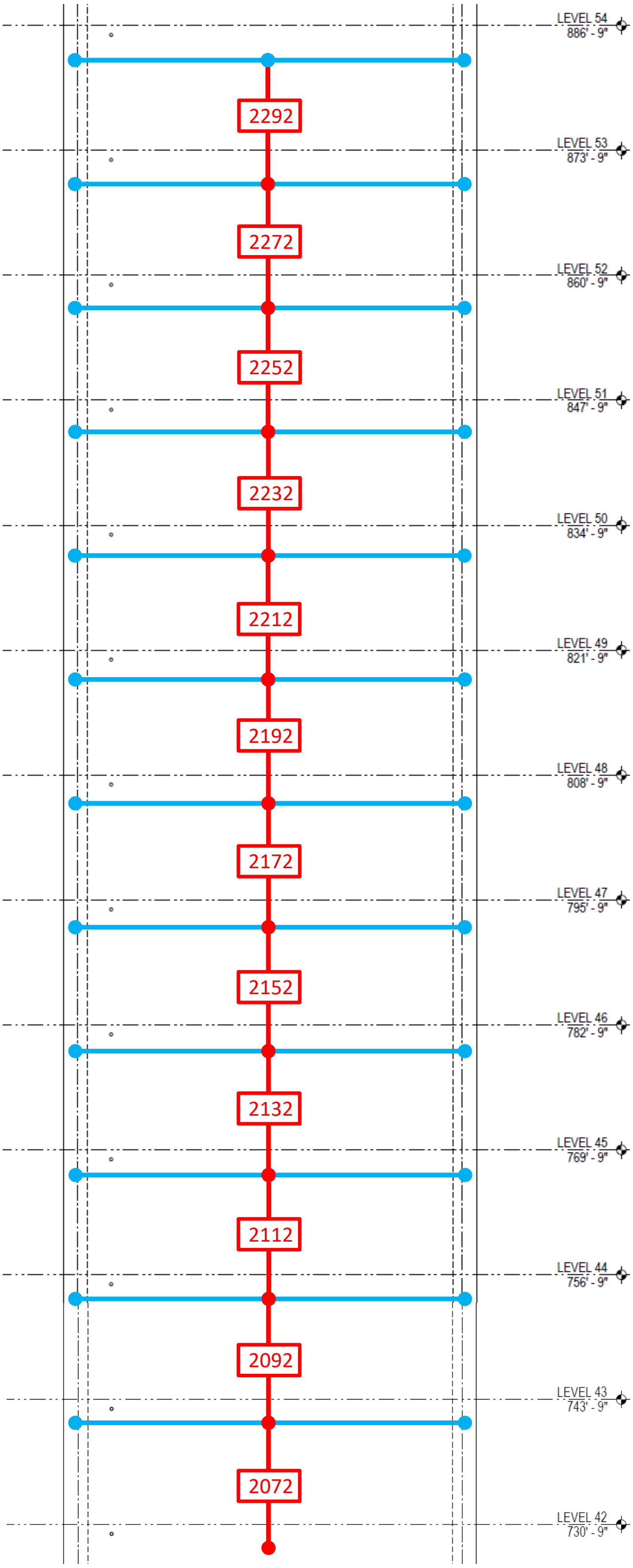
LEVEL 54
886' - 9"
2292
LEVEL 53
873' - 9"
2272
LEVEL 52
860' - 9"
2252
LEVEL 51
847' - 9"
2232
LEVEL 50
834' - 9"
2212
LEVEL 49
821' - 9"
2192
LEVEL 48
808' - 9"
2172
LEVEL 47
795' - 9"
2152
LEVEL 46
782' - 9"
2132
LEVEL 45
769' - 9"
2112
LEVEL 44
756' - 9"
2092
LEVEL 43
743' - 9"
2072
LEVEL 42
730' - 9"

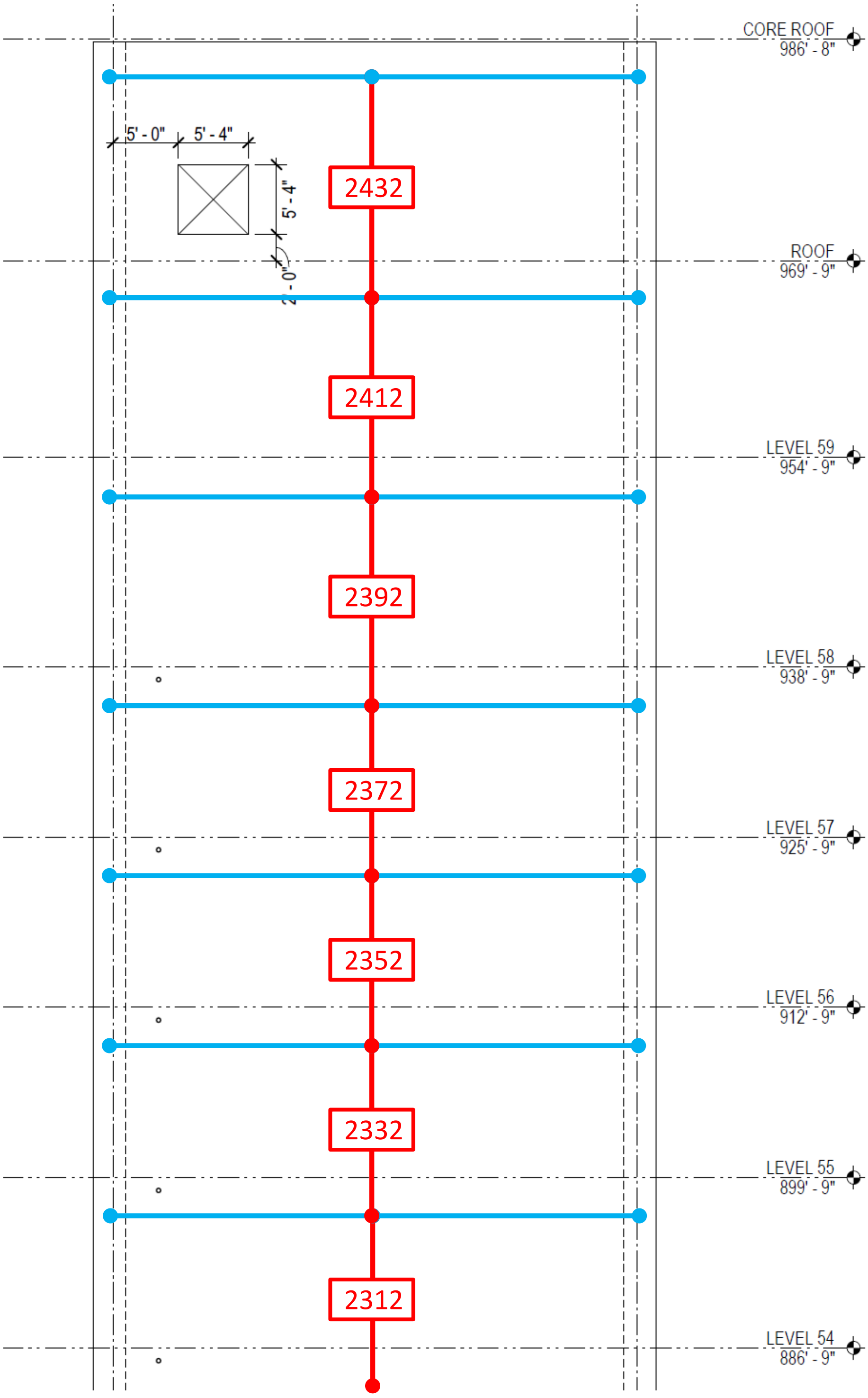

CORE ROOF
986' - 8"
ROOF
969' - 9"
LEVEL 59
954' - 9"
LEVEL 58
938' - 9"
LEVEL 57
925' - 9"
LEVEL 56
912' - 9"
LEVEL 55
899' - 9"
LEVEL 54
886' - 9"
5' - 0"
5' - 4"
5' - 4"
2' - 0"
2432
2412
2392
2372
2352
2332
2312

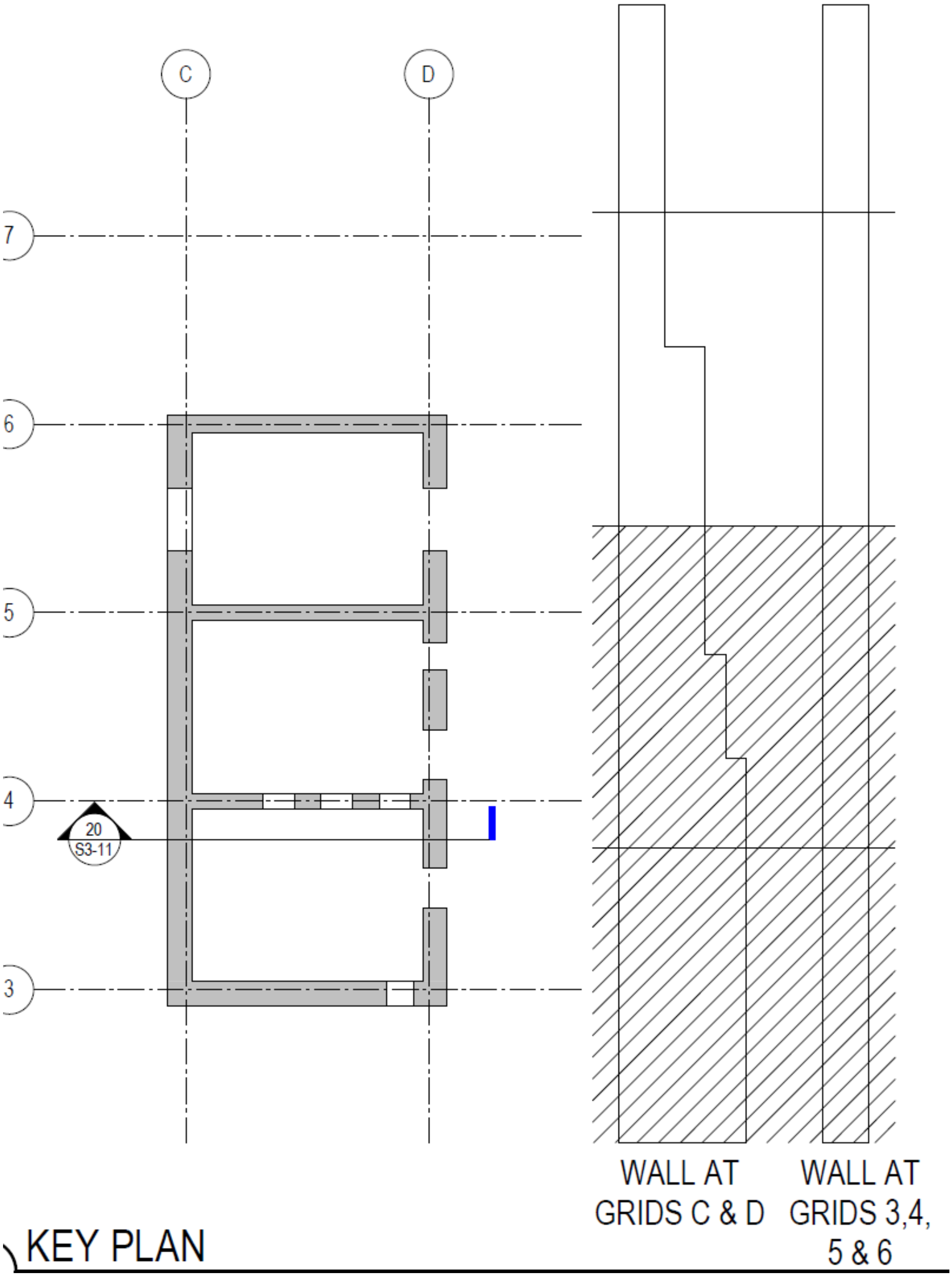
C
D
7
6
5
4
3
20
S3-11
WALL AT
GRIDS C & D
WALL AT
GRIDS 3,4,
5 & 6
KEY PLAN

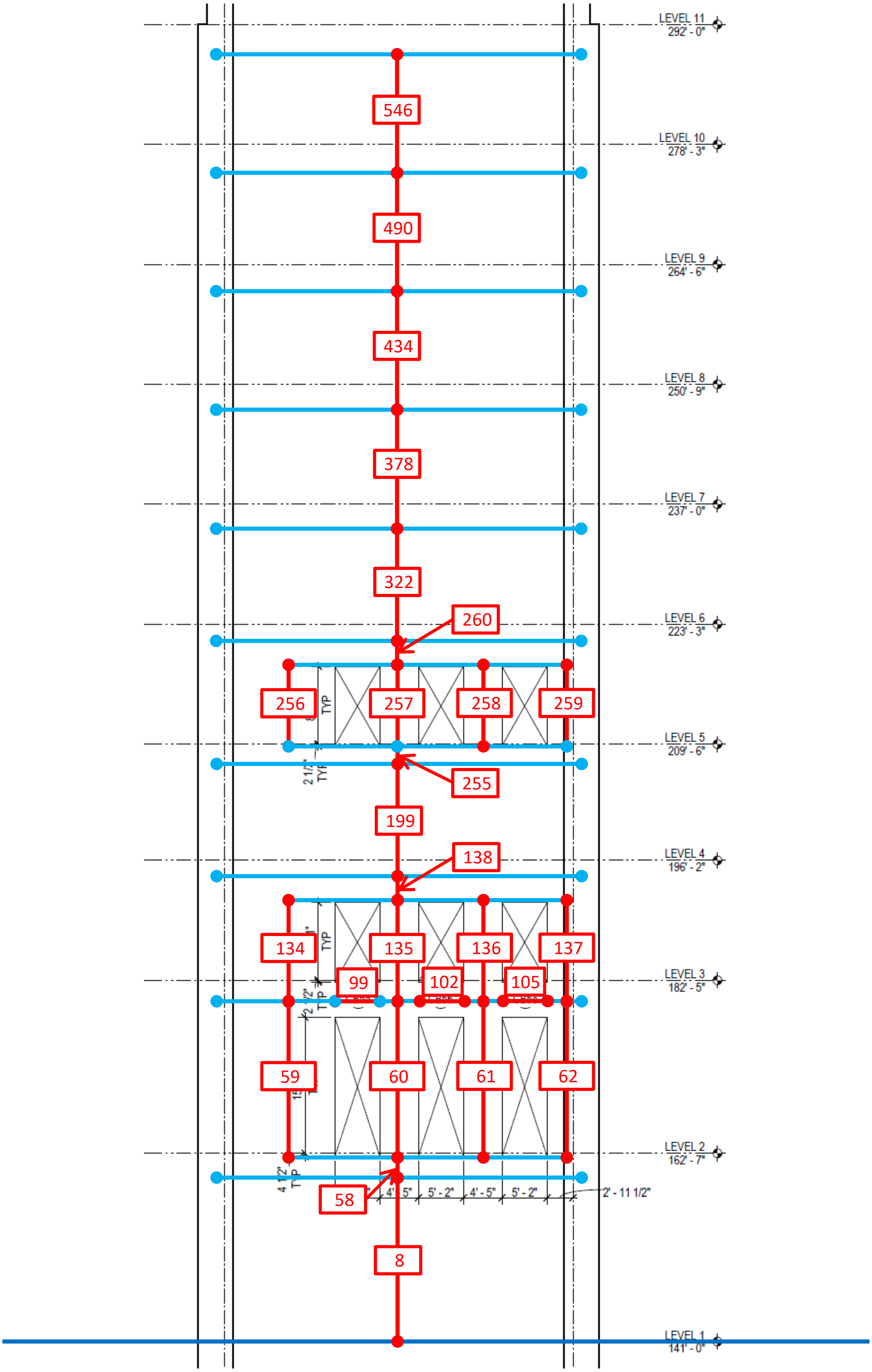

LEVEL 11
292' - 0"
LEVEL 10
278' - 3"
LEVEL 9
264' - 6"
LEVEL 8
250' - 9"
LEVEL 7
237' - 0"
LEVEL 6
223' - 3"
LEVEL 5
209' - 6"
LEVEL 4
196' - 2"
LEVEL 3
182' - 5"
LEVEL 2
162' - 7"
LEVEL 1
141' - 0"
546
490
434
378
322
260
256
257
258
259
255
199
138
134
135
136
137
99
102
105
59
60
61
62
58
8
4' 5"
5' - 2"
4' - 5"
5' - 2"
2' - 11 1/2"
TYP

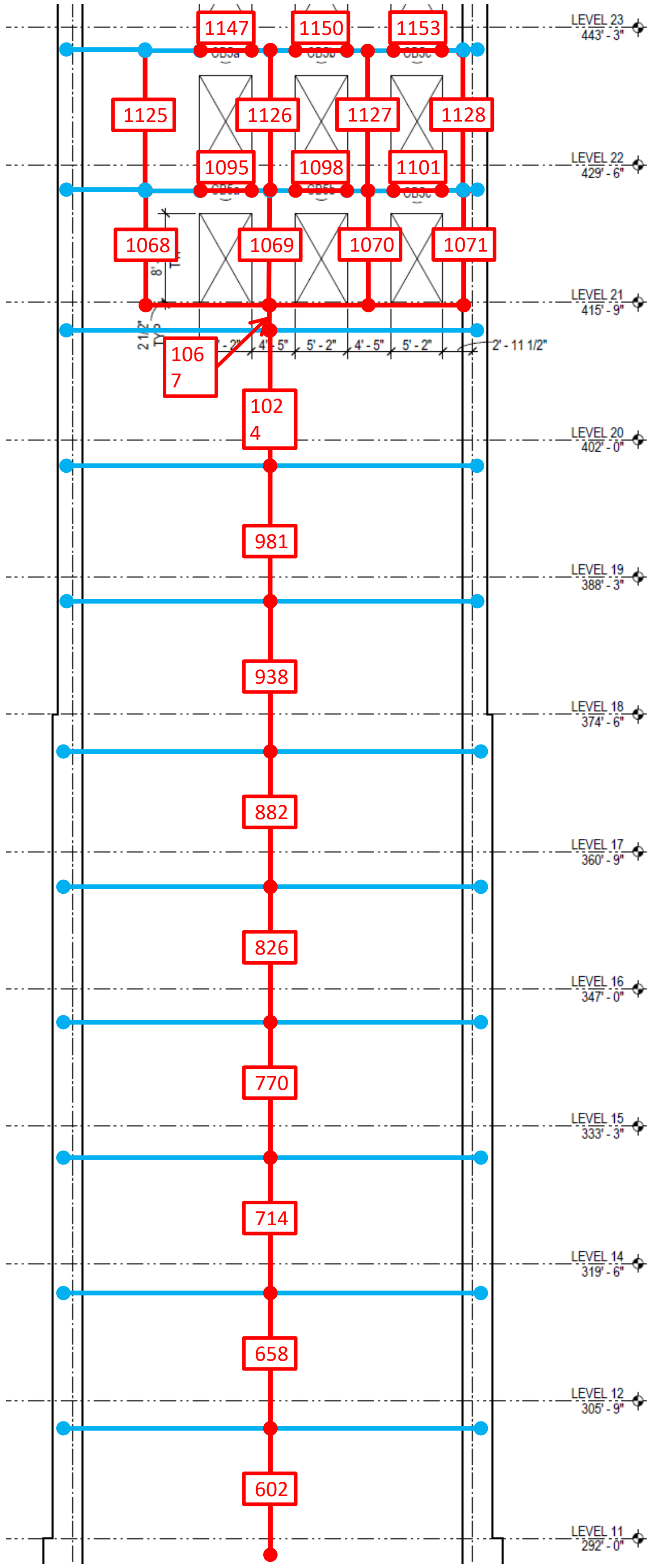
1147
1150
1153
1125
1126
1127
1128
1095
1098
1101
1068
1069
1070
1071
106
7
102
4
981
938
882
826
770
714
658
602
LEVEL 23
443' - 3"
LEVEL 22
429' - 6"
LEVEL 21
415' - 9"
2' - 11 1/2"
LEVEL 20
402' - 0"
LEVEL 19
388' - 3"
LEVEL 18
374' - 6"
LEVEL 17
360' - 9"
LEVEL 16
347' - 0"
LEVEL 15
333' - 3"
LEVEL 14
319' - 6"
LEVEL 12
305' - 9"
LEVEL 11
292' - 0"

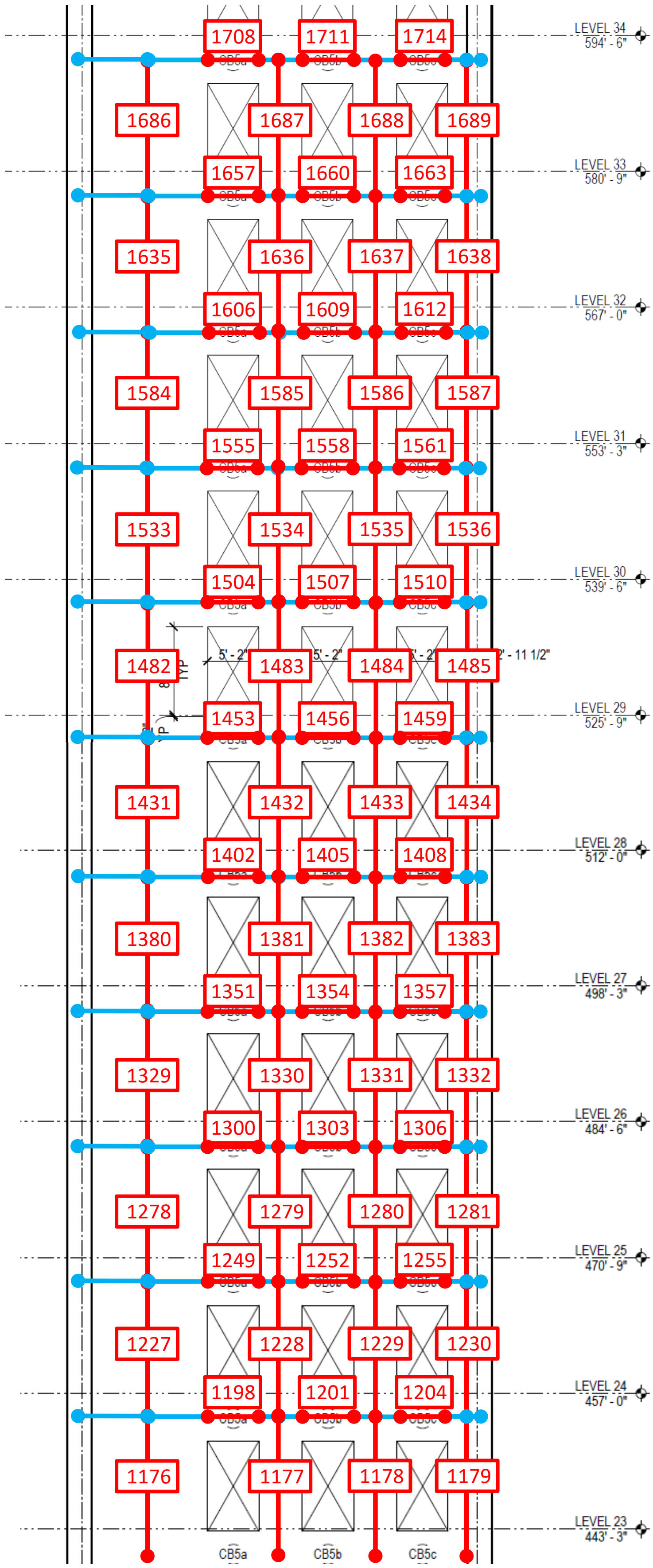
1708 1711 1714
LEVEL 34
594' - 6"
1686 1687 1688 1689
1657 1660 1663
LEVEL 33
580' - 9"
1635 1636 1637 1638
1606 1609 1612
LEVEL 32
567' - 0"
1584 1585 1586 1587
1555 1558 1561
LEVEL 31
553' - 3"
1533 1534 1535 1536
1504 1507 1510
LEVEL 30
539' - 6"
5' - 2" 5' - 2"
2' - 11 1/2"
1482 1483 1484 1485
1453 1456 1459
LEVEL 29
525' - 9"
1431 1432 1433 1434
1402 1405 1408
LEVEL 28
512' - 0"
1380 1381 1382 1383
1351 1354 1357
LEVEL 27
498' - 3"
1329 1330 1331 1332
1300 1303 1306
LEVEL 26
484' - 6"
1278 1279 1280 1281
1249 1252 1255
LEVEL 25
470' - 9"
1227 1228 1229 1230
1198 1201 1204
LEVEL 24
457' - 0"
1176 1177 1178 1179
LEVEL 23
443' - 3"
CB5a CB5b CB5c

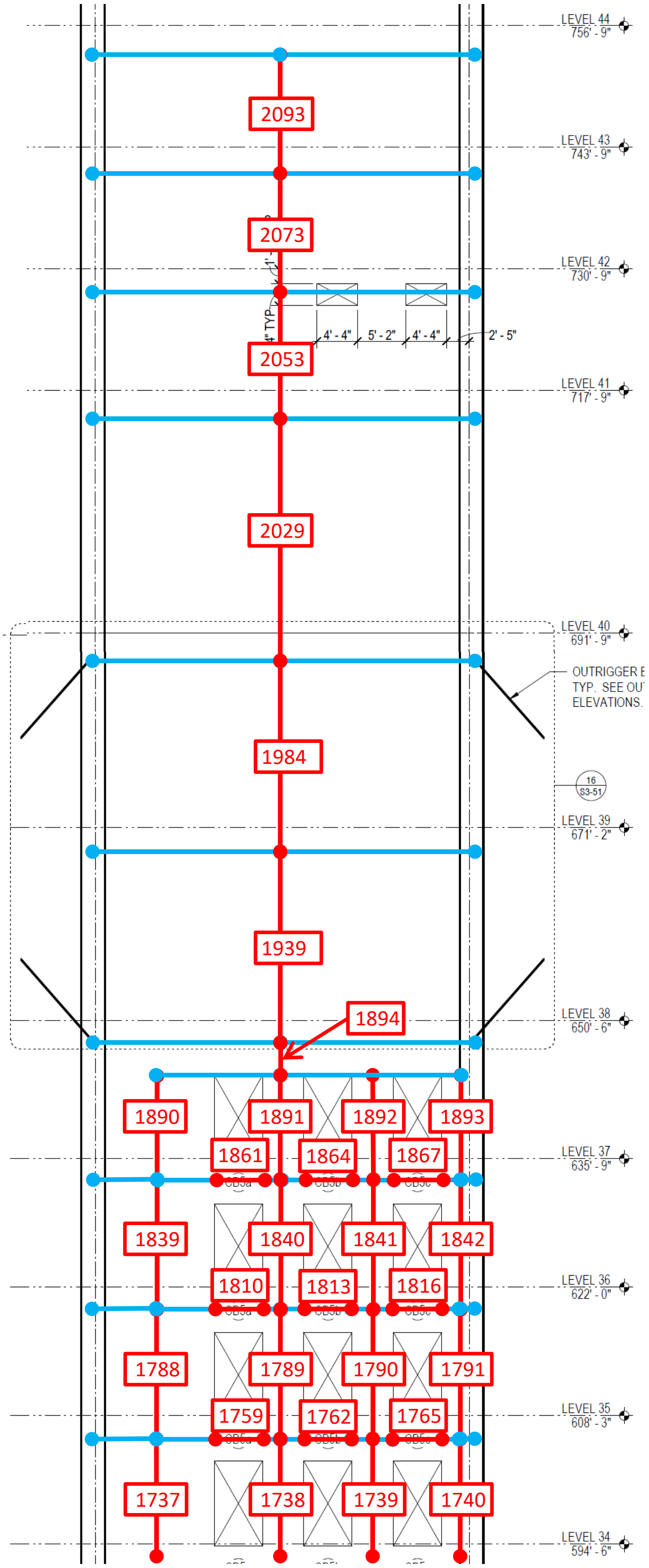
LEVEL 44
756' - 9"
LEVEL 43
743' - 9"
LEVEL 42
730' - 9"
LEVEL 41
717' - 9"
LEVEL 40
691' - 9"
LEVEL 39
671' - 2"
LEVEL 38
650' - 6"
LEVEL 37
635' - 9"
LEVEL 36
622' - 0"
LEVEL 35
608' - 3"
LEVEL 34
594' - 6"
2093
2073
2053
2029
1984
1939
1894
1890
1891
1892
1893
1861
1864
1867
1839
1840
1841
1842
1810
1813
1816
1788
1789
1790
1791
1759
1762
1765
1737
1738
1739
1740
4' - 4"
5' - 2"
4' - 4"
2' - 5"
OUTRIGGER E
TYP. SEE OU
ELEVATIONS.
16
S3-51

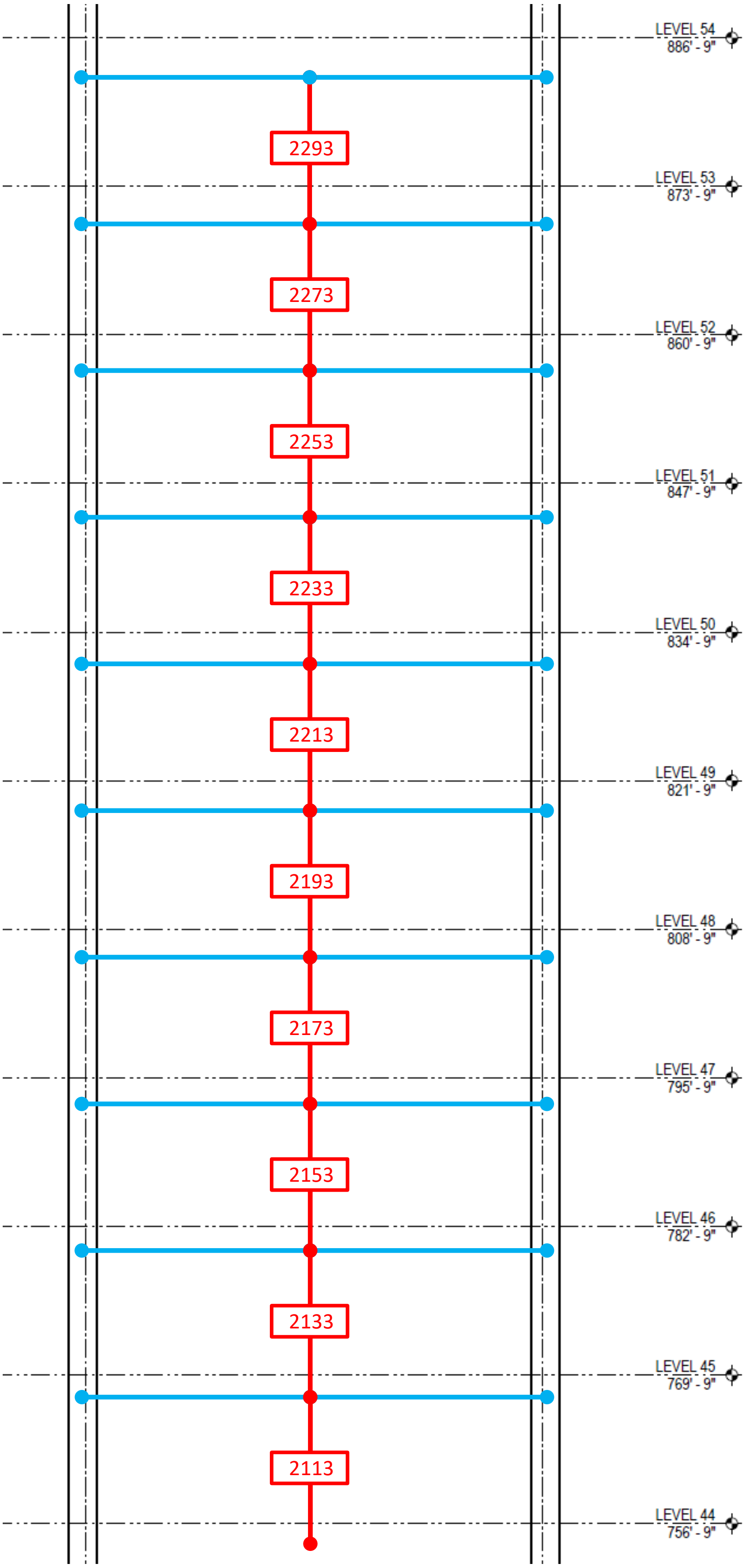

LEVEL 54
886' - 9"
2293
LEVEL 53
873' - 9"
2273
LEVEL 52
860' - 9"
2253
LEVEL 51
847' - 9"
2233
LEVEL 50
834' - 9"
2213
LEVEL 49
821' - 9"
2193
LEVEL 48
808' - 9"
2173
LEVEL 47
795' - 9"
2153
LEVEL 46
782' - 9"
2133
LEVEL 45
769' - 9"
2113
LEVEL 44
756' - 9"

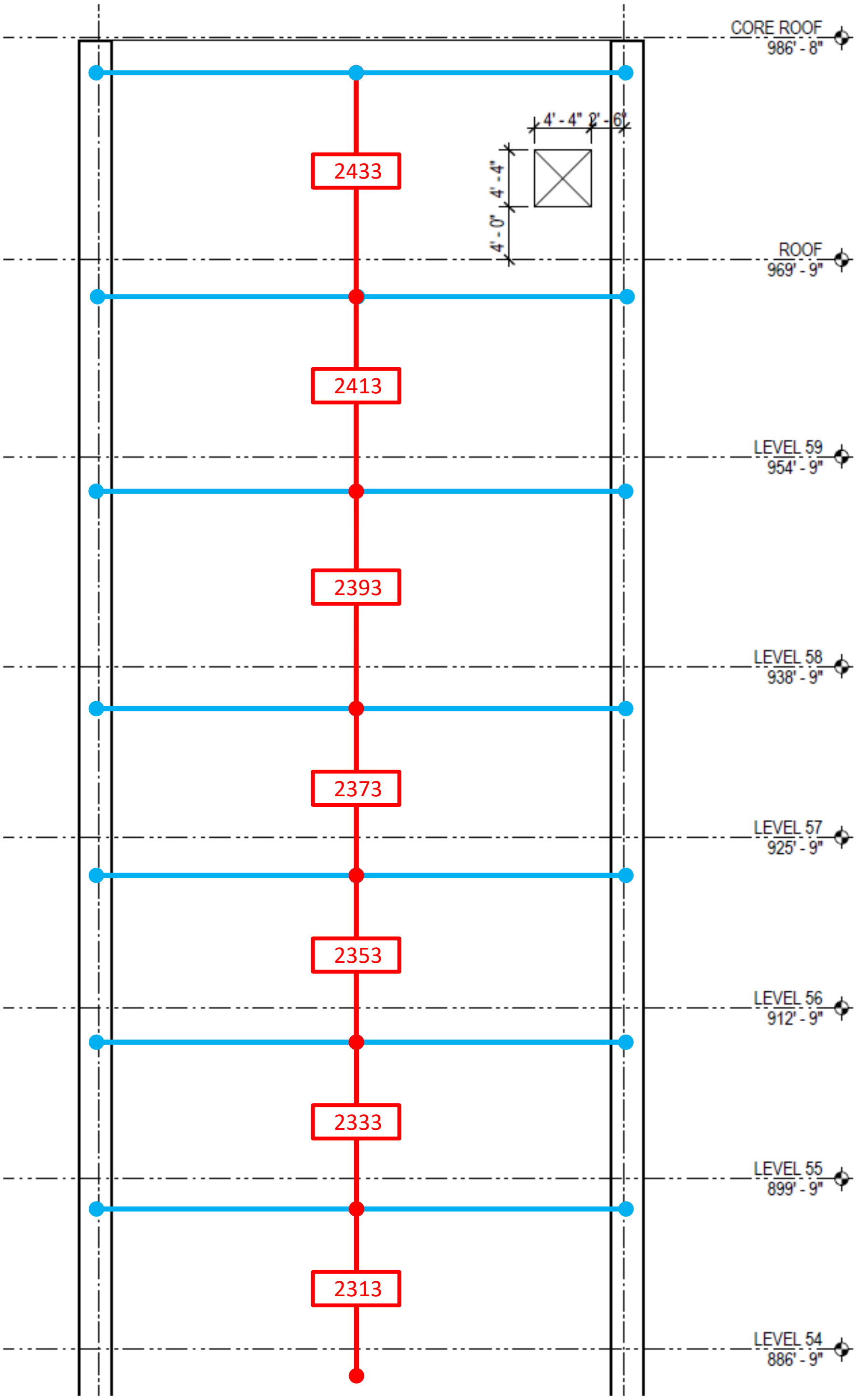

CORE ROOF
986' - 8"
4' - 4"
2' - 6"
4' - 4"
4' - 0"
2433
ROOF
969' - 9"
2413
LEVEL 59
954' - 9"
2393
LEVEL 58
938' - 9"
2373
LEVEL 57
925' - 9"
2353
LEVEL 56
912' - 9"
2333
LEVEL 55
899' - 9"
2313
LEVEL 54
886' - 9"

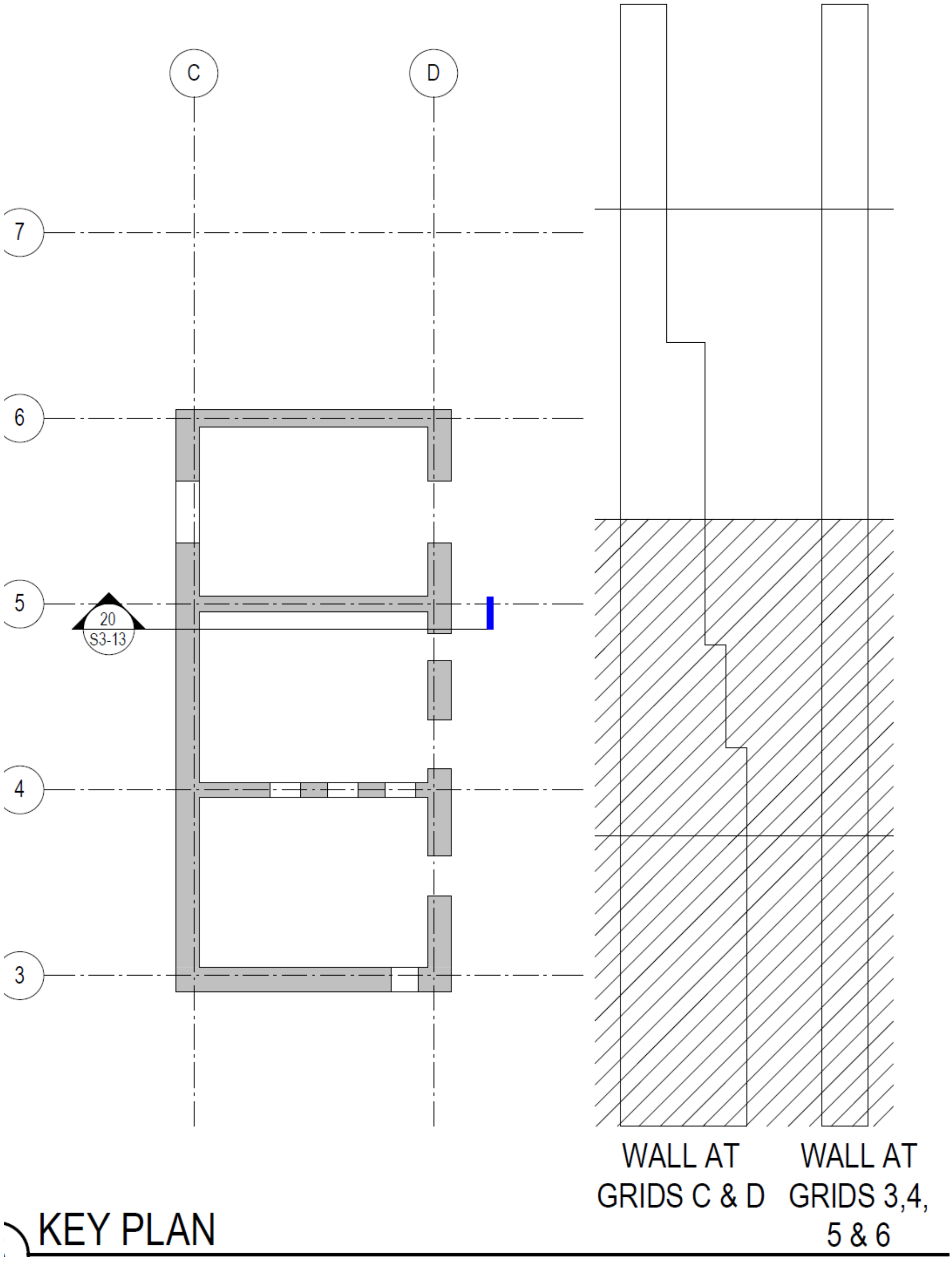
C
D
7
6
5
4
3
20
S3-13
WALL AT
GRIDS C & D
WALL AT
GRIDS 3,4,
5 & 6
KEY PLAN

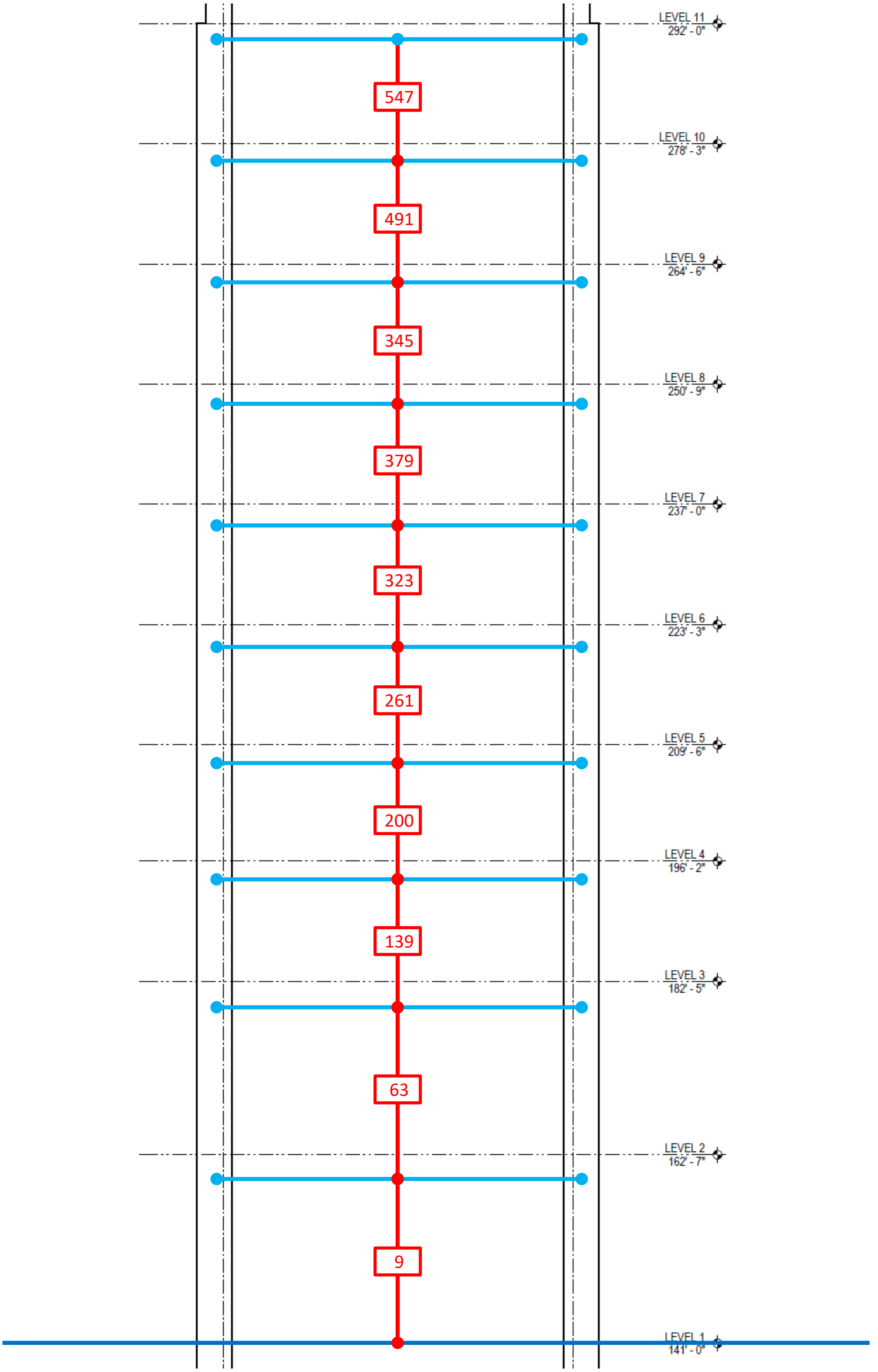
LEVEL 11
292' - 0"
547
LEVEL 10
278' - 3"
491
LEVEL 9
264' - 6"
345
LEVEL 8
250' - 9"
379
LEVEL 7
237' - 0"
323
LEVEL 6
223' - 3"
261
LEVEL 5
209' - 6"
200
LEVEL 4
196' - 2"
139
LEVEL 3
182' - 5"
63
LEVEL 2
162' - 7"
9
LEVEL 1
141' - 0"

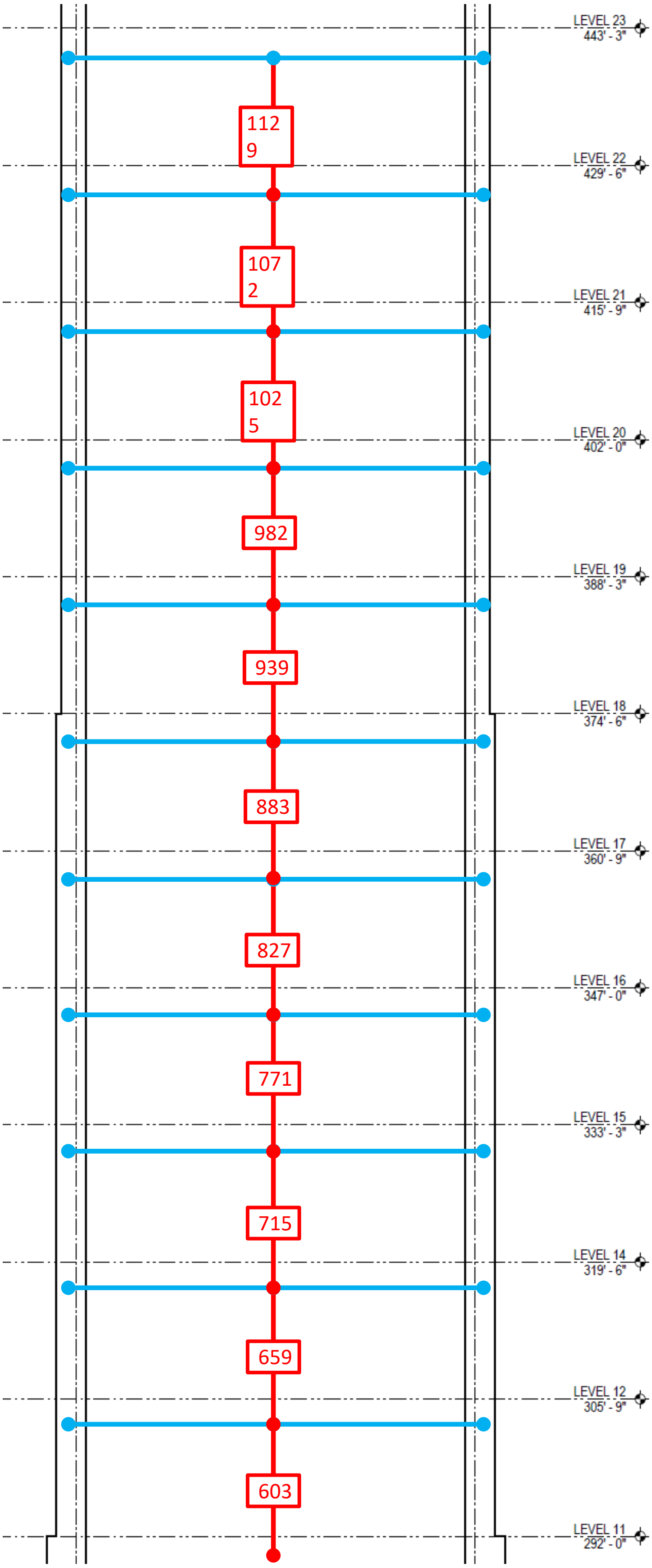
LEVEL 23
443' - 3"
112
9
LEVEL 22
429' - 6"
107
2
LEVEL 21
415' - 9"
102
5
LEVEL 20
402' - 0"
982
LEVEL 19
388' - 3"
939
LEVEL 18
374' - 6"
883
LEVEL 17
360' - 9"
827
LEVEL 16
347' - 0"
771
LEVEL 15
333' - 3"
715
LEVEL 14
319' - 6"
659
LEVEL 12
305' - 9"
603
LEVEL 11
292' - 0"

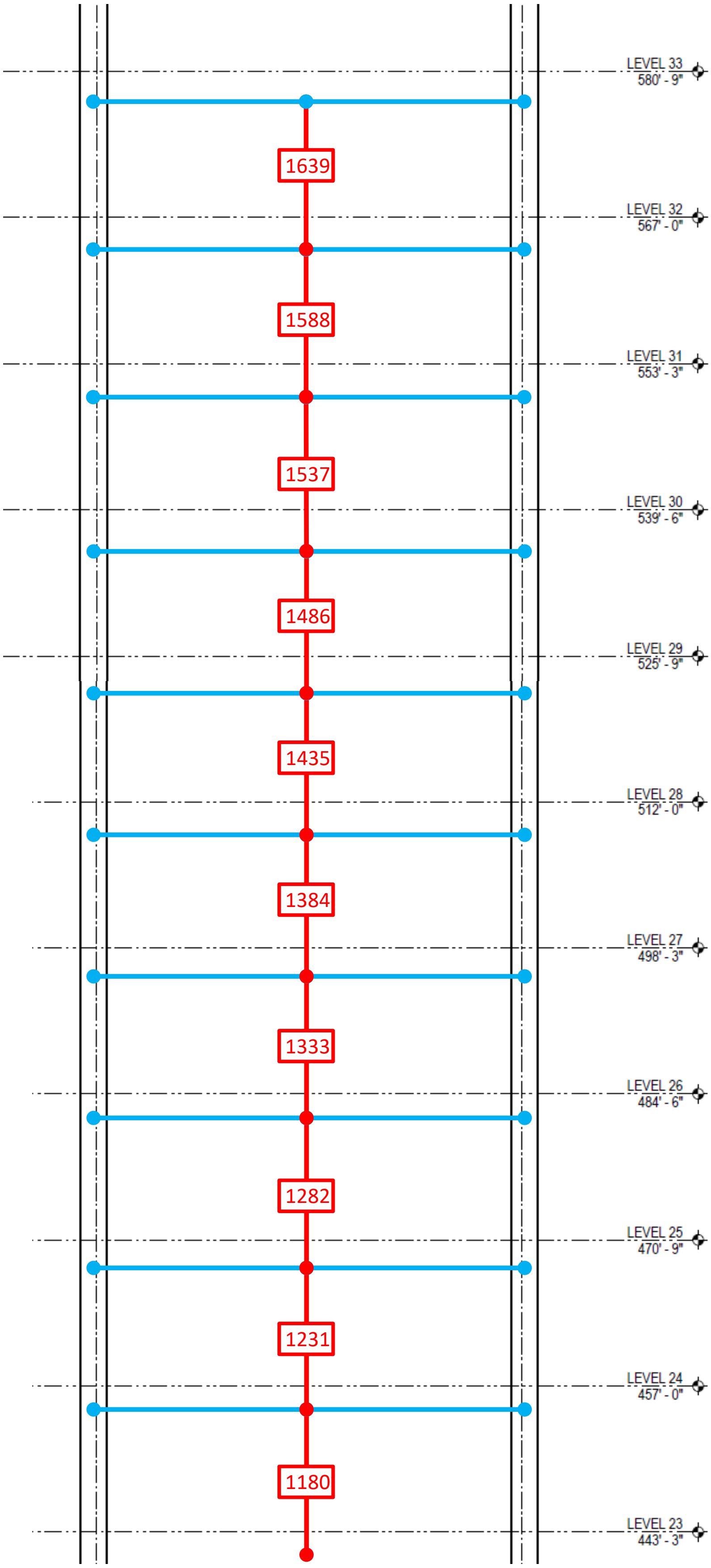
LEVEL 33
580' - 9"
1639
LEVEL 32
567' - 0"
1588
LEVEL 31
553' - 3"
1537
LEVEL 30
539' - 6"
1486
LEVEL 29
525' - 9"
1435
LEVEL 28
512' - 0"
1384
LEVEL 27
498' - 3"
1333
LEVEL 26
484' - 6"
1282
LEVEL 25
470' - 9"
1231
LEVEL 24
457' - 0"
1180
LEVEL 23
443' - 3"

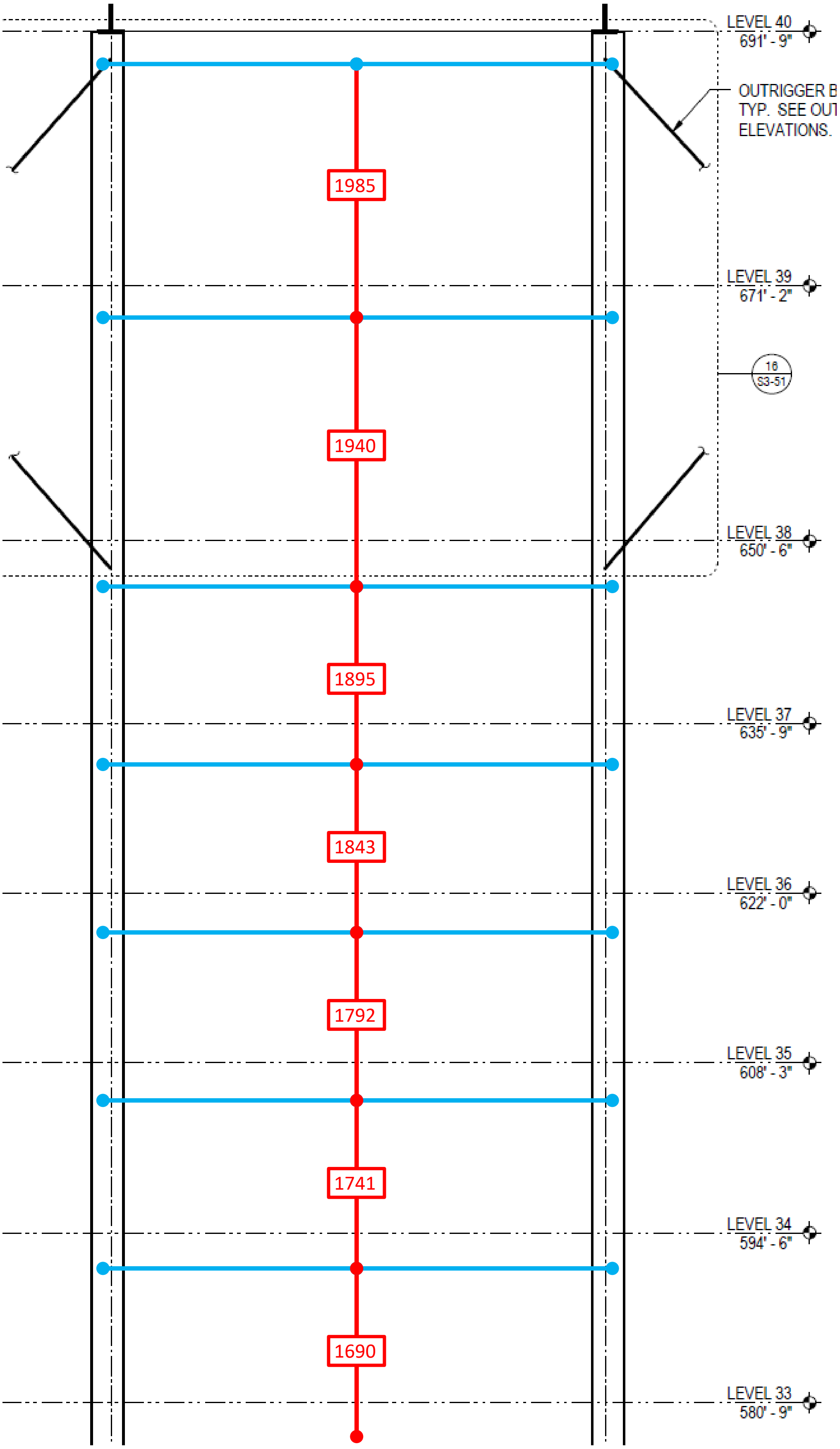
LEVEL 40
691' - 9"
OUTRIGGER B
TYP. SEE OUT
ELEVATIONS.
1985
LEVEL 39
671' - 2"
16
S3-51
1940
LEVEL 38
650' - 6"
1895
LEVEL 37
635' - 9"
1843
LEVEL 36
622' - 0"
1792
LEVEL 35
608' - 3"
1741
LEVEL 34
594' - 6"
1690
LEVEL 33
580' - 9"

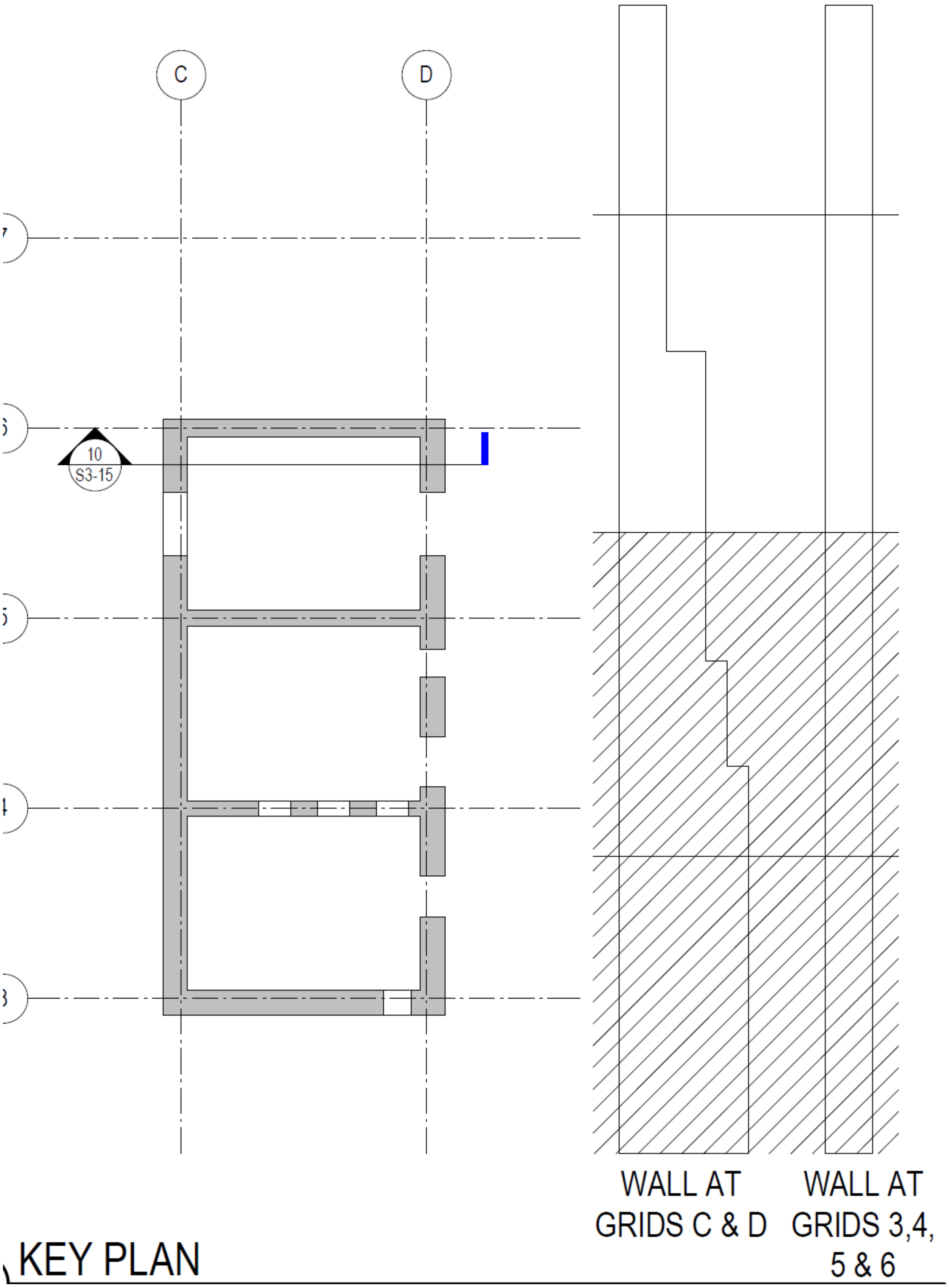
C
D
7
6
5
4
3
10
S3-15
WALL AT
GRIDS C & D
WALL AT
GRIDS 3,4,
5 & 6
KEY PLAN

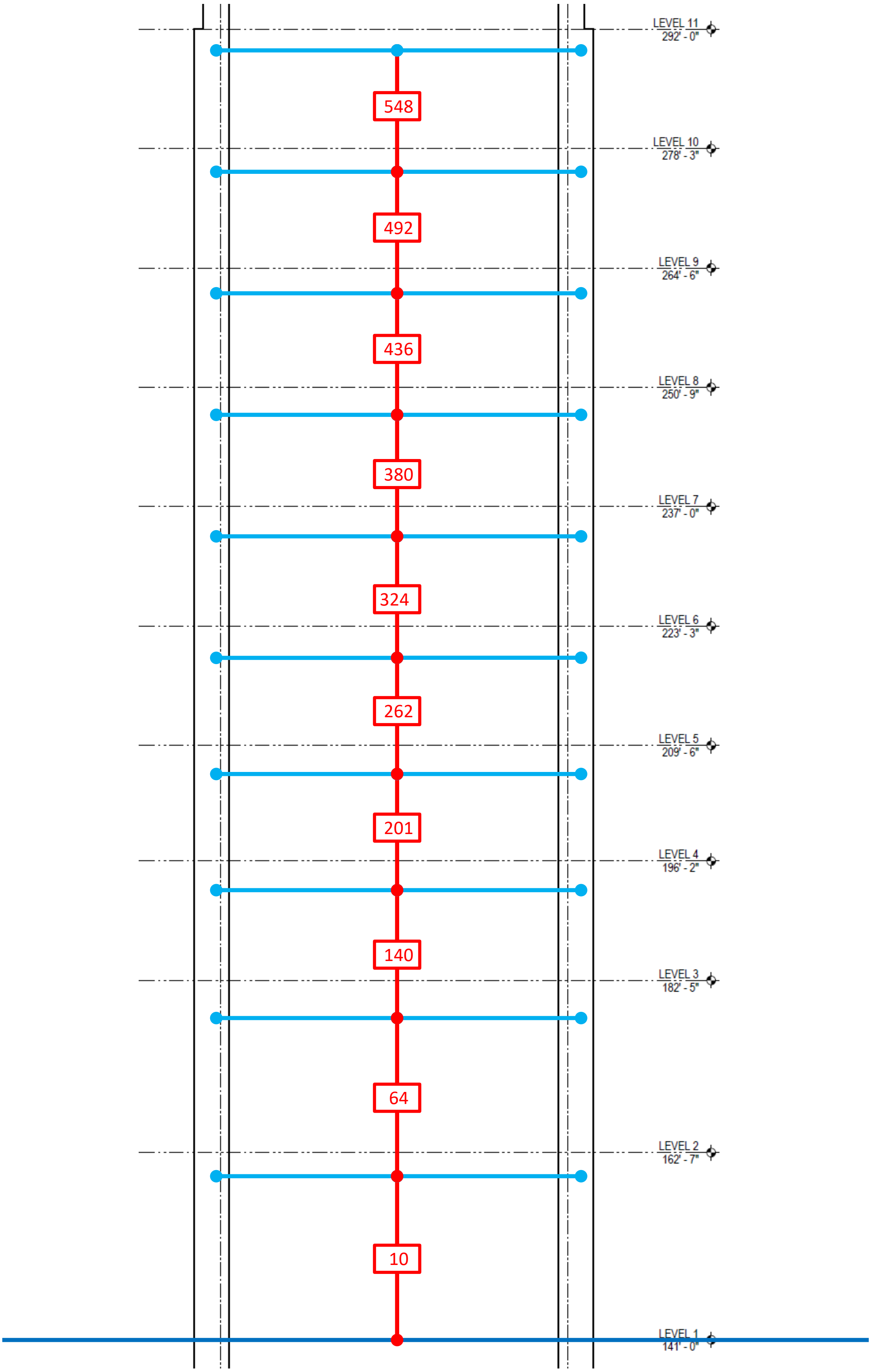
LEVEL 11
292' - 0"
548
LEVEL 10
278' - 3"
492
LEVEL 9
264' - 6"
436
LEVEL 8
250' - 9"
380
LEVEL 7
237' - 0"
324
LEVEL 6
223' - 3"
262
LEVEL 5
209' - 6"
201
LEVEL 4
196' - 2"
140
LEVEL 3
182' - 5"
64
LEVEL 2
162' - 7"
10
LEVEL 1
141' - 0"

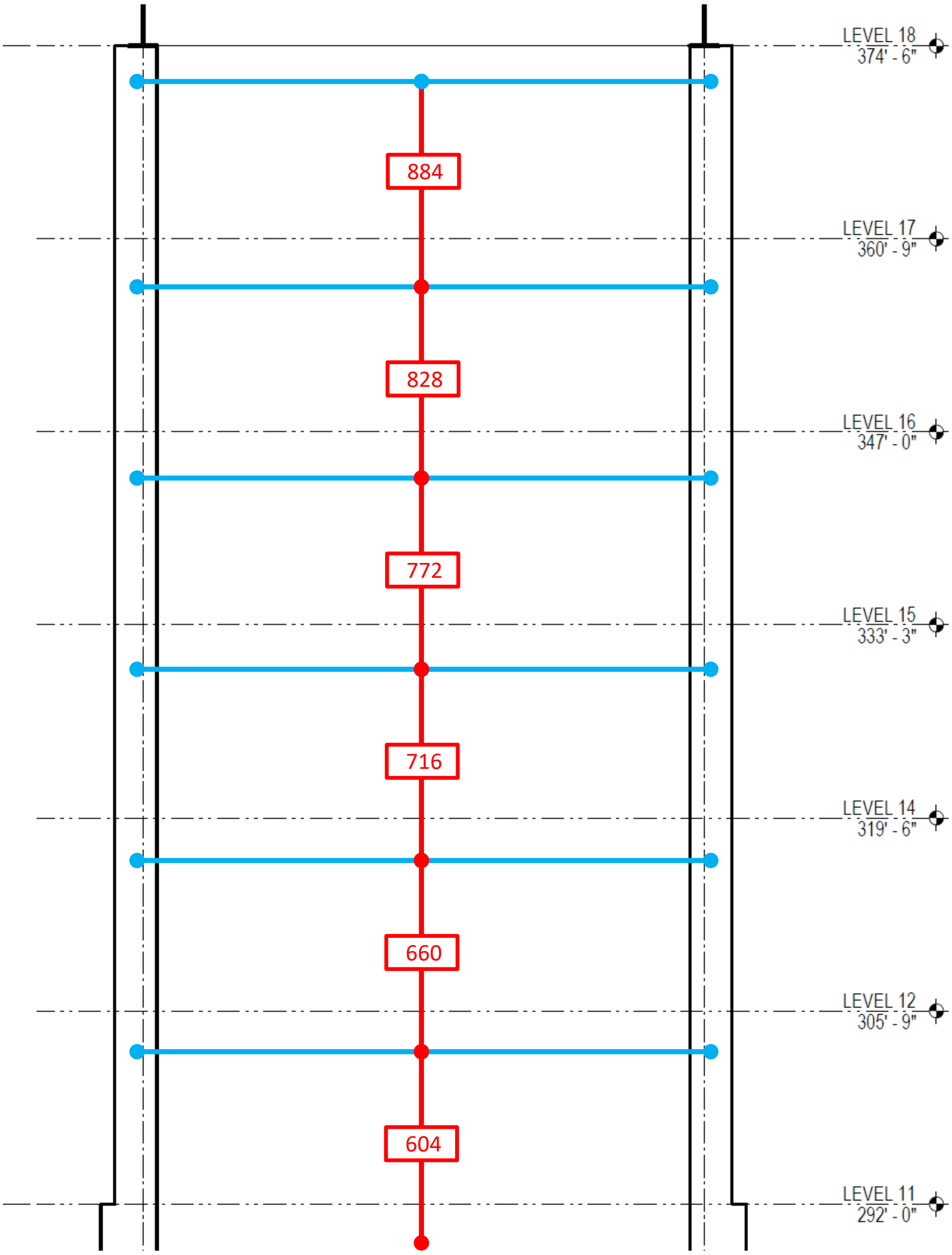
LEVEL 18
374' - 6"
884
LEVEL 17
360' - 9"
828
LEVEL 16
347' - 0"
772
LEVEL 15
333' - 3"
716
LEVEL 14
319' - 6"
660
LEVEL 12
305' - 9"
604
LEVEL 11
292' - 0"

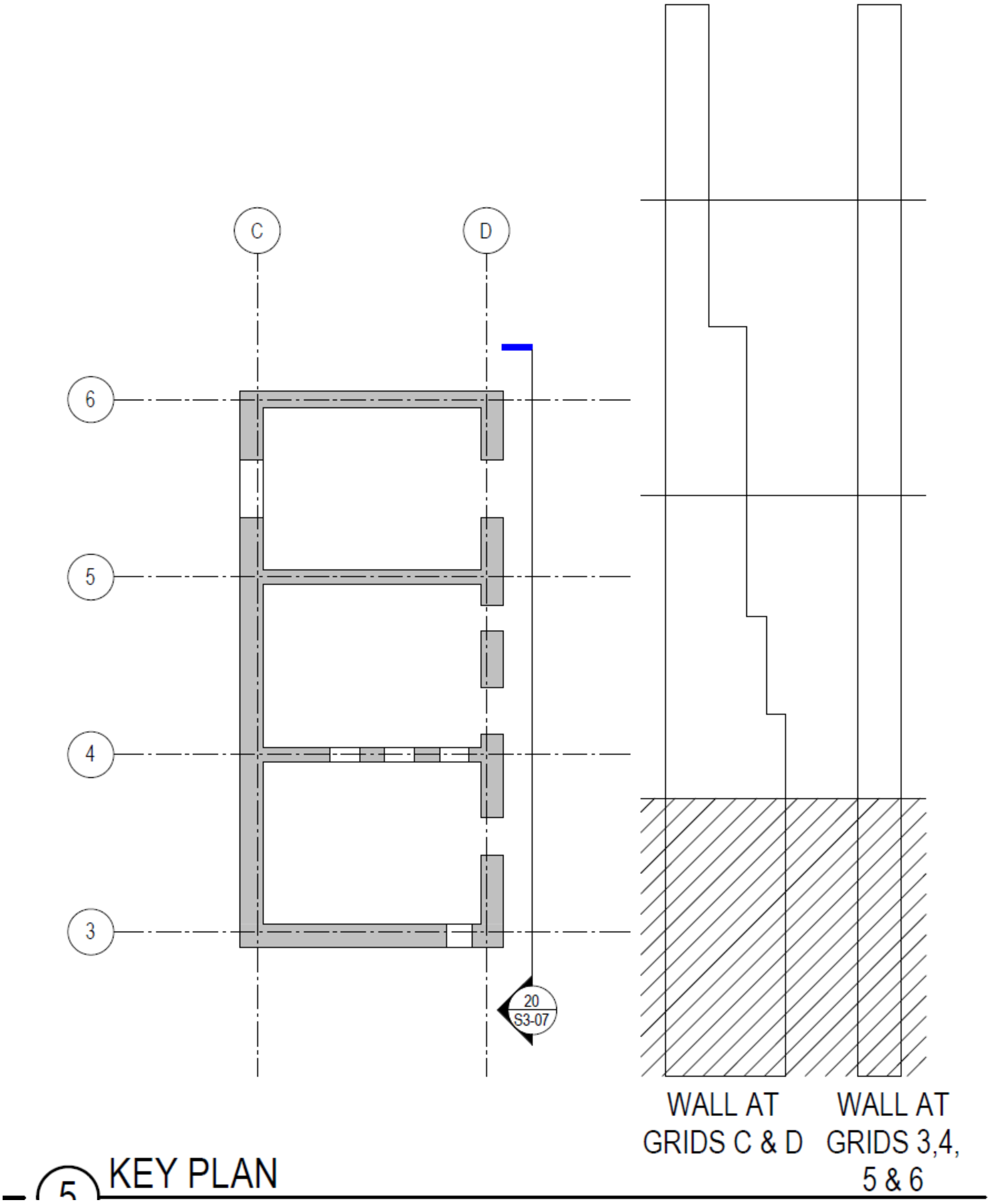
C
D
6
5
4
3
20
S3-07
WALL AT GRIDS C & D
WALL AT GRIDS 3,4, 5 & 6
5
KEY PLAN

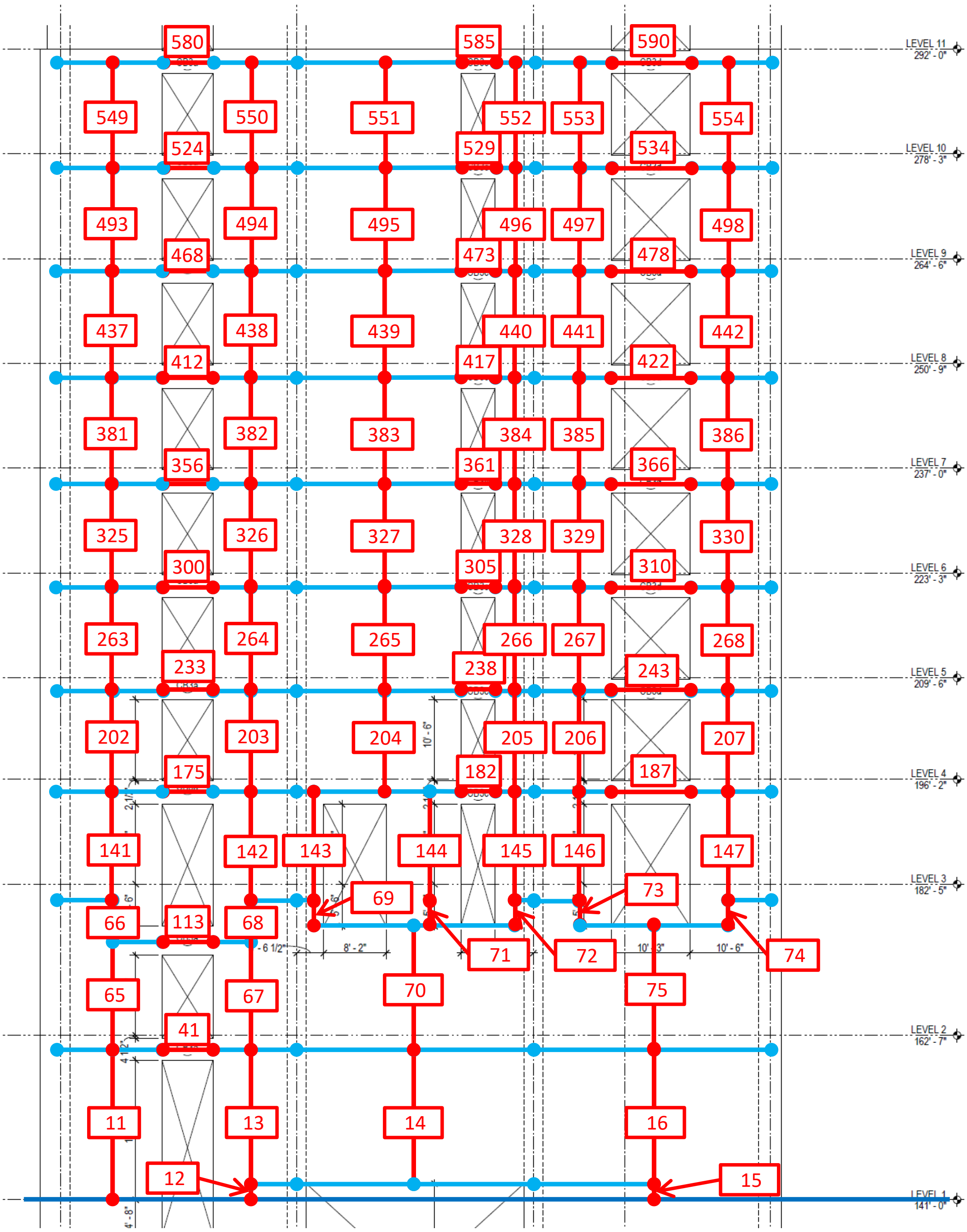
580
585
590
LEVEL 11 292' - 0"
549
550
551
552
553
554
524
529
534
LEVEL 10 278' - 3"
493
494
495
496
497
498
468
473
478
LEVEL 9 264' - 6"
437
438
439
440
441
442
412
417
422
LEVEL 8 250' - 9"
381
382
383
384
385
386
356
361
366
LEVEL 7 237' - 0"
325
326
327
328
329
330
300
305
310
LEVEL 6 223' - 3"
263
264
265
266
267
268
233
238
243
LEVEL 5 209' - 6"
202
203
204
205
206
207
175
182
187
LEVEL 4 196' - 2"
141
142
143
144
145
146
147
69
73
LEVEL 3 182' - 5"
66
113
68
71
72
74
65
67
70
75
41
LEVEL 2 162' - 7"
11
13
14
16
12
15
LEVEL 1 141' - 0"

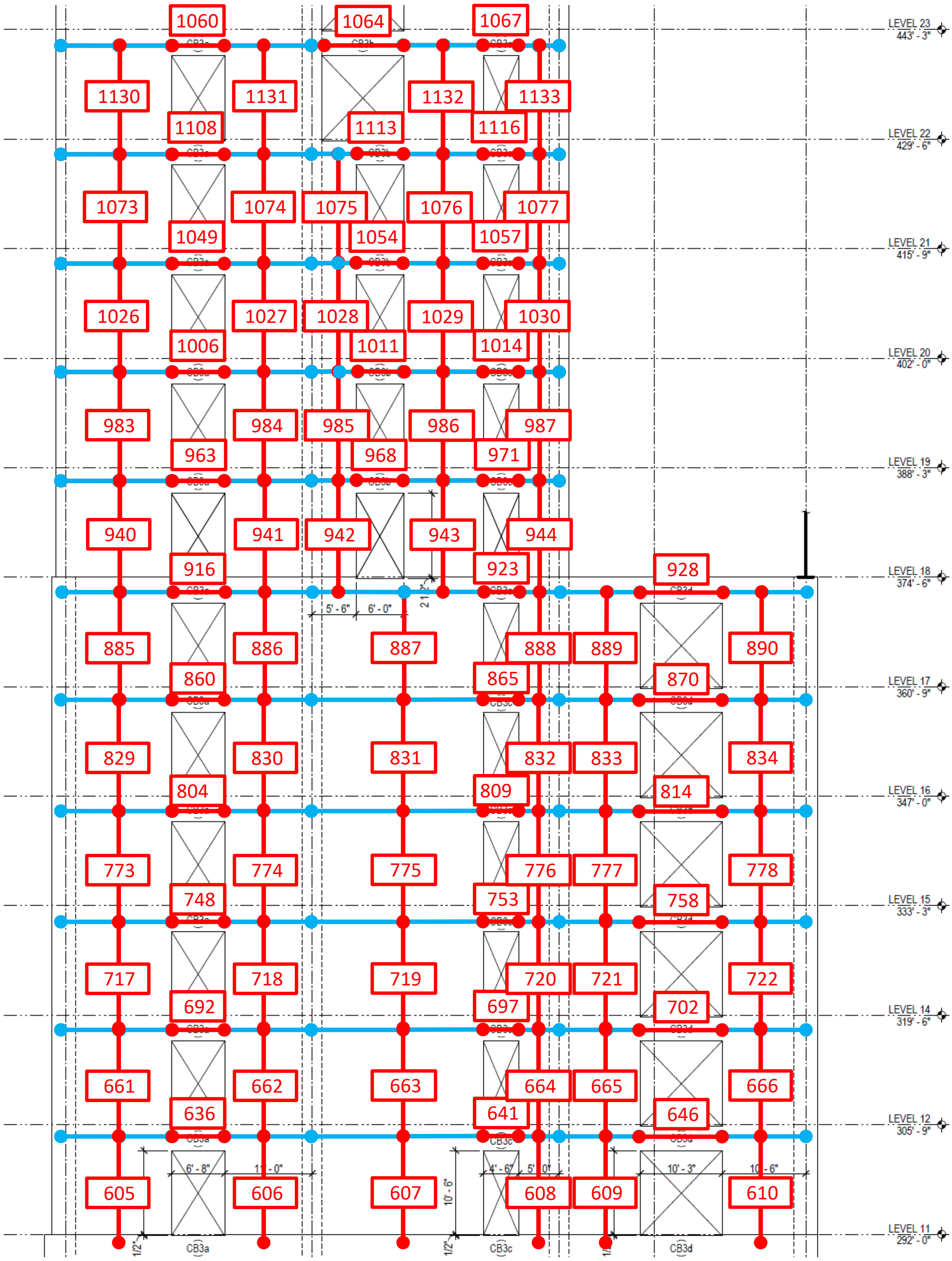
1060
1064
1067
1130
1131
1132
1133
1108
1113
1116
1073
1074
1075
1076
1077
1049
1054
1057
1026
1027
1028
1029
1030
1006
1011
1014
983
984
985
986
987
963
968
971
940
941
942
943
944
916
923
928
885
886
887
888
889
890
860
865
870
829
830
831
832
833
834
804
809
814
773
774
775
776
777
778
748
753
758
717
718
719
720
721
722
692
697
702
661
662
663
664
665
666
636
641
646
605
606
607
608
609
610
LEVEL 23
443' - 3"
LEVEL 22
429' - 6"
LEVEL 21
415' - 9"
LEVEL 20
402' - 0"
LEVEL 19
388' - 3"
LEVEL 18
374' - 6"
LEVEL 17
360' - 9"
LEVEL 16
347' - 0"
LEVEL 15
333' - 3"
LEVEL 14
319' - 6"
LEVEL 12
305' - 9"
LEVEL 11
292' - 0"
5' - 6"
6' - 0"
6' - 8"
10' - 6"
10' - 3"
CB3a
CB3c
CB3d

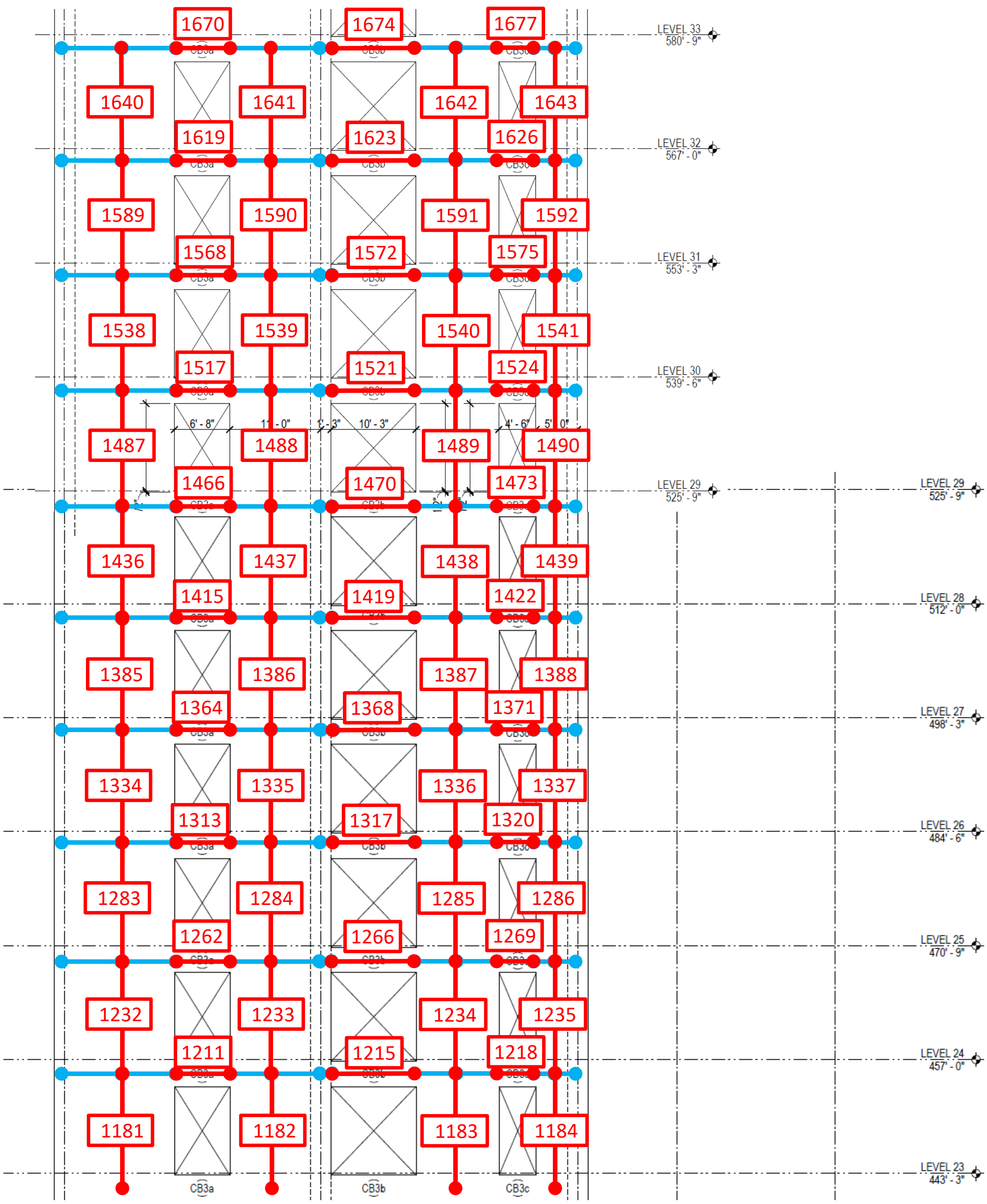
1670
1674
1677
LEVEL 33
580' - 9"
1640
1641
1642
1643
1619
1623
1626
LEVEL 32
567' - 0"
1589
1590
1591
1592
1568
1572
1575
LEVEL 31
553' - 3"
1538
1539
1540
1541
1517
1521
1524
LEVEL 30
539' - 6"
1487
1488
1489
1490
1466
1470
1473
LEVEL 29
525' - 9"
LEVEL 29
525' - 9"
1436
1437
1438
1439
1415
1419
1422
LEVEL 28
512' - 0"
1385
1386
1387
1388
1364
1368
1371
LEVEL 27
498' - 3"
1334
1335
1336
1337
1313
1317
1320
LEVEL 26
484' - 6"
1283
1284
1285
1286
1262
1266
1269
LEVEL 25
470' - 9"
1232
1233
1234
1235
1211
1215
1218
LEVEL 24
457' - 0"
1181
1182
1183
1184
LEVEL 23
443' - 3"
CB3a
CB3b
CB3c

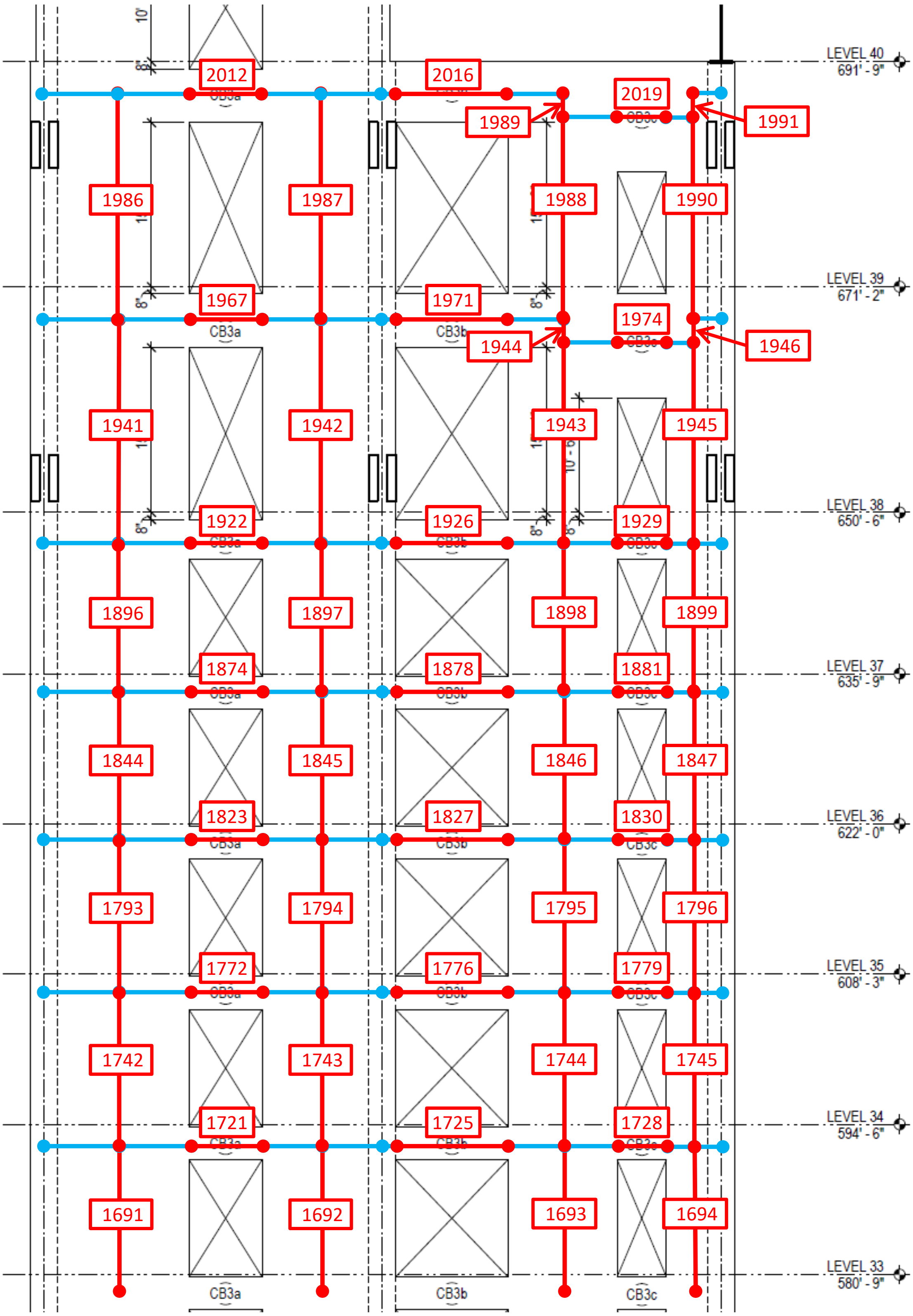
2012
2016
2019
1989
1991
LEVEL 40
691' - 9"
1986
1987
1988
1990
1967
1971
1974
1944
1946
LEVEL 39
671' - 2"
CB3a
CB3b
1941
1942
1943
1945
1922
1926
1929
LEVEL 38
650' - 6"
1896
1897
1898
1899
1874
1878
1881
LEVEL 37
635' - 9"
1844
1845
1846
1847
1823
1827
1830
LEVEL 36
622' - 0"
1793
1794
1795
1796
1772
1776
1779
LEVEL 35
608' - 3"
1742
1743
1744
1745
1721
1725
1728
LEVEL 34
594' - 6"
1691
1692
1693
1694
LEVEL 33
580' - 9"
CB3a
CB3b
CB3c

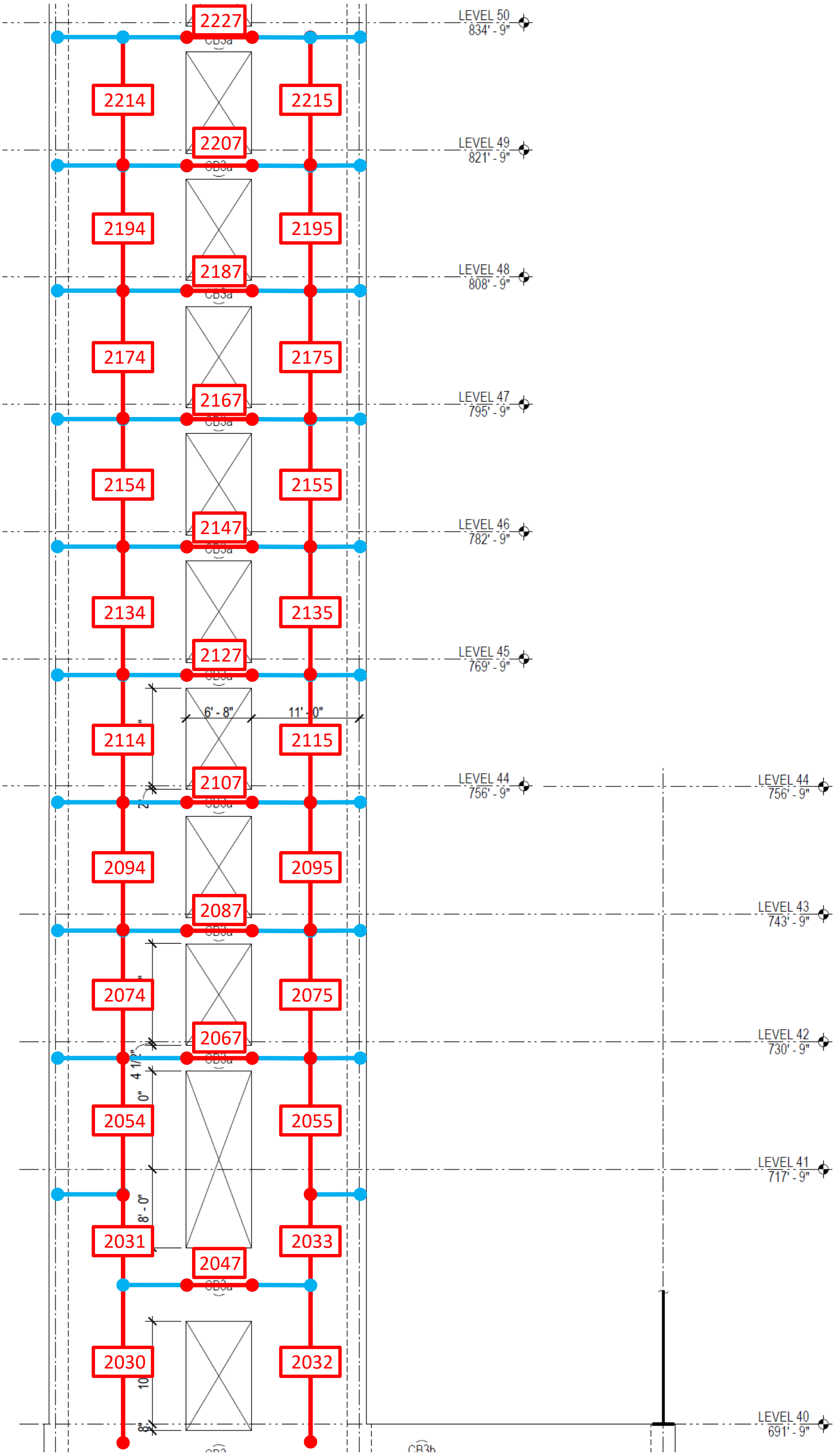
LEVEL 50
834' - 9"
LEVEL 49
821' - 9"
LEVEL 48
808' - 9"
LEVEL 47
795' - 9"
LEVEL 46
782' - 9"
LEVEL 45
769' - 9"
LEVEL 44
756' - 9"
LEVEL 43
743' - 9"
LEVEL 42
730' - 9"
LEVEL 41
717' - 9"
LEVEL 40
691' - 9"
2227
2214
2215
2207
2194
2195
2187
2174
2175
2167
2154
2155
2147
2134
2135
2127
2114
2115
2107
2094
2095
2087
2074
2075
2067
2054
2055
2031
2033
2047
2030
2032
6' - 8"
11' - 0"
8' - 0"

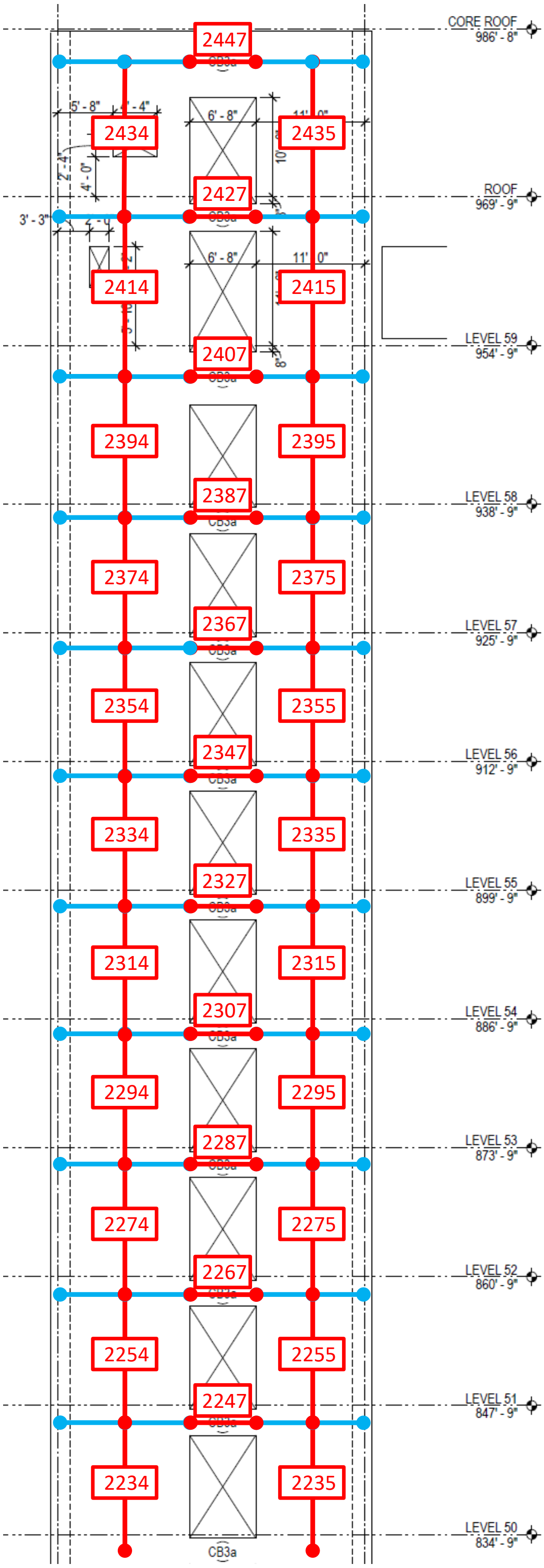
CORE ROOF
986' - 8"
2447
2434
2435
2427
ROOF
969' - 9"
2414
2415
2407
LEVEL 59
954' - 9"
2394
2395
2387
LEVEL 58
938' - 9"
2374
2375
2367
LEVEL 57
925' - 9"
2354
2355
2347
LEVEL 56
912' - 9"
2334
2335
2327
LEVEL 55
899' - 9"
2314
2315
2307
LEVEL 54
886' - 9"
2294
2295
2287
LEVEL 53
873' - 9"
2274
2275
2267
LEVEL 52
860' - 9"
2254
2255
2247
LEVEL 51
847' - 9"
2234
2235
CB3a
LEVEL 50
834' - 9"

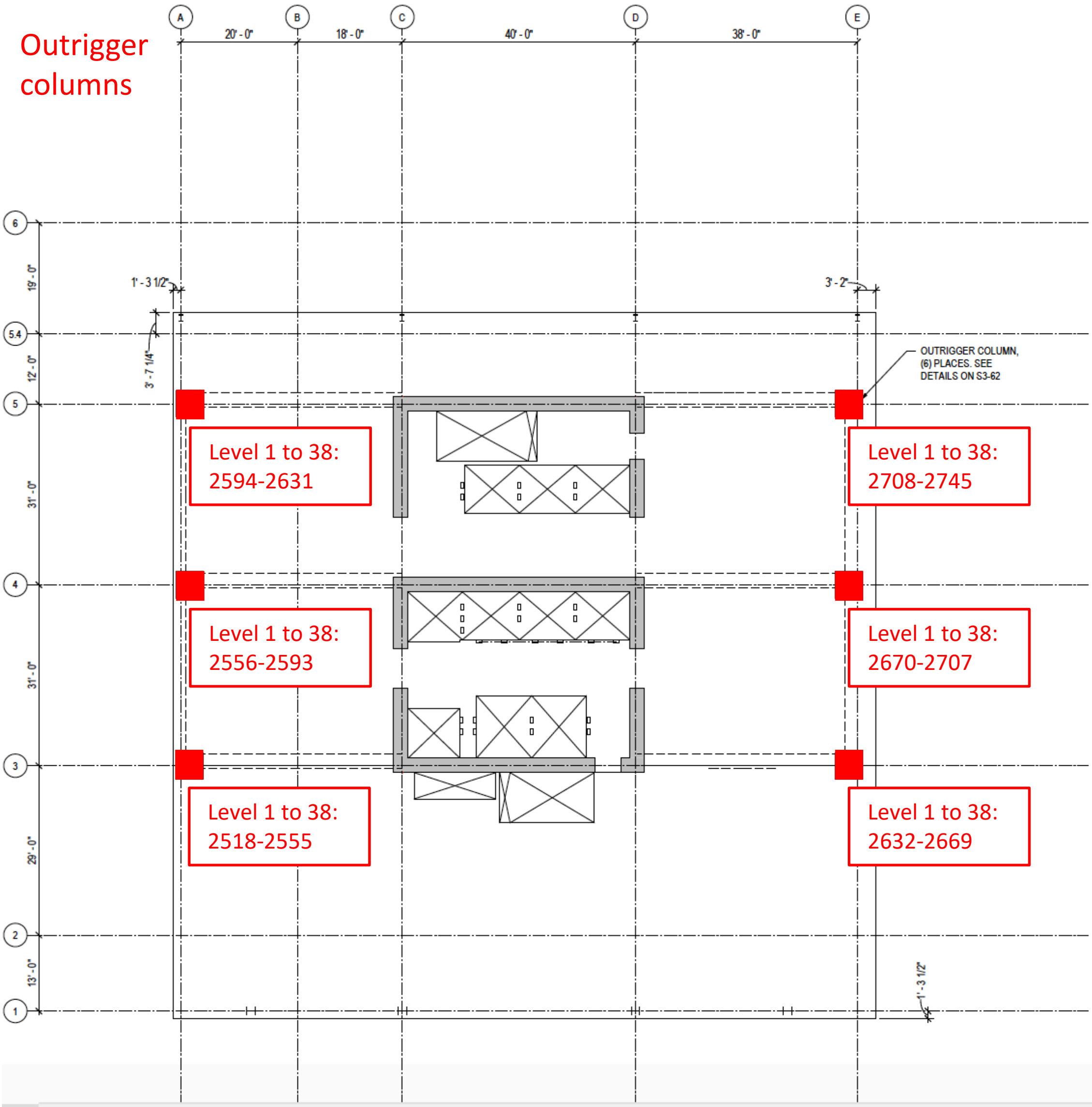
Outrigger columns
A
B
C
D
E
20' - 0"
18' - 0"
40' - 0"
38' - 0"
6
5.4
5
4
3
2
1
19' - 0"
12' - 0"
31' - 0"
31' - 0"
29' - 0"
13' - 0"
1' - 3 1/2"
3' - 2"
3' - 7 1/4"
1' - 3 1/2"
OUTRIGGER COLUMN, (6) PLACES. SEE DETAILS ON S3-62
Level 1 to 38: 2594-2631
Level 1 to 38: 2708-2745
Level 1 to 38: 2556-2593
Level 1 to 38: 2670-2707
Level 1 to 38: 2518-2555
Level 1 to 38: 2632-2669